

Silvia Romero Tamayo

# Insights into the conformational landscape and interaction networks in human Apoptosis Inducing Factor

Director/es

Ferreira Neila, Patricia  
Medina Trullenque, María Milagros

<http://zaguan.unizar.es/collection/Tesis>



Universidad de Zaragoza  
Servicio de Publicaciones

ISSN 2254-7606

Tesis Doctoral

INSIGHTS INTO THE CONFORMATIONAL  
LANDSCAPE AND INTERACTION NETWORKS IN  
HUMAN APOPTOSIS INDUCING FACTOR

Autor

Silvia Romero Tamayo

Director/es

Ferreira Neila, Patricia  
Medina Trullenque, María Milagros

**UNIVERSIDAD DE ZARAGOZA**  
**Escuela de Doctorado**

Programa de Doctorado en Bioquímica y Biología Molecular

2022





# Insights into the conformational landscape and interaction networks in human Apoptosis Inducing Factor



SILVIA ROMERO TAMAYO

TESIS DOCTORAL

2022



**UNIVERSIDAD DE ZARAGOZA**

**FACULTAD DE CIENCIAS**



DEPARTAMENTO DE BIOQUIMICA Y BIOLOGÍA MOLECULAR Y CELULAR

TESIS DOCTORAL

**Insights into the conformational landscape and interaction networks in  
human Apoptosis Inducing Factor**

Memoria presentada por SILVIA ROMERO TAMAYO,

Graduada en Biotecnología para optar al Grado de

Doctora por la Universidad de Zaragoza

Enero 2022



Dña. Milagros Medina Trullenque y Dña. Patricia Ferreira Neila, Catedrática y Profesora Contratado Doctor, respectivamente, del Departamento de Bioquímica y Biología Molecular y Celular de la Universidad de Zaragoza

**CERTIFICAN:**

Que la Tesis Doctoral **“Insights into the conformational landscape and interaction networks in human Apoptosis Inducing Factor”** ha sido realizada por la graduada **Silvia Romero Tamayo** en el Departamento de Bioquímica y Biología Molecular y Celular de la Facultad de Ciencias, y en el Instituto de Biocomputación y Física de Sistemas Complejos (BIFI), ambos de la Universidad de Zaragoza bajo su dirección, y que reúne, a su juicio, las condiciones requeridas para optar al grado de Doctora por la Universidad de Zaragoza.

Zaragoza, enero de 2022



Fdo.: Milagros Medina Trullenque



Fdo.: Patricia Ferreira Neila



---

***“Saber lo que quieres y para qué lo quieres,  
es la clave del éxito”.***

---

***Andrés Roca Rey***





***A MIS PADRES,***

***A VÍCTOR Y CAYETANA***

***POR SER SIEMPRE MI APOYO, MI REMANSO DE PAZ, CARIÑO Y PACIENCIA.***



## AGRADECIMIENTOS

---

Una vez finalizado el viaje, es momento de mirar atrás para agradecer a todas las personas que de un modo u otro me han acompañado en este camino. **Y para recorrer ese camino, hay que responder tres preguntas en el orden que aquí sigo:**

### **Primero, ¿Quién soy?**

En este aspecto he de agradecer a las Doctoras Milagros Medina y Patricia Ferreira, por haberme dado la opción de formarme bajo su tutela, demostrando una paciencia inagotable.

He de mencionar también al resto de profesorado y personal del departamento Carlos, Marta, Javier, que siempre han aportado consejos y compartido su buen hacer. A Raquel y Patricio, por su ayuda en la parte más “mitocondrial” de esta tesis y a Adrián y Sonia por su inestimable ayuda con el ITC.

### **Segundo ¿Dónde voy?**

Si en este camino, alguna vez me perdí he de agradecer a mi brújula personal. Lo más valioso que una persona pueda tener, mi familia. Gracias por todo el apoyo que siempre me ha brindado. A mis padres Jose y Manoli que tanto se han sacrificado a lo largo de estos años, para que hoy esto sea posible. Siempre me habéis hecho creer que podría conseguirlo, aunque a veces fuera duro. Me habéis inculcado el valor del trabajo y del esfuerzo y eso siempre os lo agradeceré. A Víctor, gracias por tu infinita paciencia, porque siempre estás ahí, incluso cuando yo no estoy. Gracias por acompañarme en este camino, dentro del viaje de la vida.

### **Tercero ¿Quién viene conmigo?**

Por suerte tengo buena compañía en mis viajes, y doy gracias a toda la gente que ha compartido esta aventura conmigo. Solo espero, que como no han sido pocos, no me deje a nadie en el tintero, pido perdón de antemano.

A mis compañeros de laboratorio, porque sin ellos este viaje hubiera pasado igual pero menos divertido y enriquecedor. A mis chicas del CIBIR, con vosotras empezó todo. Nerea, como no iba a acordarme de la que fui pollito una vez, gracias porque siempre estás ahí (aunque sigo sin perdonarte lo del Bromuro), y a Yoly, gracias por tus consejos y por tu ayuda.

Dicen que los amigos son la familia que uno elige. Por ello los englobo en familias que así no me dejo a nadie. A mis bebebirras (porque desde el instituto hemos pasado de bebebirras a bebé-birras), gracias por tantos años, tantos momentos y todo lo que nos queda por delante. Al clan de la magdalena y su emisora, gracias por vuestros “family days” y tantas y tantas “fiestas”. A mis pomelitas, Regi y Laura. Gracias por tantas risas, viajes, tantos momentos especiales y gracias por estas últimas semanas y a tantos amigos que “deje” en Zaragoza. Doy gracias de haberos conocido a todos.

Gracias por estar siempre ahí MI GENTE!!!.



## PUBLICACIONES DE ESTA TESIS DOCTORAL

---

El presente trabajo, ha permitido la publicación de los manuscritos aquí enumerados.

Villanueva, R., Romero-Tamayo, S., Laplaza, R., Martínez-Olivan, J., Velázquez-Campoy, A., Sancho, J., Ferreira, P. & Medina, M. 2019. Redox- and Ligand Binding-Dependent Conformational Ensembles in the Human Apoptosis-Inducing Factor Regulate Its Pro-Life and Cell Death Functions. *Antioxid Redox Signal*, 30, 2013-2029.

Romero-Tamayo S., Laplaza R, Velazquez-Campoy A., Villanueva R., Medina M & Ferreira P. 2021. W196 and the  $\beta$ -Hairpin Motif Modulate the Redox Switch of Conformation and the Biomolecular Interaction Network of the Apoptosis-Inducing Factor. *Oxid Med Cell Longev*, v.2021; 2021.



# INDEX

---

<b>1 INTRODUCTION .....</b>	<b>13</b>
1.1 THE APOPTOSIS INDUCING FACTOR.....	15
1.2 THE OXIDO-REDUCTASE ACTIVITY OF HAIF .....	24
1.3 THE PROGRAMMED CELL DEATH ROLE OF AIF .....	28
1.4 THE PRO-LIFE ROLE OF AIF IN THE MITOCHONDRIA .....	34
1.5 AIF AND DISEASE .....	38
<b>2 OBJECTIVES.....</b>	<b>45</b>
2.1 OBJECTIVES.....	47
<b>3 MATERIALS AND METHODS.....</b>	<b>49</b>
3.1 BIOLOGICAL MATERIAL .....	51
3.2 EXPRESSION VECTOR.....	52
3.2.1 EXPRESSION VECTOR CONSTRUCTIONS .....	53
3.3 MOLECULAR BIOLOGY METHODS .....	56
3.3.1 HIBRIDATION OF DNA.....	56
3.3.2 ISOLATION OF PLASMIDS .....	57
3.3.3 PRODUCTION OF <i>E. coli</i> THERMO-COMPETENT CELLS.....	57
3.3.4 TRASFORMATION OF COMPETENT <i>E. coli</i> CELLS.....	58
3.4 PRODUCTION OF RECOMBINANT PROTEINS .....	58
3.4.1 EVALUATION OF PROTEIN EXPRESSION .....	58
3.4.2 MEDIUM SCALE PROTEIN PRODUCTION .....	59
3.5 PURIFICATION OF RECOMBINANT PROTEINS .....	60
3.5.1 PREPARATION OF CRUDE EXTRACTS .....	60
3.5.2 His-TAG AFFINITY CHROMATOGRAPHY.....	60
3.5.3 SIZE-EXCLUSION CHROMATOGRAPHY.....	62
3.5.4 REMOVAL OF His <sub>6</sub> -TAGS FROM PURIFIED PROTEINS .....	62
3.6 GENERAL BIOCHEMICAL METHODS .....	63
3.6.1 DETERMINATION OF PROTEIN MOLECULAR WEIGTHS BY SIZE EXCLUSION CROMATOGRAPHY .....	63
3.6.2 ANALYSIS OF PROTEIN-DNA INTERACTIONS BY ELECTROPHORETIC MOBILITY SHIFT ASSAY .....	64
3.6.3 POLIACRYLAMIDE GEL ELECTROPHORESIS .....	65

3.6.4	CROSSLINKING STABILIZATION OF OLIGOMERIC ASSEMBLIES .....	67
3.6.5	CLEAR NATIVE COLORLESS POLYACRYLAMIDE GEL ELECTROPHORESIS .....	67
3.6.6	TWO-DIMENSIONAL ELECTROPHORESIS .....	69
3.6.7	WESTERN BLOT .....	71
3.7	SPECTROSCOPIC METHODS IN THE FUNCTIONAL AND STRUCTURAL CHARACTERIZATION OF PROTEINS .....	73
3.7.1	ULTRAVIOLET/VISIBLE ABSORTION SPECTROSCOPY .....	73
3.7.2	CIRCULAR DICHROISM SPECTROSCOPY .....	75
3.7.3	FLUORESCENCE SPECTROSCOPY .....	76
3.7.4	PROTEIN THERMAL DENATURATION AS FOLLOWED BY CD AND FLUORESCENCE .....	78
3.7.5	SPECTROSCOPIC EVALUATION OF CHARGE TRANSFER COMPLEX STABILITY .....	79
3.8	BIOPHYSICAL METHODS .....	79
3.8.1	ISOTHERMAL TRITATION CALORIMETRY .....	79
3.8.2	METHODS IN THE STUDY OF PROTEIN KINETICS .....	83
3.8.2.1	DETERMINATION OF STEADY STATE KINETIC PARAMETERS .....	83
3.8.2.2	DETERMINATION OF PRE-STEADY STATE KINETICS PARAMETERS BY STOPPED-FLOW SPECTROPHOTOMETRY .....	84
3.8.2.2.1	EQUIPMENT AND PREPARATION OF SAMPLES .....	84
3.8.2.2.2	DETERMINATION OF OBSERVED RATE CONSTANTS ( $k_{obs}$ ) FOR DIFFERENT PROCESSES INVOLVING hAIF <sub><math>\Delta</math>1-101</sub> AND hAIFmt <sub><math>\Delta</math>1-77</sub> .....	86
3.8.2.2.3	DETERMINATION OF THE RATES FOR CTC FORMATION UPON MIXING PHOTOREDUCED hAIF <sub><math>\Delta</math>1-101</sub> WITH NAD <sup>+</sup> .....	87
3.9	ANALYSIS SOFTWARE, BIOINFORMATIC AND COMPUTATIONAL TOOLS .....	89
<b>4</b>	<b>REDOX AND LIGAND BINDING-DEPENDENT CONFORMATIONAL ENSEMBLES IN THE HUMAN APOPTOSIS-INDUCING FACTOR REGULATE ITS PRO-LIFE AND CELL DEATH FUNCTIONS .....</b>	<b>91</b>
4.1	ABSTRACT .....	93
4.2	RESUMEN .....	94
4.3	INTRODUCTION .....	95
4.4	EXPERIMENTAL PROCEDURES .....	97
4.4.1	PROTEINS PRODUCTION .....	97
4.4.2	SPECTROSCOPIC CHARACTERIZATION .....	97
4.4.3	KINETIC MEASUREMENTS .....	98
4.4.4	THERMAL DENATURATION .....	98
4.4.5	FAD FLUORESCENCE BASED HIGH-THROUGHPUT SCREENING (HTS) .....	99
4.4.6	CELL VIABILITY ASSAYS .....	100



4.4.7 PRODUCTION OF STRUCTURAL MODELS .....	100
4.4.8 DATA ANALYSIS AND STATISTICS .....	101
4.5 RESULTS AND DISCUSSION .....	102
4.5.1 THE pH OF SUBCELLULAR COMPARTMENTS MODULATES hAIF FOLDING AND CONFORMATION .....	102
4.5.2 THERMAL STABILITY OF hAIF IS HIGHLY MODULATED BY FORMATION OF THE CTC .....	106
4.5.3 SOME ALLELIC PATHOGENIC MUTATIONS ALTER hAIF <sub>Δ1-101</sub> STABILITY .....	112
4.5.4 HTS ALLOWED THE IDENTIFICATION OF MOLECULES POTENTIALLY BINDING hAIF <sub>Δ1-101</sub> .....	120
4.5.5 EFFECT OF HTS HITS ON CELLULAR VIABILITY .....	124
4.5.6 EFFECTS OF SELECTED HTS HITS ON THE MOLECULAR AND REDOX PROPERTIES OF hAIF <sub>Δ1-101</sub> .....	125
4.6 CONCLUSION .....	128
<b>5 W196 AND THE β-HAIRPIN MOTIF MODULATE THE CONFORMATIONAL LANDSCAPE AND THE BIOMOLECULAR INTERACTION NETWORK OF THE APOPTOSIS INDUCING FACTOR.....</b>	<b>133</b>
5.1 ABSTRACT .....	135
5.2 RESUMEN .....	136
5.3 INTRODUCTION .....	137
5.4 MATERIAL AND METHODS .....	141
5.4.1 EXPRESSION AND PRODUCTION OF PROTEINS .....	141
5.4.2 MOLECULAR WEIGHT DETERMINATION BY SIZE EXCLUSION CHROMATOGRAPHY .....	142
5.4.3 STABILIZATION OF CROSS-LINKED PROTEIN OLIGOMERS AND ELECTROPHORETIC ANALYSIS .....	142
5.4.4 SPECTROSCOPIC CHARACTERIZATION .....	143
5.4.5 THERMAL DENATURATION ASSAYS .....	143
5.4.6 KINETICS MEASUREMENTS .....	144
5.4.7 ISOTHERMAL TITRATION CALORIMETRY (ITC) .....	145
5.4.8 GENERATION OF STRUCTURAL MODELS .....	146
5.4.9 MD SIMULATIONS .....	146
5.4.10 DATA ANALYSIS .....	147
5.5 RESULTS AND DISCUSSION .....	148
5.5.1 MUTATIONS AT W196 RESIDUE HARDLY IMPACTS THE OVERALL hAIF <sub>Δ1-101</sub> CORE CONFORMATIONAL PROPERTIES IN OXIDIZED AND NADH-REDUCED STATES .....	148
5.5.2 W196 SIDE-CHAIN MODULATES THE MONOMER-DIMER EQUILIBRIUM IN hAIF <sub>Δ1-101</sub> .....	152

5.5.3 W196 HIGHLY CONTRIBUTES TO MODULATE THE LOW EFFICIENCY OF hAIF <sub>Δ1-101</sub> AS NADH OXIDASE .....	154
5.5.4 W196 CONTRIBUTES TO STABILIZE THE CTC STATE .....	162
5.5.5 W196 MUTATIONS REDUCE THERMOSTABILITY OF hAIF <sub>Δ1-101</sub> , BUT NOT OF THE CTCS.....	164
5.5.6 W196 HAS A KEY IMPACT IN THE CONFORMATION OF THE INTERACTION SURFACES OF hAIF <sub>Δ1-101</sub> WITH ITS PHYSIOLOGICAL PARTNERS .....	165
5.5.7 W196 CONTRIBUTES TO CONTROL THE hAIF CONFORMATIONAL LANDSCAPE TO ADAPT TO ITS PHYSIOLOGICAL ROLES.....	173
5.6 CONCLUSIONS .....	175
<b>6 ANALYSIS OF MITOCHONDRIAL VARIANTS IN THE REDOX FUNCTION OF HUMAN APOPTOSIS INDUCING FACTOR .....</b>	<b>177</b>
6.1 ABSTRACT .....	179
6.2 RESUMEN .....	180
6.3 INTRODUCTION .....	181
6.4 MATERIAL AND METHODS .....	183
6.4.1 OVEREXPRESSION AND PURIFICATION OF hAIF AND CHCHD4 VARIANTS.....	183
6.4.2 SPECTROSCOPIC CHARACTERIZATION.....	184
6.4.3 EVALUATION OF MONOMER-DIMER STATES BY SIZE-EXCLUSION CHROMATOGRAPHY.....	184
6.4.4 ISOTHERMAL TITRATION CALORIMETRY (ITC) .....	184
6.4.5 KINETICS MEASUREMENTS.....	185
6.4.6 DATA ANALYSIS AND STATISTIC .....	186
6.5 RESULTS AND DISCUSION.....	186
6.5.1 QUATERNARY ORGANIZATION OF MITOCHONDRIAL VARIANTS AND THE INFLUENCE OF CHCHD4 ON THEIR STABILITY .....	186
6.5.2 hAIF MITOCHONDRIAL VARIANT AFFINITY FOR CHCHD4 .....	189
6.5.3 IMPACT OF CHCHD4 ON STEADY STATE KINETIC PARAMETERS OF hAIF MITOCHONDRIAL VARIANT .....	192
6.5.4 PRE-STEADY-STATE PARAMETERS FOR THEIR FORMATION AND STABILITY.....	193
6.5.5 STABILITY OF CHARGE TRANSFER COMPLEXES .....	195
6.6 CONCLUSIONS .....	196
<b>7 INSIGHTS INTO THE DEGRADOSOME FORMATION: HUMAN APOPTOSIS INDUCING FACTOR INTERACTION WITH PRO-APOPTOTIC PARTNERS .....</b>	<b>199</b>
7.1 ABSTRACT .....	201
7.2 RESUMEN .....	202

7.3 INTRODUCTION .....	203
7.4 MATERIAL AND METHODS .....	204
7.4.1 OVEREXPRESSION AND PURIFICATION OF PROTEINS .....	204
7.4.2 CLEAR NATIVE AND 2D DENATURING ELECTROPHORESIS .....	205
7.4.3 SIZE EXCLUSION CHROMATOGRAPHY .....	206
7.4.4 ATOMIC FORCE MICROSCOPY .....	206
7.4.5 ISOTHERMAL TITRATION CALORIMETRY .....	207
7.5 RESULTS AND DISCUSSION .....	209
7.5.1 VISUALISING THE DEGRADOSOME ASSEMBLY AT MOLECULAR LEVEL .....	209
7.5.2 BINARY INTERACTIONS BETWEEN DEGRADOSOME COMPONENTS .....	213
7.5.3 DNA-DEGRADOSOME ASSEMBLY AND COOPERATIVE EFFECTS .....	216
7.5.4 FREE GIBBS ENERGY FLOW IN THE DEGRADOSOME ASSEMBLY .....	221
7.5.5 PROTEIN-DNA VISUALIZATION BY AFM IMAGING .....	223
7.6 CONCLUSIONS .....	226
<b>8 DISCUSSION .....</b>	<b>229</b>
<b>9 CONCLUSIONS .....</b>	<b>239</b>
<b>10 BIBLIOGRAPHY .....</b>	<b>245</b>



# INDEX OF FIGURES AND TABLES

---

## 1. INTRODUCTION

### Figures

1.1	Alignment of hAIF	16
1.2	hAIF processing, subcellular localization, and partners	17
1.3	Cartoon representation of the three-dimensional structure of hAIF $_{\Delta 1-101}$	19
1.4	Structure of the hAIF $_{\Delta 1-101}$ rd:2NAD(H) dimer	20
1.5	Comparative of the oxidoreductase active site of hAIF $_{\Delta 1-101}$ and hAIF $_{\Delta 1-101}$ :2NAD(H)	21
1.6	Conformational changes observed in hAIF upon NADH induced dimerization and reduction	22
1.7	Schematic representation of the five different isoforms reported for hAIF	23
1.8	Physiological forms of hAIF and CTC formation	26
1.9	Major cell death subroutines	29
1.10	Schematic representation of main apoptotic pathways	30
1.11	AIF mediates nuclear and cytoplasmic effects of PCD in response to select stimuli	32
1.12	Molecular model illustrating the potential organisation of a DNA degradosome	33
1.13	Function of AIF in OXPHOS	35
1.14	Ribbon diagram of the lowest-energy conformer of MIA40 2S-S	36
1.15	Schematic representation of the CHCHD4 import and interaction with AIF	37
1.16	Pathophysiological effects of hAIF mutations	38
1.17	Structural and <i>in vitro</i> analyses of hAIF and hAIF $_{\Delta R201}$	41
1.18	Structural Comparison of the WT and hAIF E493V	43

### Tables

1.1	Steady-state and pre-steady-state kinetic parameters for the NADH oxidase activity of hAIF	25
1.2	Steady-state and pre-steady-state kinetic parameters for the NADH oxidase activity of hAIF variants	28
1.3	Differences between the main apoptotic paths	31
1.4	Summary of identified hAIF disease-causing mutations and their clinical presentations in patients	40

## 3. MATERIAL AND METHODS

### Figures

3.1	Map of the pET-28a(+) expression vector	52
3.2	Basic steps for plasmid purification using the GenElute plasmid Miniprep kit	57
3.3	Affinity column scheme for purification of proteins containing His6-tags	61
3.4	Schematic representation of a size-exclusion chromatography column	62
3.5	Scheme of a His <sub>6</sub> -tag removal process	63
3.6	Calibration of the column	64
3.7	Assembly of the Mini-PROTEAN	66
3.8	Bis(sulfoacetic acid)suberate (BS <sup>3</sup> )	67
3.9	Assembly for gradient preparation	69
3.10	Workflow of a 2-D gel electrophoresis protocol	70
3.11	Transference system	71
3.12	Schematic representation of an UV-Vis spectrophotometer	73
3.13	Representative CD spectra of secondary structure elements in proteins	75
3.14	Jablonski diagram	77
3.15	Scheme of an ITC system and example of typical results	80
3.16	Scheme of the diaphorase steady-state activity	83
3.17	Stopped Flow spectrophotometer	85

3.18 Scheme of the anaerobic manifold system .....	87
--	----

## Tables

3.1 Colour code for the elements present in the protein constructions .....	53
3.2 Summary of the constructions used for the production of proteins .....	55
3.3 Summary of the hAIF $\Delta$ 1-101 and hAIFmt $\Delta$ 1-77 mutants .....	56
3.4 Summary of conditions for expression and purification of the different proteins .....	59
3.5 Solution mixtures for preparation of gels with different polyacrylamide contents .....	65
3.6 Solutions for preparation of clear native gels .....	68
3.7 Composition of the second-dimension electrophoretic gel .....	70
3.8 Summary of antibodies used for protein detection .....	72
3.9 Molar extinction coefficients for the different proteins used in this study .....	74
3.10 Enthalpies of ionization of different buffers .....	82
3.11 Volumes used for the reaction mixture .....	83

## 4. REDOX AND LIGAND BINDING-DEPENDENT CONFORMATIONAL ENSEMBLES IN THE HUMAN APOPTOSIS-INDUCING FACTOR REGULATE ITS PRO-LIFE AND CELL DEATH FUNCTIONS

## Figures

4.1 Visible absorption spectra of WT hAIF isoforms as a function of pH .....	102
4.2 Spectral evolution upon reduction of hAIF $\Delta$ 1-101ox/hAIFmt $\Delta$ 1-77 .....	104
4.3 Circular dichroism spectra of WT hAIF .....	105
4.4 Fluorescence emission spectra of hAIF $\Delta$ 1-101 .....	106
4.5 Conformation of hAIF $\Delta$ 1-101ox and its CTC .....	106
4.6 Thermal unfolding curves for hAIF $\Delta$ 1-101 .....	107
4.7 Conformation of hAIF $\Delta$ 1-101ox and its CTC .....	109
4.8 Dynamics of relaxation of models of hAIF $\Delta$ 1-101 variants .....	111
4.9 Conformational changes in hAIF $\Delta$ 1-101 induced by CTC formation and R201 deletion .....	112
4.10 The $\Delta$ R201, G308E, and E493V hAIF $\Delta$ 1-101 variants .....	113
4.11 Circular dichroism spectra of $\Delta$ R201, G308E, and E493V hAIF $\Delta$ 1-101 variants .....	115
4.12 Effect of $\Delta$ R201A, G308E and E493V hAIF $\Delta$ 1-101 pathogenic mutations on the temperature for FAD release .....	114
4.13 Unfolding properties of hAIF $\Delta$ 1-101 variants .....	116
4.14 Predicted hAIF $\Delta$ 1-101 conformational changes by R201 deletion .....	119
4.15 Effect of binders on the thermal stability of hAIF $\Delta$ 1-101 .....	120
4.16 Interaction of hAIF $\Delta$ 1-101 with ATA .....	121
4.17 Thermo FAD HTS screening for compounds binding hAIF $\Delta$ 1-101 .....	122
4.18 Viability of HeLa cells in the presence of hAIF $\Delta$ 1-101ox HTS hits .....	124
4.19 Effect of binders on the spectroscopic properties of hAIF $\Delta$ 1-101 .....	126
4.20 Effect of selected HTS hits on hAIF $\Delta$ 1-101 thermal unfolding and predicted binding modes .....	128

## Tables

4.1 Effect of the pH on the pre-steady kinetic rates for the aerobic reduction of hAIF $\Delta$ ox by NADH .....	103
4.2 Effect of pH on the thermal stability of Wild Type hAIF $\Delta$ 1-101ox, hAIFmt $\Delta$ 1-77ox, and of their Charge Transfer Complexes .....	110
4.3 Effect of the $\Delta$ R201, G308E and E493V hAIF $\Delta$ 1-101 mutations on the thermal stability of hAIF $\Delta$ 1-101 and of its CTC .....	118
4.4 Properties of hAIF $\Delta$ 1-101 HTS hits .....	123
4.5 Effect of ATA, C2 and C11 on the thermal stability of hAIF $\Delta$ 1-101 .....	127
4.6 Effect of selected compounds on the steady state kinetic parameters of the hAIF $\Delta$ 1-101 DCPIP diaphorase activity .....	127

## 5. W196 AND THE $\beta$ -HAIRPIN MOTIF MODULATE THE CONFORMATIONAL LANDSCAPE AND THE BIOMOLECULAR INTERACTION NETWORK OF THE APOPTOSIS INDUCING FACTOR

### Figures

5.1 Comparative overview of the crystallographic structures of WT hAIF $\Delta$ 1-101 WT CTC hAIF $\Delta$ 1-101rd: 2NAD(+H) and W196A variant .....	138
5.2 Comparative overview of the crystallographic structures of WT hAIF $\Delta$ 1-101, W196A hAIF $\Delta$ 1-101 and WT hAIF $\Delta$ 1-101:2NAD(H) CTC. ....	139
5.3 Visible absorption spectra of WT, W196Y,W196L and W196A .....	148
5.4 Spectral properties of the W196 hAIF $\Delta$ 1-101 variants .....	149
5.5 Dynamics of the models of hAIF $\Delta$ 1-101 variants .....	150
5.6 Dynamics of the active site in hAIF $\Delta$ 1-101 variants .....	151
5.7 Effect of W196 replacement on the hAIF $\Delta$ 1-101 ability to stabilize dimers .....	153
5.8 Kinetic characterization of W196 hAIF $\Delta$ 1-101 variants .....	156
5.9 Kinetic characterization of W196 hAIF $\Delta$ 1-101 variants .....	158
5.10 Impact of mutations on hAIF $\Delta$ 1-101 flexibility. ....	159
5.11 Impact of W196 hAIF $\Delta$ 1-101 mutations on the dynamics of the $\beta$ -hairpin and its environment. ....	161
5.12 Effect of W196 replacements on the CTC half-life and the thermal stability of hAIF $\Delta$ 1-101. ....	163
5.13 Effect of the W196 replacement in the binding of CHCHD4 to hAIF $\Delta$ 1-101. ....	167
5.14 Effect of W196 mutations on the binding to CypA and dsDNA to hAIF $\Delta$ 1-101. ....	168
5.15 Thermodynamic dissection of the interaction of the different hAIF $\Delta$ 1-101 variants with interacting partners. ....	170
5.16 Dynamics of the interaction surfaces for partners in hAIF $\Delta$ 1-101 variants .....	173

### Tables

5.1 Steady-state and pre-steady state kinetic parameters of WT hAIF $\Delta$ 1-101 and its W196 variants .....	155
5.2 Thermal stability for flavin release of WT and W196 hAIF $\Delta$ 1-101 variants in oxidized and CTC states. ....	165
5.3 Thermodynamic parameters for the binary interaction of hAIF $\Delta$ 1-101 variants with CHCHD4, CypA and DNA .....	171

## 6- ANALYSIS OF MITOCHONDRIAL VARIANTS IN THE REDOX FUNCTION OF HUMAN APOPTOSIS INDUCING FACTOR

### Figures

6.1 Dimerization assays upon NADH binding .....	187
6.2 Interaction of the mitochondrial forms with CHCHD4 .....	189
6.3 Thermodynamic contributions to the binding of CHCHD4 to the hAIFmt variants .....	191
6.4 Effect of CHCHD4 on the pre-steady-state kinetics for NADH reduction of hAIFmt $\Delta$ 1-77 and its triple variant .....	194
6.5 Lifetime for hAIFmt $\Delta$ 1-77 and hAIF3Mmt $\Delta$ 1-77 CTCs versus molecular oxygen reoxidation .....	195

### Tables

6.1 Apparent molecular weights of major hAIF eluting peaks detected by molecular exclusion chromatographic .....	188
6.2 Thermodynamic parameters for the interaction of hAIF $\Delta$ 1-101 and hAIFmt $\Delta$ 1-77 variants with CHCHD4 .....	190
6.3 Kinetic parameters of hAIF variants in steady state and pre-steady state .....	192

## 7. INSIGHTS INTO THE DEGRADOSOME FORMATION: HUMAN APOPTOSIS INDUCING FACTOR INTERACTION WITH PRO-APOPTOTIC PARTNERS

### Figures

7.1 Quaternary composition of the degradosome.....	209
7.2 AFM imaging of proteins involved in the degradosome formation and of their binary and ternary associations.....	212
7.3 Calorimetric titrations and thermodynamic parameters for binary interactions among the DNA-degradosome components.....	214
7.4 Calorimetric titrations for ternary and quaternary interactions among the different DNA-degradosome complex components.....	217
7.5 Thermodynamic dissection of the interactions in ternary and quaternary organizations.....	219
7.6 Binding cooperativity of the DNA-degradosome components to hAIF $\Delta$ 1-101.....	220
7.7 Free Gibbs energy flow in the DNA-degradosome assembly.....	222
7.8 AFM imaging study of the binding of dsDNA to the degradosome components.....	223

### Tables

7.1 Enthalpies of ionisation of different buffers used.....	208
7.2 Quaternary assemblies of hAIF $\Delta$ 1-101 with its apoptotic partners.....	210
7.3 Distribution of quaternary species identified by AFM.....	213
7.4 Thermodynamic parameters for the interaction of hAIF $\Delta$ 1-101 with CypA, H2AX and dsDNA.....	215
7.5 Thermodynamic parameters for the interaction of AIF $\Delta$ 1-101 with dsDNA in different buffers.....	216
7.6 Influence of the association order of components of the DNA-degradosome on the binding thermodynamic parameters.....	218
7.7 Cooperativity coefficients ( $\alpha$ ) for the binding to hAIF $\Delta$ 1-101 of the different components of the DNA-degradosome complex.....	219
7.8 Effect of dsDNA binding on the quaternary organisation distribution of the degradosome components.....	225

## 8. DISCUSSION

### Figures

8.1 Proposed Model for the degradosome formation.....	239
---	-----



## ABBREVIATURES

---

<b>ΔT<sub>m</sub></b>	Melting temperature variation
<b>ΔT<sub>m</sub>max</b>	Maximal melting temperature variation
<b>ΔΨ<sub>m</sub></b>	Mitochondrial transmembrane potential
<b>5-dRF</b>	5-deazariboblastin
<b>Abs</b>	Absorbance
<b>ADP</b>	Adenosine diphosphate
<b>AFM</b>	Atomic Force Microscopy
<b>AIF</b>	Apoptosis Inducing Factor
<b>APAF-1</b>	Apoptotic protease activating factor 1
<b>APS</b>	Ammonium persulfate
<b>ATA</b>	Aurintricarboxylic acid
<b>ATP</b>	Adenosine triphosphate
<b>BN-PAGE</b>	Blue native polyacrylamide electrophoresis
<b>BS3</b>	Homobifunctional-Bis[sulfosuccinimidyl]-suberate
<b>cDNA</b>	Complementary DNA
<b>CHCHD4</b>	Coiled-coil-helix-coiled-coil-helix domain containing 4
<b>CTC</b>	Charge transfer complex
<b>CV</b>	Column volume
<b>CypA</b>	Cyclophilin A
<b>Cyt c</b>	Cytochrome c
<b>Da</b>	Dalton (atomic mass unit)
<b>DCPIP</b>	2,6-dichlorophenolindophenol
<b>DMSO</b>	Dimethyl sulfoxide
<b>DNA</b>	Desoxyribonucleic acid
<b>DTT</b>	Dithiotreitol dUTP 2'-deoxyuridine 5'-triphosphate
<b>EDTA</b>	Ethylene diamine tetraacetic acid
<b>Endo G</b>	Endonuclease G
<b>ETC</b>	Electron transport chain
<b>FAD</b>	Flavin adenine dinucleotide
<b>FADH<sub>2</sub></b>	Reduced flavin adenine dinucleotide
<b>hAIF</b>	Human AIF isoform
<b>hAIFox</b>	Oxidized hAIF
<b>hAIFrd</b>	Reduced hAIF
<b>hAIF<sub>Δ1-101</sub></b>	hAIF truncated at aminoacid 101
<b>hAIF<sub>Δ1-54</sub></b>	hAIF truncated at aminoacid 54
<b>Hq</b>	Harlequin
<b>Hsp70</b>	Heat-shock protein 70
<b>HT</b>	Hydride transfer
<b>HTS</b>	High Throughput Screening
<b>IMM</b>	Inner mitochondrial membrane
<b>IMS</b>	Intermembrane space
<b>IMSS</b>	Inner membrane sorting signal
<b>IPTG</b>	Isopropyl-β-thio-D-galactopyranoside
<b>ITC</b>	Isothermal titration calorimetry
<b>k<sub>cat</sub></b>	Catalytic constant
<b>K<sub>d</sub></b>	Dissociation constant
<b>K<sub>m</sub></b>	Affinity constant
<b>KO</b>	Knock-out
<b>k<sub>obs</sub></b>	Observed constant
<b>KPi</b>	Potassium phosphate
<b>LB</b>	Luria Bertani culture media
<b>mAIF</b>	Mouse AIF isoform
<b>MLS</b>	Mitochondrial localization sequence
<b>MOMP</b>	Mitochondrial outer membrane permeabilization
<b>MOPS</b>	3-(N-morpholino) propanesulfonic acid
<b>NADH</b>	Nicotinamide adenine dinucleotide

<b>NADPH</b>	Nicotinamide adenine dinucleotide phosphate
<b>NLS</b>	Nuclear leading sequence
<b>OD</b>	Optical density
<b>OPA1</b>	Optic atrophy 1 protein
<b>OXPHOS</b>	Oxidative phosphorylation
<b>PAGE</b>	Polyacrylamide gel electrophoresis
<b>PARP-1</b>	Poly-[ADP-ribose] polymerase 1
<b>PCD</b>	Programmed cell death
<b>PDB</b>	Protein Data Bank
<b>PEST</b>	Proline/ Glutamic acid/ Serine/ Theronine rich
<b>PS</b>	Phosphatidylserine
<b>PVDF</b>	Polyvinylidene difluoride
<b>RNA</b>	Ribonucleic acid
<b>ROS</b>	Reactive oxygen species
<b>r.p.m</b>	Revolutions per minute
<b>SDS</b>	Sodium dodecyl sulfate
<b>SPR</b>	Surface plasmon resonance
<b>TBS</b>	Tris-buffered saline
<b>TBST</b>	Tris-buffered saline with tween
<b>TEMED</b>	N,N,N',N'-tetramethylethylenediamine
<b>Tm</b>	Melting temperature
<b>TM</b>	Transmembrane region
<b>dUTP</b>	Nick End Labeling
<b>UV</b>	Ultraviolet
<b>WT</b>	Wild type



## *1- INTRODUCTION*



There are numerous examples in nature where multicellular organizations have to prioritise the proper functioning of the system in detriment of any individual consideration. That is why some proteins can be found playing functions that are contradictory at a glance, but necessary to maintain the main goals of any living organism: development, reproduction and survival (Bich et al., 2019).

The apoptosis-inducing factor (AIF) is a clear example of such type of proteins. It was firstly described as a mitochondrial flavoprotein involved in caspase independent programmed cell death (PCD) (Susin et al., 1999b), but soon after a key role for this protein in the integrity and/or biogenesis of respiratory complexes was envisaged (Vahsen et al., 2004). Thus, AIF is a moonlight protein that participates in the “decision” between cell life and death (Jeffery, 2014).

## 1.1 THE APOPTOSIS INDUCING FACTOR

In 1996, Susin and co-workers found that the mitochondrial intermembrane protein fraction contained an activity which sufficed to force isolated HeLa nuclei to adopt an apoptotic morphology and to lose part of their DNA content. That activity was termed “apoptosis-inducing factor” (Zamzami et al., 1996, Susin et al., 1996). Later on, in 1999, the same group purified a protein that maintained apoptosis inducing activity in the presence of a broad range of caspase inhibitors. This protein was termed as the detected activity, “apoptosis-inducing factor” (herein AIF) (Susin et al., 1999a). Thus, AIF was first identified as a highly conserved FAD-dependent protein located in the intermembrane mitochondrial space (IMS) and able to induce caspase independent apoptosis (Susin et al., 1999b). AIF is a flavoprotein/flavoenzyme, a type of proteins that contain as prosthetic group at least one of the riboflavin derivatives Flavin Mononucleotide (FMN) and/or Flavin Adenine Dinucleotide (FAD). These cofactors allow flavoproteins and flavoenzymes to be involved in a variety of biochemical reactions, including hydroxylation and dehydrogenation of metabolites, but which are particularly relevant in oxido-reduction processes (Barile et al., 2013, Massey et al., 1978, Macheroux, 1999).

The gene encoding AIF is codified by 16 exons and located on chromosome X (Xq25 - Xq26 and A6 regions in humans and mice, respectively) (Daugas et al., 2000, Loeffler et al., 2001). The most abundant AIF transcript, known as AIFM1 or AIFexon2a, is translated in the cytoplasm into a protein of approximately 67 kDa with 613 residues in humans (herein hAIF) and 612 in mice (herein mAIF). hAIF and mAIF show 92 % aminoacid identity, and hAIF is expressed ubiquitously in human tissues (Daugas et al., 2000). In addition, AIF is phylogenetically preserved, sharing homology with oxidoreductases from

other vertebrates (*Xenopus laevis*), non-vertebrate animals (*Caenorhabditis elegans*, *Drosophila melanogaster*), ascorbate reductases of plants, as well as NADH oxidases from fungi and bacterial (Lorenzo et al., 1999, Susin et al., 1999a).

AIF's sequence (**Figure 1.1**) contains:

- A bipartite-type mitochondrial leading sequence (MLS):
  - i) MLS1 (1-MFRCGGLAAGAFKQKLVLVVRTVYVQRPKQRNRLP-37)
  - ii) MLS2 (63-IDNSVLVLIVGLSTVGAGAYAYKTMK-89)
- An inner membrane sorting signal (IMSS) at its 36-82 N-terminal residues
- A transmembrane region through its 67-83 residues
- Two nuclear localisation sequences (NLS):
  - i) NLS1 (278-KSRTTLFRKIGDFRSLEKISREVK-302)
  - ii) NLS2 (446-KLBRRRV-452)

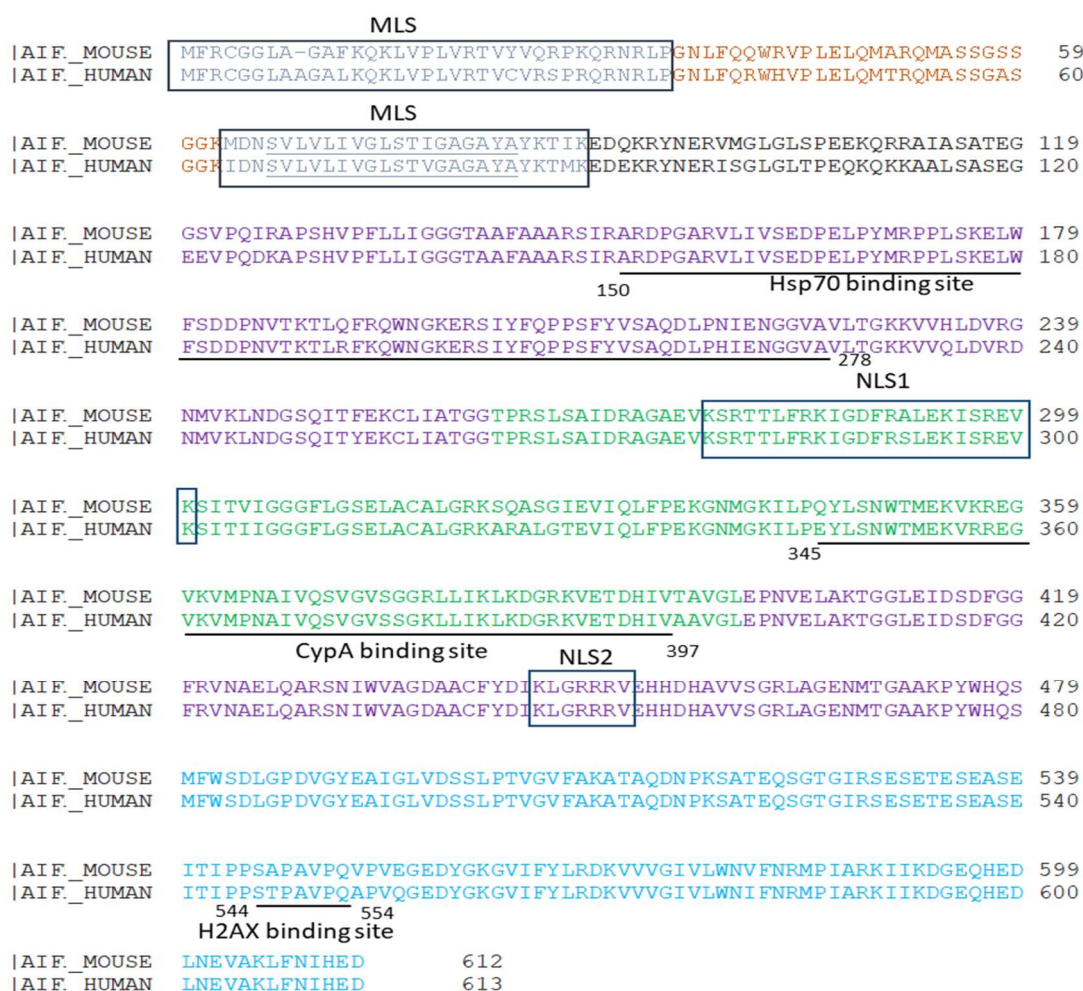


**Figure 1.1: Alignment of hAIF (GenBank AF100928) and mAIF (GenBank AF100927) amino-acid sequences.** Residues corresponding to the FAD-binding, NADH-binding and C-terminal domains are shown in purple, green and blue respectively. Boxes indicate MLS and NLS regions. Transmembrane residues in the MLS sequence are underlined. Regions predicted for interaction with protein partners are black bold underlined (Ye et al., 2002, Lipton and Bossy-Wetzel, 2002, Susin et al., 1999b).

Once in the mitochondrial IMS, the MLS of the hAIF precursor is proteolytically truncated after Met53, generating the hAIF $_{\Delta 1-53}$  62 kDa mature mitochondrial isoform. hAIF $_{\Delta 1-53}$  anchors to the inner mitochondrial membrane (IMM) through the specific IMSS contained in its N-terminal helix, while the main protein portion folds towards the IMS and incorporates one molecule of FAD cofactor (Robinson and Lemire, 1996, Otera et al., 2005, Modjtahedi et al., 2006). There, under physiological conditions, it interacts with the CHCHD4 protein, related to the biogenesis of the respiratory chain complexes (see section 1.3).

Specific death stimuli induce the hAIF $_{\Delta 1-54}$  proteolytically cleavage after Leu101, resulting in the apoptotic hAIF $_{\Delta 1-101}$  form of 54 kDa that is released into the cytosol (**Figure 1.2**) (Bano and Prehn, 2018). In the cytosol, hAIF $_{\Delta 1-101}$  can interact with the heat shock 70-kDa protein (HSP70) or with the endonuclease Cyclophilin A (CypA) in antagonistic and redox-controlled manners (Gurbuxani et al., 2003).

Thioredoxin (TRX1) mediates the regulation of the AIF redox status and favours its binding to either HSP70 or CypA (Shelar et al., 2015). The interaction with HSP70 promotes hAIF retention in the cytoplasm (Ravagnan et al., 2001). On the contrary, formation of the hAIF:CypA complex somehow activates the hAIF $_{\Delta 1-101}$  NLSs and facilitates the translocation of this complex into the nucleus. hAIF:CypA complex recruits the Histone H2AX in the nucleus and promotes DNA degradation into 20- to 50-kb fragments, consequently inducing chromatin condensation and cell disassembly (Susin et al., 1999b, Farina et al., 2017, Zhu et al., 2007, Cande et al., 2004).

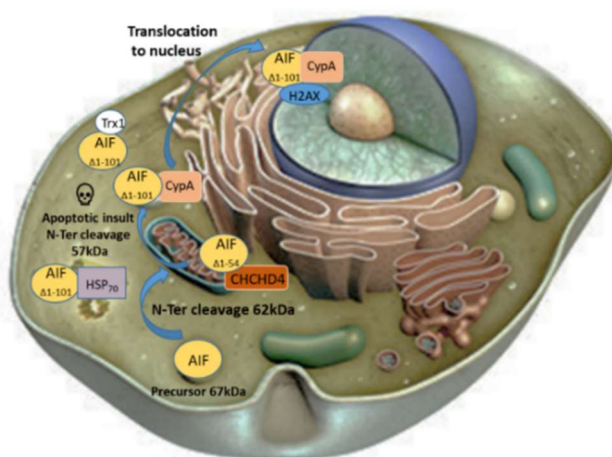


**Figure 1.2: hAIF processing, subcellular localization, and partners.** hAIF is synthesised by cytoplasmic ribosomes and imported into the IMS. There, it is tethered to the IMM through its N-terminal, folds towards the IMM and incorporates the FAD cofactor. Upon an apoptotic insult, hAIF is cleaved at amino acid 101, released from mitochondria to the cytosol, and translocated into the nucleus.

In 2002, the first three-dimensional structures of the oxidised states of both mAIF (residues 121-610, 2.0 Å, PDB 1GV4) (Maté et al., 2002) and hAIF (residues 128-608, 1.8 Å, PDB 1M6I) (Ye et al., 2002) were reported. Oxidised structures at improved resolution were provided afterwards (mAIF 128-610, PDB 3GD3 (Sevrioukova, 2009) and hAIF 1.8 Å, PDB 4BV6 (Ferreira et al., 2014)), as well as structures of the reduced proteins in complex with the NAD<sup>+</sup> coenzyme (mAIF in PDB 3GD4 (Sevrioukova, 2009), hAIF:NAD<sup>+</sup> at 2.88 Å in PDB 4BUR (Ferreira et al., 2014)). AIF folds in three structural domains. Two of them, a discontinuous FAD-binding domain (aa 130-262 and 401-480 in hAIF) and a NAD(P)H-binding domain (aa 263-400 in hAIF), both characterised by the classical Rossmann fold topology, form the oxido-reductase modulus of the protein. The third domain (aa 481-613 in hAIF), folding in five antiparallel  $\beta$ -strands followed by two  $\alpha$ -helices, is known as the C-terminal domain (**Figure 1.3**). Noticeably, the C-terminal domains of both hAIF and mAIF contain a short flexible region not detected in the crystallographic structures (residues 545-559 in 4BV6 and 546-553 in 3GD4). In hAIF, the apoptotic C-terminal domain (residues 478-610) includes a long and flexible region (509-559) that apparently occludes access to the redox active site and it is an insertion regarding other members of its structural family (Maté et al., 2002). The refined hAIF $_{\Delta 1-121}$  model provides additional information on this elusive but key fragment. Moreover, this region contains a Pro-rich motif (544-554 in hAIF) that is a potential recognition and interaction site for proteins implicated in the regulation of different cellular processes, as well as a PEST-sequence 529-560 in hAIF) typically involved in protein-protein interactions (Maté et al., 2002). These regions can modulate the calpain proteolytic activity, acting as proteolytic signal via proteosomal degradation (Maté et al., 2002).

The isoalloxazine ring of the FAD cofactor is stabilised at the interface of the three domains, being partially accessible from the solvent, while the adenine, pyrophosphate and ribityl moieties reside in the FAD-domain. The structure of hAIF also reveals the presence of a strong positive electrostatic potential at the surface, although the calculated theoretical isoelectric point for the entire protein is neutral (Ye et al., 2002).

Altogether, the NADH- and FAD-binding domains fold in a conformation typical of enzymes exhibiting a NADH/NADPH-dependent reductase activity. In agreement, hAIF proteins have been shown to get reduced by NADH, with hydride transfer (HT) from this coenzyme producing full reduction of its FAD cofactor and with the concomitant formation of an exceptionally air-stable FADH:NAD<sup>+</sup> charge-transfer complex (CTC), as well as protein dimerization both *in vitro* and *in vivo* (Miramar et al., 2001, Ferreira et al., 2014, Sevrioukova, 2009).



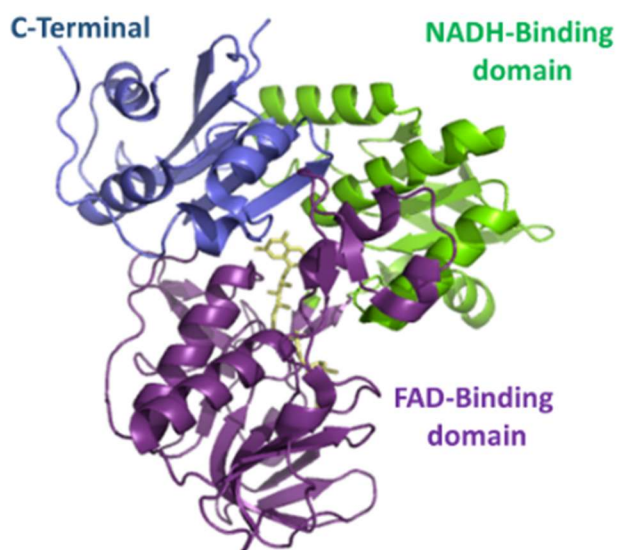


**Figure 1.3: Cartoon representation of the three-dimensional structure of hAIF $_{\Delta 1-101}$**  (PDB 4BV6). The NADH-binding, FAD-binding and C-terminal domains are respectively shown in green, purple and blue.

It is worth to mention that a CTC is the non-covalent association of two chemical entities, where a fraction of the electronic density of one of them (the electron donor) is transferred to the other (the electron acceptor), causing the modification of the electronic structure of the engaged entities and generating new allowed electronic transitions corresponding to characteristic new bands in the light absorption spectrum of the CTC (Miramar et al., 2001).

Crystal structures of mAIF and hAIF in mixtures with NADH confirm the formation as well as the stability of the FADH:NAD<sup>+</sup> CTC homodimers. In addition, in the case of hAIF two NAD(H) molecules have been detected per protein protomer, named NAD(H)<sub>A</sub> and NAD(H)<sub>B</sub> (**Figure 1.4**) (Ferreira et al., 2014). Herein, we will refer to this later CTC structure as hAIF $_{\Delta 1-101}$ :2NAD(H), where the FAD and the two NAD(H) molecules occupy identical positions in both chains of the dimer (**Figure 1.4 A**). In all cases, the colour of the crystals confirmed that in the CTC the FAD cofactor is in the reduced state, indicating that at least one of the coenzyme molecules is in the NAD<sup>+</sup> form. The dimeric organization is stabilised by several H-bonds and salt bridges, creating an interface that involves residues 439-453. In particular, the carboxylate of E426 from one protomer interacts with the O- $\gamma$  and N atoms of S431 from the other protomer, while N424 and A429 from each protomer are H-bound to each other. The dimer is additionally stabilised by salt bridges involving the carboxylic O- $\epsilon$ 1 and O- $\epsilon$ 2 atoms of E413 and the N- $\epsilon$  and NH<sub>2</sub> of R449, and the N- $\epsilon$  of R430 and O- $\epsilon$ 2 of E426 from each protomer. Finally, R422 residues from each protomer stack on each other through their guanidinium groups (**Figure 1.4 B**). Equivalent residues are also involved in stabilisation of the mAIF dimer (Sevrioukova, 2009).

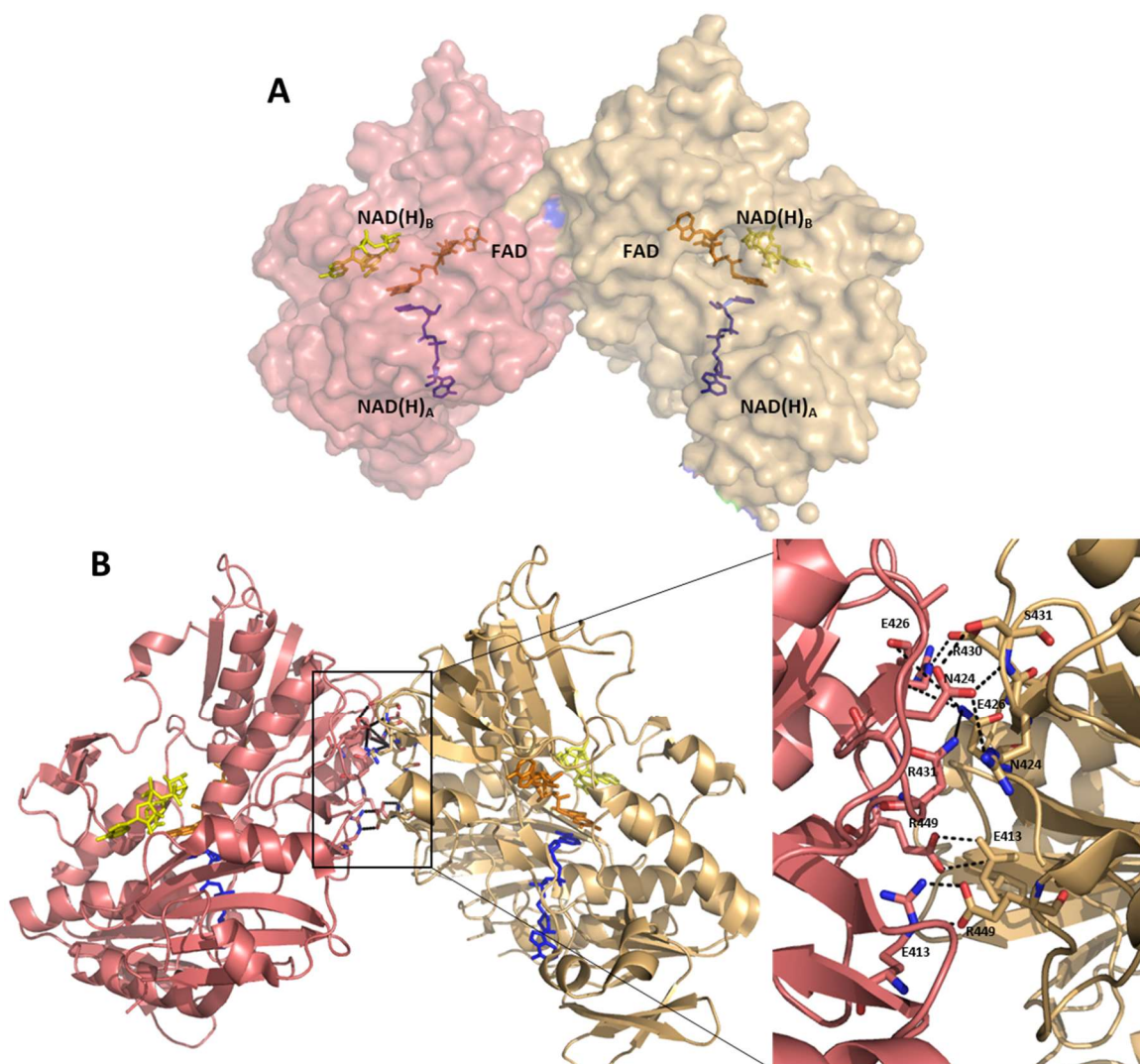


**Figure 1.4: Structure of the hAIF $\Delta 1-101$ :2NAD(H) dimer.** (A) Surface representation. Chains A and C are in red and wheat respectively. FAD, NAD(H)<sub>A</sub>, and NAD(H)<sub>B</sub> are shown as sticks in orange blue and yellow respectively. (B) Cartoon representation with interface residues shown as sticks. A zoom of the interface area with interactions in dashed lines is also shown. Figure modified from (Ferreira et al., 2014).

In the hAIF $\Delta 1-101$ :2NADH structure, the NAD(H)<sub>A</sub> molecule shows an extended conformation with its nicotinamide stacking between the *re*-face of the FAD flavin and the F310 rings. Its binding is stabilised through an H-bond network involving several residues (G308, F310, L311, E314, E336, G399, E453, H454, and W483), with coenzyme side chains of K177, F310, and H454 becoming displaced to allocate the NADH nicotinamide portion (**Figure 1.5 A**). Mutational analysis at active site environment indicated that: i) K177 and E314 contribute to its conformation; ii) P173 determines the flavin properties and modulates the affinity for NADH; and iii) F310 and H454 contribute to the compactness of the active site, essential for NADH binding, CTC stabilisation, and strong NAD<sup>+</sup> affinity for the reduced state (Villanueva et al., 2015). The second NAD(H) molecule, NAD(H)<sub>B</sub>, binds at the *si*-face of the flavin, with the side chain of W483 stacking at one side with its

nicotinamide ring and at the other with the flavin ring (**Figure 1.5**) (Ferreira et al., 2014). F582 and, particularly, W196 became displaced to accommodate the adenine of NAD(H)<sub>B</sub> through stacking interactions, and together with E493 also contribute to stabilise its pyrophosphate, ribose, and nicotinamide moieties of the coenzyme (**Figure 1.5 B**).

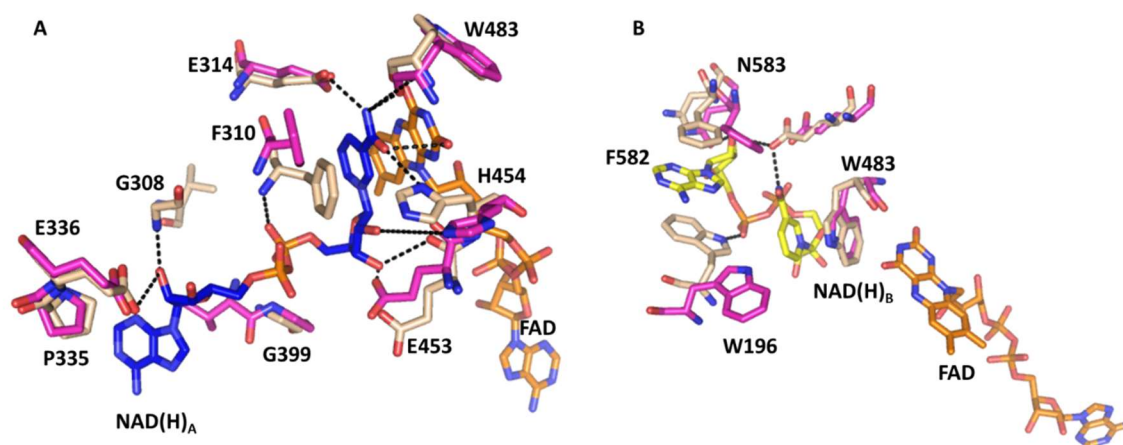


**Figure 1.5: Comparative of the oxidoreductase active site of hAIF<sub>Δ1-101</sub> and hAIF<sub>Δ1-101:2NAD(H)</sub>.** Environments of (A) NAD(H)<sub>A</sub> and (B) NAD(H)<sub>B</sub>. Nicotinamide access of NAD(H)<sub>B</sub> to the flavin ring is blocked by W483 side-chain. This residue also plays an important role in the stabilisation of NAD(H)<sub>A</sub> by forming a H-bond network and stacking on the flavin ring. Side chains for key residues are shown in pink for hAIF<sub>Δ1-101</sub> in wheat for and hAIF<sub>Δ1-101:2NAD(H)</sub>, NAD(H)<sub>A</sub> and NAD(H)<sub>B</sub> are respectively shown in blue and yellow, and the FAD is in orange. Image modified from (Ferreira et al., 2014).

Transformation of hAIF<sub>Δ1-101</sub> into hAIF<sub>Δ1-101:2NAD(H)</sub> produces conformational changes in the 190-202  $\beta$ -hairpin and in the 509-560 segment (**Figure 1.6**), as well as in the molecular dimerization interface (439-453 segment). Noticeably, the 509-560 insertion in mammalian enzymes is a part of the apoptotic C-terminal domain that in hAIF<sub>Δ1-101ox</sub> shows its 517-533 moiety folded into two short  $\alpha$  helices (517-524 and 529-533) which decrease the solvent accessibility to the flavin ring active site through W483 (Maté et al., 2002). These two short propellers are stabilised by interactions with the 190-202  $\beta$ -hairpin side-chains through H-bonds with the R201 residue. In the hAIF<sub>Δ1-101:2NAD(H)</sub> these helices become disordered, and their position is occupied by NAD(H)<sub>B</sub>. In the reduced hAIF structure, the R201 residue forms a new H-bond network with Y204 and S202 chains, facilitating the destabilisation of the aforementioned  $\alpha$ -helices. This allows the accommodation and stabilisation NAD(H)<sub>B</sub> by W196 and E493 residues. In this structure, the access of the nicotinamide of NAD(H)<sub>B</sub> to the flavin ring is blocked by the side chain of W483. In addition, structural analysis shows that FAD reduction and monomer-dimer transition after NADH binding induce conformational changes at the apoptotic and oxidoreductase domains of hAIF, suggesting that both protein functions are somehow structurally interconnected.



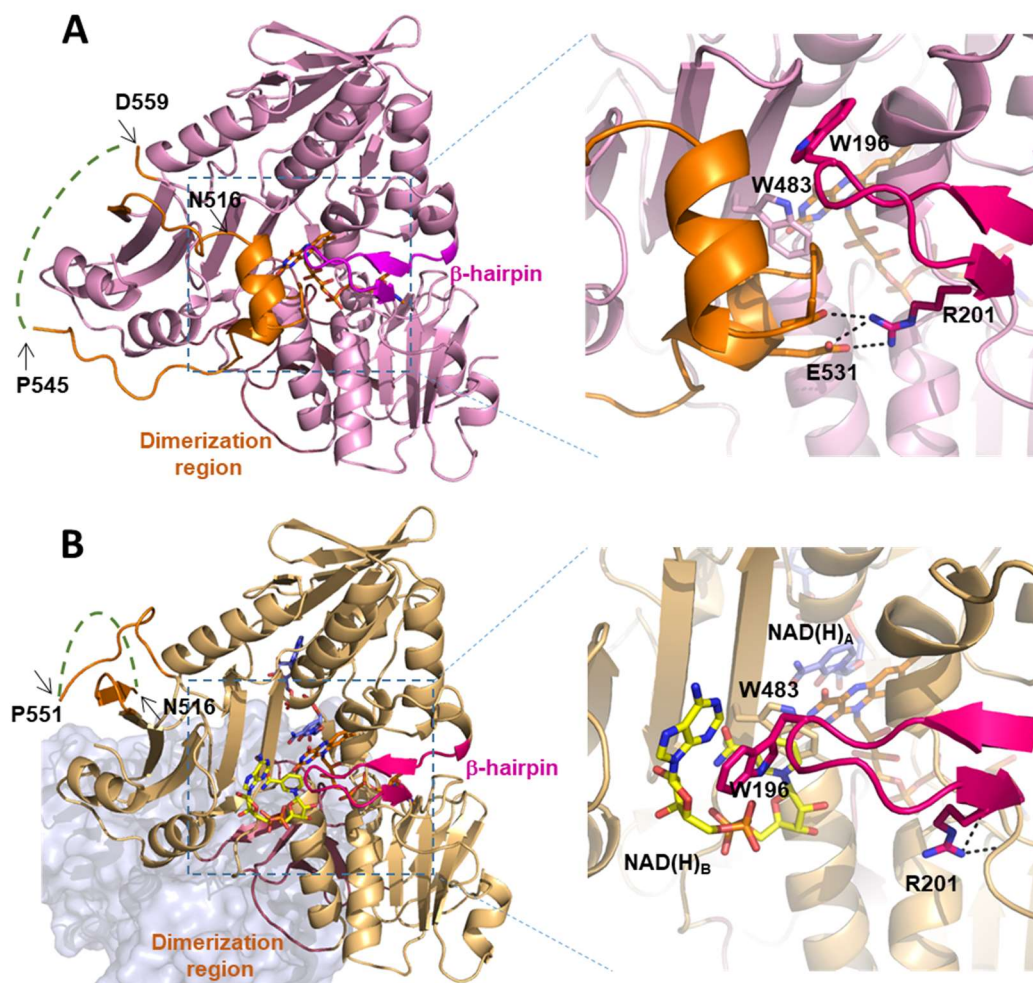


**Figure 1.6: Conformational changes observed in hAIF upon NADH induced dimerization and reduction.** Cartoon representation of (A) hAIF $\Delta_{1-101}$  (pink) (PDB ID: 4BV6) and (B) hAIF $\Delta_{1-101}$ :2NAD(H) (wheat) (PDB ID: 4BUR). Visible residues in the 508–560 segments are drawn in orange, residues involved in the dimerization surface in dark salmon and those of the  $\beta$ -hairpin in hot pink. FAD, NAD(H)<sub>A</sub>, and NAD(H)<sub>B</sub> are drawn in sticks with C in orange, blue, and yellow, respectively. Missing fragments are indicated as dotted green lines. Enlarged regions show a detail of the NAD(H)<sub>B</sub> binding site for each structure (Ferreira et al., 2014).

The above described hAIF isoform (**Figure 1.1**) is the considered as canonical, but up to five more isoforms can be found for this protein in the databases (**Figure 1.7**). In 2001, the existence of a second splice form that uses an alternative exon2b instead of exon2a during transcription was reported. This spliced variant, AIF2 or AIFexon2b, differs from the canonical one in its IMS, being more hydrophobic and, therefore, producing a stronger membrane anchorage (AIF: residues 35-82; AIF2: residues 35-78) (Hangen et al., 2010, Loeffler et al., 2001, Otera et al., 2005). AIF2 is brain-specific, its expression increases as neuronal precursor cells differentiate and it is able to dimerise with the canonical variant, preventing its release from mitochondria. Thus, AIF2 may have been 'designed' to be retained in mitochondria and to minimise its potential neurotoxic activity (Hangen et al.,

2010). Three shorter AIF isoforms named AIF short or AIFsh have been reported. AIFsh1 is restricted to the cytoplasm in health cells, while AIFsh2 is in the mitochondria (Delettre et al., 2006a, Delettre et al., 2006b). AIFsh is a 35 kDa protein resulting from transcription of exons10-16 of the *aifm1* gene by using an alternate transcriptional site located at intron9. AIFsh can be translocated to the nucleus. The isoforms AIFsh2 and AIFsh3 result from the alternative use of exon 9b, AIFsh2 contains the MLS and the oxidoreductase domain but lacks the C-terminal part due to the transcription of an additional exon9b containing a transcription stop-code. Therefore, it can be released from mitochondria but cannot be translocated to the nucleus. Finally, AIFsh3 is formed by residues 87-322, and lacks the MLS, part of the FAD domain, the C-terminal domain and the NLS2 and, therefore, cannot translocate to the nucleus.

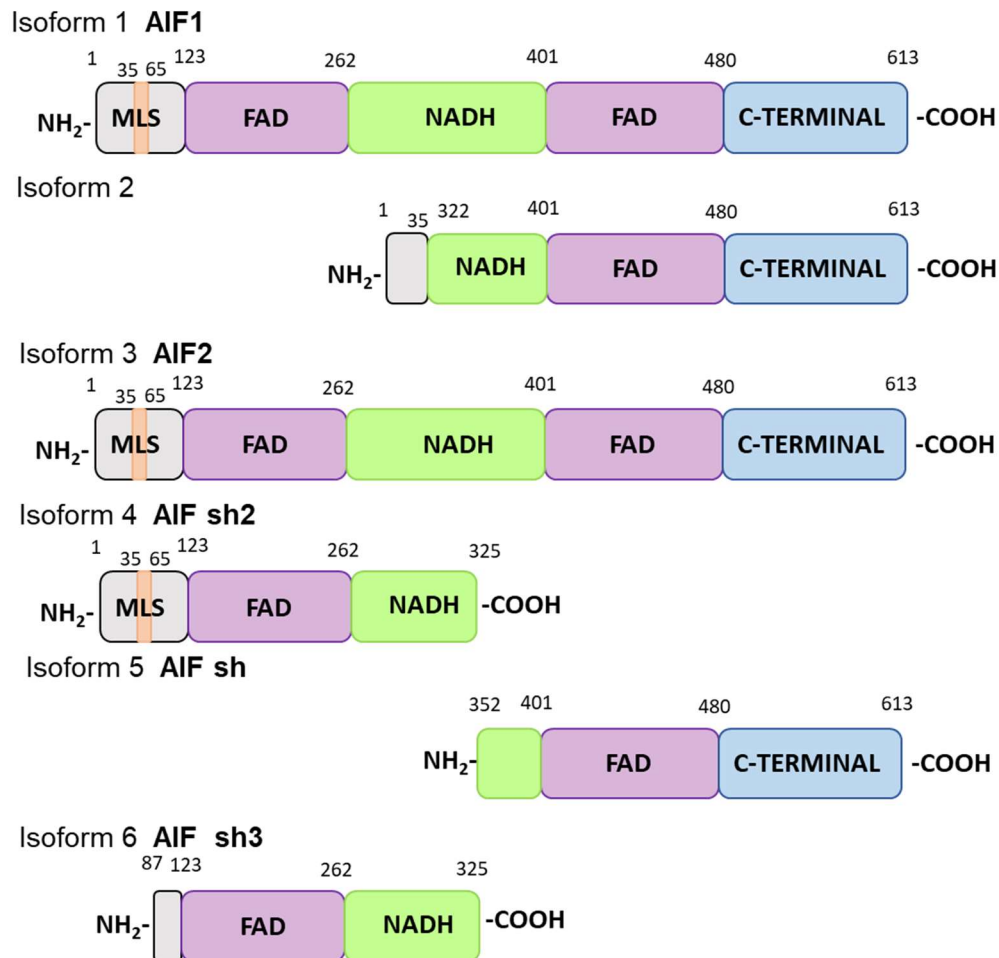


**Figure 1.7: Schematic representation of the five different isoforms reported for hAIF.** The FAD-bipartite, NADH-binding and C-terminal domains are shown in purple, green and blue, respectively. The IMSS region is in orange and the MLS in grey.

## 1.2 THE OXIDO-REDUCTASE ACTIVITY OF AIF

hAIF plays an essential function, still not well understood, in the mitochondrial bioenergetics metabolism through its NADH-dependent redox activity. The biochemical characterization of mAIF<sub>Δ1-120</sub> in 2001, confirmed that this protein was able to transfer electrons at low rate from NAD(P)H to small artificial electron acceptors and cytochrome C (Cyt C), and that this activity could be dissociated from its apoptosis-inducing function (Miramar et al., 2001). Working with the mAIF, it was found that the absorption spectrum of AIF shows the typical features of an oxidised FAD flavoprotein, with the visible maximum at 378 nm and 450 nm and a shoulder at 467 nm (Miramar et al., 2001). AIF has a redox potential strongly influenced by pH. Assuming a two-electron reduction step, the midpoint redox potential is -308 mV at pH 7.5, whereas it reaches -373.15 mV at pH 9.0 (Miramar et al., 2001). In the same publication, these authors also showed that natural AIF purified from mitochondria and recombinant AIF purified from bacteria (AIF<sub>Δ1-120</sub>) exhibit NADH oxidase activity and can generate superoxide anion (O<sup>2-</sup>) upon addition of NADH or NADPH. The affinity for NADH ( $K_m$ ) was calculated as 99 μM with a turnover number ( $k_{cat}$ ) of 2.1 min<sup>-1</sup>, whereas if NADPH is used as an electron donor, the  $K_m$  value was 53 μM and the  $k_{cat}$  was 2.8 min<sup>-1</sup>. These kinetics parameters were very similar to values described for other related NADH oxidases forming O<sup>2-</sup>. AIF also catalyses Cyt C reduction in the presence of NADH, with a  $K_m$  of 460 μM and a  $k_{cat}$  of 21.8 min<sup>-1</sup>. In addition, AIF exhibits monodehydroascorbate reductase activity with a specific activity of 8.8 units/mg and a  $k_{cat}$  of 0.505 min<sup>-1</sup>, a feature common to several AIF homologues described in plants (Lorenzo et al., 1999). Both the Cyt C reductase and the monodehydroascorbate reductase activity of AIF can be inhibited by the enzyme superoxide dismutase (SOD), indicating that the reaction occurs via O<sup>2-</sup> formation. In addition, the same authors show that AIF does not exhibit peroxidase activity. Altogether, these results indicated that AIF has a NADH oxidase activity.

Very importantly, these early analyses indicated that AIF has an oxidoreductase function that can be dissociated from its apoptogenic activity, both in cell-free systems and in intact cells (Miramar et al., 2001). Thus, addition of NADH or NADPH fails to enhance the apoptogenic activity of AIF<sub>Δ1-120</sub> and inhibition of the oxidoreductase activity by removal of FAD or external addition of SOD or diphenyliodonium (an inhibitor of flavonoid containing enzymes) fails to modify the apoptogenic activity of AIF (Loeffler et al., 2001, Miramar et al., 2001). In contrast, p-chloromercuriphenyl sulphonate (pCMPS) abolishes the pro-apoptotic function of AIF without affecting its oxidoreductase activity. Moreover, the recombinant AIF-precursor protein becomes apoptogenic after refolding on a nickel-

affinity matrix even in the absence of FAD, indicating that the oxidoreductase activity is unnecessary for its apoptogenic function (Susin et al., 1999b).

Even though the putative role of hAIF as mitochondrial oxido-reductase remains still not fully understood, altogether the evaluation of these different activities indicates that WT hAIF<sub>Δ1-101</sub> does not exhibit an efficient NAD(P)H oxidase activity. Moreover, AIF redox partners are neither proteins containing iron-sulphur centres nor glutathione, and it does not have any relevance in the *in vivo* bio-reductive activation of quinones (Ferreira et al., 2014, Villanueva et al., 2015). In fact, 2,6-dichlorophenol-indophenol (DCPIP), ferricyanide and Cyt C were more efficient than the above mentioned acceptors in accepting electrons from NADH reduced hAIF<sub>Δ1-101</sub>. When using those acceptors  $k_{cat}$  values were low and  $K_m^{NADH}$  large, and in the same range for hAIF and mAIF isoforms (**Table 1.1**). Nonetheless, the similar low efficiencies to Cyt C and artificial electron acceptors reduce the possibilities of Cyt C being the *in vivo* hAIF<sub>Δ1-101</sub> redox partner, even though both proteins are in the IMS.

In healthy mitochondria, under physiological conditions, hAIF is present in a monomer-dimer equilibrium. The monomer is the predominant form, moving towards the dimer due to the NADH binding and the flavin reduction (**Figure 1.8**) (Ferreira et al., 2014). The *in vitro* reaction of the AIF<sub>Δ1-101</sub> recombinant enzyme with NADH yields a highly oxygen-stable FADH<sup>-</sup>:NAD<sup>+</sup> CTC coupled to an increase in the proportion of dimers (**Figure 1.8**).

**Table 1.1:** Steady-state and pre-steady-state kinetic parameters for the NADH oxidase activity of hAIF.

Electron acceptor	Steady-state		
	$k_{cat}$ (s <sup>-1</sup> )	$K_m^{NADH}$ (μM)	$k_{cat}/K_m^{NADH}$ (s <sup>-1</sup> mM <sup>-1</sup> )
<b>WT</b>			
<b>DCPIP</b>	1.5 ± 0.1	273 ± 31	5.3 ± 0.2
<b>Ferricyanide</b>	3.1 ± 0.4	1375 ± 249	2.3 ± 0.4
<b>Cyt C</b>	0.6 ± 0.2	25 ± 4	6.4 ± 0.7
	Pre-steady-state		
	$k_{HT}$ (s <sup>-1</sup> )	$K_d^{NADH}$ (μM)	$k_{HT}/K_d^{NADH}$ (s <sup>-1</sup> mM <sup>-1</sup> )
<b>WT</b>	1.5 ± 0.1	4090 ± 300	0.4 ± 0.05
Assays performed at 25 °C in 50 mM potassium phosphate, pH 8.0 (Ferreira et al., 2014)			

The CTC and dimer species are proposed to be both physiologically relevant in a model where hAIF would act as a sensor of the mitochondrial redox state. In this model FAD reduction would be sufficient to promote hAIF dimerization, while coenzyme binding might initiate the conformational changes associated with CTC formation (Sorrentino et al., 2015, Ferreira et al., 2014). The low efficiency of AIF as a reductase when using artificial electron acceptors, together with the high stability of the CTC dimer suggests that  $\text{NAD}^+$  dissociation limits the overall reaction rate. *In vivo*, interaction with the suitable physiological acceptor might in addition decrease the enzyme affinity for  $\text{NAD}^+$  (Ferreira et al., 2014). Moreover, the mutational disruption of the dimerization interface decreases the enzyme capacity to stabilise the CTC, suggesting a close relationship between the formation of the CTC and the dimer (Hangen et al., 2015, Ferreira et al., 2014).

The residues P173, K177, F310, E314 and H454, which contribute to fit the isoalloxazine ring and the nicotinamide ring of  $\text{NAD(H)}_A$ . These residues are fully conserved among AIF from different organisms supporting the idea that they must have a role in the binding or even in the HT itself (Senda et al., 2000, Ferreira et al., 2014). Noticeably, F310 and H454 are not highly conserved in AIF-related proteins. The highly conserved P173, K177 and E314 residues are required for FAD incorporation, while F310 and H454 are important for pyridine nucleotide binding, CTC stabilisation as well as to determine the typical *in vitro* low catalytic efficiency of hAIF proteins to accept a hydride from NADH (Villanueva et al., 2015, Ferreira et al., 2014).

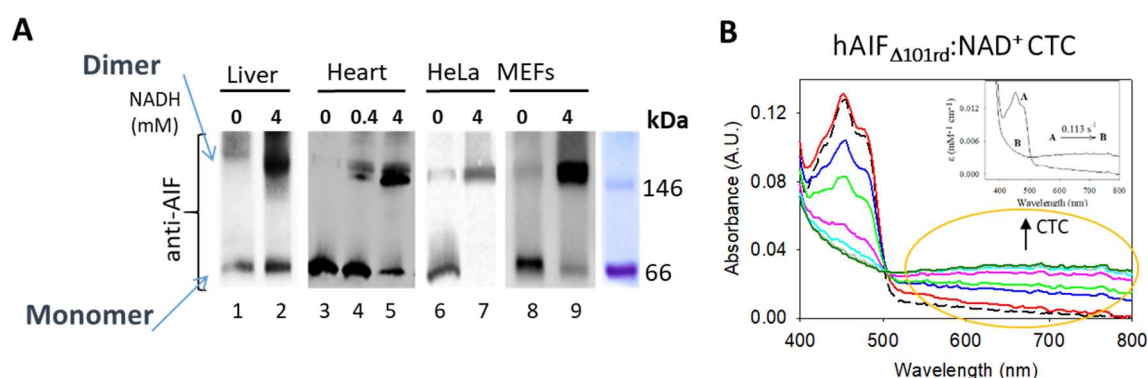


**Figure 1.8: Physiological forms of hAIF and CTC formation.** (A) Western Blot of digitonin solubilised mitochondrial fractions obtained from mouse liver (lanes 1 and 2), mouse heart (lanes 3-5), HeLa cells (lanes 6 and 7), and MEFs cells (lanes 8 and 9) after separation by high-resolution clear native gel electrophoresis-1. The blot was probed with AIF specific antibodies. Molecular markers are indicated at the right side. (B) Spectral changes during the reduction of hAIF $_{\Delta 1-102}$  by NADH are shown. Spectra recorded for the reaction of NADH (150  $\mu\text{M}$ ) with 8  $\mu\text{M}$  of protein at 0.03, 3.6, 6.9, 16.7, 26.5, 36.4, and 46 s after mixing. The insets show the absorbance spectra for the intermediate species obtained by fitting the spectral evolution to a single step model (A  $\rightarrow$  B). Image from (Ferreira et al., 2014).



The efficiency of the different mutants at hAIF key catalytic positions to oxidise NADH was evaluated under steady-state conditions using typical electron acceptors already proved for their ability to exchange electrons with the WT enzyme DCPIP and Cyt C (Ferreira et al. 2014). The H454S variant turnover with DCPIP was similar to that of the WT enzyme ( $1.6 \pm 0.1 \text{ s}^{-1}$ ), while the P173G and F310G mutations caused a modest increase in  $k_{\text{cat}}$  (2- and 3-fold, respectively). When using Cyt C as acceptor, the turnover rate for F310G was in the same range as that reported for the WT protein ( $\sim 1.3 \text{ s}^{-1}$ ), whereas the rate was increased and decreased for P173G ( $k_{\text{cat}}$  within  $\sim 2$ -fold increase) and H454S ( $k_{\text{cat}}$  within  $\sim 3$ -fold decrease), respectively.  $K_{\text{m}}^{\text{NADH}}$  values for the P173G and H454S variants were similar to that for the WT, independently of the acceptor used, while the F310G variant showed a considerable increase (4- and 10-fold when respectively using DCPIP and Cyt C). None of the variants showed the ability to efficiently be oxidised by molecular oxygen upon NADH reduction, so they hardly have NADH oxidase activity similar to WT protein (Villanueva et al., 2015).

The ability of the different variants as reductases was also evaluated by using NADPH as electron-donor and DCPIP as electron acceptor. Under such conditions the WT protein is considerably less efficient than when NADH is used. No activity was detected for P173G and H454S mutants when NADPH was used as a reductant. In contrast, the F310G variant exhibited a strong increase in turnover. Overall, the  $k_{\text{cat}}$  and  $K_{\text{m}}$  values determined for F310G indicate that this mutation reduces the specificity for NADH versus NADPH when compared with the WT protein.

Contrary to what was observed for the WT, the NADH reduced P173G, F310G, and H454S mutants were sensitive to reoxidation by molecular oxygen. Therefore, assays for the mutants were conducted under anaerobic conditions. Spectral evolution upon mixing the P173G, F310G and H454S variants with NADH showed a decrease in the absorbance at 451 nm consistent with full reduction of the FAD cofactor. HT from NADH to FAD in the P173G and F310G mutants, as well as in the WT enzyme, was accompanied by the progressive formation of a long-wavelength broad band related to the CTCs formation (Ferreira et al., 2014). In contrast, FAD reduction in the H454S variant took place without the spectroscopic detection of any CTC. This indicates either a considerable reduction of the amount of CTC stabilised or the production of CTCs with different charge distribution between the reacting rings. The lower or absence of CTC stabilisation in the mutants indicates that substrate accommodation is modulated by these active-site mutations.

The time courses of the reaction fit to a one step model ( $A \rightarrow B$ ) for the three mutants where A and B are the oxidized and reduced form of these proteins. As reported for the WT enzyme (Ferreira et al., 2014), also the  $k_{\text{HT}}$  values for the P173G, F310G and H454S variants

indicated processes ~5-, ~17- and ~4-fold faster, respectively, than that of the WT enzyme, suggesting that HT event by itself is favoured by the mutations. On the other hand, a decrease in the affinity for the pyridine nucleotide was produced, with  $K_d^{\text{NADH}}$  values 12-, 5- and 3-fold higher for P173G, F310G and H454S variants, respectively, than for WT (**Table 1.2**). These changes make the P173G variant slightly less efficient than the WT in the HT event, while the other two mutants are slightly more efficient (up to ~3-fold for F310G). Therefore, the P173, K177, and E314 residues have key roles in FAD binding, creating a particular environment required for the hAIF NADH dependent functions. Additionally, the conservation of these residues in other family members suggests the existence of a general motif for FAD binding. In contrast, the F310 and H454 residues contribute to NAD(H)<sub>A</sub> binding and stabilisation in the hAIF active site after the HT to the flavin. The fact that these residues are not conserved in other members of the family, where less compact active sites are found in the coenzyme-bound state, indicated that they strongly contribute to the CTC stabilisation and to the low efficiency of AIF as a reductase. This low efficiency of AIF when accepting a hydride from NADH appears key in redox metabolism of healthy cells, since mutations altering it have been related to several mitochondrial human disorders causing progressive mitochondrial encephalomyopathy (Berger et al., 2011, Ghezzi et al., 2010, Hangen et al., 2010, Rinaldi et al., 2012).

**Table 1.2:** Steady-state and pre-steady-state kinetic parameters for the NADH oxidase activity of hAIF variants.

Electron acceptor	Steady-state		
	$k_{\text{cat}}$ (s <sup>-1</sup> )	$K_m^{\text{NADH}}$ (μM)	$k_{\text{cat}}/K_m^{\text{NADH}}$ (s <sup>-1</sup> mM <sup>-1</sup> )
WT	1.5 ± 0.1	273 ± 31	5.3 ± 0.2
P173G	3.2 ± 0.1	312 ± 111	11.8 ± 2.1
F310G	4.2 ± 0.2	75 ± 19	53.1 ± 8.5
H454S	1.6 ± 0.1	224 ± 70	7.6 ± 1.6
	Pre-steady-state		
	$k_{\text{HT}}$ (s <sup>-1</sup> )	$K_d^{\text{NADH}}$ (μM)	$k_{\text{HT}}/K_d^{\text{NADH}}$ (s <sup>-1</sup> mM <sup>-1</sup> )
WT	1.5 ± 0.1	4090 ± 300	0.4 ± 0.05
P173G	4.9 ± 0.3	12060 ± 1289	0.41 ± 0.05
F310G	17.3 ± 0.7	5585 ± 499	3.10 ± 0.30
H454S	3.7 ± 0.2	2743 ± 295	1.35 ± 0.16
Assays performed at 25 °C in 50 mM potassium phosphate, pH 8.0 (Ferreira et al., 2014)			

This set of observations suggests that both the direct environments of the isoalloxazine ring and of the nicotinamide of the coenzymes should be key for AIF to exhibit its functionalities both in healthy cells and in apoptosis.

### 1.3 THE PROGRAMMED CELL DEATH ROLE OF AIF

Programmed Cell Death (PCD) is known to play a major role in the development and stress responses in all three metazoan kingdoms (Plantae, Animalia and Fungi). It is essential for organ development, tissue homeostasis, aging and removal of infected or damaged cells, being the biochemical and ultrastructural features of PCD highly conserved throughout the evolution of multicellular animals (Jacobson, 1997). Mammalian cells exposed to unrecoverable perturbations of the intracellular or extracellular microenvironment can activate one of many signal transduction cascades ultimately leading to their demise. Each of such regulated cell death (RCD) modes is initiated and propagated by molecular mechanisms that exhibit a considerable degree of interconnectivity (**Figure 1.9**). Moreover, each type of RCD can manifest with an entire spectrum of morphological features ranging from fully necrotic to fully apoptotic, and with an immunomodulatory profile ranging from anti-inflammatory and tolerogenic to pro-inflammatory and immunogenic (Galluzzi et al., 2018).

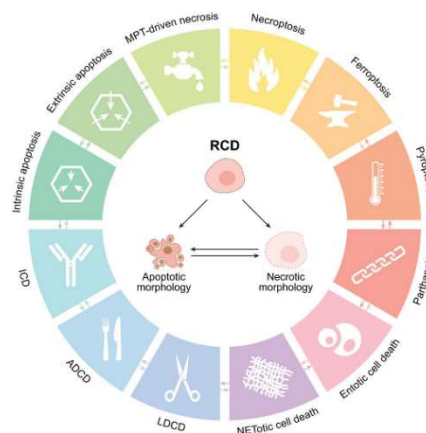


**Figure 1.9: Major cell death subroutines.** ADCD: autophagy-dependent cell death, ICD: immunogenic cell death, LDCD: lysosome-dependent cell death, MPT: mitochondrial permeability transition. Image from (Galluzzi et al., 2018).

The mechanisms of apoptosis are highly complex and sophisticated, involving an energy-dependent cascade of molecular events. To date, research indicates that there are two main apoptotic pathways: the extrinsic or death receptor pathway and the intrinsic or mitochondrial pathway. However, there is now evidence that these two pathways are linked and that molecules in one pathway can influence the other one (Igney and Krammer, 2002). The molecular mechanisms of the hAIF lethal function have been deeply characterised (Chinta et al., 2009, Susin et al., 2000), showing that permeabilization of mitochondria is an obligatory event in the hAIF-mediated apoptotic signalling. Thus, hAIF

plays a crucial role in the so called intrinsic, or mitochondrial, apoptotic pathway in a special way of apoptosis called *parthanatos* (**Figure 1.10 and Table 1.3**).

The intrinsic pathway is regulated by proteins of the Bcl-2 family that modulate mitochondrial membrane permeability and can act as either pro-apoptotic (Bid, Bak, Bax) or anti-apoptotic (Bcl-2, Bcl-XL) factors (Norberg et al., 2010). The physiologic function of Bcl-2 and Bcl-XL is to avoid the release of mitochondrial proteins, probably by controlling the activation of caspase proteases (Joza et al., 2009). Smac/DIABLO and Omi/HtrA2 facilitate caspase activation by sequestering and/or degrading several members of the inhibitor of apoptosis protein family (Galluzzi et al., 2012). In response to multiple intracellular stress conditions, such as DNA damage or cytosolic  $\text{Ca}^{2+}$  overload, pro-death signals are generated and converged to a mitochondrion-centred control mechanism producing mitochondria outer membrane permeabilization (MOMP). The respiratory chain gets then uncoupled, leading to over generation of reactive oxygen species (ROS) and releasing into the cytosol proteins normally confined within the IMS. Among these, Cyt C drives -together with the cytoplasmic adaptor protein APAF1 and dATP, the assembly of the so-called apoptosome, a multiprotein complex that triggers the caspase-9 → caspase-3 proteolytic cascade.

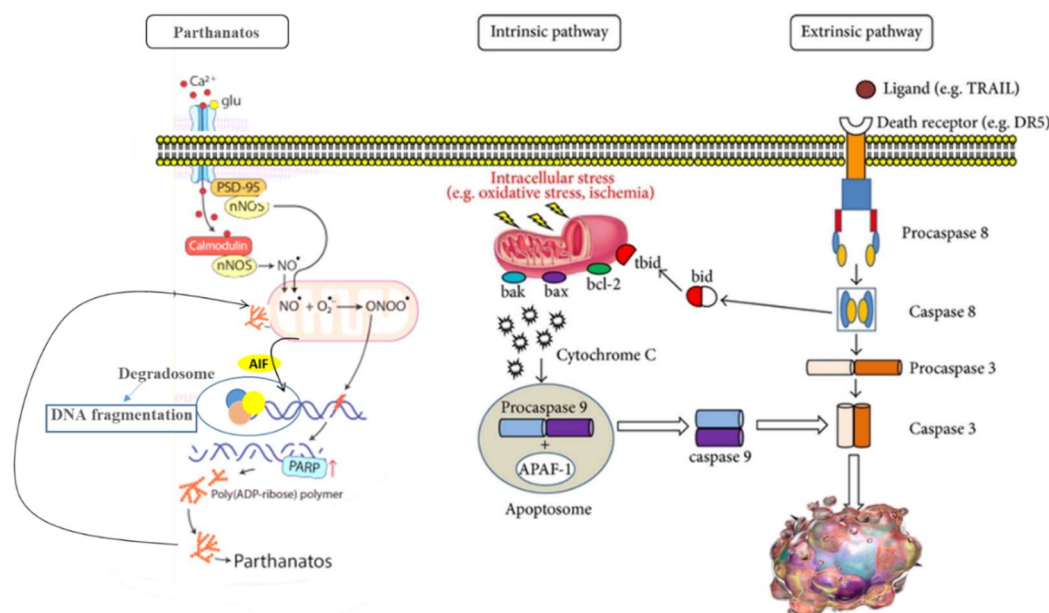


**Figure 1.10: Schematic representation of main apoptotic pathways.** The main pathways of apoptosis are extrinsic and intrinsic, as well as parthanatos. Each requires specific triggering signals to begin an energy-dependent cascade of molecular events. Each pathway activates its own initiator caspase (8, 9, 10), which in turn will activate the executioner caspase-3. Parthanatos is presented as death resulting from the execution of a well-choreographed cascade of events, with key distinguishing molecular events described in sequence, including the rapid activation of poly-(ADP-ribose) polymerase (PARP-1), the synthesis and accumulation of the poly (ADP-ribose) (PAR) polymer and the translocation of AIF protein from the mitochondria to the nucleus, where AIF interacts with the DNA in a yet-unclear fashion to produce large-scale DNA fragmentation and chromatin condensation and, eventually, parthanatos cell death. Modified from (Loreto et al., 2014).

**Table 1.3:** Differences between the main apoptotic paths.

Summary of differences between parthanatos, apoptosis and necrosis		
	Parthanatos	Apoptosis
Chromatin Condensation	Yes	Yes
Nuclear fragmentation	Yes	Yes
Apoptotic bodies	No	Yes
Mitochondrial Swelling	No	Sometimes
Membrane Blebbing	No	Yes
Caspase Dependent	No	Yes
Regulated Pathway	Yes	Yes

As it was previously mentioned, AIF takes part in a type of cell death independent from caspases called parthanatos. AIF is therefore incorrectly named, since it should have been named after parthanatos rather than apoptosis (Lorenzo and Susin, 2007). The parthanatos process depends on the protein PARP-1 (Poly (ADP-ribose) polymerase 1), which under normal conditions helps in DNA repair after it is damaged. Overexpression of PARP-1 acts as a cell death signal, and makes this protein to form aggregates that will then move towards mitochondria. There, they will activate AIF through a physical interaction with the AIF PARP-1 binding motif (residues 567 and 592), inducing conformational changes in AIF that favour its calpain proteolytic cleavage at residue 101. This cleavage makes AIF to be released in the cytosol (Wang et al., 2011, Wang et al., 2009). Once released from the mitochondrion, AIF is translocated to the nucleus, where it induces chromatin condensation and DNA rupture in fragments of 50 kb. The mechanism of action of hAIF inside the nucleus is still partially unknown. Nevertheless, it is known that AIF does not have endonuclease activity, so it needs to interact with a nuclease in order to induce DNA fragmentation. In some studies, the interaction of AIF and the endonuclease CypA has been observed (Farina et al., 2017). This interaction induces the formation of a ternary complex with the histone H2AX, AIF-CypA-H2AX, forming a degradosome, that upon binding the DNA is responsible for chromatolysis, a process through which chromatin is degraded inside the cells (Artus et al., 2010, Cande et al., 2004). Currently, two models have been proposed to describe the mechanism through which AIF is released to the cytosol. According to the first model, opening of mitochondrial permeability transition pore (MPTP) allows small molecules to enter the mitochondrial matrix, leading to swelling of the organelle. Under these conditions, the PARP-1 triggers dissipation of the mitochondrial membrane potential ( $\Delta\psi_m$ ) altering mitochondrial  $\text{Ca}^{2+}$  homeostasis. In the second model, pro-apoptotic Bcl-2 family members could promote the formation of pores that cause permeabilization of mitochondria, without affecting  $\Delta\psi_m$  (Hurst et al., 2017).

In both models, after mitochondrial permeabilization, the membrane tethered AIF<sub>Δ1-54</sub> undergoes proteolytic cleavage by the action of the Ca<sup>2+</sup>-dependent calpain. Several *in vitro* evidences of the involvement of other proteases, like cathepsins B, L, S, have been provided but still have to be validated *in vivo* (Łopatiński and Witkowski, 2011). Proteolytic cleavage leads to the production of the soluble and apoptogenic form of AIF, called hAIF<sub>Δ1-101</sub>, which can be easily released from mitochondria to the cytosol (**Figure 1.11**).

This release could be blocked by addition of the calpain inhibitor, calpastatin, residing within the IMS and activated by calcium signalling (Urbano et al., 2005, Polster et al., 2005, Vosler et al., 2009, Bano et al., 2010).

Once in the cytosol, hAIF<sub>Δ1-101</sub> can interact with HSP70 and CypA. These two proteins regulate the cellular localization of hAIF<sub>Δ1-101</sub>, in an antagonistic and redox-controlled manner by thioredoxin (Trx). When subjected to pro-apoptotic oxidative stress conditions, Trx is oxidized, resulting in the dissociation of the Trx-AIF complex, which may lead to increased nuclear translocation of AIF mediated by CypA (Shelar et al., 2015).

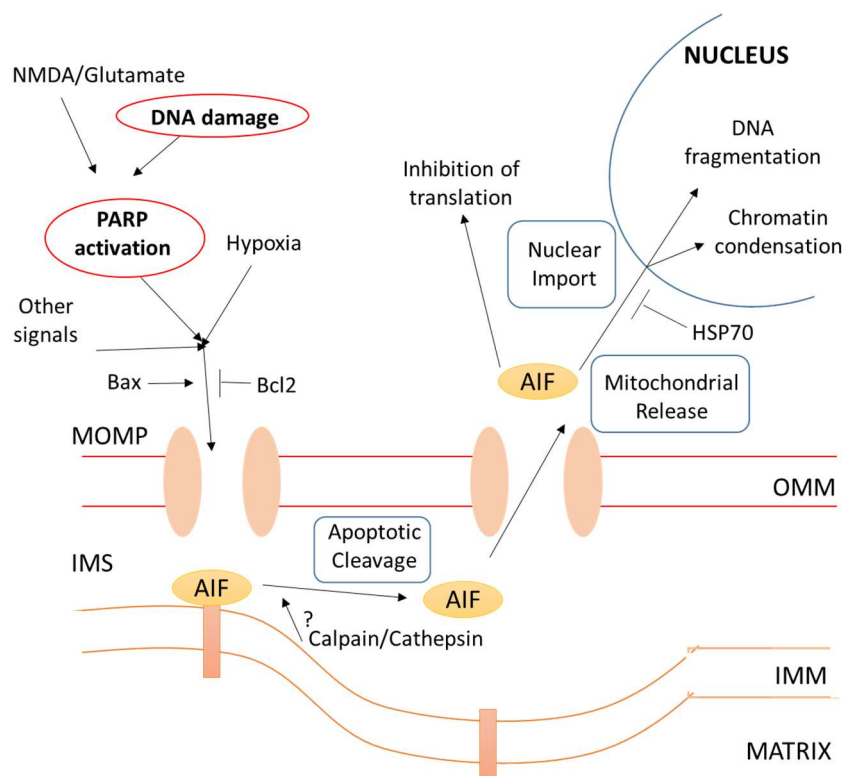


**Figure 1.11: AIF mediates nuclear and cytoplasmic effects of PCD in response to select stimuli.** In healthy cells, AIF is anchored to the inner mitochondrial membrane (IMM) by an amino-terminal transmembrane segment. After an apoptotic stimulus and MOMP, AIF is cleaved at amino acid 101 to generate the mature apoptogenic protein, which is released from the IMS. AIF translocate first to cytosol and then to the nucleus, where it mediates chromatin condensation and degradation of DNA into ~50 kb fragments. Image modified from (Kroemer and Reed, 2000).

This TRX1-mediated regulation of the AIF redox status determines its binding to either HSP70 or CypA. In this regard, HSP70 promotes AIF retention in the cytoplasm (Ravagnan et al., 2001), whereas CypA facilitates its translocation to the nucleus (Farina et al., 2017, Zhu et al., 2007, Cande et al., 2004). Once in the nucleus, since AIF does not possess any obvious nuclease activity, its primary function is to modulate the activity of the non-specific endonuclease that directly cleaves DNA. Thus, the complex CypA:AIF binds the histone H2AX organizing a ternary DNA-degrading complex (**Figure 1.12**), AIF: CypA:H2AX, that has been given the name of degradosome. This association promotes DNA degradation by chromatinolysis via CypA as latent endonuclease (Zhu et al., 2007).

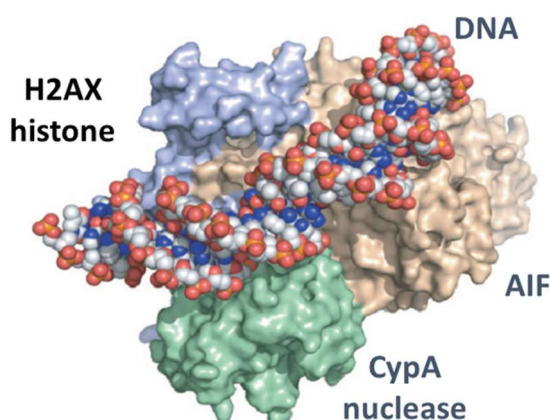


**Figure 1.12: Molecular model illustrating the potential organisation of a DNA degradosome complex generated during parthanatos** (surface representation). AIF (brown), H2AX (violet) and CypA (green). DNA is depicted in spheres (N, C, O and P atoms are coloured in blue, grey, red and orange, respectively). This model, obtained by homology with the crystal structures of the individual partners, was generated with SwissPDBViewer, DALI and GRAMM-X. The previously described DNA-binding residues of AIF were used as structural restraints and the DNA-trimer complex was improved in the HADDOCK Web Docking server (Utrecht University, Netherland). The atomic coordinates (PDB) used were: 1GV4 (mouse AIF), 1W74 (CypA), 1P3A chain C (H2AX) and 1P3A chains I-J (nucleotides 14-47 and 247-280; DNA). Refinement was performed with CHARMM/SwissPDBViewer and edited with PyMol. Image from (Baritaud et al., 2010).

Therefore, AIF plays a the central role in organizing the DNA degradosome to produce a caspase-independent PCD process that mediates nuclear features of apoptosis such as chromatin condensation and large-scale (~50 kb) DNA degradation by the parthanatos apoptotic pathway (Wang et al., 2009).



## 1.4 THE PRO-LIFE ROLE OF AIF IN THE MITOCHONDRIA

Many studies support the fact that, apart from its apoptotic function, AIF also plays a pivotal role in some vital functions in mitochondria (Wang and Youle, 2009).

Mitochondria are mighty, microscopic, energy-producing structures that are essential in cell health. These organelles (specialised structures within a cell performing specific functions) live within almost every eukaryotic cell. Mitochondria provide energy to the organs in the form of ATP generated by the Mitochondrial Oxidative Phosphorylation System (OXPHOS). This system is integrated by a respiratory electron transport chain (ETC) and ATP synthase. The ETC is formed by a series of sequential protein complexes that transfer electrons from a donor molecule to an acceptor molecule (NADH and oxygen respectively in the case of higher Eukaryotes). The energy release from these oxidation-reduction processes is storage into a proton gradient across the IMM, and this proton force is then used by the ATP synthase complex to produce a mechanical work that is subsequently converted into chemical energy in the form of ATP (Jonckheere et al., 2012).

Despite early studies on AIF suggested that it was important to maintain the OXPHOS systems, the real function of this protein in mitochondria is just starting to be revealed (**Figure 1.13**). Homozygous AIF knockout in mice resulted embryonically lethal (Brown et al., 2006), suggesting an altered function of respiratory complex I (Bénit et al., 2008). Nonetheless, consequences of severe AIF deficiency in mitochondria were revealed by the Harlequin (Hq) mouse model, which presents an 80 % decreased expression of AIF. Hq mice are viable at early life stages without phenotypic alterations, but adults show lack of hair, develop progressive neurodegeneration, ataxia and blindness, and are resistant to weight gain and lipid accumulation (Pospisilik et al., 2007). Moreover, the AIF-deficient neurons and cardiomyocytes are sensible to peroxides and ROS. This led to the hypothesis that AIF could function as an antioxidant and/or ROS scavenger that plays a role in OXPHOS. This possibility was later rejected by *in vitro* experiments on isolated mitochondria (Vahsen et al., 2004, Klein et al., 2002), where expression of AIF targeted to the IMM totally restores the alterations in cristae and respiratory defects. No association of AIF with any of the respiratory complexes has been proven, but AIF deficiency or tissue-specific gene inactivation has been also related to defects in the assembly and function of respiratory complexes I and III, also causing OXPHOS impairment (Breuer et al., 2013). Only expression of full-length AIF in AIF-deficient cells could restore a proper OXPHOS function. Altogether these observations suggested that AIF plays an important role in OXPHOS regulation and energy homeostasis as an assembly factor and/or redox sensor that assists the biogenesis of the multi-subunit complexes I and III (Bano and Prehn, 2018).



Unfortunately, despite many efforts in the characterization of metabolic changes caused by AIF removal *in vivo*, the precise role of the mitochondrial flavoprotein is still under study.

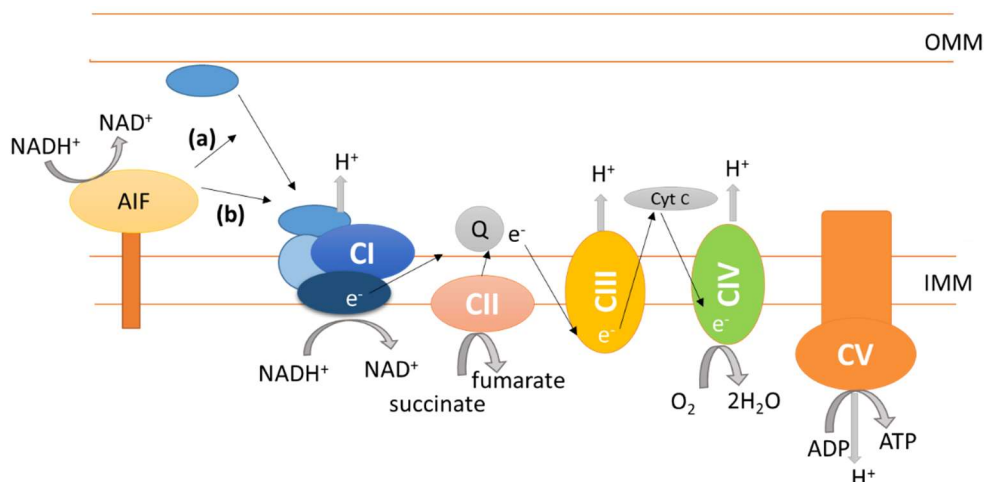


**Figure 1.13: Function of AIF in OXPHOS.** Two potential functions where initially proposed for AIF oxidoreductase activity in the OXPHOS system **(A)** AIF might be involved in the assembly of the 46 respiratory complex I subunits (and of complex III subunits, not shown). **(B)** AIF may have a role in the maintenance of complex I. Image modified from (Hangen et al., 2010).

Recently, a role of AIF as a regulator agent involved in the mitochondrial IMS import machinery and respiratory complexes assembly is being envisaged. Such a function will take place by assisting the Coiled-coil-helix-coiled-coil-helix Domain Containing 4 protein, so called CHCHD4 (Hangen et al., 2015), also referred to as Mia40 in Eukarya cells different than humans. Mia40, was initially isolated in mitochondria of budding yeast (Ghezzi et al., 2010). It is a soluble 16 KDa IMS protein characterised by the presence of seven cysteine residues, six of which are conserved and engaged in three disulphide bonds constituting a redox-sensitive cysteine-proline-cysteine site (or CPC motif) and a -CX9C-CX9C-motif. CHCHD4 contains a small helical segment in residues 56-59 (helix  $\alpha$ 1) and two longer helical segments (helix  $\alpha$ 2, residues 65-77, and helix  $\alpha$ 3, residues 88-100), whereas the other 80% of residues, mainly located at the N- and C-termini, do not adopt any defined secondary structure, being a large part of them highly flexible. The first and only available structure of the human CHCHD4 was obtained by NMR (PDB 2K3J) (**Figure 1.14**), showing that the CPC motif exists in a solvent-exposed conformation protruding from a hydrophobic cleft. This hydrophobic region consists of the strictly conserved phenylalanine residues F68, F72, F75 and F91, as well as L42, I43, I49, W51, L56, M59, A60, M94, M98 and may function as a substrate binding site (Heimer et al., 2018).

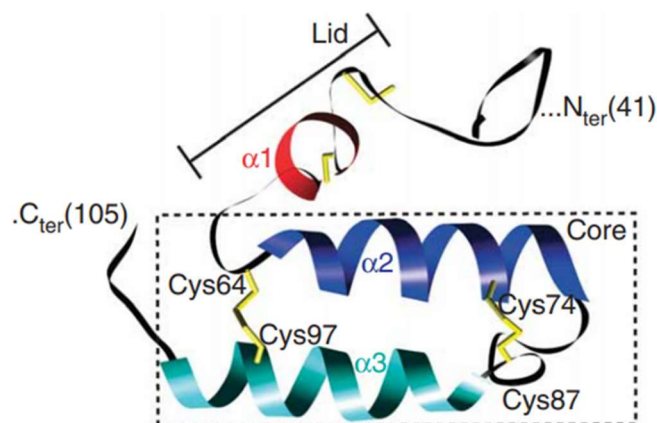
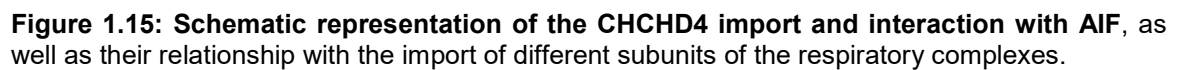


**Figure 1.14: Ribbon diagram of the lowest-energy conformer of MIA402S-S.** Helix  $\alpha 1$  of the N-terminal lid is shown in red, and helices  $\alpha 2$  and  $\alpha 3$  composing the  $\alpha$ -hairpin core are shown in blue and cyan. Disulphide pairings (or free thiols) are shown in yellow. Image from (Banci et al., 2009).

In healthy mitochondria, CHCHD4 acts as an oxidoreductase able to introduce disulphide bonds into its substrates, including several disulphide bonds-containing IMS proteins that are implicated in the biogenesis of respiratory chain complexes. Thus, CHCHD4 depletion results in reduced protein expression of several respiratory chain subunits leading to functional defects in complexes I and IV (Otera et al., 2005). CHCHD4 works as an import receptor that performs two functions. During the first step of its action, the peptide-binding cleft of CHCHD4 specifically binds to the IMS-targeting region of the incoming precursor through hydrophobic interactions. In the subsequent step, CHCHD4 covalently binds to one cysteine of the bound substrate through an intermolecular disulphide bond engaging its CPC active site (Kettwig et al., 2015). Thus, CHCHD4 acts as a chaperone that promotes both the entrapment of the substrate into the IMS and its oxidative folding. At the end of its catalytic cycle, after generating a disulphide in the protein substrate, the CPC motif of CHCHD4 is reduced and its reoxidation is ensured by its interaction with FAD-linked sulphhydryl oxidase Erv1 (ALR in humans) (Chatzi et al., 2016).

The human CHCHD4 (hCHCHD4) lacks an N-terminal membrane-anchoring sequence. It has lost its hydrophobic IMM anchor and has acquired the capacity to interact with a new partner, the flavoprotein AIF, which in turn is tethered to the IMM. Thus, AIF was shown to interact and stabilise the mitochondrial protein CHCHD4 providing new insights on the AIF pro-survival role (Hagen et al., 2015). Using *in vitro* and *in vivo* experiments, Hagen and collaborators provided evidences on the translation-dependent import of CHCHD4 into mitochondria and showed that it was affected by the presence of AIF. The biochemical and functional consequences of AIF depletion were found to be similar to those observed as a result of CHCHD4 depletion, causing selective defects of respiratory chain complexes



37

## 1.5 AIF AND DISEASE

As above mentioned, under physiological healthy conditions AIF has a vital role in the mitochondrial bioenergetics supporting OXPHOS, having an impact on multiple catabolic and anabolic pathways as well as on epigenetic processes that depend on mitochondrial metabolites. On the other hand, upon detrimental stimuli, AIF forms a degradosome complex in the nucleus that is responsible for chromatinolysis and PCD. Due to these dual roles, AIF deficiency or dysfunction can lead to diverse and severe pathologies, including severe mitochondrial dysfunction, causing muscle atrophy and neurodegeneration, as well as pathogenic processes that alter metabolism and ultimately compromise cellular homeostasis. Therefore, these molecular processes have been associated to an array of pathological conditions, including inherited diseases (**Figure 1.16**). In this context, after the initial discovery of the first hAIF pathogenic variant,  $\Delta R201$ , an increasing number of clinical reports have described mutations in the *afim1* gene causally linked to mitochondrial diseases (Bano et al., 2010, Ghezzi, 2010, Hu et al., 2017, Sancho et al., 2017, Mierzevska et al., 2017, Kettwig et al., 2015, Ardisson et al., 2015, Diodato et al., 2016, Morton et al., 2017b, Rinaldi et al., 2012, Bano and Prehn, 2018, Villanueva et al., 2019). These mutations are associated with a wide spectrum of clinical presentations, including slowly progressive mitochondrial encephalomyopathy, neuropathy, infantile motor neuron dysfunction and hypomyelinating leukodystrophy associated with neurodegeneration (**Table 1.4**).

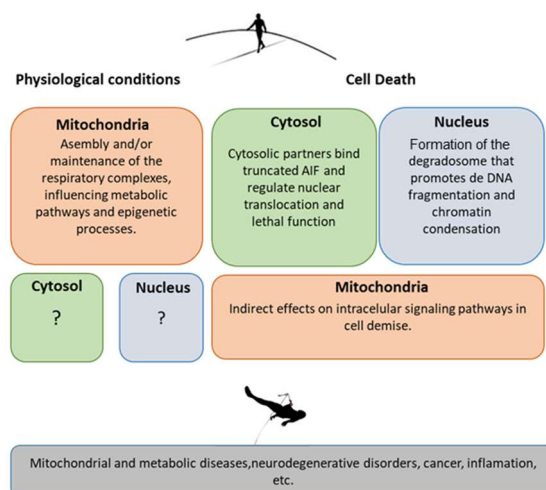


**Figure 1.16: Pathophysiological effects of hAIF mutations.** Image modified from (Bano et al., 2010).

Most hAIF pathogenic variants induce typical characteristics of mitochondrial diseases, which may have autosomal, X-linked and maternal inheritance, with rare sporadic cases that can occur especially in adults. Impaired mitochondrial bioenergetics and aberrant metabolic intermediates are the primary defects observed in patients suffering such

diseases, and therefore pathogenic mutations are generally considered useful biomarkers. Thus, mitochondrial diseases are a heterogeneous group of clinically relevant metabolic disorders that manifest with a wide range of symptoms and typically involve multiple tissues, being organs that are highly dependent on ATP the most severely affected. These syndromes have often childhood onset, although they can also occur with certain prevalence in adolescents as well as in adults (Gorman et al., 2016, Turnbull and Rustin, 2016, Koopman et al., 2016).

To date, around twenty hAIF allelic variants have been found to cause severe mitochondrial pathologies, with neurodegeneration as a general and common feature (**Table 1.4**). The deletion of R201 (Rinaldi et al., 2012), as well as the G308E (Mierzevska et al., 2017), G262S (Diodato et al., 2016), G338E (Sevrioukova, 2016) and T141I (Churbanova and Sevrioukova, 2008) replacements are reported to cause mitochondrial encephalopathies. The V243L (Sevrioukova, 2016), F210S (Sancho et al., 2017) and E493V (Rinaldi et al., 2012) replacements mainly cause peripheral symptoms such as muscular atrophy, neuropathy and deafness, with the condition associated to the latter mutation being also known as the Cowchock syndrome. In addition to progressive neurodegeneration, the D237G replacement (Forneris et al., 2009) was found to cause skeletal deformities and hypomyelination. Biochemical and molecular studies have been performed in a number of these hAIF allelic variants in the last decade, either using hAIF or the mAIF homologue, trying to determine their structural/functional properties.

The  $\Delta$ R201 mutation was discovered in two male patients affected by a severe mitochondrial encephalomyopathy during their childhood (Ghezzi, 2010). Their symptoms included severe retardation in neuronal and psychomotor development, associated to mitochondrial ETC defects due to a reduced functionality of respiratory complexes III and IV, therefore affecting to OXPHOS. Only riboflavin administration seemed to temporally rescue their clinic condition. As the two patients were born from two twin sisters, it was speculated that the pathology was linked to the X chromosome and the deletion of the entire codon of the Arg201 was found in the *aifm1* genes of both children. Arg201 is localised in a  $\beta$ -hairpin (191-203 residues) that in the hAIF oxidised structure contributes to bridge the oxidoreductase domain to the C-terminal domain (**Figures 1.6 and 1.17**) (Ferreira et al., 2014).

**Table1.4:** Summary of identified hAIF disease-causing mutations and their clinical presentations in patients.

RESIDUE	MUTATION	LOCATION	CLYNICAL SYMPTOMS	OXPHOS DEFECTS	REDOX ACTIVITY	DNA BINDING	AIF THERMAL STABILITY	APOPTOSIS
R201	Deletion	FAD-Binding domain	Encephalomyopathy	CI -80% CIII -40% CIV -90%	↑↑	+	↓↓	↑
F210	F210L F210S	FAD-Binding domain	Axonal polyneuropathy	ND	ND	ND	ND	-
D237	D237G	FAD-Binding domain	Spondyloepimetaphysol displasia, mental retardation	ND	ND	ND	ND	ND
V243	V243L	FAD-Binding domain	Muscle atrophy, ataxia hearing loss	CI CIII CIV	ND	-	ND	↑
G262	G262S	FAD-Binding domain	Encephalomyopathy, neuropathy	CI -80% CIII -40%	↑↑	-	ND	ND
G308	G308E	NADH-Binding domain	Encephalomyopathy	CI -80% CIV -90%	↓↓↓	-	↓	ND
G338	G338E	NADH-Binding domain	Ataxia neuropathy	CIV -(20-45%)	↓	-	ND	ND
Q479	Q479R	FAD-Binding domain	Encephalopathy, Myopathy,Neuropathy	ND	ND	ND	ND	ND
E493V	E493V	C-Terminus	Cow Chock, Neuropathy, Mental retardation	None	↑	+	↓	↑
T260 L344 G360 R422 R422 R430 R451 A472 P475 V498 I591	T260A L344F G360R R422W R422Q R430C R451Q A472V P475L V498M I591M	FAD-Binding domain NADH-Binding domain NADH-Binding domain FAD-Binding domain FAD-Binding domain FAD-Binding domain FAD-Binding domain FAD-Binding domain FAD-Binding domain C-Terminus C-Terminus	Neuropathy	ND	ND	ND	ND	ND

Colour-code rectangles indicate AIF domains. Data from: (Ghezzi, 2010; Hu et al., 2017; Sancho et al., 2017; Mierzevska et al., 2017; Kettwig et al., 2015; Ardisson et al., 2015; Diodato et al., 2016; Morton et al., 2017b; Rinaldi et al., 2012; Bano and Prehn, 2018 and Villanueva et al., 2019).

Further studies indicated that the  $\Delta$ R201 mutation does not dramatically impair AIF structure, but it leads to a decreased stability of the protein which, in addition, becomes more susceptible to FAD release and proteases digestion. As a consequence, the biochemical features of hAIF are altered, dramatically decreasing CTC AIF-FADH<sup>+</sup>:NAD<sup>+</sup> stability with respect to that of the wild type protein (Sevrioukova, 2016, Bano et al., 2010, Ghezzi et al., 2010)..



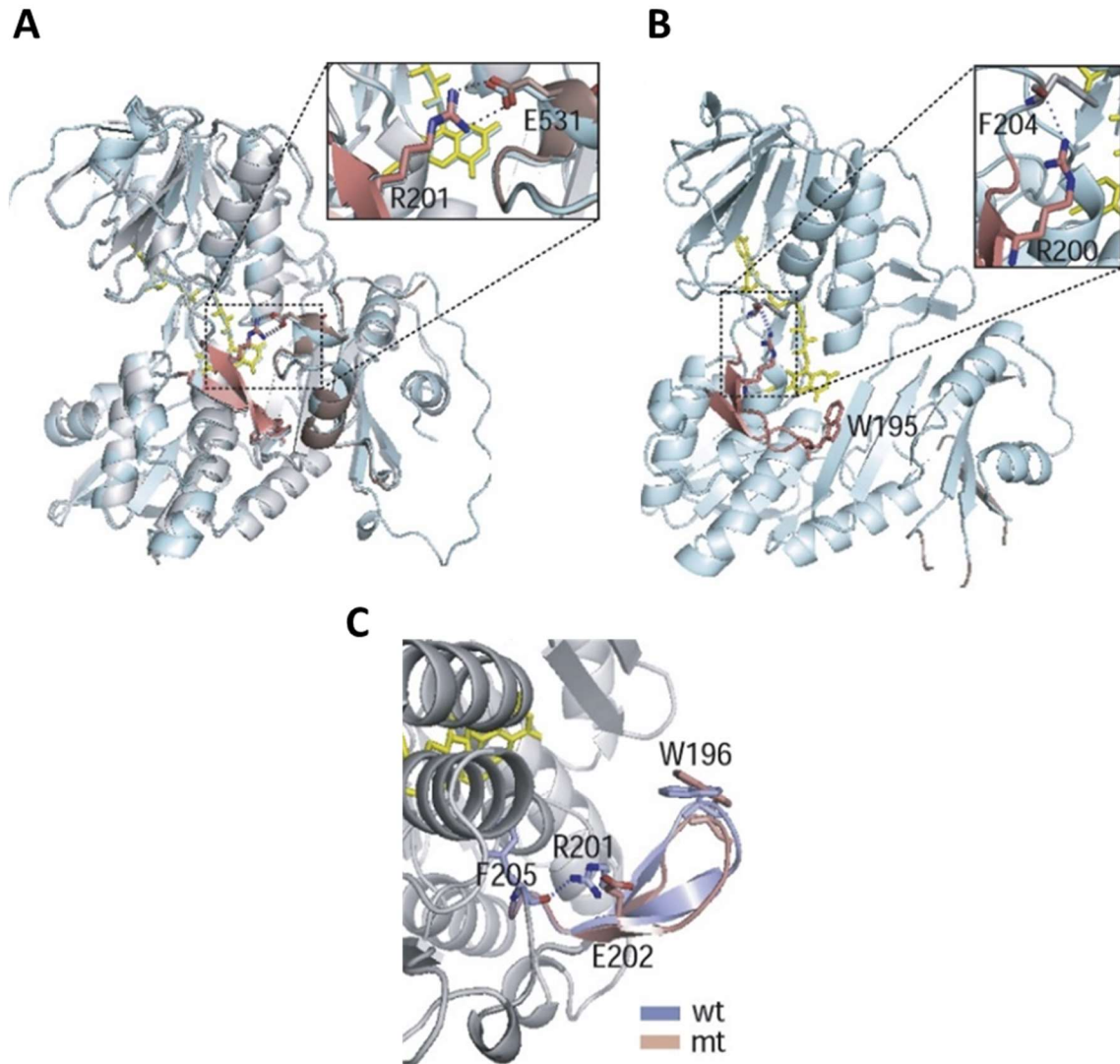


**Figure 1.17: Structural and *in vitro* analyses of hAIF and hAIF $\Delta$ R201.** (A) Superimposed X-ray structures of oxidised (NAD-less) human and murine AIFs (PDB codes: 1M6I and 1DV4) show that R201 (R200 in mouse) assists in the folding of two peptide stretches, near the FAD-binding pocket. The R201 residue, contained in the first stretch (in pink), establishes a link with the second stretch (in brown) by forming a salt bridge with the E531 residue. (B) In the reduced NAD-bound dimer of mAIF (PDB code 3GD4), the active form of the flavoprotein, R200 (R201 in humans), establishes a H-bond with F204, helping the functionally important  $\beta$ -hairpin, including the W195 residue (shown in pink), to get properly oriented. F204 and W195 correspond to human F205 and W196, respectively. (C) Computer modelling predicts that deletion of R201 in reduced hAIF can disrupt the H bond with F205 and thus shorten and distort the 191-203  $\beta$ -hairpin (rendered in blue for the wild-type and in pink for the mutant). Image from (Ghezzi et al.,2010).

The G308E mutation was associated with severe muscle weakness and atrophy in two brothers from healthy parents as a consequence of a missense mutation in exon 9 of the *aifm1* gene (Berger, 2011). This mutation is a loss-of-function mutation that profoundly perturbs AIF redox activity and affinity for NADH (Sevrioukova, 2016). The patients exhibited enlarged brain lateral ventricles and developed muscle weakness and atrophy within the first two months after birth. They also presented Cyt C oxidase deficiency accompanied by reduced complex I activity affecting OXPHOS (Berger, 2011). The equivalent amino acid substitution in mAIF (G307E) showed an *in vitro* dramatic decrease in the rate of reduction of AIF by NADH, but neither the rates of NAD<sup>+</sup> dissociation nor the O<sub>2</sub> reactivity of the resulting dimeric CTC were affected (Sorrentino et al., 2015). A detailed rapid-mixing and steady-state kinetic study of the reaction between AIF and NAD<sup>+</sup>/H allowed to describe a two-step mechanism for CTC formation. In addition, the FAD reduction induced a partial conformational reorganization of the protein, triggering dimerization independently from ligand binding and CTC formation. The G308 residue is located in a crucial region for NADH binding to the protein, occupying the second position of the canonical Rossmann fold GXGXXG motif (see **section 1.1** and **Figure 1.18**) (Sorrentino et al., 2017). Altogether these observations indicate that the pathogenic G308E replacement disrupts the AIF *in vivo* functions by specifically slowing down the formation of the dimeric CTC.

The E493V mutation was described in an Italian-American family with hereditary Cowchock syndrome, a form of Charcot-Marie-Tooth disease with childhood-onset. Males displayed recessive axonal motor and sensory neuropathy, progressive intellectual decline and muscle wasting and differences in Cyt C oxidase as well as succinate dehydrogenase activities (Rinaldi et al., 2012). Compared to the other two mutations, the E493V mutation induces only modest structural changes and does not cause major OXPHOS defects, but perturbs the electrostatic surface potential near the redox centre altering the surface profile (**Figure 1.19**). This, in turn, could increase solvent accessibility of FAD and affect the redox reactivity of AIF (Rinaldi et al., 2012).

E493V mutation is located on the novel NAD(H)<sub>B</sub> binding site (Ghezzi et al., 2010, Rinaldi et al., 2012). Such mutation would prevent the interaction of the E493 side-chain with the two short helices in hAIF<sub>Δ1-102</sub> and with the ribose of NAD(H)<sub>B</sub> in hAIF<sub>Δ1-102</sub>:2NAD(H), explaining some of the effects reported for the E493V hAIF variant (Churbanova and Sevrioukova, 2008, Rinaldi et al., 2012). The finding of these pathogenic mutations in this site support the importance of the folding conservation of this region for the proper protein function (Ferreira et al., 2014).



It is worth to mention that this pathogenic mutation E493V, as well as the  $\Delta$ R201 deletion, are related to a prominent activation of the AIF-specific cell death pathway and they showed CTCs with shorter lifetimes versus molecular oxygen reoxidation than the WT protein (Ghezzi et al., 2010, Rinaldi et al., 2012).

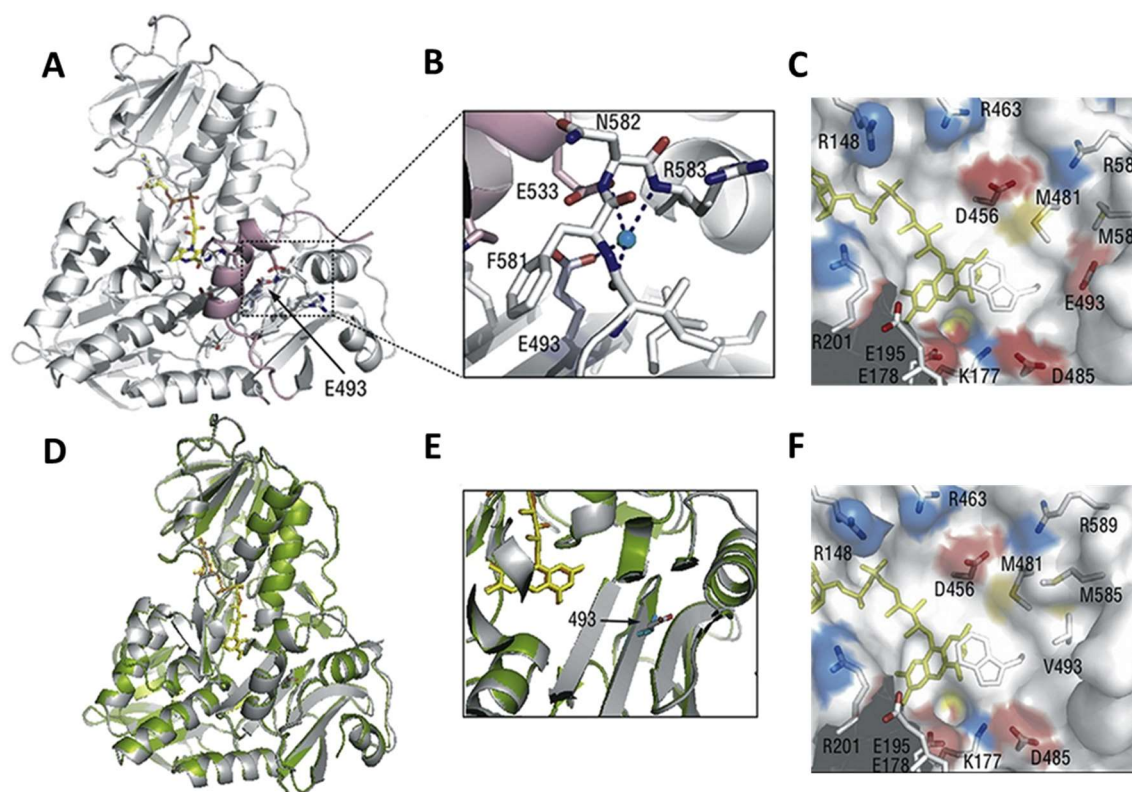


**Figure 1.18: Structural Comparison of the WT and hAIF E493V.** (A) Position of E493 (indicated by an arrow) in oxidised human WT (PDB code 1M6I). FAD is shown in yellow and a partially disordered regulatory peptide is in pink. (B) Water-bridged contacts involving E493 hold the 512-533 helical fragment of the regulatory peptide (pink) close to the active site. (C) Charge distribution near the flavin cofactor. Positively and negatively charged residues are depicted in blue and red, respectively. E493 is 10 Å away from FAD and is part of an acidic cluster adjacent to the isoalloxazine ring. (D) Superposition of the structures of the WT and E493V mutant of human AIF (green, PDB code 4FDC). (E) A magnified view at the region of AIF near the site of the E493V residue demonstrating that the substitution does not alter the structure near the active site of AIF. (F) The E493V substitution changes both the surface profile and electrostatic potential, which may affect solvent accessibility and redox properties of FAD. Image from (Rinaldi et al., 2012).

The E493V mutation did not alter the absorbance spectrum, extinction coefficient, and midpoint redox potential of AIF (Breuer et al., 2013). Similar to the WT, it also has high affinity for NADH, binds the cofactor tightly and in a stoichiometric fashion, and forms CTC upon reduction. Nevertheless, a subtle difference in circular dichroism spectra and slightly higher FAD fluorescence suggest structural dissimilarities relative to the WT (Rinaldi et al., 2012). The most notable changes caused by the E493V substitution were observed in electron transfer ability, it has lower  $K_m^{\text{NADH}}$  (by 20 %) than the WT.

The fact that there are so many pathogenic variants, highlights the importance of AIF in human metabolism, and reflects the high variability in terms of clinical manifestations that can induce mutations in a single gene. This heterogeneous group of pathologies further hampers the development of therapeutic treatments for mitochondrial diseases (Bano and Prehn, 2018). Considering the wide range and importance of cellular processes regulated by AIF and the little knowledge about the molecular mechanisms of AIF on the OXPHOS and PCD pathways, it is of interest to better understand the molecular components contributing to the pathogenesis of AIF-related mitochondrial diseases.



## *2- OBJECTIVES*



## 2.1 OBJECTIVES

The general aim of this thesis is to better understand how the interaction of the human Apoptosis Inducing Factor (hAIF) with different biomolecules, including the NADH coenzyme, DNA, and its different protein partners, modulates its pro-life and pro-death activities.

To achieve this general goal, the following partial objectives were proposed in this study:

1. Improve the overexpression and purification procedures for apoptotic and mitochondrial soluble forms, hAIF $_{\Delta 1-101}$  and hAIFmt $_{\Delta 1-77}$  respectively, as well as for its CHCHD4, CypA and H2AX protein partners.
2. Study hAIF plasticity by evaluating the effect of protein length, subcellular pH, CTC formation, and pathogenic mutations on its stability.
3. Evaluate the role of W196, sited at the NADH<sub>B</sub> binding site, in the redox activity of the protein and in its interaction with physiological partners.
4. Assess the effect of the physiological interaction of hAIF on its mitochondrial soluble form with the CHCHD4 in its oxidoreductase activity.
5. Characterise the *in vitro* molecular interaction of hAIF, as well as of its variants, with DNA, CHCHD4, CypA, and H2AX.
6. Contribute to the description of the assembly of the degradosome.





### *3- MATERIALS AND METHODS*





### 3.1 BIOLOGICAL MATERIAL

#### Bacterial strains.

All human proteins used in this study were produced by heterologous expression in *Escherichia coli*, using the following strains:

- DH5 $\alpha$ : Genotype: F<sup>-</sup>  $\Phi$ 80lacZ $\Delta$ M15  $\Delta$ (lacZYA-argF) U169 recA1 endA1 hsdR17(rk<sup>-</sup>,mk<sup>+</sup>) phoA supE44 thi-1 gyrA96 relA1  $\lambda^-$  (Invitrogen). This strain was developed by Dr. Hanahan as a cloning strain with multiple mutations that enable high efficiency transformations (Taylor et al., 1993). This strain has three representative mutations: recA1 that inhibits homologous recombination, endA1 that inactivates intracellular endonucleases to prevent degradation of the plasmid and lacZM15 that allows selection by  $\alpha$  complementation. In this study, it was used to amplify and conserve plasmids.
- BL21 (DE3): Genotype: fhuA2 [lon] ompT gal ( $\lambda$  DE3) [dcm]  $\Delta$ hsdS $\lambda$  DE3 =  $\lambda$ SbamHlo  $\Delta$ EcoRI-B int:: (lacI::PlacUV5::T7 gene1) i21  $\Delta$ nin5 (Invitrogen). This strain is a descendant of the *E. coli* B strain specifically constructed for high-level expression of recombinant proteins. This strain has two important attributes that make it useful for protein expression: i) key genetic markers which help recombinant RNA or protein to accumulate at high levels without degradation, and ii) inducibility of protein expression to minimise the toxic effects of some recombinant proteins (Life Technologies). The (DE3) designation indicates that it contains the DE3 lysogen that carries the gene for T7 RNA polymerase under control of the lac UV5 promoter. Isopropyl  $\beta$ -D-1-thiogalactopyranoside (IPTG) is required to induce expression of the T7 RNA polymerase (Invitrogen).
- C41 (DE3): The C41 strain (DE3) derives from the BL21 (DE3) strain. This strain has some mutations that prevent cell death associated with the expression of toxic recombinant proteins (Schreiber et al., 2017).

The following culture media were used for *E. coli* growth (Sambrook and Russell, 2001):

- Luria-Bertani (LB): 10 g/L Tryptone, 10 g/L NaCl and 5 g/L yeast extract.
- LB-agar: 10 g/L Tryptone, 10 g/L NaCl, 5 g/L yeast extract and 20 g/L agar.

Strains were conserved at -80 °C with 10 % glycerol.

### DNA samples.

- To evaluate hAIF and degradosome ability to bind DNA, the following desalting-purified 15-bp single-stranded DNA (ssDNA) samples, forward and reversed, were obtained from Integrated DNA Technologies:

Forward: 5' - GGT TAG TTA TGC GCG -3' ;

Reverse: 5' - CGC GCA TAA CTA ACC -3' ;

- The *in vitro* affinity of hAIF<sub>Δ1-101</sub> and of its variants for different DNA fragments was analysed by the electrophoretic mobility shift assay (EMSA) in agarose gels using a GeneRuler 100 bp DNA Ladder (Thermo Fisher Scientific).

## 3.2 EXPRESSION VECTOR

The pET-28a(+) vector (Novagen, Catalogue number 69864-3) was employed for heterologous protein expression (**Figure 3.1**). The pET system allows the expression of recombinant proteins, including those of eukaryotic origin, in *E. coli*. It was developed by Studier and collaborators (Studier and Moffatt, 1986, Rosenberg et al., 1987, Studier et al., 1990). These plasmids have transcription recognition sequences for the bacteriophage T7 and ribosome binding sequences with a high level of transcription efficiency. The pET-28a(+) vector allows to clone the sequence of the gene of interest in such a way that the expressed protein can be fused to a His-tag tail at the N-terminal end (or C-terminal end). In addition, this plasmid confers resistance to kanamycin. The host cells for this vector are strains of *E. coli* that present a chromosomal copy of the gene corresponding to the T7 RNA polymerase under control of the lacUV5 promoter, inducible by IPTG.

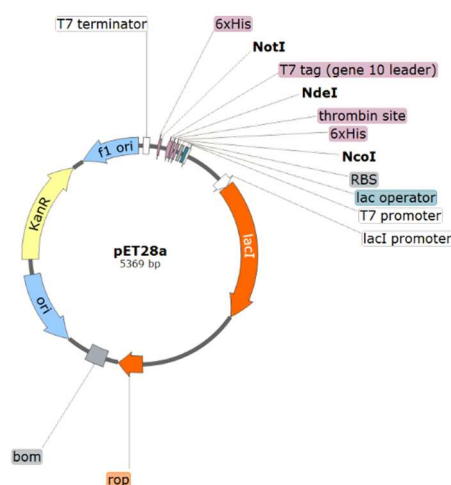


**Figure 3.1:** Map of the pET-28a(+) expression vector.

### 3.2.1 EXPRESSION VECTOR CONSTRUCTIONS

Constructions to produce the recombinant proteins were obtained from GenScript. All proteins were designed as fusion proteins with His-tags to facilitate their purification (Hengen, 1995). Thus, all cDNAs included a string coding for a His<sub>6</sub>-tag fused to its N- or C-terminus. Below are shown the different constructions used for protein expression.

**Table 3.1:** Colour code for the elements present in the protein constructions

Interest sequence	Colour
START of the transcription	Pink
PRESCISSION PLUS PROTEASE recognition site	Green
THROMBIN protease recognition site	Blue
LINKER	Light Blue
HISTIDINE- Tag	Grey
STOP of the transcription	Red

#### pET-28a(+)-hAIF<sub>Δ1-101</sub>:

The cDNA for hAIF<sub>Δ1-101</sub> (*aifm1*, apoptosis inducing factor mitochondria associated 1 [*Homo sapiens*] GenBank code 9131 with Δ1-101 deletion) was cloned into the *NdeI/NotI* sites of the pET-28a(+) expression vector with a N-terminal His<sub>6</sub>-tag followed by a cleavable recognition site for the thrombin protease (Thb) (Miramar, 2008).

> His<sub>6</sub>-Thb-hAIF<sub>Δ1-101</sub> nucleotide sequence.

ATCGGCAGTTCTCATCATCATCATCATCATCGGCAGTTCACTGGTGCCCAAGGGCAGCGGCAGTTCTATGAAGCTGGGCCT  
 GACCCCCGAGCAGAAGCAGAAGAAGGCCGCCCTGAGCGCCAGCGAGGGCGAGGAGGTGCCCCAGGACAAGGCCCCAGCC  
 ACGTGCCCTTCTGCTGATCGGCGGGCGGCCACCGCCGCCCTTCGCCGCCGCCAGGAGCATCAGGGCCAGGGACCCCGCGGCC  
 AGGGTGCTGATCGTGAGCGAGGACCCCGAGCTGCCCTACATGAGGCCCCCCTGAGCAAGGAGCTGTGGTTCAGCGACGA  
 CCCCCACGTGACCAAGACCCTGAGGTTCAAGCAGTGGAACGGCAAGGAGAGGAGCATCTACTTCCAGCCCCCAGCTTCT  
 ACGTGAGCGCCAGGACCTGCCCCACATCGAGAACGGCGCGCTGGCCGTGCTGACCGGCAAGAAGGTGGTGCACTGGAC  
 GTGAGGGACAACATGGTGAAGCTGAACGACGGCAGCCAGATCACCTACGAGAAGTGCTGATCGCCACCGCGCGCACCCCC  
 CAGGAGCCTGAGCGCCATCGACAGGGCCGGCGCCGAGGTGAAGAGCAGGACCACCCTGTTCAAGGAAGATCGGCGACTTCA  
 GGAGCCTGGAGAAGATCAGCAGGGAGGTGAAGAGCATCACCATCATCGGCGCGCGCTTCTTGGGCAGCGAGCTGGCCTGC  
 GCCCTGGGCAGGAAGGCCAGGGCCCTGGGCACCGAGGTGATCCAGCTGTTCCCCGAGAAGGGCAACATGGGCAAGATCCT  
 GCCCGAGTACCTGAGCAACTGGACCATGGAGAAGGTGAGGAGGGAGGGCGTGAAGGTGATGCCCAACGCCATCGTGCGAGA  
 CGGTGGGCGTGAGCAGCGGCAAGCTGCTGATCAAGCTGAAGGACGGCAGGAAGGTGGAGACCGACCATCGTGGCCGCGC  
 GTGGGCGTGAGCCCCACGTGGAGCTGGCCAAGACCGCGCGCCTGGAGATCGACAGCGACTTCGGCGGCTTCAGGGTGAA  
 CGCCGAGCTGCAGGCCAGGAGCAACATCTGGGTGGCCGCGCAGCGCCGCTGCTTCTACGACATCAAGCTGGGCAGGAGGA  
 GGGTGGAGCACCACGACCGCCGCTGGTGAGCGGCAGGCTGGCCGCGCGAGAACATGACCGCGCGCGCCAAGCCCTACTGG  
 CACCAGAGCATGTTCTGGAGCGACCTGGGCCCCGACGTGGGCTACGAGGCCATCGGCCCTGGTGACAGCAGCCTGCCAC  
 CGTGGGCGTGTTCCGCAAGGCCACCGCCAGGACAACCCCAAGAGCGCCACCGAGCAGAGCGGCACCGGCATCAGGAGCG  
 AGAGCGAGACCGAGAGCGAGGCCAGCGAGATCACCATCCCCCAGCACCCCGCCGTGCCAGGCCCCCGTGCAGGGC  
 GAGGACTACGGCAAGGGCGTGATCTTCTACCTGAGGGACAAGGTGGTGGTGCGCATCGTGTGTGGAACATCTTCAACAG  
 GATGCCCATCGCCAGGAAGATCATCAAGGACGGCGAGCAGCAGGACCTGAACGAGGTGGCCAAGCTGTTCAACATCC  
 ACGAGGAC TGA

> Resulting His<sub>6</sub>-Thb-hAIF<sub>Δ1-101</sub> fusion protein.

MGSSHHHHHHGSSLVPRGSGSSKLGLTPEQKQKKAALSASEGEEVVDKAPSHVPFLLIGGGTAFAAARSIRARDPGAR  
 RLIVSEDPFLPYMRPPLSKELWFSDDPNVTKTLRFKQWNGKERSIYFQPPSFYVSAQDLPHIENGGAVALTGKKVVQLDV  
 RDNMVKLNDGSQITYEKLIAITGGTTPRLSAIDRAGAEVKSRTTLFRKIGDFRSLEKISREVKSIITIGGGFLGSELACA  
 LGRKARALGTEVIQFLFPEKGNMGKILPEYLSNWTMEKVRREGVKVMPNAIVQSVGVSSGKLLIKLKDGRKIVETDHIIVAAV  
 GLEPNVELAKTGGLIDSDFGGFRVNAELQARSNIWVAGDAACFYDIKLRRRVEHHDHAVVSGRLAGENMTGAAPYWH  
 QSMFWSDLGPDVGYEATGLVDSSLPTVGVFAKATAQDNPKSATEQSGTGIRSESETESEASEITIPPSTPAVPQAPVQGE  
 DYKGKGVIFYLRDKVVVGIVLWNIFNRMPIARKI IKDGEQHEDLNEVAKLFNIHED\*

**pET-28a(+)-hAIFmt $\Delta$ 1-77:**

This construction is the mitochondrial form of hAIF, designed without the residues of the transmembrane helix to obtain it in a soluble way.

The cDNA for hAIFmt $\Delta$ 1-77 (*aifm1*, apoptosis inducing factor mitochondria associated 1 [*Homo sapiens*] GenBank code 9131 with  $\Delta$ 1-77 deletion) was cloned into the *NcoI/NdeI* sites of the pET-28a(+) expression vector with a C-terminal His<sub>6</sub>-tag followed by a cleavable recognition site for Thb.

> hAIFmt $\Delta$ 1-77-Thb-His<sub>6</sub> nucleotide sequence.

ATCGTGGGCGCCGGCGCTACGCCTACAAGACCATGAAGGAGGACGAGAAGAGGTACAACGAGAGGATCAGCGGCCTGGG  
CCTGACCCCCGAGCAGAAGCAGAAGAAGCCGCTGAGCGCCAGCGAGGGCGAGGAGTCCCCAGGACAAGGCCCCCA  
GCCACGTGCCCTTCTGCTGATCGGCGCGGCACCGCCGCTTCCGCCGCCAGGAGCATCAGGGCCAGGGACCCCGGC  
GCCAGGTGCTGATCGTGAGCGAGGACCCGAGCTGCCCTACATGAGGCCCCCTGAGCAAGGAGCTGTGGTTTCAGCGA  
CGACCCCAACGTGACCAAGACCCTGAGGTTCAAGCAGTGGAACGGCAAGGAGAGGAGCATCTACTTCCAGCCCCCAGCT  
TCTACGTGAGCGCCCAAGACCTGCCCAACATCGAGAACGGCGCGTGGCCGTGCTGACCGCAAGAAGGTGGTGCAGCTG  
GACGTGAGGGACAACATGGTGAAGCTGAACGACGGCAGCCAGATCACCTACGAGAAGTGCTGATCGCCACCGGCGGCAC  
CCCCAGGAGCCTGAGCGCCATCGACAGGGCGCGCGCGAGGTGAAGAGCAGGACCACCCTGTTTTCAGGAAGATCGGCGACT  
TCAGGAGCCTGGAGAAGATCAGCAGGGAGGTGAAGAGCATCACCATCATCGGCGCGCGCTTCTTGGGACGAGCTGGCC  
TGCGCCTGGGACGAAGGCCAGGGCCCTGGGCACCGAGGTGATCCAGCTGTTCCCCGAGAAGGGCAACATGGGCAAGAT  
CCTGCCCCAGTACCTGAGCAACTGGACCATGGAGAAGGTGAGGAGGGAGGGCGTGAAGGTGATGCCCAACGCCATCGTGC  
AGAGCGTGGGCGTGAGCAGCGGCAAGCTGCTGATCAAGCTGAAGGACGGCAGGAAGGTGGAGACCGACCACATCGTGGCC  
GCCGTGGGCGTGGAGCCCAACGTGGAGCTGGCCAAGACCGGCGCGCTGGAGATCGACAGCGACTTCGGCGGCTTCAGGGT  
GAACGCCGAGCTGCAGGCCAGGAGCAACATCTGGGTGGCGGCGACGCCGCTGCTTCTACGACATCAAGTGGGACGA  
GGAGGTGGAGCACCACGACCGCGTGGTGAGCGGCAGGCTGGCCGGCGAGAACATGACCGGCGCCGCAAGCCCTAC  
TGGACACGAGCATGTTCTGGAGCGACCTGGGCCCCGACGTGGGCTACGAGGCCATCGGCTGGTGGACAGCAGCCTGCC  
CACCGTGGGCGTGTTCGCCAAGGCCACCGCCAGGACAACCCCAAGAGCGCCACCGAGCAGAGCGGCACCGGCATCAGGA  
GCGAGAGCGAGACCGAGAGCGAGGCCAGCGAGATCACCATCCCCCAGCACCCCGCCGTGCCCCAGGCCCCCGTGCAG  
GGCGAGGACTACGGCAAGGGCGTGATCTTCTACCTGAGGGACAAGGTGGTGGTGGGCATCGTGTGTGAACATCTTCAA  
CAGGATGCCCATCGCCAGGAAGATCATCAAGGACGGCAGCAGCAGGACCTGAACAGGTGGCCAAGCTGTTCAACA  
TCCACGAGGACGGCAGTTCTCTGGTGGCCAGGGGCGAGGGCAGTTCTCACCACCACCACCACCACGGCAGTTCTTGA

> Resulting hAIFmt $\Delta$ 1-77-Thb-His<sub>6</sub> fusion protein.

MVGAGAYAYKTMKEDERYNERISGLGLTPEQKQKKAALSASEGEEVPPQDKAPSHVPFLLIIGGGTAFAAARSIRARDPG  
ARVLIVSEDPPELPMRPLSKELWFSDDPNVTKTLRFKQWNGKERSIYFQPPSFYVSAQDLPHIENGVAVLTKGKVVQL  
DVRDNMVKLNDGSQITYEKLIATGGTPRSLSAIDRAGAEVKSRTTLFRKIGDFRSLKISREVKSITIIGGGFLGSELA  
CALGRKARALGTEVIQLFPEKGNMGKILPEYLSNWTMEKVRREGVKVMPNAIVQSVGVSSGKLLIKLDGRKVETDHIVA  
AVGLEPNVELAKTGGLLEIDSDFGFRVNAELQARSNIWVAGDAACFYDIKLGRRRVEHHDHAVVSGRLAGENMTGAAKPY  
WHQSMFWSDLGPDVGYEAIGLVDSSLPVGVFAKATAQDNPKSATEQSGTGIRSESETESEASEITIPPSTPAVPQAPVQ  
GEDYKGKIVIFYLRDKVVVGIVLWNI FNRMPIARKIIKDGEQHEDLNEVAKLFNIHEDGSSLVPRGSGSSHHHHHHGSS\*

**pET-28a(+)-H2AX:**

The cDNA for H2AX (*h2afx* H2A histone family member X [*Homo sapiens*] GenBank code 3014) was cloned into the *NcoI/NdeI* sites of the pET-28a(+) expression vector with a N-terminal His<sub>6</sub>-tag followed by a cleavable recognition site for PreScission Plus protease (PP).

> His<sub>6</sub>-PP-H2AX nucleotide sequence.

ATCGGCAGTTCTCATCATCATCATCATGGCAGTTCTAGAAAGTATTATTCAGGGGCGCGGCAGTTCTATGAGCGG  
CAGGGGCAAGACCGGCGCAAGGCCAGGGCCCAAGGCCAAGAGCAGGAGCAGCAGGGCCGCGCTGCAGTTCCCCGTGGGCA  
GGGTGCACAGGCTGCTGAGGAAGGGCCACTACGCCAGAGGGTGGGCGCGCGCCCCGTGTACCTGGCCGCCGTGCTG  
GAGTACCTGACCGCCGAGATCCTGGAGCTGGCCGGCAACGCCCGCAGGGACAACAAGAAGACCAGGATCATCCCCAGGCA  
CCTGCAGCTGGCCATCAGGAACGACGAGGAGCTGAACAAGCTGCTGGGCGCGGTGACCATCGCCAGGGCGCGGTGCTGC  
CCAACATCCAGGCCGTGCTGCTGCCAAGAAGACCAGCGCCACCGTGGGCCCCAAGGCCCCAGCGGCGGCAAGAAGGCC  
ACCCAGGCCAGCCAGGAGTACGAGTGA

> Resulting His<sub>6</sub>-PP-H2AX fusion protein.

MGSSHHHHHHGSSLEVLFQGPSSMSGRGKTGGKARAKAKSRSSRAGLQFPVGRVHRLLRKHGHAERVGAGAPVYLA  
EYLTAEILELAGNAARDNKKTRIIPRHLQLAIRNDEELNKLGGVTIAQGGVLPNIQAVLLPKKTSATVGPAPSGGKKA  
TQASQEY

**pET-28a(+)-CypA:**

The cDNA for CypA (*ppia* peptidyl prolyl isomerase A [*Homo sapiens*] GenBank code: 5478) was cloned into the *NdeI/NotI* sites of the pET-28a(+) expression vector with a N-terminal His<sub>6</sub>-tag followed by a cleavable recognition site Thb.

> His<sub>6</sub>-Thb-CypA nucleotide sequence.

ATGGGCAGTTCTCATCATCATCATCATCATGGCAGTTCACTGGTGCCCAAGGGCAGCGGCAGTTCTATGGTGAACCCAC  
CGTGTCTTCGACATCGCCGTGGACGGCAGCCCCCTGGGCAGGGTGAGCTTCGAGCTGTTCGCCGACAAGGTGCCCCAAGA  
CCGCCGAGAACTTCAGGGCCCTGAGCACCGGCGAGAAGGGCTTCGGCTACAAGGGCAGCTGCTTCCACAGGATCATCCCC  
GGCTTCATGTGCCAGGGCGGCGCACTTACCAGGCACAACGGCACCGGCGGCAAGAGCATCTACGGCGAGAAGTTCGAGGA  
CGAGAACTTCATCTGAAGCACACCGGCCCCGGCATCTGAGCATGGCCAACGCCGGCCCCAACCAACGGCAGCCAGT  
TCTTCATCTGCACCGCCAAGACCGAGTGGCTGGACGGCAAGCAGCTGGTGTTCGGCAAGGTGAAGGAGGGCATGAACATC  
GTGGAGGCCATGGAGAGGTTTCGGCAGCAGGAACGGCAAGACCAGCAAGAAGATCACCATCGCCGACTGCGGCCAGCTGGA  
G TGA

> Resulting His<sub>6</sub>-Thb-CypA fusion protein.

MGSSHHHHHHGSSLVPRGSGSSMVNPTVFFDIAVDGEPLGRVSFELFADKVPKTAENFRALSTGEKGFYKGSFCFHRIIP  
GFMCQGGDFTRHNGTGGKSIYGEKFEDENFILKHTGPGILSMANAGPNTNGSQFFICTAKTEWLDGKHVVFQKVKEGMNI  
VEAMERFGSRNGKTSKKITIADCGQLE

**pET-28a(+)-CHCHD4:**

The cDNA for CHCHD4 (*coiled-coil-helix-coiled-coil-helix domain containing 4* [*Homo sapiens*] GenBank code: 131474) was cloned into the *NdeI/NotI* sites of the pET-28a(+) expression vector with a N-terminal His<sub>6</sub>-tag followed by a cleavable recognition site for Thrombin (Thb).

> His<sub>6</sub>-Thb-CHCHD4 nucleotide sequence.

ATGGGCAGTTCTCATCATCATCATCATCATGGCAGTTCACTGGTGCCCAAGGGCAGCGGCAGTTCTATGAGCTACTGCAG  
GCAGGAGGGCAAGGACAGGATCATCTTCGTGACCAAGGAGGACCACGAGACCCCCAGCAGCGCCGAGCTGGTGGCCGACG  
ACCCCAACGACCCCTACGAGGAGCAGCGCTGATCTGCCCAACGGCAACATCAACTGGAAGTGCCTGGGCGGC  
ATGGCCAGCGCCCCCTGCGGCGAGCAGTTCAAGAGCGCCTTCAGCTGCTTCCACTACAGCACCGAGGAGATCAAGGGCAG  
CGACTGCGTGGACCAGTTCAGGGCCATGCAGGAGTGCATGCAGAAGTACCCCGACCTGTACCCCGAGGAGCAGGAGACG  
AGGAGGAGGAGAGGAGAAGAAGCCCGGAGCAGGCCGAGGAGACCGCCCCCATCGAGGCCACCGCCACCAAGGAGGAG  
GAGGGCAGCAGC TGA

> Resulting His<sub>6</sub>-Thb-CHCHD4 fusion protein.

MGSSHHHHHHGSSLVPRGSGSSMSYCRQEGKDRIIFVTKEDEHETPSSAELVADDPNDPYEEHGLILPNGNINWNCPLGG  
MASGPCGEQFKSAFSCFHYSTEEIKGSDCVDQFRAMQECMQKYPDLYPQEDDEDEEEEREKKPAEQAEETAPIEATATKEE  
EGSS\*

**Table 3.2:** Summary of the constructions used for the production of proteins.

Constructions Name	Protein	His-Tag Site	Cloning Sites	Protease	GenBank Code
pET-28a(+)-hAIFmt <sub>Δ1-77</sub>	hAIFmt <sub>Δ1-77</sub>	C-Ter	<i>NcoI/NdeI</i>	Thrombin	9131
pET-28a(+)-hAIF <sub>Δ1-101</sub>	hAIF <sub>Δ1-101</sub>	N-Ter	<i>NdeI/NotI</i>	Thrombin	9131
pET-28a(+)-H2AX	H2AX	N-Ter	<i>NcoI/NdeI</i>	PreScission plus	3014
pET-28a(+)-CypA	CypA	N-Ter	<i>NdeI/NotI</i>	Thrombin	5478
pET-28a(+)-CHCHD4	CHCHD4	N-Ter	<i>NdeI/NotI</i>	Thrombin	131474

The site-directed mutants of hAIF<sub>Δ1-101</sub> and hAIF<sub>Δ1-77</sub> isoforms (**Table 3.3**) were similarly synthesised and subcloned into pET-28a(+) by Mutagenex®.

**Table 3.3:** Summary of the hAIF<sub>Δ1-101</sub> and hAIF<sub>Δ1-77</sub> mutants generated in this study by site-directed mutagenesis. The modified codifying codon and the new codon after mutation are highlighted in red. All sequences are in the 5'-3' sense.

Protein	Mutant	Sequence	Codon Change
hAIF <sub>Δ1-101</sub>	W196A	GCC <b>TGG</b> AGA	GCC <b>GCT</b> AGA
hAIF <sub>Δ1-101</sub>	W196L	GCC <b>TGG</b> AGA	GCC <b>CTT</b> AGA
hAIF <sub>Δ1-101</sub>	W196Y	GCC <b>TGG</b> AGA	GC <b>TAC</b> AGA
hAIF <sub>Δ1-101</sub>	G308E	AAGACC <b>GGC</b> GGC	AAGACC <b>GAA</b> GGC
hAIF <sub>Δ1-101</sub>	ΔR201	ATCAGC <b>AGG</b> GAGGTG	ATCAGCGAGGTG
hAIF <sub>Δ1-101</sub>	E493V	GACGGC <b>GAG</b> CAGCAC	GACGGC <b>GTT</b> CAGCAC
hAIF <sub>Δ1-101</sub>	E413A/R422A/R430A	CTG <b>GAG</b> ATAGAC	CTG <b>GCC</b> ATAGAC
		TTC <b>AG</b> AGTA	TTC <b>GCC</b> GTA
		GCA <b>AG</b> ATCT	GCA <b>GCT</b> TCT
hAIF <sub>Δ1-77</sub>	E337/R346A/R354A	CTG <b>GAG</b> ATAGAC	CTG <b>GCC</b> ATAGAC
		TTC <b>AG</b> AGTA	TTC <b>GCC</b> GTA
		GCA <b>AG</b> ATCT	GCA <b>GCT</b> TCT

### 3.3 MOLECULAR BIOLOGY METHODS

#### 3.3.1 HIBRIDATION OF DNA

The double-stranded DNA (dsDNA), used for binding assays to hAIF and degradosome samples, was produced by hybridization of the 15-bp ssDNA. The ssDNA stocks were dissolved in distilled water to obtain 0.5 mM solutions of the forward and reverse oligonucleotides; then, they were mixed at equimolar ratio and annealed using a Stratagene Mx3005P qPCR real-time thermocycler (Agilent Technologies). The thermal annealing profile consisted in:

- Equilibration at 25 °C for 30 s.
- Heating ramp up to 99 °C.
- Equilibration at 99 °C for 60 s.
- 3-hour cooling process down to 25 °C at a rate of 1 °C/180 s.

The concentration of the final dsDNA was estimated by the equation 3.1:

$$\frac{1}{[\text{dsDNA}]} = \frac{1}{[\text{ssDNA}_{\text{FW}}]} + \frac{1}{[\text{ssDNA}_{\text{RV}}]} \quad (\text{Eq. 3.1}).$$

Where dsDNA is the double-stranded DNA, the ssDNA is the single-stranded DNA and the DNA<sub>FW</sub>, and DNA<sub>RV</sub> are the forward and reverse oligonucleotides respectively.

### 3.3.2 ISOLATION OF PLASMIDS

Purification of plasmids was carried out by starting from the culture, in 5 mL of LB contained in a 50 mL plastic tube, of a colony containing the construct of interest inoculated and grown overnight at 37 °C and 180 r.p.m Purification was performed using the GenElute Plasmid Miniprep kit (alkaline lysis method) (Sigma Aldrich) and following manufacturer instructions (**Figure 3.2**).

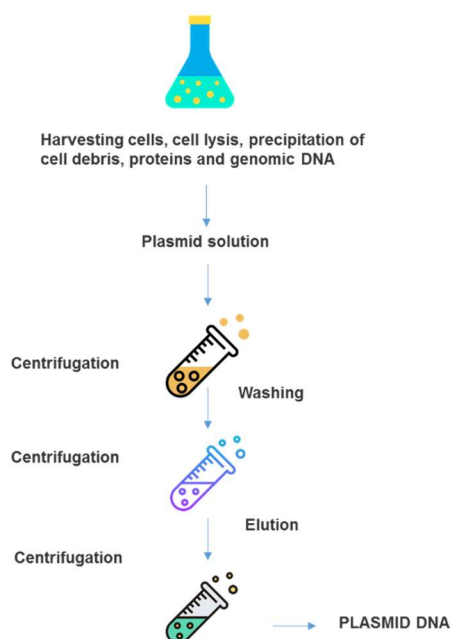


**Figure 3.2: Basic steps for plasmid purification** using the GenElute plasmid Miniprep kit (Sigma Aldrich).

### 3.3.3 PRODUCTION OF *E. coli* THERMO-COMPETENT CELLS

To achieve the heterologous expression of a recombinant protein in bacteria, it is necessary to introduce the expression plasmid that contains the cDNA of the desired protein. However, cDNA does not enter efficiently by itself and the bacterium cell wall has to be made permeable. This process is known as making bacterial cells competent. Competent cells used in this study were produced by treatment of *E. coli* cells with  $\text{CaCl}_2$  to achieve a state of competence during which DNA molecules may be admitted to the cell (Sambrook and Russell, 2001). Aseptic conditions are required for the whole process, therefore, all material must be sterilised in an autoclave or filtered by Millipore™ 0.22 µm sterile filters. Here, competent cells of *E. coli* BL21 (DE3), C41 (DE3) or DH5α strains were produced. A single bacterial colony from a LB-agar plate was picked and transferred into 10 mL of LB in a 50 mL plastic tube that was incubated at 37 °C and 180 rpm overnight. On the next day, 5 mL of this culture were used to inoculate 200 mL of LB lacking antibiotic

in a 500 mL glass bottle. This culture was incubated at 37 °C and 180 r.p.m, monitoring the growth by its turbidity until an optical density between 0.3 and 0.5 was reached at 600 nm ( $OD_{600nm}$ ). At this point, culture growth was stopped by immersion on ice for 20 min. Herein, temperature was maintained at 4 °C. Then, the cells were recovered by centrifugation for 15 min at 4000 r.p.m and 4 °C in a JA-25.50 rotor using a centrifuge Avanti J-25 (Beckman Coulter). The pellet was resuspended in 40 mL of ice-cold preparatory buffer (100 mM  $CaCl_2$ , 70 mM  $MgCl_2$ , 40 mM NaAc, pH 5.5). This sample was centrifuged in the same conditions. The supernatant was discarded, and the pellet was resuspended in 4 mL of conservation buffer (100 mM  $CaCl_2$  and 15 % glycerol). The obtained competent cells were dispensed in 200  $\mu$ L aliquots and immediately frozen under liquid nitrogen to improve their transformation capacity. Then, they were stored at -80 °C.

### 3.3.4 TRASFORMATION OF COMPETENT *E. coli* CELLS

Transformation refers to the process by which competent cells capture the DNA present in the medium. Transformation of competent cells with our expression vectors was carried out following a thermal shock methodology under aseptic conditions. 100  $\mu$ L of competent cells were transferred to sterile microcentrifuge tubes, and then 1  $\mu$ L (40-100 ng) of the plasmid was added, mixing the contents of the tube by gently shaking. The tubes were then stored on ice for 15 min. After that, they were incubated for exactly 50 s at 42 °C and then rapidly were transferred to an ice bath for 2 min. 500  $\mu$ L of LB were added to each tube, and the mixture was incubated for 1 h at 180 r.p.m and 37 °C, allowing bacteria to recover and to express the antibiotic resistance marker encoded by the plasmid (Sambrook and Russell, 2001). The transformed cells were then transferred in an appropriate volume (50, 100 and 200  $\mu$ L per 90 mm plate) onto LB-agar plates containing the antibiotic (30  $\mu$ g/mL kanamycin), homogeneously distributed and incubated overnight at 37 °C.

## 3.4 PRODUCTION OF RECOMBINANT PROTEINS

### 3.4.1 EVALUATION OF PROTEIN EXPRESSION

The ability of transformed *E. coli* cells to express the heterologous protein codified by the introduced expression vector was confirmed by small-scale production. Three isolated colonies containing the recombinant expression plasmid were inoculated separately in 5 mL of culture medium (LB containing 30  $\mu$ g/mL kanamycin) in 50 mL plastic tubes. The cultures were incubated overnight at 180 r.p.m and 37 °C. 100  $\mu$ L of each overnight culture



were used to inoculate 5 mL of fresh LB culture medium in 50 mL plastic tubes and incubated at 180 r.p.m and 37 °C until cell culture reached the desired OD<sub>600nm</sub> of 0.5-1. Then, IPTG was added to a final concentration of 1 mM to induce recombinant protein expression and cultures were incubated at 25 °C and 100 r.p.m for 18 h. On the following day, cells were harvested by centrifugation at 12000 r.p.m in an Eppendorf centrifuge 5427 R for 5 min at 4 °C and resuspended in 500 µL of 50 mM Tris/HCl buffer, pH 8.0. This solution was lysed in an ultrasonic equipment Up200S (Hielscher), with the solution kept in an ice bath, for 5 cycles of 30 s with an amplitude of 80 % and 0.5 s pulses, and 30 s of rest between cycles. Then, it was centrifuged in an Eppendorf centrifuge 5427 R for 5 min at 12000 r.p.m at 4 °C to separate the pellet from the supernatant. Protein expression was analysed using 12-15 % polyacrylamide denaturing electrophoresis. Different pre- and/or post- induction conditions, including time, OD<sub>600nm</sub>, agitation or temperature, were evaluated to achieve the optimal expression conditions for each protein (**Table 3.4**).

**Table 3.4:** Summary of conditions for expression and purification of the different proteins produced in this study.

Protein	OD <sub>600nm</sub>	IPTG (mM)	Induction Conditions	Buffers for affinity chromatography purification
<b>hAIF<sub>Δ1-101</sub> and variants*</b>	0.8	1	25 °C 100 r.p.m 18 h	A: 50mM Potassium phosphate (Kpi), pH 7.4, 0.4 M KCl, 4 mM Imidazole. B: 50mM Kpi, pH 7.4, 1 M Imidazole.
<b>hAIFmt<sub>Δ1-77</sub> and variants*</b>	0.8	1	25 °C 100 r.p.m 18 h	A: 50mM Kpi, pH 7.4, 0.4 M KCl, 4 mM Imidazole. B: 50mM Kpi, pH 7.4, 1 M Imidazole.
<b>CypA</b>	0.5	0.5	37 °C 180 r.p.m 3 h	A: 50mM Tris/HCl, pH 8.0, 150 mM NaCl. B: 50mM Tris/HCl, pH 8.0, 150 mM NaCl, 1 M Imidazole, 10 % Glycerol.
<b>CHCHD4</b>	0.5	1	37 °C 180 r.p.m 3 h	A: 50mM Kpi, pH 7.0, 150 mM NaCl. B: 50mM Kpi, pH 7.0, 1 M Imidazole.
<b>H2AX</b>	0.6	1	37 °C 180 r.p.m 3 h	A: 50mM Kpi, pH 7.4, 150 mM NaCl. B: 50mM Kpi, pH 7.4, 150 mM NaCl, 1M Imidazole.

A and B are respectively the binding and elution buffers used in the affinity chromatography gradient. \*LB medium supplemented with riboflavin (8 mg/L final concentration).

The culture of the isolated colony showing the highest expression was stored in 500 µL aliquots containing 10 % glycerol at -80 °C and subsequently used for protein overexpression.

### 3.4.2 MEDIUM SCALE PROTEIN PRODUCTION

For medium-scale expression and purification of the target protein, 100  $\mu$ L of the glycerol containing the *E. coli* selected expression colony were used to inoculate 500 mL of LB containing 30  $\mu$ g/mL kanamycin in a 1L Erlenmeyer flask, and then incubated overnight at 180 r.p.m and 37 °C. The next day, 10 Erlenmeyer flasks of 2 L containing 1 L of LB supplemented with kanamycin (30  $\mu$ g/mL), and when required riboflavin (8 mg/L), were inoculated with 40 mL of the overnight culture and incubated under the selected conditions until the OD<sub>600nm</sub> reached the optimum value for each protein (**Table 3.4**). At that point, IPTG was added and cultures were incubated under the required conditions to achieve maximum protein expression (**Table 3.4**). Cells were harvested by centrifugation for 10 min at 9000 r.p.m at 4 °C in a JA-10 rotor in an Avanti J-25 centrifuge (Beckman Coulter). The precipitate was washed with 0.15 M NaCl and the cells were centrifuged again. The supernatant was discarded, and the pellet was stored at -20 °C.

## 3.5 PURIFICATION OF RECOMBINANT PROTEINS

Due to the His<sub>6</sub>-tag included in all the proteins produced in this work, their purification protocols were very similar, with only small variations (**Table 3.4**).

### 3.5.1 PREPARATION OF CRUDE EXTRACTS

The cell pellet was resuspended in 120 mL of 50 mM Tris/HCl, pH 8.0 with cOmplete™ Protease Inhibitor Cocktail (Roche) and lysed by sonication in a glass container placed on ice (10 cycles of 30 s with 30 s in between) using an Up200S Ultrasonic equipment (Hielscher) with an amplitude of 80 % and 0.5 s pulses. The cell lysate was centrifuged for 1 h at 9000 r.p.m at 4 °C in a JA-10 rotor in an Avanti J-25 centrifuge (Beckman Coulter) to remove the insoluble debris. The supernatant was collected, transferred to a clean tube, and then was centrifuged again for 30 min under the same conditions. The clarified supernatant constituted the crude extract.

### 3.5.2 His-TAG AFFINITY CHROMATOGRAPHY

All proteins contained a His<sub>6</sub>-tag was purified by gel affinity chromatography using Immobilised metal ion affinity chromatography (IMAC) Sepharose 6 Fast Flow gel (GE Healthcare) activated with Ni<sup>2+</sup> (**Figure 3.3**). This gel is an immobilised metal affinity resin, a beaded agarose modified with a chelating ligand (NTA, Nitrilotriacetic acid) specifically

designed to bind recombinant proteins with His<sub>6</sub>-tags by charging with the desired metal ion (Ni<sup>2+</sup> in this case) and exhibiting low non-specific binding of other proteins. Binding of the His<sub>6</sub>-tag to the gel affinity matrix can be disturbed by high concentrations of imidazole that displaces the bound proteins during the chromatography, thus allowing its recovery from the matrix.

The Ni<sup>2+</sup> IMAC resin was regenerated by washing with 5 Column volumes (CV) of 1.5 M imidazole, followed by 5 CV of 1 M NaCl and 10 CV of distilled water. For long-term storage the resin was washed with 5 CV of 20 % ethanol. To activate the IMAC resin with Ni<sup>2+</sup>, it was first washed with 10 CV of distilled water to remove the ethanol, followed by 1 CV of 100 mM NiSO<sub>4</sub> and 10 CV of distilled water to remove NiSO<sub>4</sub> in excess. Finally, the activated resin was equilibrated in 10 CV of appropriate binding buffer (**Table 3.4**).

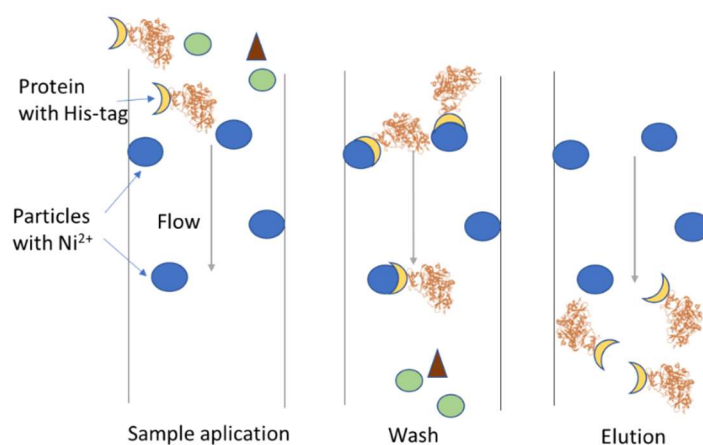


**Figure 3.3: Affinity column scheme for purification of proteins** containing His<sub>6</sub>-tags. Immobilised metal ion affinity chromatography (IMAC) is based on the specific coordinate binding of histidine residues to metals. This technique works by allowing proteins with the His<sub>6</sub>-tag to be retained in a column containing immobilised metal ions, such as nickel. For the purification of histidine-containing proteins, elution of the column is achieved by adding a competitive molecule, such as imidazole, that binds to the matrix stronger than the protein.

To initiate the purification procedure, the crude extract was incubated with the activated Ni<sup>2+</sup> resin equilibrated in the appropriate binding buffer (**Table 3.4**) in a bidirectional orbital rocker for at least 1 h at 4 °C. The mixture was then loaded and packed into a glass column with the aid of a syringe and washed with 5 CV of the desired binding buffer. The protein was then eluted with a linear imidazole gradient from 40 to 500 mM in the appropriate elution buffer, using a flow rate of 4 mL/min and collected from the column in 5 mL fractions using an ÄKTAprime system (GE Healthcare). Fractions containing the protein of interest were combined, concentrated, and dialysed against 50 mM Kpi pH 7.4 to remove imidazole traces. The CHCHD4 dialysis buffer contained also 10 mM DTT to facilitate a reducing environment.

### 3.5.3 SIZE-EXCLUSION CHROMATOGRAPHY

Size exclusion chromatography separates molecules by size as they pass through a resin packed in a column. Size exclusion resins consist in a matrix of spherical particles with pores of selected diameters (**Figure 3.4**). After sample has been applied, molecules larger than the pores are unable to diffuse into the beads, so they elute first. Smaller molecules can penetrate the pores, so their elution is slower.

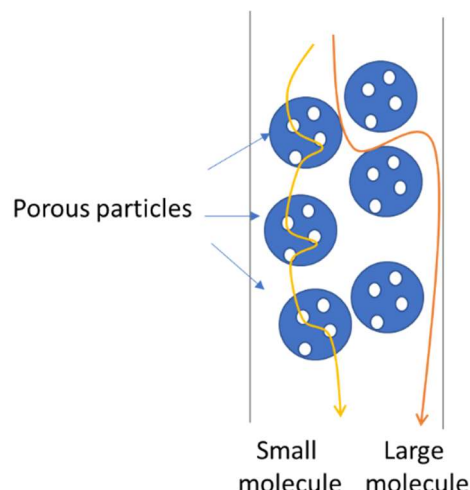


**Figure 3.4: Schematic representation of a size-exclusion chromatography column.** Small particles (yellow) diffuse between the pores of the particles in the matrix, so their path is longer, and they are delayed in their exit from the column. Larger molecules (red) that cannot spread into pores make a shorter path through the column, going through it faster than the small particles.

A HiPrep 26/60 Sephacryl<sup>TM</sup>S-200 High Resolution (GE Healthcare) size exclusion chromatography column was used to purify each protein to homogeneity. Proteins were loaded into the column, eluted using 50 mM Kpi, 150 mM NaCl, pH 7.4 and, subsequently dialysed against 50 mM Kpi pH 7.4 and stored at -80 °C until used.

### 3.5.4 REMOVAL OF His<sub>6</sub>-TAGS FROM PURIFIED PROTEINS

When required, the His<sub>6</sub>-tags fused to the N-terminal or C-terminal end of proteins can be removed by proteolytic cleavage using thrombin. The process to remove the His<sub>6</sub>-tag is based on the cleavage at the (L-V-P-R-G-S) amino acid sequence. 1 mL of protein was incubated with 0.2 U of thrombin (GE Healthcare) for 1 h at room temperature and then overnight at 4 °C. A Ni<sup>2+</sup> activated HiTrap Chelating HP column (GE Healthcare) was then used to remove the His<sub>6</sub>-tag (**Figure 3.5**).

The mixture containing the protein was manually loaded onto the top of the column and eluted with 50 mM Kpi, pH 7.4. The protein without the His<sub>6</sub>-tag was then recovered from the column, while the His<sub>6</sub>-tag and the non-digested His<sub>6</sub>-tag protein molecules remained retained on the column. Eluted proteins were dialysed against the required buffer and stored at -80 °C until used.

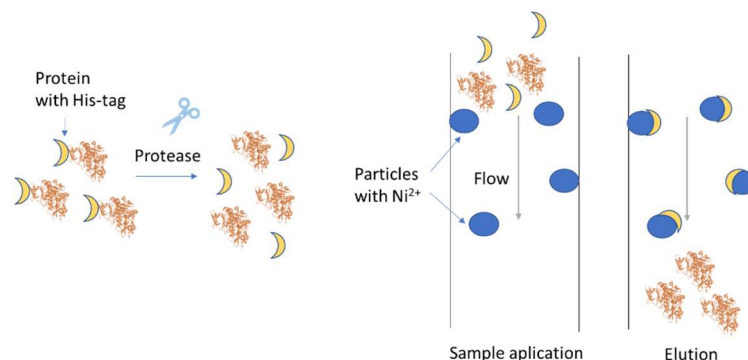


**Figure 3.5: Scheme of a His<sub>6</sub>-tag removal process.** After incubation with the protease the His<sub>6</sub>-tag is released from the protein, and then separated from the mixture by using an affinity column.

## 3.6 GENERAL BIOCHEMICAL METHODS

### 3.6.1 DETERMINATION OF PROTEIN MOLECULAR WEIGHTS BY SIZE EXCLUSION CHROMATOGRAPHY

Size exclusion chromatography was used to evaluate the apparent molecular weight (MW) of proteins, as well as their association states (quaternary assemblies and complexes). Samples were loaded into a HiPrep 26/60 Sephacryl<sup>TM</sup>S-200 High Resolution (GE Healthcare) column, previously equilibrated in 50 mM Kpi, 150 mM NaCl, pH 7.4 when evaluating hAIF<sub>Δ1-101</sub> monomer/dimer species or in 50 mM Kpi, 10 mM NaCl, pH 7.4, when performing interactions assays. The low molecular weight calibration kit (LMW) (GE Healthcare), which consists of 6 proteins in the 6400-160000 Da range, was used to calibrate the column. The column was connected to an ÄKTA purifier FPLC system (GE Healthcare) and run at a flow rate of 0.4 mL/min (**Figure 3.6**).

Considering the elution volume of the proteins contained in the calibration kit, it is possible to relate the elution volume of a protein to its apparent MW. Equation 3.2 was used to evaluate the relative mobility ( $K_{av}$ ) for each of the samples contained in the calibration kit, as well as of the ones here evaluated:

$$K_{av} = \frac{V_e - V_o}{V_c - V_o} \quad (\text{Eq. 3.2}).$$

Where  $V_o$  is the column void volume,  $V_e$  the protein elution volume, and  $V_c$  the geometric column volume. A calibration curve was produced by representing  $K_{av}$  of the proteins included in the LMW kit versus the logarithm of their MWs.

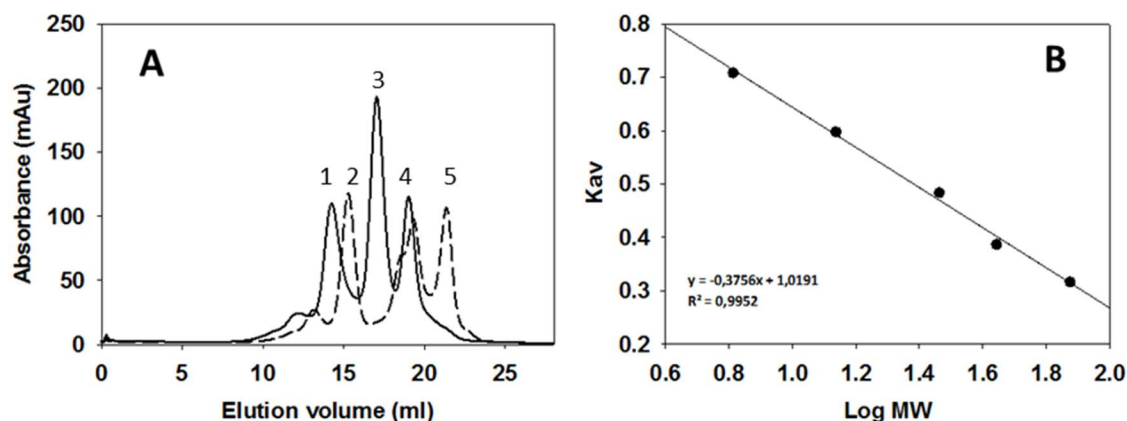


**Figure 3.6: Calibration process (A)** Calibration curves. Elution profile of the five proteins with known MW used to calibrate the HiPrep 26/60 Sephacryl<sup>TM</sup>-200 High Resolution column (GE Healthcare) equilibrated in 50 mM Kpi, 150 mM NaCl, pH 7.4 and with a flow rate of 0.4 mL/min in 1 Conalbumin 75KDa, 2 Ovalbumin 44 KDa, 3 Carbonic Anhydrase 29 KDa, 4 Ribonuclease 13,7 KDa and 5 aprotinin 6,5 KDa. **(B)** Example of a pattern with which the MW of proteins is calculated.

This calibration curve was then used to determine the apparent MW of the protein specie or complex here studied after determining their  $K_{av}$  values (**Figure 3.6 B**).

### 3.6.2 ANALYSIS OF PROTEIN-DNA INTERACTIONS BY ELECTROPHORETIC MOBILITY SHIFT ASSAY

The *in vitro* affinity of hAIF<sub>Δ1-101</sub> and its variants by different DNA fragments was analysed by electrophoretic mobility shift assay (EMSA) in agarose gels, where the negatively charged DNA migrates to the cathode in the presence of an electric field. If a protein interacts with DNA, these complexes will differ in charge and, in general, will have reduced electrophoretic mobility relative to the free DNA (Sambrook and Gething, 1989).

In this study, mixtures containing 0.5 µg of DNA GeneRuler 100 bp DNA Ladder (Thermo Fisher Scientific) and 25 µM of hAIF<sub>Δ1-101</sub> were loaded in 2 % agarose gels prepared in 90 mM Tris-Borate, 2 mM ethylenediaminetetraacetic acid (EDTA), (TBE), pH 8.0 and containing 5 µg/mL of ethidium bromide. Electrophoresis was run for 90 min at 80 V. DNA fragments can be detected using a transilluminator ChemiDoc<sup>TM</sup> XRS+ System (Bio Rad), because the ethidium bromide intercalated within DNA becomes fluorescent when excited with UV light.

### 3.6.3 POLYACRYLAMIDE GEL ELECTROPHORESIS

Polyacrylamide gel electrophoresis (SDS-PAGE) is an analytical technique used to separate denatured proteins based on their different mobility in an electric field as a consequence of their particular MW (Laemmli, 1970). The use of sodium dodecyl sulphate (SDS), an anionic detergent, eliminates the protein structure and charge influence. SDS binds to proteins in a non-specifically way providing them with a constant size/charge relation. So, when the protein-SDS complex migrates in the SDS-PAGE, proteins become separated according their size, allowing to determine their MW by comparison with protein markers of known MW.

The gels here used were prepared in a Mini-Protean Tetra Cell (Bio Rad) system. Gels were prepared with polyacrylamide ranging 12-20 %, depending on each particular experiment and on the MW of the studied protein (**Figure 3.7**).

**Table 3.5:** Solution mixtures for preparation of gels with different polyacrylamide contents.

Reagent	Resolving gel 12 %	Resolving gel 15 %	Resolving gel 20 %	Resolving gel 4 %
Distilled H <sub>2</sub> O	4.3 mL	3.6 mL	2.3 mL	3.6 mL
Acrylamide:Bisacrylamide (37.5:1)	3.0 mL	3.7 mL	5 mL	666 µL
Tris/HCl 1.5 M pH 8.8 *	2.5 mL	2.5 mL	2.5 mL	625 µL
SDS 20 %	50 µL	50 µL	50 µL	25 µL
Ammonium persulfate (APS) 10 % **	100 µL	100 µL	100 µL	50 µL
Tetramethylethylenediamine TEMED **	10 µL	10 µL	10 µL	5 µL

\*For stacking gel: 1 M Tris/HCl pH 6.8. \*\*Added at the end to the mix.

For gel preparation, both glasses were carefully cleaned with water and ethanol, and completely dried. The glasses were assembled following the manufacturer instructions (**Figure 3.7 A-C**). The resolving gel was prepared according the required volumes (**Table 3.5**), being APS and TEMED the last components added to the mixture. The mixture was slowly poured between the glasses, covered with isopropanol and allowed to polymerise. Once the gel polymerised, the isopropanol was removed, and the space between the glasses was washed with distilled water. The stacking gel was then prepared and poured on the top of the separation gel. Then, the comb was carefully inserted in the stacking gel avoiding formation of bubbles and the gel was allowed to polymerise (**Figure 3.7 D**).

To start the electrophoresis, the gel was placed in the cassette faced with another gel or a piece of plastic and the comb was removed. The space between gels and the tank were filled with electrophoresis buffer (0.025 M Tris/HCl, 0.2 M glycine, 12.5 % SDS, pH 8.8).

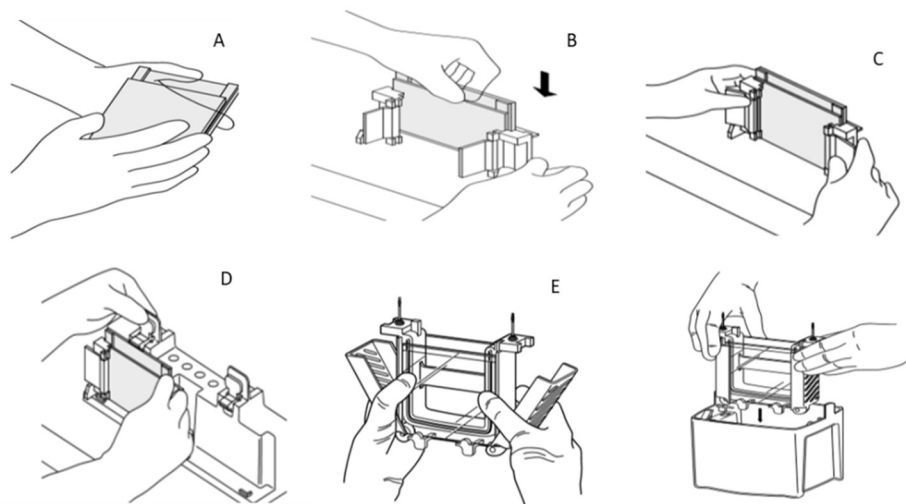


**Figure 3.7: Assembly of the Mini-PROTEAN** casting stand and frame, and insertion into the electrophoretic tank. **(A-D)** The glasses were assembled following the manufacturer instructions with the notch towards the inside. **(E)** The gel was placed in the cassette with the notch towards the inside, the tabs were closed. **(F)** The assembly was introduced in the tank and the tank was filled with electrophoresis buffer. The lid was placed, and the system connected to the power supply. Figure from Mini-PROTEAN Tetra Cell instruction manual (Bio-Rad).

Samples consisting of 16  $\mu\text{L}$  of proteins and 4  $\mu\text{L}$  of 5x sample buffer (50 mM Tris/HCl, 50 mM EDTA, 12.5 % SDS, 25 %  $\beta$ -mercaptoethanol, 35 % glycerol, 0.1 % bromophenol blue) were heated for 5 min at 100  $^{\circ}\text{C}$ . The samples and the MW marker Precision Plus Protein Dual Colour (Bio Rad) or the PageRuler Plus Prestained Protein Ladder (Thermo Fisher Scientific) were then loaded onto each of the wells produced by the comb in the stacking gel. After placing the lid, the system was connected to the power supply.

An amperage of 20 mA was used until the sample front reached the resolving gel. At this point the amperage can be increased up to 40 mA per gel. The electrophoresis was run until the sample front arrived at the end of the gel. The gel was removed from the cassette and placed in a container with staining solution (0.5 g Coomassie Brilliant Blue R-250, 450 mL methanol, 100 mL acetic acid, 20 mL glycerol, 630 mL water) until the protein blue bands appeared. Then it was submerged in a de-staining solution (250 mL methanol, 100 mL acetic acid, 20 mL glycerol and 630 mL water) to remove the colorant excess.



### 3.6.4 CROSSLINKING STABILISATION OF OLIGOMERIC ASSEMBLIES

The quaternary assemblies in hAIF<sub>Δ1-101</sub> and its variants was evaluated by their stabilisation using a crosslinking agent, and their subsequent separation and identification by SDS-PAGE.

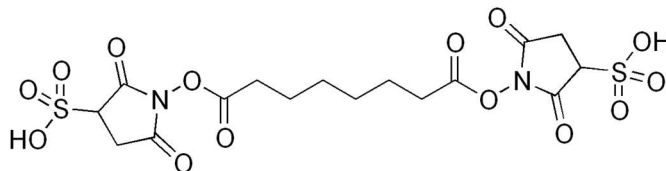


**Figure 3.8: Bis(sulphoccinimidyl)suberate (BS<sup>3</sup>).**

As crosslinker Bis(sulphoccinimidyl)suberate (BS<sup>3</sup>) (Thermo Fisher Scientific) was used. BS<sup>3</sup> is an amine-to-amine crosslinker that is water-soluble, non-cleavable, membrane impermeable and homobifunctional. It contains an amine-reactive *N*-hydroxysulphosuccinimide (NHS) ester at each end of an 8-carbon spacer arm (**Figure 3.8**). NHS esters react with primary amines at pH 7-9 to form stable amide bonds, releasing *N*-hydroxysulphosuccinimide. Proteins, including antibodies, generally have several primary amines, the side chain of Lys residues and the N-terminus of each polypeptide, which are targets for the NHS-ester crosslinking reagents. Therefore, the reaction with the Lys side chains is the major occurring reaction that occurs.

In this study, 3  $\mu$ M solutions of the studied hAIF<sub>Δ1-101</sub> variant, incubated at room temperature for 5 min in the absence and presence of 300  $\mu$ M NADH, were mixture with 0.3 mM BS<sup>3</sup>. Mixtures were incubated for 1 h at room temperature. Then, SDS-PAGE loading buffer 5x was added and the samples were boiled for 5 min at 95 °C. Samples were then analysed by 15 % SDS-PAGE. Denaturant electrophoresis was used because the crosslinker avoids breaking the covalent interactions that now stabilise oligomeric assemblies.

### 3.6.5 CLEAR NATIVE COLORLESS POLYACRYLAMIDE GEL ELECTROPHORESIS

Native gels in polyacrylamide gradient (BN-PAGE) were first described in 1991 (Schägger and von Jagow, 1991), allowing the electrophoretic resolution of protein complexes or assemblies formed by more than one subunit or protein.

Blue native PAGE (BN-PAGE) can be used for one-step isolation of protein complexes from biological membranes, as well as from total cell and tissue homogenates. It can also be used to determine masses of native protein and assemblies, and to identify

physiological protein-protein interactions. Coomassie dyes were introduced to induce a shift in protein charge, while aminocaproic acid served to improve solubilisation of membrane proteins. Due to some charge interaction between hAIF<sub>Δ1-101</sub> and the dye, this protein resulted unable to enter and migrate into the gel. Therefore, the variant Clear Native colourless polyacrylamide gel electrophoresis (CN-PAGE) was used. In CN-PAGE deoxycholate replaces Coomassie to induce charge shift of the protein.

The use of polyacrylamide gels with an increasing gradient in acrylamide concentration (and hence decreasing the pore size) has sometimes advantages over acrylamide gels of fixed concentration. During electrophoresis using gradient gels, proteins migrate until the decrease mm pore size avoids further progress. Once the “pore limit” is reached, the protein banding pattern does not change appreciably with time, although migration does not cease completely. By this method, proteins are separated according to their hydrodynamic size and shape in the polyacrylamide matrix.

This technique can be used to separate a mixture of proteins based on their MWs. Proteins with close MW values are more likely to separate in a gradient gel than in a linear gel, being therefore easier to visualise quaternary assemblies formed by more than one protein. If a tiny protein interacts with a bigger one, this one appears in the gel in a size bigger than its own because of the formation of the complex. In this thesis, CN-PAGE was used after molecular exclusion chromatography, to evaluate whether hAIF<sub>Δ1-101</sub> variants form stable complexes with their partner proteins.

CN-PAGE resolving gels were prepared the day before used, according to the composition indicated in **Table 3.6** and using 1.5 mm spacers.

**Table 3.6:** Solutions for preparation of clear native gels.

Reagent	Resolving Gel 4 %	Resolving Gel 20 %	Stacking Gel
<b>Acrylamide:Bisacrylamide (48:1.5)</b>	0.40 mL	1.33 mL	0.25mL
<b>Gel Buffer 3X (50 mM Bis- Tris, 1.5 M aminocaproic acid pH 7)</b>	1.66 mL	1.11 mL	1 mL
<b>Distilled H<sub>2</sub>O</b>	2.93 mL	0.33 mL	1.75 mL
<b>Glycerol</b>	-	0.56 mL	-
<b>Ammonium persulfate (APS) 20 % *</b>	20 µL	12µL	12.50 µL
<b>Tetramethylethylenediamine TEMED *</b>	4 µL	3 µL	3 µL

\*Add just before placing the solutions in the gradient maker to cast the gel.

A peristaltic pump at a speed of 3 mL/min was used for gradient mixing, (**Figure 3.9**). Once in the cassette, the top of the gel was covered with isopropanol. Once polymerization took place, isopropanol was removed, the gel was washed with distilled water and covered with gel buffer, protected with plastic film and storage at 4 °C until used.

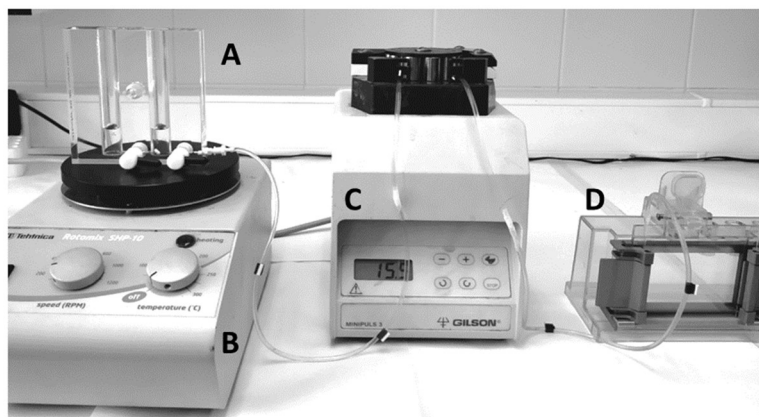


**Figure 3.9: Assembly for gradient preparation.** (A) The acrylamide solutions were placed in the mixer. (B) The 4 % acrylamide in the left chamber and the 20 % in the right, both containing magnetic stirrers for their shaking. (C) After turning on the peristaltic pump, the valve of the 20 % mixture was opened until it travels 1 cm from the tube, then the 4 % valve was opened, travelling to the right chamber and creating the gradient while filling the gel assembly. (D) On the top, space must be left for the stacking gel.

Just before running the CN-PAGE, the stacking gel is prepared by mixing the components 30 min before of running the electrophoresis (**Table 3.6**). When the polymerization had taken place, the comb was removed, and the wells cleaned by eliminating unpolymerized acrylamide. The well positions were marked to facilitate loading. The space between gels (the upper chamber) was loaded with the cold cathode buffer (50 mM Tricine, 7.5 mM imidazole, pH 7.0) supplemented with 0.02 % dodecyl maltoside and 0.05 % deoxycholate, and the bucket was filled with the cold anode buffer (25 mM imidazole/HCl, pH 7.0). The electrophoresis was run at 80 V for 25-30 min in the cold room at 4 °C, then it continued running by using an amperage of 12 mA/gel and the voltage was limited to 300 V, until the samples front reached the bottom of the gel (around 120 min in total). When finished, gels were either dyed with Coomassie or transferred by western blot.

### 3.6.6 TWO-DIMENSIONAL ELECTROPHORESIS

Two-dimensional (2-D) gel electrophoresis allow separating mixtures of proteins by a different property in each of the two dimensions (**Figure 3.10**).

2-D electrophoresis starts by running a 1-D electrophoresis that separates proteins in one dimension along an electrophoretic lane, usually according to isoelectric point. This lane

is then cut and stacked onto the second gel. Thus, proteins in this lane are then spread out across the second dimension (in a 90 ° direction from the first) using a different property, usually MW. Since it is in general unlikely that two molecules will behave similarly regarding two distinct properties, they can be more effectively separated in 2-D electrophoresis than in 1-D electrophoresis. Therefore, 2-D electrophoresis is particularly useful to determine the protein composition of complexes or assemblies.

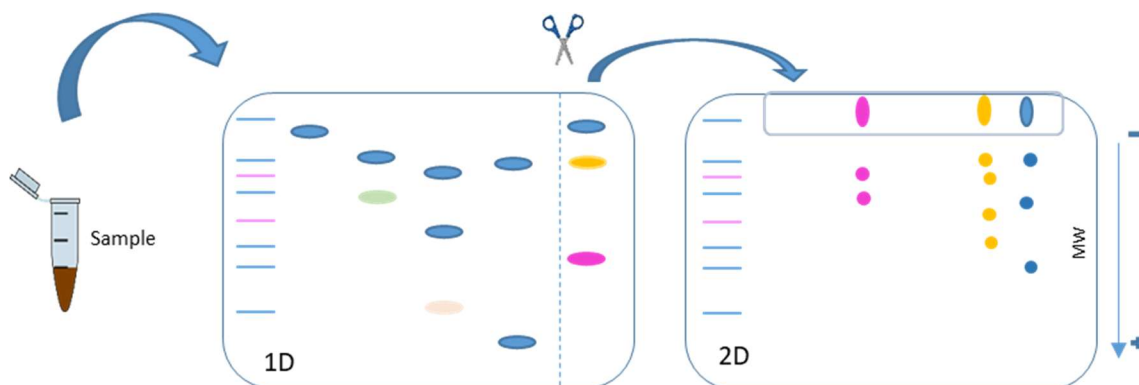


**Figure 3.10:** Workflow of a 2-D gel electrophoresis protocol. In the first-dimension molecules are linearly separated according to their isoelectric point. Then, the lane of interest is cut and mounted on the top on a new electrophoretic gel where the second dimension will separate the samples previously separated by isoelectric point in 90° according to their MW.

In this thesis, 2-D gels were used to identify the proteins forming the degradosome, using commercial BN-PAGE™ 3-12 % Bis-Tris gels (Thermo Fisher Scientific) with 1 mm width and the above described Clear Native buffers. When the first electrophoresis dimension came to the end, the lane of interest was trimmed and incubated in a solution containing 1 %  $\beta$ -mercaptoethanol and 1 % SDS for 1h to denaturalise proteins within it. During that time, the second dimension 15 % SDS-PAGE gel of 1.5 mm (resolving plus stacking) was prepared (**Table 3.7**).

**Table 3.7:** Composition of the second-dimension electrophoretic gel

Reagent	Resolving Gel 15 %	Stacking Gel 4 %
<b>Acrylamide:Bisacrylamide (48:1.5)</b>	3.6 mL	0.6 mL
<b>Gel Buffer 3x (Tris/HCl 3 M, SDS 0.3 % pH 8.5)</b>	4 mL	1 mL
<b>Distilled H<sub>2</sub>O</b>	4.4 mL	1.4 mL
<b>Ammonium persulfate (APS) 20 % *</b>	40 $\mu$ L	12 $\mu$ L
<b>TEMED *</b>	8 $\mu$ L	3 $\mu$ L

\*Add just before placing the solutions in the gradient maker to cast the gel.

When preparing the stacking gel, a special comb, made by attaching cellophane tape to the regular comb, was used to prepare a large well to accommodate the trimmed lane as well as a regular one. The regular well was then loaded with the marker, while the denatured strip lane from the 1-D gel was loaded in the large well with the help of two palettes. The upper and lower chambers were loaded, respectively, with the cold cathode (0.1 M Tris/HCl, 0.1 M Tricine and 0.1 % SDS, pH 8.25) and anode (0.2 M Tris/HCl, pH 8.9) buffers. The 2-D electrophoresis was run in a cold chamber (4 °C) at 30 V for 25-30 min, then the voltage was set in the 80-120 V range until the dye reached the bottom of the gel. When the running was finished, the gel was either revealed with Coomassie or transferred by western blot.

### 3.6.7 WESTERN BLOT

Western blot is a technique widely used to identify proteins within an electrophoretic pattern. Proteins previously separated by SDS-PAGE, CN-PAGE or 2-D, are transferred to a membrane that is incubated with specific labelled antibodies that recognise an specific protein (Mahmood and Yang, 2012). Here, the protein bands resulting in the electrophoretic gels were transferred to a polyvinylidene difluoride (PVDF) membrane using a mini Trans Blot cell (Bio Rad). The membrane previously activated with absolute methanol for 10 s, was rinsed with water and transferred to the buffer transfer (BSN) containing 18 mM Tris/HCl, 39 mM glycine and 20 % methanol, before preparing the stacking system (**Figure 3.11**).

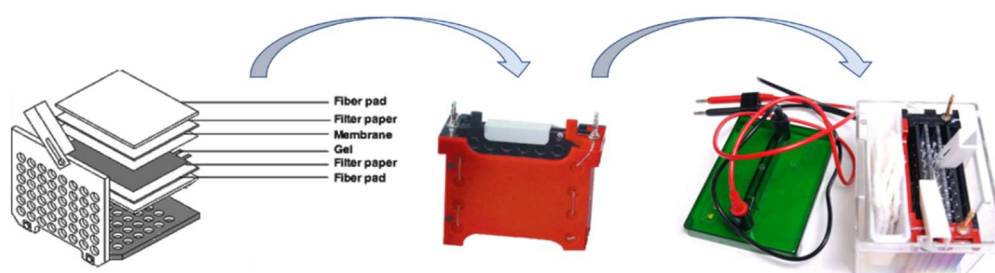


**Figure 3.11: Transference system.** A sandwich is prepared containing the following layers; fibre pad, filter paper, the gel, the PVDF membrane, filter paper and the fibre pad. This sandwich is then enclosed into the cassette and inserted into the bucket. Figure modified from (Thériault et al., 2016).

The gel was then placed in contact with the activated PVDF membrane, being both sandwiched between filter papers and fibre pads and enclosed in the stack cassette. The cassette was then placed on the bucket and filled with BSN buffer. Transference was allowed for 1h at 100 V and 4 °C. Then, the membrane was washed and blocked by

incubation for 1 h at room temperature, or overnight at 4 °C, with 5 % milk in 1 % PBS, 0.1 % (v/v) Tween-20 (PBS-T).

**Incubation with primary and secondary antibodies.** The membrane was washed three times with PBS-T to remove the milk traces. The membrane was then incubated with the primary antibody, diluted in the appropriate proportion (**Table 3.8**) in a PBS-T solution, during 1-2 h at room temperature, or overnight at 4 °C, with agitation. The membrane was then washed with PBS-T two times of 10 min each. The secondary antibody, mouse or rabbit, conjugated with radish peroxidase was diluted in PBS-T (**Table 3.8**). The membrane was incubated with this solution for 45-60 min. After that, it was washed for 15 min with PBS-T followed by three additional washes of 5 min each.

**Protein detection.** The detection of the protein of interest was performed by the reaction of the radish peroxidase conjugated to the secondary antibody when coming into contact with luminol (Thermo Fisher Scientific), a chemiluminescent Pierce™ ECL Western Blotting Substrate. The membrane, previously incubated with primary and secondary antibodies, was incubated for 1 min with the luminol substrate, and then was revealed by using an automated Western Blot processor Amersham™ Imager 600 (GE Healthcare).

**Table 3.8:** Summary of antibodies used for protein detection

Target Protein	Primary Antibody	Supplier	Secondary Antibody*	Supplier
<b>CypA Nuclease</b>	Anti-Cyclophilin A (EPR7511) (1:1000 0.3 % milk)	Abcam	Anti-Rabbit IgG (1:5000 0.1 % milk)	Invitrogen
<b>H2AX Histone</b>	Anti-His-Tag (1:10000 0.1 % milk)	GenScript	Anti-Mouse IgG (1:1000 0.1 % milk)	GenScript
<b>AIF</b>	Anti-hAIF (1:20000 0.3 % milk)	Sigma	Anti-Rabbit IgG (1:6000 0.1 %milk)	Invitrogen
<b>CHCHD4</b>	Anti-CHCHD4(C-12):sc-365137 (1:1000 0.3 % milk)	Santa Cruz Biotechnology	Anti-Rabbit IgG (1:5000 0.1 % milk)	Thermofisher

\*Secondary antibodies were produced in goat

**Reuse of membranes.** Elimination of antibodies and proteins attached to the membrane makes possible to reuse them. Membranes are immersed in stripping solution (100 mM 2-β-mercaptoethanol, 2 % SDS, 1 M Tris/HCl, pH 6.7), and incubated at 58 °C for 30 min. Three subsequent washes of 10 min at room temperature with PBS-T make the membranes ready to be used again.

## 3.7 SPECTROSCOPIC METHODS IN THE FUNCTIONAL AND STRUCTURAL CHARACTERIZATION OF PROTEINS

### 3.7.1 ULTRAVIOLET/VISIBLE ABSORPTION SPECTROSCOPY

Ultraviolet/visible (UV-Vis) absorption spectroscopy is a widely used technique for determining concentrations of absorbing species (chromophores) in solution. It is also employed as detector of sample impurities (when compared to spectra of standard raw materials) or transformation of compounds (as for example measurement of enzymatic activities). The wavelengths of light for UV-Vis absorption are in the 200-800 nm range of the electromagnetic spectrum. The UV-Vis absorption is the process by which a molecule absorbs UV or Vis light, causing excitation of electrons from a ground state molecular orbital to an excited state. Chromophores are functional groups of a molecule that absorb light at a particular wavelength in this UV-Vis region, most of the time characterised by delocalised  $\pi$  electrons (Kütt et al., 2006). The outcome of this can be measured by a UV-visible spectrophotometer (**Figure 3.12**), which produces a spectrum that represents absorption *versus* wavelength. This pattern can be used to learn properties of the molecule, including purity and concentration.

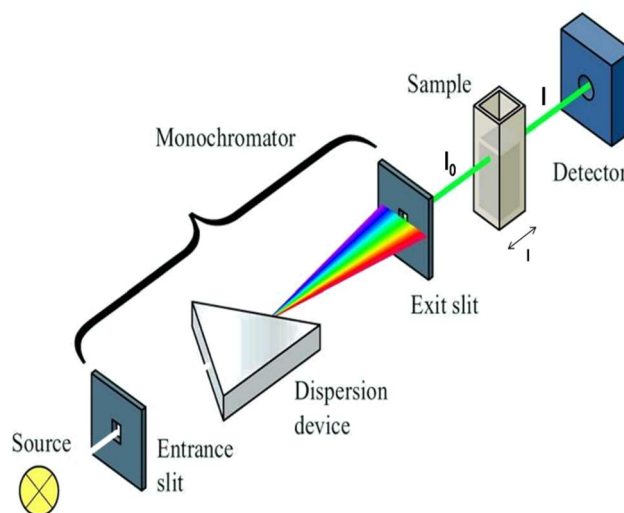


**Figure 3.12: Schematic representation of an UV-Vis spectrophotometer.** The UV-Vis spectrophotometer measures the difference in intensity between the incident light,  $I_0$ , and the light detected,  $I$ , after passing through the sample. The light path length ( $l$ ) is the thickness of the sample through which the light beam is travelling, usually 1 cm cuvettes are used. Once this constant is determined, unknown concentrations can be determined employing the Beer-Lambert's law. Image from Aprentas UV-Vis Spektroskopie, Springer, 2017.

The Beer-Lambert's law linearly relates the absorption of a sample to its concentration according to the equation 3.3.

$$A_{\lambda} = \varepsilon_{\lambda} \cdot c \cdot l \quad (\text{Eq. 3.3}).$$

Where A is the absorption at a particular wavelength ( $\lambda$ ),  $\varepsilon$  is the molar extinction coefficient at this wavelength, l the path length, and c the sample concentration.  $\varepsilon$  at a particular wavelength ( $\text{M}^{-1} \cdot \text{cm}^{-1}$ ) indicates how strongly a molecule absorbs light at this wavelength.

A Cary 100 Bio (Varian) spectrophotometer, was routinely used to check the protein integrity and to determine concentrations. Molar extinction coefficients for each of the proteins used in this study are listed (**Table 3.9**). To calculate the  $\varepsilon$  of each hAIF $_{\Delta 1-101}$  or hAIFmt $_{\Delta 1-77}$  variant, the equation 3.4 was employed. For that, a spectrum of the protein was recorded, and then the protein was denatured by adding 450  $\mu\text{L}$  of 6 M guanidinium chloride over 450  $\mu\text{L}$  of protein. A spectrum of the supernatant was then recorded. The  $\varepsilon$  value was calculated using the following equation:

$$\frac{\text{Abs FAD}}{\text{Abs AIF}} = \frac{\varepsilon_{\text{FAD}}}{\varepsilon_{\text{AIF}}} \quad (\text{Eq. 3.4}).$$

Abs FAD and Abs hAIF $_{\Delta 1-101}$  are measured experimentally, and  $\varepsilon$  FAD at 450 nm is 11300  $\text{M}^{-1} \cdot \text{cm}^{-1}$  (Macheroux, 1999, Jorns et al., 1987).

**Table 3.9:** Molar extinction coefficients for the different proteins used in this study.

Protein / wavelength of the maximum	Molar extinction coefficients ( $\text{mM}^{-1} \cdot \text{cm}^{-1}$ )
hAIF $_{\Delta 1-101}$ (451 nm)	13.7 <sup>a</sup>
hAIF $_{\Delta 1-101}$ E413A/R422A/R430A(451 nm)	13.3 <sup>a</sup>
hAIF $_{\Delta 1-101}$ W196A (451 nm)	13.4 <sup>b</sup>
hAIF $_{\Delta 1-101}$ W196Y (452 nm)	14.0 <sup>b</sup>
hAIF $_{\Delta 1-101}$ W196L (451 nm)	13.9 <sup>b</sup>
hAIF $_{\Delta 1-101}$ G308E (451 nm)	13.4 <sup>c</sup>
hAIF $_{\Delta 1-101}$ E493V (452 nm)	14.8 <sup>c</sup>
hAIF $_{\Delta 1-101}$ $\Delta$ R201(452 nm)	12.2 <sup>c</sup>
hAIFmt $_{\Delta 1-77}$ (451 nm)	13.6 <sup>b</sup>
hAIFmt $_{\Delta 1-77}$ E413A/R422A/R430A (451 nm)	13.4 <sup>b</sup>
H2AX (280 nm)	6.0 <sup>d</sup>
CYPA (280 nm)	8.7 <sup>d</sup>
CHCHD4 (280 nm)	13.3 <sup>d</sup>

<sup>a</sup>Data from (Ferreira et al., 2014), <sup>b</sup>data calculated in this work, <sup>c</sup>data from (Villanueva et al., 2019), <sup>d</sup>H2AX, CYPA, and CHCHD4 are the theoretical ones obtained using the ProtParam tool from the ExPASy Bioinformatic Resource Portal, <https://web.expasy.org/protparam/>.



### 3.7.2 CIRCULAR DICHROISM SPECTROSCOPY

Circular dichroism (CD) is a spectroscopy technique based on optically active samples differentially absorbing left- and right- circularly polarised light (Whitmore and Wallace, 2008). CD is extensively used to study chiral molecules of all types and sizes. The presence of an asymmetric carbon centre is one of several structural features that induces chirality in molecules. Chiral molecules are described by various ways of designating their absolute configuration, which codify either the entity's geometry or its ability to rotate the plane-polarised light.

One of the most important applications of CD in proteins is the analysis of their secondary structure, as well as how it can be modified by environmental conditions or interaction with other molecules (**Figure 3.13**).

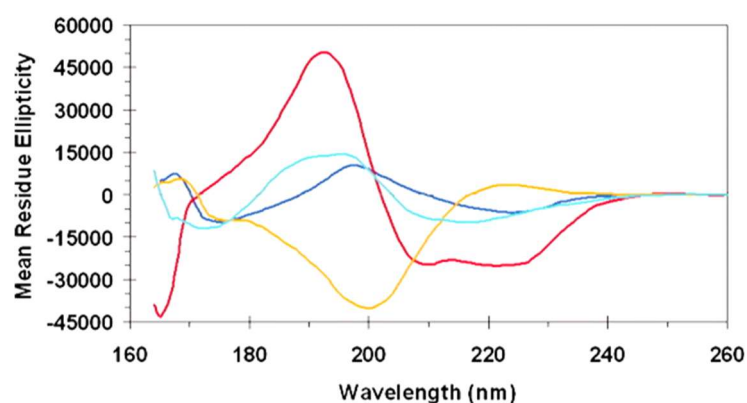


**Figure 3.13: Representative CD spectra of secondary structure elements in proteins.** CD spectra of myoglobin (red), a mostly helical protein, of concanavalin A (blue) and  $\beta$ -lactoglobulin (cyan), two mostly  $\beta$ -sheet proteins, and of collagen (orange) a polyproline-rich protein lacking defined secondary structure (Whitmore and Wallace, 2008).

Linearly polarised light when passed through an optically active sample becomes elliptically polarised, because its circular polarised components might be differentially absorbed by the sample (circular dichroism).

The degree of ellipticity ( $\theta$ ) (mdeg) is defined as the tangent of the ratio of the minor to major elliptical axis. The measurement in the Near-UV-Vis were employed to calculate the molar ellipticity  $[\theta]$ , considering concentration and cell path length according to the Beer Lamberts law, equation 3.5, (Metha et al., 2012). Another interesting parameter is the molar ellipticity by residue  $[\theta_{mr}]$  ( $\text{deg cm}^2 \text{dmol}^{-1}$ ). This is a specific unit for secondary structure of proteins and reports the molar ellipticity for individual protein residues instead of whole protein molecule. This allows easy comparison of secondary structure content of different proteins with vastly different molecule weights, and, therefore, is usually applied to data recorded in the Far-UV-Vis, equation 3.6.

$$[\theta] = \frac{\theta}{10 \cdot c \cdot l} \quad (\text{Eq. 3.5}).$$

$$[\theta_{\text{mr}}] = \frac{\theta}{10 \cdot c \cdot l (N-1)} \quad (\text{Eq. 3.6}).$$

Where  $\theta$  is the measured raw ellipticity (mdeg),  $[\theta]$  is the molar ellipticity,  $[\theta_{\text{mr}}]$  the molar ellipticity by residue ( $\text{deg cm}^2 \text{ dmol}^{-1}$ ),  $c$  is the protein concentration (M),  $l$  is the optical path length (cm) and  $N$  is the number of amino acid residues.

CD spectra of hAIF $_{\Delta 1-101}$ , hAIFmt $_{\Delta 1-77}$ , its variants, and their proteins partners were recorded in a thermostated Chirascan spectrometer (Applied Photophysics) at 25 °C in 50 mM Kpi, at a 150 mM of ionic strength, pH 7.4. The assays were performed in the Far-UV CD spectra (190-260 nm), using a 0.1 cm path length cuvette (Hellma) with 1  $\mu\text{M}$  of protein. This measurement provides information about the secondary structure. Near-UV-Vis CD spectra (250-700 nm), which provide information about the aromatic residues and its environment, were recorded in a 1 cm path length cuvette with 20  $\mu\text{M}$  of protein. Oxygen was purged from the spectrometer through a nitrogen flow before data recording. All spectra were baseline-corrected (subtraction of buffer signal).

### 3.7.3 FLUORESCENCE SPECTROSCOPY

Fluorescence is another spectroscopy broadly used in protein structural studies. Absorption of a photon to excite electrons from a ground state molecular orbital ( $S_0$ ) to an excited molecular orbital ( $S_1$ ) must occur prior to the fluorescence process occurring. Once in the excited state the electron returns to the ground state releasing energy by radiative or non-radiative processes. If energy release by radiative processes is faster than by non-radiative processes, then the molecule will be fluorescent.

Since after the excited electron will quickly drop in energy to the lower vibrational energetic state of the excited state ( $S_1$ ), the energy emitted in the form of photons (fluorescence) will be less than that of the absorbed photon. Therefore, the emission spectrum will be 'shifted' to longer wavelengths relative to the absorption one (**Figure 3.14**).

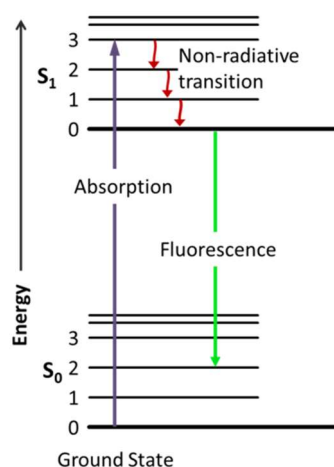


**Figure 3.14: Jablonski diagram of absorbance, non-radiative vibrational decay, and fluorescence processes.** The purple arrow represents the absorption of light. The green arrow represents vibrational relaxation from singlet excited state,  $S_2$  to  $S_1$ . The green arrow represents the fluorescence process. Image from Atkins, Physical Chemistry Oxford University Press, 1994.

Within proteins, tryptophans (Trp) absorb at 280 nm and have a relatively good intrinsic fluorescence property that is influenced by its environment. This allows us to follow changes in protein structure by monitoring its changes in fluorescence. Thus, fluorescence spectroscopy, is particularly useful in the study of protein folding/unfolding or protein interaction equilibria (Vivian and Callis, 2001). Flavoproteins, which have either flavin adenine dinucleotide (FAD) or flavin mononucleotide (FMN) as prosthetic group, also offer a unique possibility of probing the dynamical behaviour of their active sites via the fluorescence of these specific cofactors. The fluorescence yield of their isoalloxazine ring highly depends on its particular environment when binding to particular protein, being, in general, highly quenched by the protein environment. These properties reflect structural and dynamical differences in the cofactor environment, and allow to follow flavin dissociation from the protein (van den Berg et al., 1998).

In this study, we use flavin fluorescence to monitor stability of the active site of hAIF. Fluorescence spectra and fluorescence based thermal unfolding curves were obtained in a Cary Eclipse fluorescence spectrophotometer (Agilent Technologies) using a 1 cm path-length quartz cuvette (Hellma). Fluorescence emission of aromatic residues were recorded from 300 to 400 nm upon excitation at 280 nm, while flavin fluorescence emission spectra were collected from 480 to 600 nm after excitation at 450 nm. All spectra were recorded in 50 mM Kpi, at 150 mM of ionic strength, pH 7.4 at 10 °C.

### 3.7.4 PROTEIN THERMAL DENATURATION AS FOLLOWED BY CD AND FLUORESCENCE

Thermal denaturation curves were followed by changes in fluorescence emission of the flavin cofactor, as well as by far- and near-UV-Vis CD. Denaturation curves were recorded from 10 °C to 90 °C with scan rates of 1 °C/min and 1.5 °C/min, respectively, for CD and fluorescence assays, both in the absence and presence of 100-fold excess of NADH (Sigma Aldrich). hAlF<sub>Δ1-101</sub> or hAlFmt<sub>Δ1-77</sub> concentrations, wavelengths, and path lengths for the CD assays were 1 μM, 210 nm (220 nm when NADH was present) and 1 mm in the far-UV CD, and 20 μM, 300 nm (or 420 and 600 nm when NADH was present) and 1 cm in the near-UV CD, respectively. For fluorescence experiment samples containing 2 μM of protein were excited at 450 nm and emission was recorded at 530 nm using a 1 cm cuvette. In all experiments, the temperature was controlled by a Peltier unit and monitored using a temperature probe.

The individual experimental data sets were globally analysed as one-transition process (two-step process, native-unfolded, N-U) or two-transition process (three-state process, native-intermediate-unfolded, N-I-U) by applying the equations 3.7 and 3.8:

$$S_{obs} = \frac{S_N + m_N T + (S_U + m_U T) e^{-(\Delta G/RT)}}{1 + e^{-(\Delta G/RT)}} \quad (\text{Eq. 3.7}).$$

$$S_{obs} = \frac{S_N + m_N T + (S_I + m_I T) e^{-(\Delta G_1/RT)} + (S_U + m_U T) e^{-((\Delta G_1 + \Delta G_2)/RT)}}{1 + e^{-(\Delta G_1/RT)} + e^{-((\Delta G_1 + \Delta G_2)/RT)}} \quad (\text{Eq. 3.8}).$$

Where  $S_{obs}$  is the measured protein signal at a given temperature ( $T$ ),  $S_N$ ,  $S_I$ , and  $S_U$  are the intrinsic signals of native, intermediate and unfolded protein conformational states respectively, and  $m_N$ ,  $m_I$ , and  $m_U$  are the slopes of the baselines before the first transition, between the first and the second transition and after the second transition, respectively. According to the unfolding model,  $\Delta G_i = \Delta H_i \left(1 - \frac{1}{T_{mi}}\right) + \Delta C_{pi} \left(T - T_{mi} - T \ln \frac{T}{T_{mi}}\right)$ , where  $\Delta H_i$  is the van't Hoff enthalpy for each unfolding transition,  $T_{mi}$  is the midpoint transition for each unfolding transition,  $\Delta C_{pi}$  is the heat capacity change for each unfolding transition, and  $R$  is the ideal gas constant.

### 3.7.5 SPECTROSCOPIC EVALUATION OF CHARGE TRANSFER COMPLEX STABILITY

The reactivity of CTCs towards flavin reoxidation by molecular oxygen was monitored by initial full reduction of 15  $\mu$ M samples of hAlF $_{\Delta 1-101}$ , hAlFmt $_{\Delta 1-77}$  or their variants with NADH (1.5-fold the concentration of the protein) in 50 mM Kpi, pH 7.4, and subsequently recording their reoxidation spectrophotometrically. Samples were kept under stirring along the process. Reoxidation was followed by absorption spectra recording at 25 °C until full reoxidation of the flavin cofactor was achieved. Data of the absorbance at 700 nm are available at each measured time, for each time the % remaining of CTC is calculated according to equation 3.9. Once the % of CTC is known for each time, the CTC half-life is the time when the 50 % of CTC still remains in the solution.

$$\% \text{ CTC} = \frac{\Delta A_{max} - \Delta A_t}{\Delta A_{max}} \quad (\text{Eq. 3.9}).$$

Where  $\Delta A_{max}$  is the difference between the minimum and the maximum absorbance at 700 nm, and  $\Delta A_t$  is the difference of each value at 700 nm minus the minimum absorbance at 700 nm.

## 3.8 BIOPHYSICAL METHODS

### 3.8.1 ISOTHERMAL TRITATION CALORIMETRY

Isothermal titration calorimetry (ITC) is an analytical technique that allows the measurement of the heat liberated (exothermic interactions) or absorbed (endothermic interactions) by a system when two molecules interact (in our case protein-protein, protein-ligand, protein-DNA) (Ladbury and Chowdhry, 1996). The calorimeter has two cells, the reference and the sample, and it is able to continuously monitor and compare the temperature difference between them. The instrument monitors the thermal power that must be provided to keep both cells at the same temperature. When there is a small temperature variation caused by ligand binding upon its injection into the sample cell, the system changes the thermal power supplied to the sample cell to keep the temperature difference relative to the reference cell equal to zero. The sequence of ligand injections is reflected in a sequence of heat peaks. The area of each peak directly relates to the heat exchanged in each ligand addition, being in turn proportional to the amount of intermolecular complex formed. Ligand addition is repeated until the molecule located in the cell is totally saturated with the ligand and no more changes in heat are detected (**Figure 3.15**).

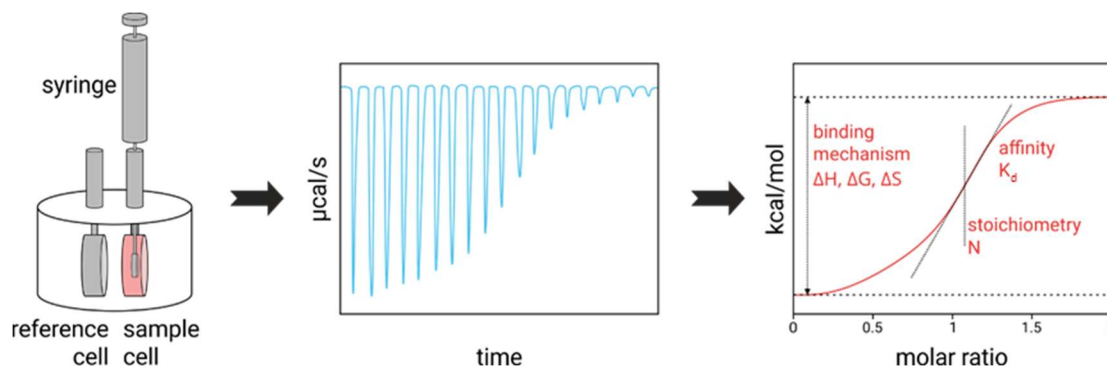


**Figure 3.15: Scheme of an ITC system and example of typical results.** Image from <https://2bind.com/itc/>. The protein solution is placed in the sample cell, while the reference cell contains water. When the ligand is injected in the sample cell it either releases or absorbs heat, depending on the association being endothermic or exothermic respectively. This heat is proportional to the variation of the fraction of the ligand bound to the sample. Heat changes become smaller when the ligand concentration in the sample cell increases because the protein saturates with ligand.

**Experimental procedure.** The calorimeter used in the present study to evaluate the interaction of WT hAIF with its physiological partners was a thermostated MicroCal Auto-ITC200 (GE Healthcare). To evaluate the interaction with DNA the calorimeter was set at 15 °C, while 25 °C was used to evaluate binding to protein partners. The reference cell contained water, and the sample cell 10 µM of the protein solution. The concentration of the ligand in the syringe was 10 times that of the protein (100 µM). The ligand and the protein were dissolved in the same buffer, 50 mM Kpi, pH 7.4. Samples and buffers were degasified for 5 min in a Thermovac before placing them in 96-well plates. During a typical experiment, a sequence of 2 µL injections of titrating solution every 150 s was programmed and the stirring speed was set to 750 r.p.m. The equipment was cleaned automatically after each experiment.

**Analysis of thermograms and determination of thermodynamic parameters.** The heat evolved after each injection was obtained from the integral of the calorimetric signal. The heat derived from the binding process was calculated as the difference between the binding heat and the dilution heat. This was estimated as a constant heat throughout the experiment and included as an adjustable parameter in the analysis. The integrated heat (Kcal/mol) for each injection was represented versus the [ligand]/[protein] molar fraction and fitted to a mathematical model for a single binding site, equation 3.10.

$$q_i = Q_i - Q_{i-1} \left(1 - \frac{v}{v_0}\right) \quad (\text{Eq. 3.10}).$$

The differential heat associated to each injection  $q(i)$  results from the difference between the total heat accumulated after the injection  $i$  and from the injection  $i-1$ . The dilution factor is considered by the  $\left(1 - \frac{v}{v_0}\right)$  term, where  $v$  and  $v_0$  are each injection and calorimetric cell volumes respectively.

The association constant ( $K_a$ ), the enthalpy change ( $\Delta H$ ), and the binding stoichiometry ( $n$ ) were estimated through non-linear regression of the experimental data employing a single ligand binding site model (1:1 protein:ligand stoichiometry) implemented in Origin 7.0 (Wiseman et al., 1989, Velázquez-Campoy et al., 2006). Using these parameters, the dissociation constant ( $K_d$ ), as well as the entropic ( $-T\Delta S$ ) and free Gibbs energy ( $\Delta G$ ) contributions to the binding were calculated by employing the equations that describe thermodynamic relationships (equations 11-13).

$$\Delta G = -RT \ln K_a \quad (\text{Eq. 3.11}).$$

$$\Delta G = \Delta H - T\Delta S \quad (\text{Eq. 3.12}).$$

$$K_d = \frac{1}{K_a} \quad (\text{Eq. 3.13}).$$

Where  $R$  is the universal gas constant ( $1.987 \cdot 10^{-3} \text{ kcal.mol}^{-1}.\text{K}$ ) and  $T$  the absolute temperature during the experiment. Errors in the measured parameters were  $\pm 0.5 \text{ kcal/mol}$  for thermodynamic parameters ( $\Delta H$ ,  $\Delta G$ , and  $T\Delta S$ ) and  $\pm 30 \%$  for binding constants,  $K_a$  and  $K_d$ .

**Protonation changes during complex formation.** Enthalpy and/or heat capacity can also be influenced by the release of protons during the interaction process, and this effect can be examined by performing ITC measurements in different buffers (Bradshaw and Waksman, 1998). If a binding process is coupled to the exchange of protons between ionisable groups and the bulk solvent, then, the measured binding enthalpy contains a contribution from the ionisation of the buffer (Martínez-Júlvez et al., 2009).  $K_a$  does not contain any buffer contribution as long as the pH of the experiment is close to the  $pK_a$  of the buffer used.

Thus, the buffer independent binding enthalpy ( $\Delta H^\circ$ ) can be obtained by eliminating the contribution of the buffer ionization enthalpy ( $\Delta H_{ion}$ ) from the observed binding enthalpy ( $\Delta H$ ), according to:

$$\Delta H = \Delta H^\circ + n_{H^+} \cdot \Delta H_{ion} \quad (\text{Eq. 3.14}).$$

Where  $n_{H^+}$  is the number of protons exchanged between the complex and the bulk solution. If  $n_{H^+}$  is positive, the complex formation occurs with capture of protons from the solvent. If  $n_{H^+}$  is negative, it takes places releasing protons to the solvent. To estimate  $\Delta H^\circ$  and  $n_{H^+}$  in binding processes involving hAIF variants, different buffers with different ionization enthalpies were used (**Table 3.10**).

**Table 3.10:** Enthalpies of ionization of different buffers. Values measured at 298.15 K and 0.1 MPa. Data from (Goldberg et al., 2002).

BUFFER	REACTION	pK <sub>a</sub>	ΔH° (Kcal/mol)
<b>Phosphate</b>	H <sub>2</sub> PO <sub>4</sub> <sup>-</sup> = H <sup>+</sup> +HPO <sub>4</sub> <sup>2-</sup>	7.19	0.86
<b>HEPES</b>	HL <sup>±</sup> = H <sup>+</sup> +L <sup>-</sup> (HL= C <sub>8</sub> H <sub>18</sub> N <sub>2</sub> O <sub>4</sub> S)	7.56	4.80
<b>MOPS</b>	HL <sup>±</sup> = H <sup>+</sup> +L <sup>-</sup> (HL= C <sub>7</sub> H <sub>15</sub> NO <sub>4</sub> S)	7.18	5.04
<b>TES</b>	HL <sup>±</sup> = H <sup>+</sup> +L <sup>-</sup> (HL= C <sub>6</sub> H <sub>15</sub> NO <sub>6</sub> S)	7.76	7.80
<b>TRIS/HCl</b>	HL <sup>±</sup> =H <sup>+</sup> +L (HL= C <sub>4</sub> H <sub>11</sub> NO <sub>3</sub> )	8.07	11.51

The linear regression of the representation of  $\Delta H_{obs}$  versus  $\Delta H_{ion}$  provides the value of  $n_{H^+}$ .

### Determination of cooperation properties of AIF<sub>Δ1-101</sub> with its degradosome partners.

When a protein is able to bind more than one ligand, cooperativity in their binding can be produced; one ligand can change the affinity of the protein for the other ligand (Velázquez-Campoy et al., 2006). This cooperativity can be either positive or negative, i.e. one ligand increases or decreases the affinity of the second ligand (Abeliovich, 2005, Aramaki et al., 2011).

Sets of experiments were carried out by locating on the calorimetric sample cell a mix of 10 μM hAIF<sub>Δ1-101</sub> and 15-bp dsDNA (Integrated DNA Technologies) at 10, 20, 40 or 80 μM. Each of these mixtures was then titrated with CypA or H2AX (100 μM in the syringe). These experiments allowed to determine the apparent association constant for H2AX or CypA ( $K_a^{app,CypA}$  and  $K_a^{app,H2AX}$  respectively) at each concentration of the DNA. These values of affinity were fit to the equation 3.15 that describes the dependency of  $K_a^{app,ligand}$  as function of DNA concentration and of the cooperation constant ( $\alpha$ ) (Velázquez-Campoy et al., 2006).

$$K_a^{app,ligand} = K_a^{ligand} \cdot \frac{1 + \alpha K_a^{DNA} [DNA]}{1 + K_a^{DNA} [DNA]} \quad (\text{Eq. 3.15}).$$

Where  $\alpha$  is the cooperation coefficient,  $K_a^{app,ligand}$  is the association constant for the ligand (CypA or H2AX) at each concentration of DNA,  $K_a^{DNA}$  is the association constant for DNA and [DNA] is the concentration of DNA. Mixtures containing 10 μM of AIF<sub>Δ1-101</sub> and 10 or 80 μM of the protein partner were also titrated with dsDNA (100 μM in the syringe), to confirm the observed effect. For all ITC experiments, errors in the measured parameters were  $\pm 0.5$  Kcal/mol for thermodynamic parameters ( $\Delta H$ ,  $\Delta G$ , and  $T\Delta S$ ) and  $\pm 30$  % for binding constants ( $K_a$  and  $K_d$ ).



### 3.8.2 METHODS IN THE STUDY OF PROTEIN KINETICS

#### 3.8.2.1 DETERMINATION OF STEADY STATE KINETIC PARAMETERS

The ability of some enzymes to catalyse the transfer of electrons from NAD(P)H to an artificial electron acceptor is known as diaphorase activity (Avron and Jagendorf, 1956, Zanetti and Curti, 1980). In this thesis DCPIP has been used as an artificial electron acceptor of hAIF (Ferreira et al., 2014) (**Figure 3.16**). The NADH oxidase activity of hAIF<sub>Δ1-101</sub>, hAIF<sub>Δ1-77</sub>, and their variants was monitored in a Cary 100 Bio (Varian) spectrophotometer by following DCPIP reduction at 620 nm during 1 min. Oxidised DCPIP absorbs in the visible with  $\epsilon_{620\text{ nm}}$  of 21 mM<sup>-1</sup>cm<sup>-1</sup>, while its reduced state does not absorb in this spectral region. Thus, reduction of DCPIP by the enzyme can be followed by the absorption decrease at 620 nm. The assays were performed in 50 mM Kpi, pH 7.4 at 25 °C, using an enzyme concentration of ~75 nM and stocks of NADH at different concentrations (0.15-10 mM). Reaction samples were prepared as indicated in **Table 3.11**.

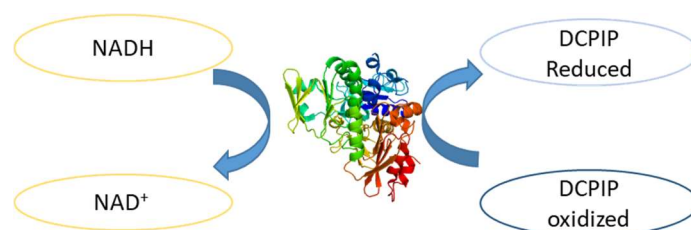


**Figure 3.16: Scheme of the diaphorase steady-state activity** of hAIF when using NADH as electron donor and DCPIP as electron acceptor. This activity provides us with measurement of the enzyme capacity to oxidise NADH.

**Table 3.11:** Volumes used for the reaction mixture.

	Sample Cuvette ( $\mu\text{L}$ )	Reference Cuvette ( $\mu\text{L}$ )
<b>50 mM Kpi pH 7.4</b>	450-x	450
<b>1.9 mM DCPIP</b>	50	50
<b>NADH</b>	500	500
<b>hAIF</b>	x	--

Prior to measure a blank was made using a cuvette that contained 950  $\mu\text{L}$  of buffer and 50  $\mu\text{L}$  of DCPIP.

When saturation profiles on the pyridine nucleotide concentration were observed, kinetic constants were estimated by fitting the hyperbolic dependence of initial reaction rates with the coenzyme concentration to the Michaelis-Menten equation (Michaelis and Menten, 1913):

$$\frac{v}{e} = \frac{k_{\text{cat}} [NADH]}{K_m^{NADH} + [NADH]} \quad (\text{Eq. 3.16}).$$

$$\frac{v}{e} = \frac{(k_{\text{cat}}/K_m^{NADH})[NADH]}{1 + \left(\frac{(k_{\text{cat}}/K_m^{NADH})}{k_{\text{cat}}}\right)} \quad (\text{Eq. 3.17}).$$

Where  $v$  stands for the experimentally determined initial velocity,  $e$  is the enzyme concentration,  $K_m^{NADH}$  is the enzyme Michaelis constant for NADH,  $k_{\text{cat}}$  is the catalytic constant or maximal turnover number of the enzyme and  $k_{\text{cat}}/K_m^{NADH}$  is the enzyme catalytic efficiency.

### 3.8.2.2 DETERMINATION OF PRE-STEADY STATE KINETICS PARAMETERS BY STOPPED-FLOW SPECTROPHOTOMETRY

Kinetic measurements using Stopped-flow spectrophotometry (SF) allow to visualise fast individual process occurring over timescales of milliseconds. This methodology is widely used to evaluate biochemical processes such as ligand binding or dissociation, complex formation, and electron and hydride transfer, as well as to obtain spectral information on initial, intermediate and final species along the course of the reaction (Gibson and Milnes, 1964, DeSa and Gibson, 1969, Eccleston et al., 2001).

#### 3.8.2.2.1 EQUIPMENT AND PREPARATION OF SAMPLES

**The stopped flow instrument.** The SF instrument is a rapid mixing device that forces the simultaneous entrance of two solutions into a mixing chamber from two independent syringes (Ferreira P and Medina M., 2021). The mix fills the optical observation cell displacing the previous contents with freshly mixed reactants. The exit of the observation cell is connected to a third syringe, the stop syringe that collects the old mixed solution limiting the volume spent with each experiment (**Figure 3.17**).

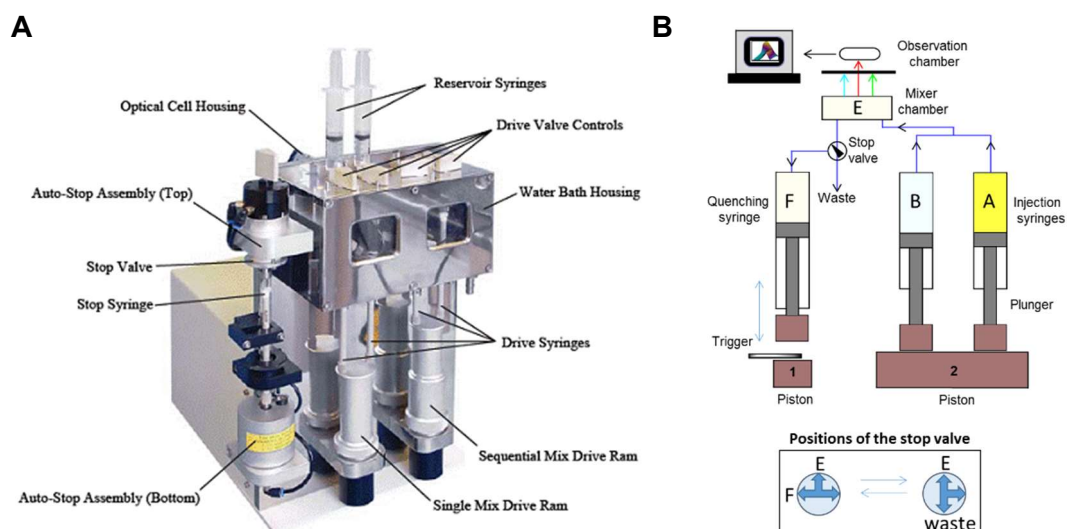


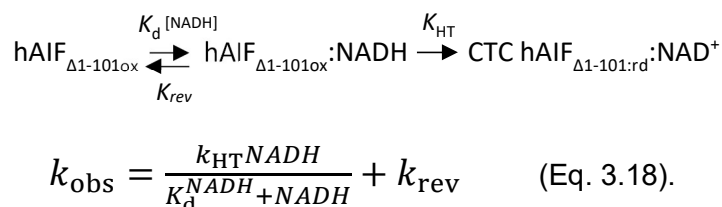
**Figure 3.17: Stopped flow system (A)** Drive unit of the SF spectrophotometer from Appl. Phot. Ltd model SX17.MV. **(B)** Diagram of the components of a SF equipment (Ferreira P and Medina M., 2021). Syringes A and B contain the solutions to be mixed. 1 and 2 denote the stop and drive pistons respectively, indicating the order in which they are activated. The arrows indicate the direction of the flow.

The process starts by the displacement of the stop syringe piston to allow emptying a fixed volume of this syringe. Then, the drive syringe piston activates the plungers of the drive syringes, allowing them to liberate their content into the mixing chamber. The entrance of these solutions into the mixing chamber flushed the old reaction mixture towards the stop syringe. In this way the total volume exiting the drive syringes equals the one liberated before from the stop syringe. The flow is then stopped at the measuring chamber and drive syringes, and the measuring device is triggered. Just prior to the flow stopping, a steady state flow is achieved at the solution entering the measuring chamber, which is only a few milliseconds old. The age of this reaction volume is known as the dead time of the SF system, which is usually in the 0.3-2 ms range. The observation cell is illuminated by a light source and the change, as a function of time, in the selected optical property can be measured by the adequate detector (Absorption, fluorescence, light scattering, turbidity, fluorescence anisotropy, etc...), which can be mounted either perpendicular or parallel to the path of the incoming light depending on the optical property.

### 3.8.2.2.2 DETERMINATION OF OBSERVED RATE CONSTANTS ( $k_{\text{obs}}$ ) FOR DIFFERENT PROCESSES INVOLVING hAIF<sub>Δ1-101</sub> AND hAIFmt<sub>Δ1-77</sub>.

A SX17.MV stopped-flow spectrophotometer (Applied Photophysics), interfaced with the Pro-Data SX software and a photodiode array detector, were here used to investigate the fast kinetics reduction of hAIF variants by the NADH coenzyme in presence and in absence of some ligands, as well as the binding of NAD<sup>+</sup>.

To evaluate protein reduction by the coenzyme, ~10 μM hAIF samples were placed in one of the SF drive syringes and missed with increasing concentrations of NADH (0.03-10 mM, placed in the second drive syringe) under aerobic conditions in 50 mM Kpi, pH 7.4, at 25 °C. The indicated enzyme and NADH concentrations are the final ones obtained after mixing equal volumes. Observed rate constants for the studied processes ( $k_{\text{obs}}$ ) were calculated by global analysis (simultaneously using all spectral data in the 400-800 nm region along time evolution) and numerical integration methods using the Pro-Kinetics software (Applied Photophysics Ltd.). In general, a single step model (A→B) best fitted to describe the overall reaction at all NADH concentrations assayed. Averaged  $k_{\text{obs}}$  values exhibiting hyperbolic behaviour on the NADH concentration were then fitted to the equation that describes the formation of an enzyme:substrate complex prior to the hydride transfer (HT) event:



Where  $k_{\text{HT}}$  is the limiting rate constant for HT from the pyridine nucleotide coenzyme to the FAD cofactor of hAIF,  $K_{\text{d}}^{\text{NADH}}$  is the hAIF:coenzyme dissociation constant and  $k_{\text{rev}}$  is the constant for the reverse process its value is practically zero.

SF was also used to characterise the effect of the interaction of hAIF with either the ATA inhibitor or the CHCHD4 protein on the coenzyme binding affinity and in the HT process. Samples containing ~10 μM of hAIF were incubated with either 50 μM ATA or 15 μM CHCHD4 for 15 min. These different samples were then mixed in the SF instrument with increasing concentrations of NADH (0.03-10 mM). Experimental data were evaluated as above described to obtain apparent  $k_{\text{obs}}$ , as well as apparent  $k_{\text{HT}}$  values in the presence of the introduced ligands.

### 3.8.2.2.3 DETERMINATION OF THE RATES FOR CTC FORMATION UPON MIXING PHOTOREDUCED hAIF<sub>Δ1-101</sub> WITH NAD<sup>+</sup>.

SF spectrophotometry was also used to evaluate the rates of CTC formation when mixing photoreduced hAIF<sub>Δ1-101</sub> (hAIF<sub>Δ1-101phrd</sub>) with increasing concentrations of NAD<sup>+</sup> (0.125 - 5 mM) under anaerobic conditions in 50 mM Kpi, pH 7.4, at 25 °C.

**Preparation of anaerobic samples and equipment.** Some processes involving reduced states of proteins are very sensitive to the presence of molecular oxygen, and they must be performed under strict anaerobic conditions to avoid protein re-oxidation. Therefore, the air atmosphere of samples, buffers and instruments (including drive syringes and the pipeline of the SF instrument) must be replaced by an oxygen free Ar/N<sub>2</sub> atmosphere. To ensure such anaerobic conditions a manifold system was here used (**Figure 3.18 A**). It allowed to perform successive cycles of air removal (vacuum) and replacement by Ar on the samples of interest. Samples for SF experiments were placed in glass tonometers with a vacuum stopcock valve at each one of their ends (**Figure 3.18 B**). The top valve ends in a glass tube of fixed diameter that is used to connect the tonometer through a butyl rubber tube to the anaerobic manifold system. The bottom of the tonometer ends in a glass tube whose diameter is decreased to fit into the female luer-lock fitting at the entrance valves of the SF drive syringes.

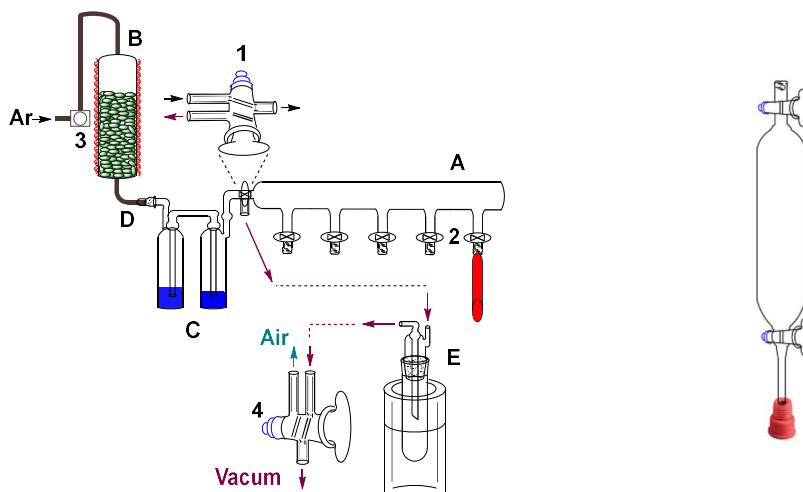


**Figure 3.18: Anaerobic system.** (A) Scheme of the anaerobic manifold system. Main components: (A) Central glass column of the anaerobic manifold system. (B) Glass column two-thirds filled with BASF catalyst (R3-11 or R3-11G). (C) In tandem 250 mL wash-bottles containing a methyl viologen solution. (D) Coils of 1/8 inch copper tubing sealed to glass tubing with epoxy cement. (E) Cold trap form by a thick round tub with a ground-glass joint and a cap with the corresponding ground-glass connections and placed into an open liquid nitrogen Dewar flask. Valves: (1) three-way vacuum stopcock valve connecting either Ar or vacuum to the manifold system, (2) stopcock vacuum valves connecting the anaerobic manifold system to the tonometers, (3) pressure regulator outlet valve, and (4) three-way vacuum stopcock valve connecting vacuum either the anaerobic system or to the atmospheric air. Image from (Ferreira P and Medina M., 2021). (Right) Glass Tonometer: The tonometer has a vacuum stopcock valve at each one of their ends. The top is used to put it into the anaerobic manifold system and the end is covered with a rubber plug.

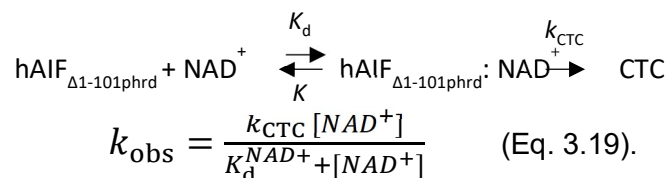
The home-made manifold system (anaerobic train), will allow gases to be evacuated from liquid samples using a vacuum pump, and then filling the samples with oxygen-free Ar during successive cycles. This manifold system is a glass column (A) ending at one side in 4-5 exit glass tubes (2), each one containing a vacuum stopcock valve attached to a butyl rubber tubing to allow joining of tonometers. The other manifold end finish in a glass tube fused to a three-way vacuum stopcock (1), key either to fill in the cylinder with the anaerobic Ar gas or to connect it to the vacuum pump.

The Ar gas enters the system through a press regulator valve (3) and a glass column (B) two-thirds filled with BASF PuriStar® catalyst (R3-11 or R3-11G) heated to 110-130 °C with a heating tape. This column traps oxygen impurities. Ar goes then through two in tandem 250 mL wash-bottles (C), filled with a methyl viologen mixture (1 mM methyl viologen, 10 mM EDTA and 5 µM 5-deazariboflavin (5-dRF), in 200 mM Tris/HCl, pH 8.0), whose exit is fused by a glass tube to the three-way vacuum stopcock (1). The methyl viologen solution is exposed to visible light until reduced and turned blue, being used as an anaerobic indicator. The third connection of the three-way vacuum stopcock valve (1) connects the anaerobic manifold system to the vacuum pump. Finally, another vacuum stopcock valve (4) is placed between the vacuum pump and the cold trap, allowing to connect directly the vacuum pump to the air atmosphere.

**Preparation of photoreduced hAIF samples.** Photoreduction of hAIF<sub>Δ1-101</sub> variants was achieved on samples which have been made anaerobic (after 8 cycles of Ar/Vacuum) and also contained 5 µM methyl viologen, 3 µM 5-dRF and 20 mM EDTA. Reduction was achieved by sample illumination with a led beam of visible light that excites the 5-dRF to its triplet state,<sup>3</sup>5-dRF, which is quickly extinguished to its radical semiquinone, 5-dRF•, by electron abstraction from EDTA. This 5-dRF• radical is produced at very low concentration, in less than 1 µM, and is prone to suffer rapid two-electron disproportionation. Nonetheless, redox proteins present in the solution might be able to get electrons from 5-dRF• faster than disproportionation, getting as consequence reduced (Tollin et al., 1993). In this study, protein photoreduction has been used to prepare reduced protein samples for SF measurements.

**Measurements.** SF spectrophotometry was also used to evaluate the rates of the CTC formation when mixing ~10 µM hAIF<sub>Δ1-101phrd</sub> with increasing concentrations of NAD<sup>+</sup> (0.125-5 mM) under anaerobic conditions. hAIF<sub>Δ1-101phrd</sub> samples were obtained as described above. The assays were performed at 25 °C in 50 mM Kpi, pH 7.4, under

anaerobic conditions. Data were globally fitted to a single step model (A→B) to determine  $k_{\text{obs}}$  at the different  $\text{NAD}^+$  concentrations assayed. These values showed an hyperbolic dependence on the coenzyme concentration, allowing to fit then to the equation describing the formation of an enzyme:substrate complex prior to the production of the CTC:



In which  $k_{\text{CTC}}$  is the limiting rate constant for CTC formation when using reduced protein and  $\text{NAD}^+$ , and  $K_d^{\text{NAD}^+}$  is the  $\text{hAIF}_{\text{rd}}:\text{NAD}^+$  dissociation constant.

### 3.9 ANALYSIS SOFTWARE, BIOINFORMATIC AND COMPUTATIONAL TOOLS

The GenBank database was used for the search of gene and protein sequences (<http://www.ncbi.nlm.nih.gov/genbank/>).

Multiple sequence alignments were performed using the tool CLUSTAL W2 (<http://www.ebi.ac.uk/Tools/msa/clustalw2/>)



The ProtParam tool on Expasy (<https://web.expasy.org/protparam/>) was used for determination of protein theoretical parameters. Molecular simulations shown in the results chapters were carried out by Ruben Laplaza.

Origin 7.0 and Origin 8.0 (OriginLab), as well as SigmaPlot 11.0 (Systat Software Inc.) were used for data analysis and production of figures.

The PyMol software (Delano, 2002) was used to produce structural figures.







## ***4- REDOX AND LIGAND BINDING- DEPENDENT CONFORMATIONAL ENSEMBLES IN THE HUMAN APOPTOSIS-INDUCING FACTOR REGULATE ITS PRO-LIFE AND CELL DEATH FUNCTIONS***

### **PERSONAL CONTRIBUTION**

- Expression and purification of mitochondrial and pathogenic AIF variants
- Spectroscopic characterization of mitochondrial and pathogenic AIF variants
- Kinetic measurements of mitochondrial and pathogenic AIF variants
- Fluorescence and CD assays of mitochondrial and pathogenic AIF variants



## 4.1 ABSTRACT

hAIF supports OXPHOS biogenesis and programmed cell death, with missense mutations producing neurodegenerative phenotypes. hAIF senses the redox environment of cellular compartments, stabilising a CTC dimer that modulates the protein interaction network. The apoptotic form of hAIF, hAIF<sub>Δ1-101</sub>, is not stable at the IMS pH, but the 77-101 residues confer stability to the mitochondrial isoform.

In this context we aimed to evaluate the subcellular pH, CTC formation, and pathogenic mutations effect on hAIF stability, and a thermal denaturation high-throughput screening (HTS) assay to discover AIF binders.

hAIF and its CTC are different conformational ensembles with the redox switch to the CTC producing a less stable and compact protein. The pathogenic G308E, ΔR201 and E493V mutations modulate hAIF stability, particularly ΔR201 causes population shift to a less stable conformation with a loss in its functionality because the structure and dynamics of the active site are remodelled. NADH-redox linked conformational changes course with strong NAD<sup>+</sup> binding and protein dimerization, but they produce a negative impact in overall hAIF stability.

We identified new molecules that modulate the association/dissociation equilibrium of reduced/oxidised nicotinamide adenine dinucleotide (NADH/NAD<sup>+</sup>) to hAIF and that regulate its catalytic efficiency.

## 4.2 RESUMEN

hAIF participa en la biogénesis del sistema OXPHOS y en la muerte celular programada. Algunas mutaciones en hAIF producen fenotipos neurodegenerativos. hAIF detecta el entorno redox de los compartimentos celulares, estabilizando un complejo de transferencia de carga (CTC) en forma de dímero de la proteína que modula su red de interacción con otras proteínas. La forma apoptótica de hAIF, hAIF<sub>Δ1-101</sub>, no es estable al pH del IMS, pero los residuos 77-101 confieren estabilidad a la isoforma mitocondrial.

En este contexto, nuestro objetivo ha sido evaluar el efecto del pH subcelular, la formación de CTC y de mutaciones patógenas en la estabilidad de hAIF, y desarrollar un ensayo de cribado de alto rendimiento mediante desnaturalización térmica (HTS) para descubrir ligandos de hAIF.

hAIF y su CTC son organizaciones conformacionales diferentes, donde la transición a la formación del CTC produce una proteína menos estable y compacta. Las mutaciones patogénicas G308E, ΔR201 y E493V modulan la estabilidad de hAIF, particularmente ΔR201 que provoca un cambio a una conformación menos estable, con una pérdida en su funcionalidad debido a la remodelación de la estructura y la dinámica del sitio activo. Los cambios conformacionales dependientes del estado redox asociados a la interacción de hAIF con NADH cursan con una fuerte unión del coenzima en la forma de NAD<sup>+</sup> y con la dimerización de la proteína, pero producen un impacto negativo en la estabilidad general de hAIF.

Hemos identificado nuevas moléculas que modulan el equilibrio de asociación/disociación de NADH/NAD<sup>+</sup> a hAIF y que regulan su eficiencia catalítica.

### 4.3 INTRODUCTION

AIF is a flavoreductase that contributes to growth, development, and maintenance of mitochondrial function, being also a caspase-independent PCD effector (Miramar et al., 2001, Modjtahedi et al., 2006, Susin et al., 1999b, Kadam et al., 2016, Natarajan and Becker, 2012). Recent research is compiling evidences of the critical roles of the AIF redox state and on its redox-dependent monomer-dimer equilibrium in both functions. The hAIF precursor is synthesised in the cytosol and imported into the IMS, where its N-terminal is enzymatically removed producing the mitochondrial mature form, hAIF<sub>Δ1-54</sub>. Then, the hAIF<sub>Δ1-54</sub> N-terminal transmembrane helix (residues ~60-78) tethers the protein to the IMM, while the soluble protein moiety folds towards the IMS and incorporates the redox FAD cofactor (Susin et al., 1999b, Otera et al., 2005, Zhang et al., 2009). hAIF assists biogenesis of respiratory chain complexes through its NADH-oxidoreductase activity, by contributing to the import to the IMS of the coiled-coil-helix-coiled-coil-helix domain containing-4-protein (CHCHD4) (Hangen et al., 2015, Meyer et al., 2015, Vahsen et al., 2004, Shelar et al., 2015). Certain apoptotic stimuli induce a second N-terminal hAIF cleavage yielding a soluble protein, hAIF<sub>Δ1-101</sub>, that translocate to the cytoplasm, where it can interact with HSP70 (Schmitt et al., 2003), thioredoxin 1 (Shelar et al., 2015) or endonuclease CypA (Zhu et al., 2007, Cande et al., 2004). Finally, hAIF<sub>Δ1-101</sub> can translocate to the nucleus where it forms, upon recruiting CypA and histone H2AX, a DNA-degradosome that induces chromatinolysis (Susin et al., 1999b, Artus et al., 2010, Cande et al., 2004).

Binding of NADH to hAIF elicits its reduction and the stabilisation of a long-lived oxygen-stable FADH<sup>-</sup>-NAD<sup>+</sup> CTC (Ferreira et al., 2014, Sevrioukova, 2009, Sevrioukova, 2011, Ferreira et al., 2018). This process triggers protein dimerization, uncouples a 50-residue region at the protein C-terminal apoptotic domain that becomes disordered in the CTC crystal structure (regulatory C-loop, 509-560), and creates a second noncatalytic and allosteric NADH binding site. In the oxidised enzyme, hAIF<sub>ox</sub>, the C-loop 517-533 residues fold in two short  $\alpha$ -helices, diminishing the isoalloxazine solvent accessibility (Ferreira et al., 2014, Sevrioukova, 2009, Sevrioukova, 2011, Ferreira et al., 2018). The NADH driven allosteric conformational changes propagate from the CTC active site through very specific molecular pathways that are claimed to control hAIF association with protein partners and DNA, and, as a consequence, its participation in mitochondrial homeostasis and PCD (Brosey et al., 2016, Sevrioukova, 2016, Hangen et al., 2015).

Thus, hAIF is envisaged as a redox and/or NADH sensor that might modulate certain signal-transduction pathways (Sevrioukova, 2011, Sorrentino et al., 2017). We are also witnessing the discovery of an increasing number of hAIF allelic variants linked to a range of human rare diseases, mainly neurodegenerative mitochondrial disorders and inherited peripheral neuropathies (Ardissone et al., 2015, Berger et al., 2011, Diodato et al., 2016, Ghezzi et al., 2010, Kettwig et al., 2015, Rinaldi et al., 2012, Zong et al., 2015, Morton et al., 2017a, Sancho et al., 2017, Heimer et al., 2018). Most of them (as  $\Delta$ R201, F210S, V243L, G262S, G308E, G338E and Q479R) produce severe mitochondriopathies associated with a substantial reduction of the CTC lifetime, reduced expression of respiratory chain complexes, and OXPHOS failure. In contrast, the E493V mutation increases cell death via apoptosis, causing the Cowchock syndrome without affecting OXPHOS. Mutations are distributed through the hAIF structure, but the most deleterious ones tend to compromise structural elements involved in the binding of the adenine moieties of the NAD(H) coenzymes or the FAD cofactor (Ferreira et al., 2014, Sevrioukova, 2016, Sorrentino et al., 2017). *In vitro* studies with some of these variants envisage defective folding, decreased stability, or higher propensity to FAD release (Ghezzi et al., 2010, Sevrioukova, 2016).

The NADH-driven allosteric behaviour and the disease-causing mutations indicate that the hAIF redox-dependent structural stability and conformation control its physiological functions. Thus, knowing how subcellular localization, ligand binding, redox state, or allelic mutations can regulate these parameters will help understand the hAIF *in vivo* behaviour. In this context, we evaluate here the hAIF stability under conditions that potentially mimic different conformational traits influenced by intracellular environment (subcellular compartments pH, NADH-redox-dependent state) and by missense pathogenic mutations. In addition, we develop and validate a FAD fluorescence-based thermal denaturation high-throughput screening (HTS) assay to search for compounds that might alter hAIF stability. To date, only one small molecule, aurintricarboxylic acid (ATA), has been identified to bind hAIF by using a photonic crystal biosensor screening (Chan et al., 2008). In this study, we propose some molecules that may serve as a starting point in the development of hAIF bioactive compounds with low cellular toxicity.

## 4.4 EXPERIMENTAL PROCEDURES

### 4.4.1 PROTEINS PRODUCTION

hAIF<sub>Δ1-101</sub> was overexpressed and purified from *Escherichia coli* as N-terminal His<sub>6</sub>-tag proteins as previously described (Ferreira et al., 2014), introducing an additional molecular exclusion chromatography step using a Superdex<sup>TM</sup> 200 10/300 GL (GE Healthcare), column in 50 mM Kpi, pH 8.0, 150 mM NaCl. The purified protein was dialyzed to remove the salt and concentrated (up to ~500 μM). Purified protein was then diluted to the desired concentration in 50 mM Kpi at the corresponding pH, 8.0, 7.4, 7.0, or 6.2, at a final ionic strength of 150 mM (ionic strength described as the physiological one (Stein et al., 1979, Cortese et al., 1991). pET-28a(+)-hAIF<sub>Δ1-101</sub> plasmids containing the ΔR201, G308E and E493V mutations, as well as pET-28a(+)-hAIFmt<sub>Δ1-77</sub>, were obtained from Mutagenex, and the corresponding proteins were similarly produced as the WT. Several independent purifications of each hAIF variant, were used thorough the study to reproduce experiments, confirming results are batch independent.

Before the HTS experiments, the His<sub>6</sub>-tag was removed by adding 0.2 U of thrombin to 1 mL of hAIF<sub>Δ1-101</sub> and loading the mixture into a 1 mL HiTrap Chelating HP column (GE Health Care) activated with NiSO<sub>4</sub>. The column containing the mixture was incubated for 4 hours at room temperature and then overnight at 4 °C. hAIF<sub>Δ1-101</sub> was eluted with 50 mM Kpi, pH 8.0.

### 4.4.2 SPECTROSCOPIC CHARACTERIZATION

UV-Visible spectra were recorded at 25 °C in a Cary 100 Bio spectrophotometer (Agilent technologies) using 1 cm-pathlength cuvettes. Protein concentrations were determined using the molar absorbance extinction coefficient of the protein ( $\epsilon_{450\text{nm}} = 13.7 \text{ mM}^{-1} \text{ cm}^{-1}$ ) (Ferreira et al., 2014). UV-Vis difference spectroscopy measurements were carried out with compartmentalised cuvettes in 50 mM Kpi, pH 8.0 by titrating ~20 μM of hAIF<sub>Δ1-101</sub> with up to 2.9 mM of ATA. Fluorescence spectra were acquired in a thermostated Cary Eclipse Fluorescence spectrophotometer (Agilent technologies) using 2 μM hAIF<sub>Δ1-101</sub> in a 1 cm-pathlength cuvette. Fluorescence emission spectra of aromatic residues were recorded from 300 to 550 nm upon excitation at 280 nm, while flavin fluorescence emission spectra were collected from 480 to 600 nm after excitation at 450 nm. CD spectra were recorded in a thermostated Chirascan (Applied Photophysics). Far-UV CD spectra were acquired in a 0.1 cm-pathlength cuvette using 1 μM hAIF<sub>Δ1-101</sub>, while near-UV-Vis CD spectra were recorded in a 1 cm-pathlength cuvette using 20 μM hAIF<sub>Δ1-101</sub>. Fluorescence and CD spectra were

acquired at 10 °C (folded state) and 90 °C (thermally denatured state). Fluorescence and CD spectra were recorded in the absence and presence of a 100-fold excess of NADH.

#### 4.4.3 KINETIC MEASUREMENTS

Steady-state kinetic analyses were carried out in a Cary 100 Bio spectrophotometer (Varian) and measured in air-saturated 50 mM Kpi, pH 8.0, using NADH (Sigma Aldrich) as the substrate donor and 95 µM dichlorophenolindophenol (DCPIP) (Sigma Aldrich) as acceptor (Ferreira et al., 2014). Reactions were followed at 620 nm ( $\Delta\epsilon_{620\text{nm}} = 21 \text{ mM}^{-1} \text{ cm}^{-1}$ ) and parameters determined by data fitting to the Michaelis-Menten equation. SF measurements were carried out under aerobic conditions in a SX17.MV spectrometer (Applied Photophysics) using a photodiode array detector and the ProData-XS software as previously reported (Ferreira et al., 2014). The observed rates for the HT event ( $k_{\text{obs}}$ ) were calculated by global analysis and numerical integration methods (simultaneously using all spectral data in the 400-800 nm region along time evolution) by fitting to either a single-step ( $A \rightarrow B$ ) or a two-step ( $A \rightarrow B \rightarrow C$ ) model. When a saturation profile on the pyridine nucleotide concentration was observed,  $k_{\text{obs}}$  values were fit to the equation (4.1.1) describing formation of an enzyme:substrate complex prior to the HT process, where  $k_{\text{HT}}$  is the limiting rate constant for HT from the pyridine nucleotide coenzyme to the FAD cofactor of hAIF, and  $K_d$  is the hAIF:coenzyme dissociation constant.

$$k_{\text{obs}} = \frac{k_{\text{HT}} \cdot [S]}{K_d + [S]} \quad (\text{Eq. 4.1})$$

#### 4.4.4 THERMAL DENATURATION

Thermal denaturation curves were followed by fluorescence emission of the aromatic residues and the flavin cofactor, far-UV CD and near-UV-Vis CD. Denaturation curves were recorded from 10 °C to 90 °C with scan rates of 1 °C/min and 1.5 °C/min respectively for CD and fluorescence assays. The thermal curves were recorded in the absence and presence of a 100-fold excess of NADH (Sigma Aldrich). hAIF<sub>Δ1-101</sub> concentrations, wavelengths and pathlengths were 1 µM, 210 nm and 1 mm in the far-UV CD (220 nm when NADH was present); 20 µM, 300 nm and 1 cm in the near-UV CD (or 420 and 600 nm when NADH was present); and 2 µM, 530 nm (excitation at 450 nm) and 1 cm for flavin fluorescence. Unless otherwise stated the individual experimental data sets (flavin fluorescence, far- and near-UV CD) were globally analysed as one-transition (i.e., two-step process, native  $\leftrightarrow$  unfolded, N  $\leftrightarrow$  U) or two-transition process (i.e. three-state process, native  $\leftrightarrow$  intermediate  $\leftrightarrow$  unfolded, N  $\leftrightarrow$  I  $\leftrightarrow$  U) by applying the following equations (Sancho, 2013):



$$S_{obs} = \frac{S_N + m_N T + (S_U + m_U T) e^{-(\Delta G/RT)}}{1 + e^{-(\Delta G/RT)}} \quad (\text{Eq. 4.2}).$$

$$S_{obs} = \frac{S_N + m_N T + (S_I + m_I T) e^{-(\Delta G_1/RT)} + (S_U + m_U T) e^{-((\Delta G_1 + \Delta G_2)/RT)}}{1 + e^{-(\Delta G_1/RT)} + e^{-((\Delta G_1 + \Delta G_2)/RT)}} \quad (\text{Eq. 4.3}).$$

Where  $S_{obs}$  is the measured protein signal at a given temperature ( $T$ ),  $S_N$ ,  $S_I$ , and  $S_U$  are the signals (origin intercept) of native, intermediate, and unfolded protein conformations at 0 K, respectively, and  $m_N$ ,  $m_I$ , and  $m_U$  are the slopes of the linear temperature dependence of those signals, respectively. On the other hand, the free energy difference in Equations 4.1.2 and 4.1.3 is as follows:  $\Delta G_i = \Delta H_i \left(1 - \frac{1}{T_{mi}}\right) + \Delta C_{pi} \left(T - T_{mi} - T \ln \frac{T}{T_{mi}}\right)$ , where  $\Delta H_i$  is the Van't Hoff enthalpy for each unfolding transition,  $T_{mi}$  is the midpoint transition for each unfolding transition,  $\Delta C_{pi}$  is the heat capacity change for each unfolding transition, and  $R$  is the ideal gas constant.

#### 4.4.5 FAD FLUORESCENCE BASED HIGH-THROUGHPUT SCREENING (HTS)

The thermal stability of WT hAIF<sub>Δ1-101</sub> (without His<sub>6</sub>-tag) was monitored on 96-well plates by following FAD fluorescence, which increases upon thermal protein unfolding and cofactor dissociation (Forneris et al., 2009, Cremades et al., 2009), using a FluoDia T70 thermostated plate reader fluorimeter (Photon Technology International). The FAD fluorescence emission at 530 nm (excitation at 450 nm) was followed to determine  $T_m$  for flavin release ( $T_{mFAD}$ ) of WT hAIF<sub>Δ1-101</sub> when free and in the presence of known ligands and compounds from two different chemical libraries. A library of ~10000 small molecules (MW<500) dissolved at 4 mM in DMSO, with high chemical diversity and mostly satisfying Lipinski's rules (Lipinski et al., 2001), was selected from the HitFinder Collection (Maybridge Chemical Company). The Prestwick Chemical Library (Prestwick Chemical), composed of 1120 compounds dissolved at 10 mM in DMSO and with known bioavailability and safety in humans, was also screened. The samples were placed in 96-V-shape well plates to ensure a homogeneous temperature distribution. The screening of the Maybridge library was performed in two phases (Cremades et al., 2009). In the first one 3 compounds were added, at a final concentration of 100 μM each, to 1 μM of WT hAIF<sub>Δ1-101</sub> in 50 mM Kpi, pH 8.0 in a 100 μL final volume. The compounds in the positive wells were screened again in a second round by testing each one individually. The screening of the Prestwick library was carried out in a single step at a final compound concentration of 500 μM and 1 μM of WT hAIF<sub>Δ1-101</sub> in 50 mM Kpi, pH 8.0 in a 100 μL final volume. After mixing, each well was overlaid with 50 μL of mineral oil (Sigma Aldrich) to

prevent sample evaporation. Internal reference control wells (WT hAIF<sub>Δ1-101</sub> without compounds) were distributed on columns 1 and 12 in the plates, with the same concentration of protein and DMSO as the wells containing compounds. The unfolding curves obtained for each well were analysed using homemade software that estimates the  $T_{mFAD}$  of each well, using two methods (termed “middle point of unfolding” and “inflection point location”) designed to complement each other and to avoid false positives (Cremades et al., 2009, Velazquez-Campoy et al., 2016). All the HTS hits were subsequently acquired from Sigma Aldrich or Maybridge and dissolved in 100 % DMSO to prepare stock solutions at 50 and 10 mM. The purity of all compounds was >95 %, as indicated by the manufacturer by high performance liquid chromatography (HPLC), thin layer chromatography, nuclear magnetic resonance, infrared or basic titration.

#### 4.4.6 CELL VIABILITY ASSAYS

Cytotoxicity of the selected compounds was analysed using HeLa cells cultured in Dulbecco's Modified Eagle Medium (DMEM) (Pan-Biotech GmbH), supplemented with 50 U/mL penicillin (Pan-Biotech GmbH), 50 mg/mL streptomycin sulphate (Pan Biotech GmbH), and 10 % fetal calf serum (Pan-Biotech GmbH) at 37 °C in a 5 % CO<sub>2</sub> atmosphere. Cells were cultured in 25 mL culture flasks and subcultured every 3 days. To test the toxicity of the compounds, HeLa cells were harvested and diluted to have 7000 cells per well (100 µL) in 96-well plates. After incubation for 24 h, the compounds were added at different concentrations ranging from 5 nM to 1 mM (except C2, for which a 50 nM to 10 mM range was used). Cell viability after 24 hours of incubation was measured using CellTiter 96® AQueous One Solution Cell Proliferation Assay (Promega) following modified manufacturer recommendations. Absorbance was recorded at 490 nm to quantify the amount of formazan produced by the cell metabolism in a Sinergy HT (BioTek) plate reader. The values obtained for control wells lacking added compounds but treated with DMSO at the same concentration than in wells with the compounds, were considered to reflect 100 % viability. Half maximal effective concentration (EC<sub>50</sub>) was calculated for each compound by fitting the viability at the different concentrations of compounds to a sigmoidal dose-response function (López et al., 2012). To test the possible protective effect of the compounds against MNNG-induced cell death, 7000 cells per well were incubated in 96-well plates for 24 h at 37 °C and 5 % CO<sub>2</sub>. Next day 0.5 mM MNNG (Abcr GmbH) was added on each well and the plate was incubated for 20 minutes. Then, the medium was replaced by fresh one and the cells were incubated for another 24 h either in the absence or the presence of compounds.

#### 4.4.7 PRODUCTION OF STRUCTURAL MODELS

Models containing the missing the C-loop residues (546-558 and 518-559 respectively for hAIF<sub>Δ1-101</sub> and hAIF<sub>Δ1-101rd</sub>:NAD<sup>+</sup>), as well as the deletion of R201 in the ΔR201 variant, were built using as templates the published coordinates of hAIF<sub>Δ1-101</sub> (4BV6) and of hAIF<sub>Δ1-101rd</sub>:NAD<sup>+</sup> (4BUR) and the Swiss-Model server (Ferreira et al., 2014, Biasini et al., 2014). Cofactors or coenzymes were then reintroduced, brief 50 ps MD simulations with Generalised-Born, Molecular Volume (GBMV) solvation (Lee et al., 2002) and CHARMM c39b1 were carried out to remove potential clashes. Protonation states were assessed using PROPKA 3.0 (Olsson et al., 2011); H131, H457 and H478 were ε-protonated, while H454 and H455 were δ-protonated (according to geometrical H-bonding). MD simulations were performed using CHARMM c39b1 and the charmm36 force field (Brooks et al., 2009). Parameters for FAD and FADH<sup>+</sup>, as well as for other ligands were generated using the CgenFF server (Vanommeslaeghe et al., 2010) and density functional theory (DFT). DFT calculations were performed with the Gaussian09 rev.D01 package (Frisch et al., 2016) at the B3LYP/def2-SVP+GD3BJ level with a water-like polarizable continuum model (Frisch et al., 2016, Grimme et al., 2011). A Monte-Carlo scheme was used for neutralization, adding ions to 150 mM. A time step of 1 fs, NVT conditions, and a TIP3P water model were used. A standard workflow routine including solvation, neutralization, minimization plus heating and equilibration over 200 ps was performed to the models, with at least three replicas for each model. Short 15 ns MD runs were then performed at 298.15 K to further ensure thermodynamic and structural stability. The CHARMM software analysis tools were used to evaluate the resulting conformational ensembles. The GOLD 5.5 software (Jones et al., 1997) and the produced WT hAIF MD structures were used to obtain interaction models with ATA, C2, and C11. The whole macromolecule as receptor and the docking software default flood algorithm were first used for binding site detection. Sites were then corroborated with the FPocket suite (Le Guilloux et al., 2009). Final docked structures were obtained using default parameters and 100 Genetic Algorithm runs with a consensus docking approach between the ChemPLP and the GoldScore scoring functions. The highest ranked clusters showed in general very similar compounds allocation. The top ranked pose of the best cluster was then used as the starting point for short MD simulations to refine protein-ligand interactions (**Figure 4.20 D-H**). VMD (Humphrey et al., 1996) and PyMol (Delano, 2002) were used to analyse and to visualise structural data.

#### 4.4.8 DATA ANALYSIS AND STATISTICS

Data were analysed and represented using Origin (OriginLab) and Pro-K (Applied Photophysics). Results are expressed as the mean  $\pm$  the standard deviation (SD) or as the mean  $\pm$  the standard error (SE) of the regression analysis. Chemical structures of the compounds were drawn using ChemDraw Professional 16 (PerkinElmer Informatics). The FAF-Drug3 web server was used to identify putative pan assay interference compounds (Lagorce et al., 2015). The Molinspiration web server ([www.molinspiration.com](http://www.molinspiration.com)) was used to calculate theoretical LogP values of Prestwick chemical library compounds and ATA. Corresponding values for compounds from the Maybridge chemical library were obtained from the collection database.

### 4.5 RESULTS AND DISCUSSION

#### 4.5.1 THE pH OF SUBCELLULAR COMPARTMENTS MODULATES hAIF FOLDING AND CONFORMATION

hAIF functions in different subcellular compartments with particular pH environments that might influence its molecular properties. To evaluate this effect, we have selected pH 6.2 as the typical of the IMS (Porcelli et al., 2005), 7.0 as representative for apoptotic cytosol (Matsuyama et al., 2000), 7.4 for cytosol and nucleus (Llopis et al., 1998, Seksek and Bolard, 1996), and 8.0 for the mitochondrial matrix (Llopis et al., 1998, Orij et al., 2009), and ionic strength under physiological conditions (150 mM).

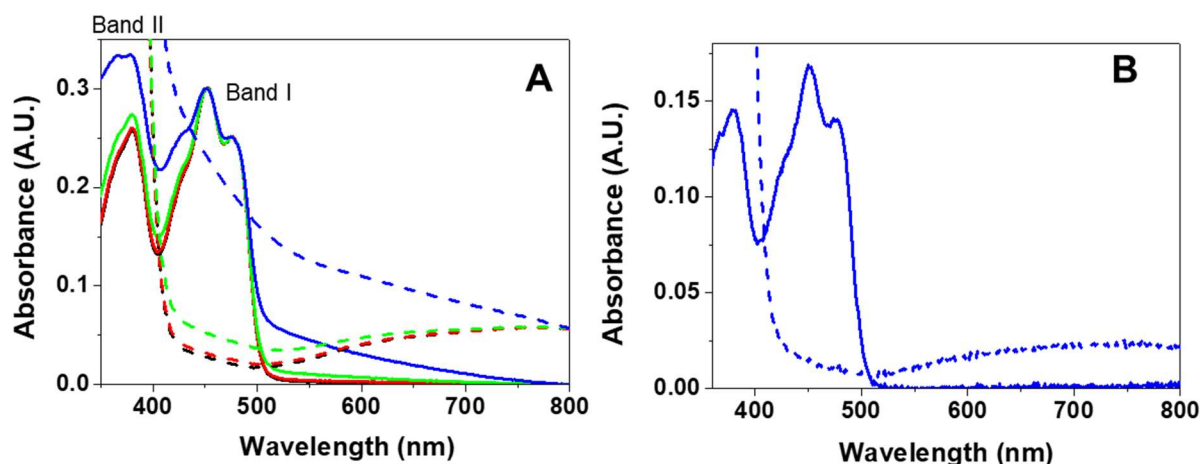


**Figure 4.1: Visible absorption spectra of WT hAIF isoforms as a function of pH.** Spectra of (A) hAIF $\Delta$ 1-101 (~22  $\mu$ M) and (B) hAIFmt $\Delta$ 1-77 (~15  $\mu$ M). Spectra were recorded at 25 °C in 50 mM Kpi, pH 8.0 (black lines), 7.4 (red lines), 7.0 (green lines), or 6.2 (blue lines), at a final ionic strength of 150 mM. Samples containing hAIF are shown as continuous lines, and those containing hAIF mixtures with NADH in a 1:100 protein:NADH ratio are shown as dashed lines.

Within the pH 7.0-8.0 range, hAIF<sub>Δ1-101ox</sub> absorption UV-Visible spectra indicate that the FAD cofactor is in the oxidised state, properly incorporated and in a similar electronic environment (bands I and II and  $A_{280}/A_{450}$  and  $A_{380}/A_{450}$  ratios) (**Figure 4.1 A**). At pH 6.2, the  $A_{280}/A_{450}$  and  $A_{380}/A_{450}$  ratios increase for hAIF<sub>Δ1-101</sub>, a drift dominates the CTC spectrum, and turbidity is observed, facts indicative of low stability and some aggregation level (**Figure 4.1 A**).

Since this IMS pH is relevant in our study, we have produced the hAIFmt<sub>Δ1-77</sub> isoform, lacking the membrane-anchoring helix but containing the IMS soluble portion. Spectra of hAIFmt<sub>Δ1-77ox</sub> confirm it is folded (**Figure 4.1 B**). Henceforth all studies at pH 6.2 will take hAIFmt<sub>Δ1-77</sub> as IMS representative, while hAIF<sub>Δ1-101</sub> will be the model for other subcellular compartments. Incubation with NADH brings about the FAD cofactor reduction with the appearance of a CTC band (hAIF<sub>Δ1-101</sub>:NAD<sup>+</sup> and hAIFmt<sub>Δ1-77</sub>:NAD<sup>+</sup> species (Ferreira et al., 2014) at all assayed pHs (**Figure 4.1**). CTC formation is corroborated by the NADH pre-steady-state hAIF reduction kinetics, with observed rate constants ( $k_{obs}$ ) within a factor of 1.5 (**Figure 4.2 Table 4.1**).

**Table 4.1:** Effect of the pH on the pre-steady kinetic rates for the aerobic reduction of hAIF by NADH. Assays were performed in 50 mM Kpi at a final ionic strength of 150 mM and 25 °C. Final concentrations were  $\sim 10 \pm 2$   $\mu$ M protein and 1, 2.5, or 5 mM for NADH.

Protein	pH	$k_{obs}$ (s <sup>-1</sup> )		
		[NADH]		
		1 mM	2.5 mM	5 mM
hAIF <sub>Δ1-101</sub>	8.0	0.53 ± 0.01	0.88 ± 0.02	1.17 ± 0.01
	7.4	0.37 ± 0.01	0.62 ± 0.01	0.82 ± 0.01
	7.0	0.35 ± 0.03	0.63 ± 0.01	0.84 ± 0.01
hAIFmt <sub>Δ1-77</sub>	6.2	0.60 ± 0.05	0.85 ± 0.07	1.10 ± 0.05

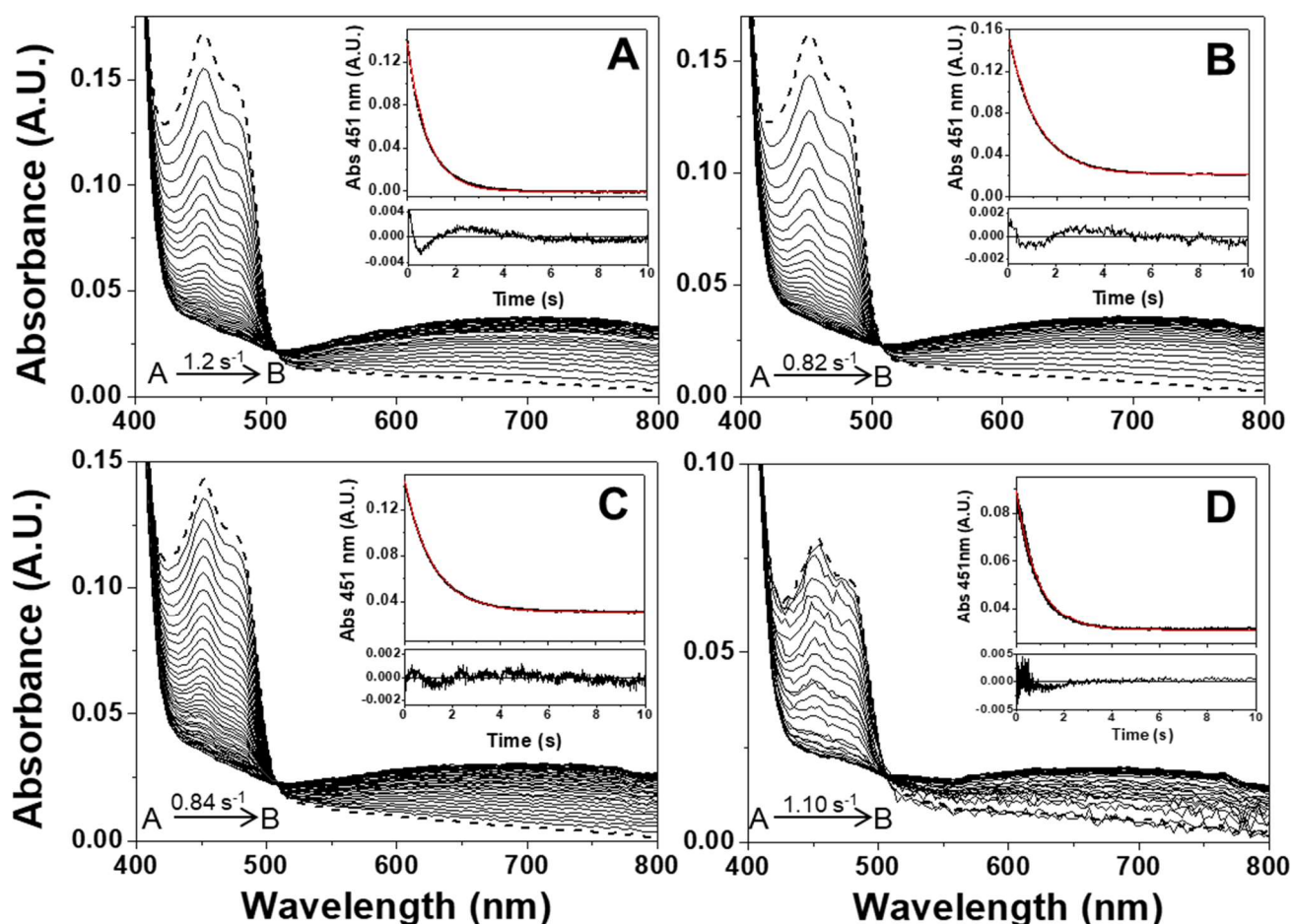


**Figure 4.2: Spectral evolution upon reduction of hAIF $\Delta_{1-101}$ /hAIFmt $\Delta_{1-77}$  ( $10 \pm 2 \mu\text{M}$ ) by NADH (5 mM) at (A) pH 8.0, (B) pH 7.4, (C) 7.0 and (D) pH 6.2. Measurements were carried out at 25 °C in 50 mM Kpi at a final ionic strength of 150 mM. The insets show the absorption evolution at 451 nm, the fit to a two species process (red line) and the corresponding residuals. Dashed lines correspond to the spectra of oxidised protein before mixing.**

Formation of the CTC slightly decreases the 208 nm minimum relative intensity (**Figure 4.3 B**), probably related to NADH binding inducing the C-loop two short  $\alpha$ -helices unfolding (Ferreira et al., 2014). The hAIF $\Delta_{1-101}$  near-UV-Vis CD spectrum shows sharp (wider in hAIFmt $\Delta_{1-77}$ ) and broad maxima at  $\sim 300$  and  $\sim 365$  nm, respectively, as well as minima at  $\sim 453$  and  $\sim 477$  nm, with minor pH effects (**Figure 4.3 C**).

CTC formation results in lack of near-UV CD signal at 300 nm and of 350-500 nm features related to the oxidised flavin in Vis CD but, shows a ~405 nm minimum and a broad band at ~600 nm consistent with CTC stabilisation (**Figure 4.3**). Far-UV and near-UV CD signals are lost at denaturing temperatures (90 °C), in agreement with protein becoming unfolded.

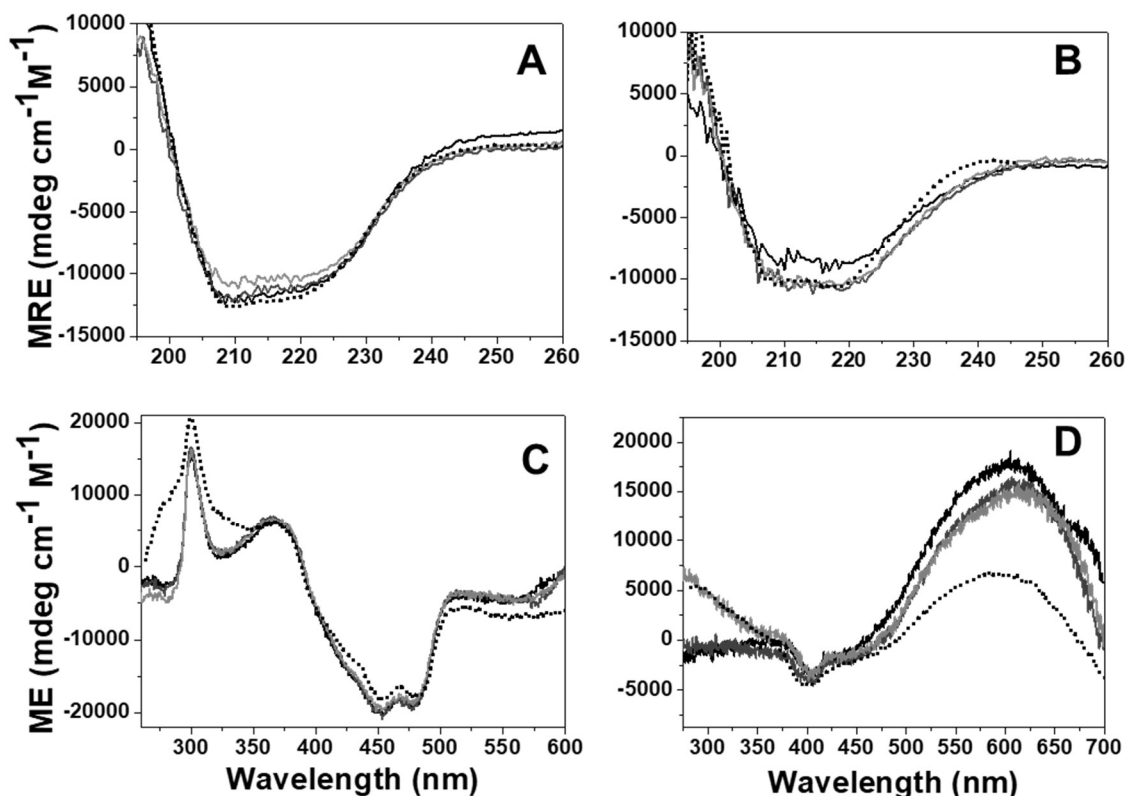


**Figure 4.3: Circular dichroism spectra of WT hAIF.** Far-UV CD spectra of samples containing (A) 1  $\mu$ M hAIF $_{\Delta 1-101}$  or hAIFmt $_{\Delta 1-77}$  (dashed line) and (B) a mixture of 1  $\mu$ M hAIF $_{\Delta 1-101}$  or hAIFmt $_{\Delta 1-77}$  (dashed line) with 100  $\mu$ M NADH. Near-UV-Vis CD spectra of samples containing (C) 20  $\mu$ M hAIF $_{\Delta 1-101}$  or hAIFmt $_{\Delta 1-77}$  (dashed line) and (D) a mixture of 20  $\mu$ M hAIF $_{\Delta 1-101}$  or hAIF $_{\Delta 1-77}$  (dashed line) with 2 mM NADH. Spectra were recorded at 25 °C in 50 mM Kpi, pH 8.0 (black line), 7.4 (dark grey line), 7.0 (grey line), and pH 6.2 (black dashed line) at a final ionic strength of 150 mM.

Then, we evaluated the pH effect on fluorescence emission spectra (**Figure 4.4**). Wild type (WT) hAIF samples display emission maxima at ~337 nm with higher quantum yield at pH 8.0. CTC spectra are dominated by a ~460 nm band related to intrinsic NADH fluorescence, whereas the aromatic band intensity decreases due to energy transfer because of the tryptophan-coenzyme proximity. When exciting at flavin band I, fluorescence is particularly low, indicative of a strong quenching of flavin emission upon



its binding to the protein. Denaturing temperatures increase fluorescent emission consistent with flavin release.

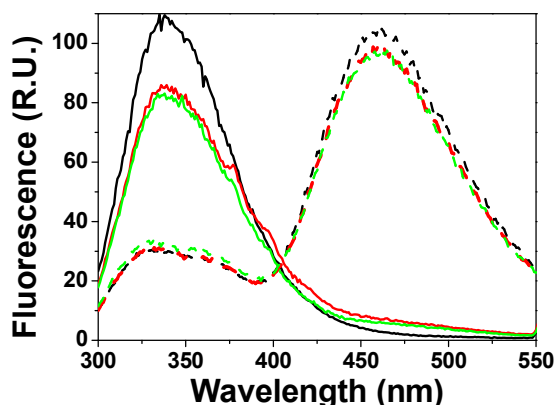


**Figure 4.4: Fluorescence emission spectra of hAIF $_{\Delta 1-101}$  (2  $\mu$ M) in the aromatic region at 10 °C with excitation wavelength 280 nm. Spectra were recorded in 50 mM potassium phosphate, pH 8.0 (black lines), 7.4 (red lines) or 7.0 (green lines) at a final ionic strength of 150 mM. Samples containing hAIF are shown as continuous lines, and those containing hAIF mixtures with NADH in a 1:100 protein:NADH ratio are shown as dashed lines.**

#### 4.5.2 THERMAL STABILITY OF hAIF IS HIGHLY MODULATED BY FORMATION OF THE CTC

Then, we recorded thermal unfolding curves to evaluate the stability of WT hAIF $_{\Delta 1-101}$ , oxidised and when forming the CTC, in the pH 7.0-8.0 range, as well as those of hAIFmt $_{\Delta 1-77}$  at pH 6.2. Far-UV CD, near-UV-Vis CD, and flavin fluorescence unfolding curves are shown in **Figures 4.5 and 4.6**.

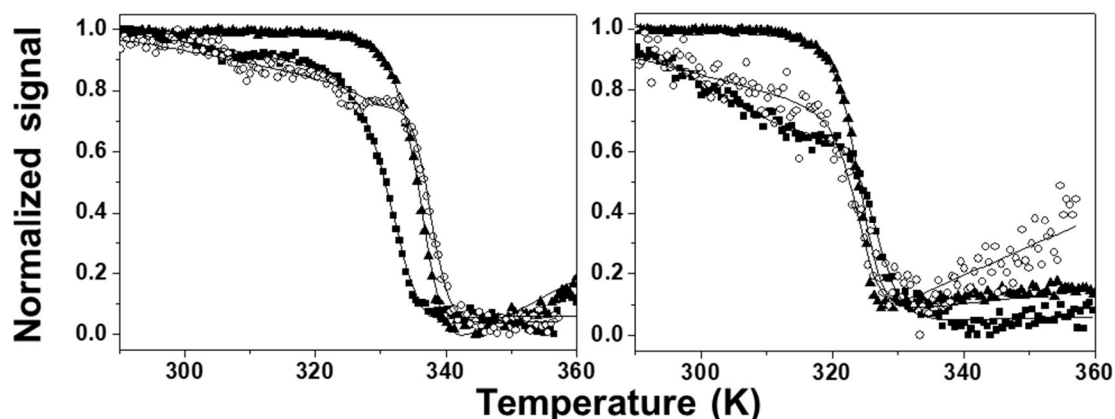


**Figure 4.5: Thermal unfolding curves of (A) hAIF $_{\Delta 1-101}$  and (B) its CTC (1:100 hAIF $_{\Delta 1-101}$ :NADH ratio) at pH 8.0. Thermal denaturation was monitored by far UVCD (210 nm, white circles) and near-UV CD (300 nm, black squares) for hAIF $_{\Delta 1-101}$ , or by far-UV CD (210 nm, white circles) and vis CD in the CTC (in B, 410 nm due to the lack of the 300 nm peak, black squares). Both samples were also monitored by flavin fluorescence emission (black triangles). The curves are shown roughly normalised from 0 to 1, and their global fits to two transition (for A) and one-transition (for B) unfolding models are represented by the continuous lines. Curves were recorded in 50mM Kpi at a final ionic strength of 150 mM.**



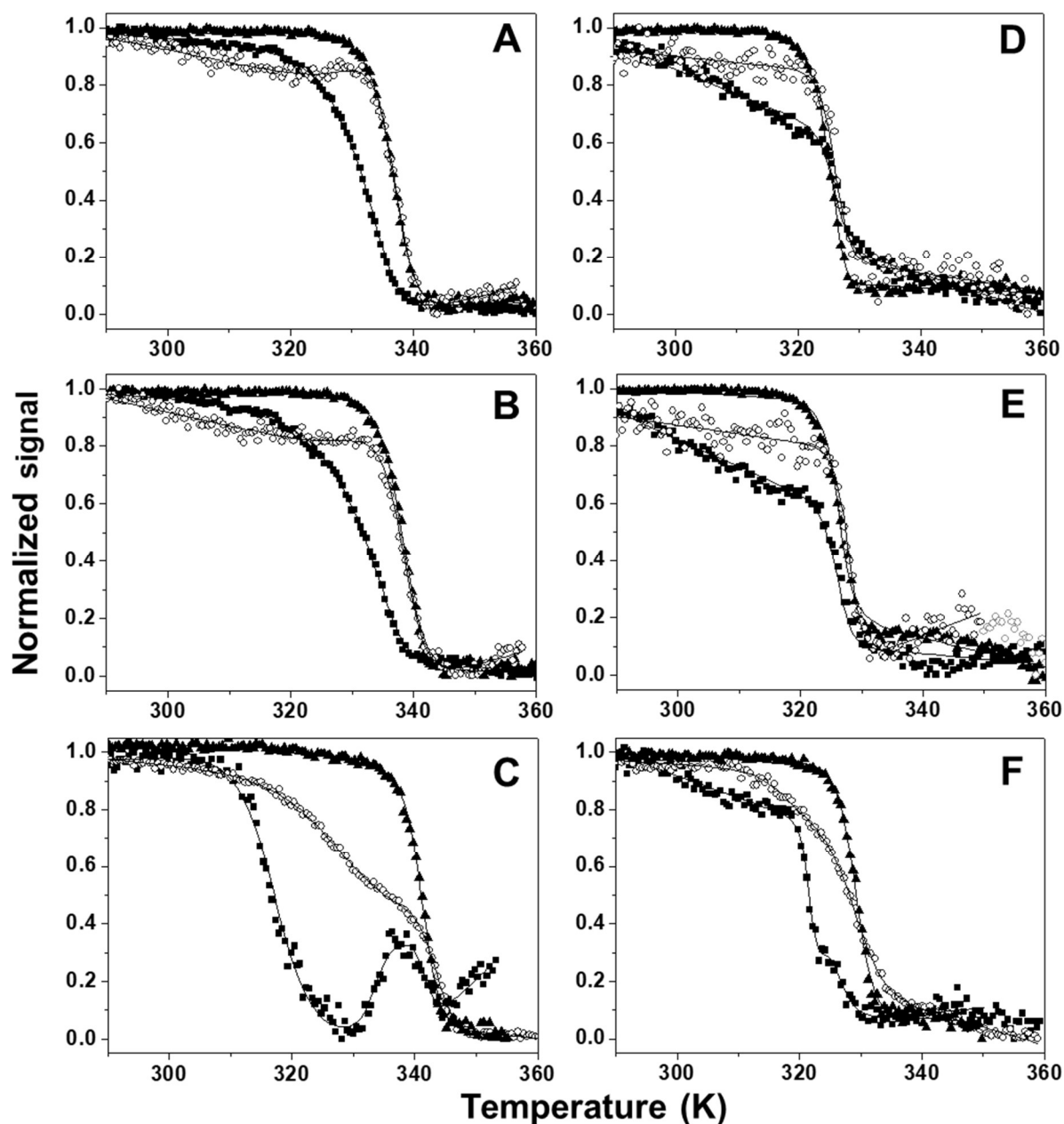


**Figure 4.6: Thermal unfolding curves for hAIF $_{\Delta 1-101}$  at (A) pH 7.4, and (B) pH 7.0, for hAIFmt $_{\Delta 1-77ox}$  at (C) pH 6.2, and for their respective CTCs (1:100 protein hAIF:NADH ratio) at (D) pH 7.4, (E) pH 7.0 and (F) pH 6.2. Thermal denaturation was monitored by far-UV CD (210 nm, white circles), near-UV CD (300 nm, black squares; or 410 nm in the CTC), and flavin fluorescence emission (black triangles, 530 nm). The curves are roughly normalised from 0 to 1, and their global fits to three-state (for A, B and F), four-state (C), and two-state (for D and E) unfolding models are represented by the continuous lines. Curves were recorded in 50 mM Kpi at a final ionic strength of 150 mM.**

hAIF $_{\Delta 1-101}$  curves indicate a three-state unfolding mechanism ( $N \leftrightarrow I \leftrightarrow U$ ), allowing determination of temperatures of midpoint denaturation ( $T_{m1}$  and  $T_{m2}$ ) and unfolding enthalpy changes ( $\Delta H_1$  and  $\Delta H_2$ ) (Table 4.2). AIF $_{\Delta 1-101}$  unfolds *via* an intermediate (I) with  $T_{m1}$  revealed by near-UV-CD transition, and the flavin fluorescence change taking place

essentially at  $T_{m2}$ . Therefore, the N→I transition is caused by loss of ternary interactions and the I state retains the FAD isoalloxazine folded environment. Noticeably, a modestly lower population of I state is detected at pH 8.0 (mitochondrial matrix) when compared with cytosolic and nuclear pH, whereas  $T_{m1}$  is 3 °C lower and the unfolding enthalpy change,  $\Delta H_1$ , is ~40 % larger (**Table 4.2**). hAIFmt $_{\Delta 1-77}$  unfolds via a four-state unfolding mechanism ( $N \leftrightarrow I_0 \leftrightarrow I \leftrightarrow U$ ) better describes unfolding (**Figure 4.6 C**). Near-UV-CD data suggest loss of overall 3D structure at lower temperatures and stabilisation of a new intermediate ( $I_0$ ,  $T_{m0}$ ) that retains secondary structure and FAD binding, while  $T_{m1}$  (now  $I_0 \rightarrow I$  transition) decreases when compared to the apoptotic hAIF $_{\Delta 1-101}$  values (**Table 4.2**). Finally, both pH 6.2 and the 77-101 tail have a thermal stabilising effect for flavin being retained at hAIFmt $_{\Delta 1-77}$  ( $T_{m2}$ ), despite unfolding of secondary and tertiary structural elements starts at lower temperatures. Formation of the dimeric hAIF $_{\Delta 1-101}$ :NADH and hAIFmt $_{\Delta 1-77}$ :NADH CTCs has an important impact on the overall protein unfolding mechanism and on the thermal stability. A two-state unfolding process is indicated by the hAIF $_{\Delta 1-101}$ :NADH denaturation curves, with  $T_m$  for CTC unfold ( $T_{mCTC}$ ) ~7 °C lower than  $T_{m1}$  and up to 13 °C lower than  $T_{m2}$  (**Table 4.2**). However, a three-state process describes hAIFmt $_{\Delta 1-77rd}$ :NAD<sup>+</sup> CTC unfolding, with loss of tertiary interactions while retaining secondary structure and flavin binding. Thus, collectively, coenzyme binding and flavin reduction have a deleterious effect on the stability of N and, particularly, I state, favouring FAD release and unfolded conformers formation. Noticeably, the CTC unfolding enthalpy ( $\Delta H_{CTC}$ ) of hAIF $_{\Delta 1-101}$  approximates the sum of  $\Delta H_1$  and  $\Delta H_2$  at pH 7.0 and 7.4, whereas at pH 8.0,  $\Delta H_{CTC}$  is lower than that at other pHs and the overall hAIF $_{\Delta 1-101}$  unfolding value. To gain insight about the lower CTC stability relative to hAIF $_{\Delta 1-101}$ , we built structural models containing the missing C-loop residues in their X-ray structures (Ferreira et al., 2014). Models were minimised and relaxed by short molecular dynamics (MD) simulations (**Figures 4.7, 4.8 and 4.9**).

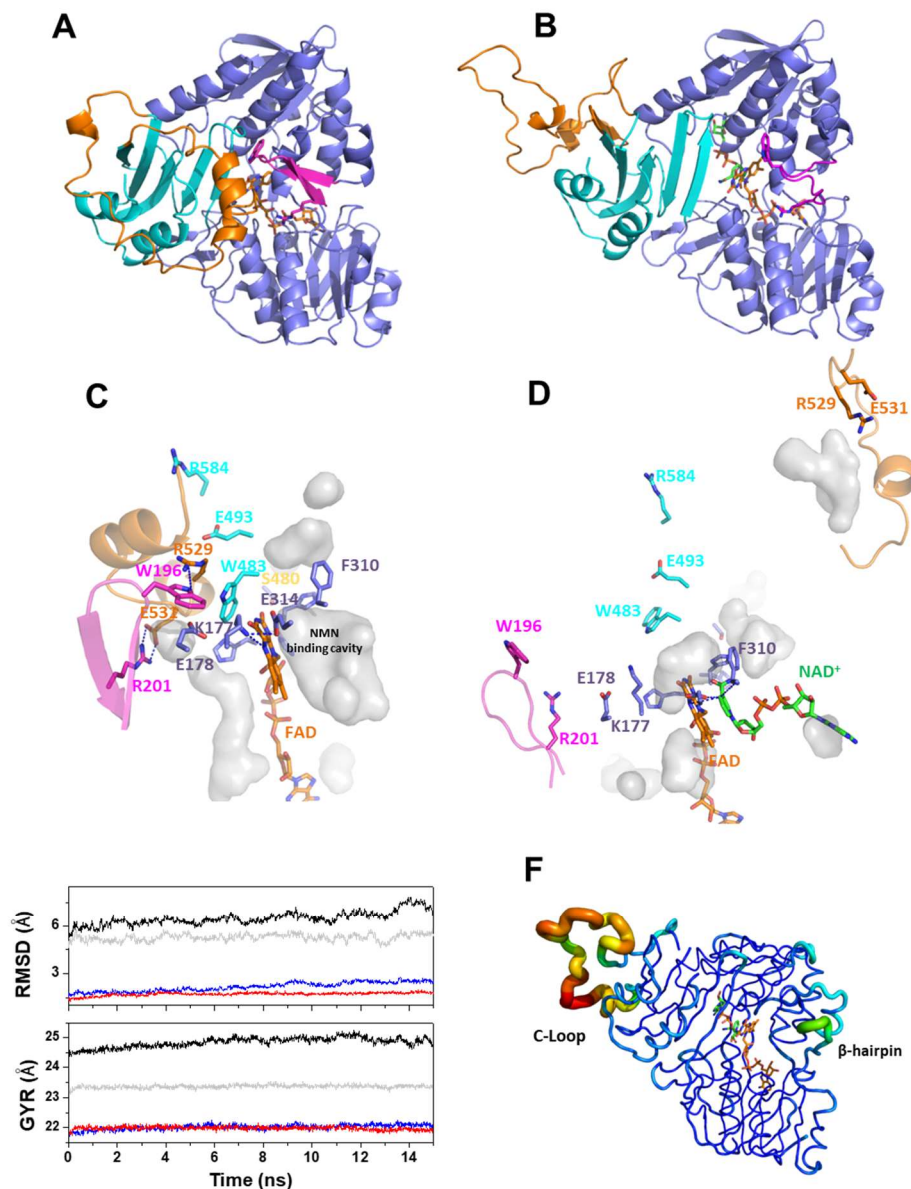


**Figure 4.7: Conformation of hAIF $\Delta_{1-101ox}$  and its CTC.** Final snapshots of representative structural models for (A) WT hAIF $\Delta_{1-101}$  and for (B) its CTC after modelling the missing C-loop residues (residues 546-558 and residues 518-559, respectively), minimization routine and 15 ns of MD relaxation at 300 K. Protein chain is represented as cartoon with the oxidoreductase domains coloured in violet and its 191-202  $\beta$ -hairpin in hot pink (R201 and W196 side chains shown in sticks), while the apoptotic domain is drawn in light blue with the C-loop (509-560 segment) highlighted in orange. FAD and NAD<sup>+</sup> are shown in sticks with carbons in orange and green respectively. Details of the active site environments in (C) hAIF $\Delta_{1-101}$  and (D) its CTC. Relevant residues are shown in sticks. Relevant interactions in the hAIF $\Delta_{1-101}$  model are shown in blue dashed lines. Grey surfaces show water accessible cavities in the active site environment. (E) RMSD ( $C_{\alpha}$ ) of hAIF $\Delta_{1-101}$  (grey line) and of its CTCs models along representative MD relaxations when overlapped on their corresponding starting models (after modelling of the missing C-loop residues and before minimization). Red and blue lines, respectively, represent the RMSD when considering only overlapping of the 128-508 core residues (388  $C_{\alpha}$  atoms, red line). (F) RMSF of backbone atoms along a representative MD of the WT CTC model. This figure shows that higher values for the black line in panel G are due mainly to the higher fluctuation in the position of the C-loop in the CTC. (G) Radius of gyration of hAIF $\Delta_{1-101}$  and of its CTC models along the MD production, colour codes as in (E).

**Table 4.2:** Effect of pH on the thermal stability of Wild Type hAIF<sub>Δ1-101</sub>, hAIFmt<sub>Δ1-77</sub>, and of their Charge Transfer Complexes.

pH	hAIF <sub>Δ1-101</sub>				CTC (hAIF <sub>Δ1-101</sub> :NAD <sup>+</sup> )				T <sub>mCTC</sub> - T <sub>m1</sub>	T <sub>mCTC</sub> - T <sub>m2</sub>
	T <sub>m1</sub>	T <sub>m2</sub>	ΔH <sub>1</sub>	ΔH <sub>2</sub>	T <sub>mCTC</sub>	ΔH <sub>CTC</sub>				
	(K)	(K)	(kcal/mol)	(kcal/mol)	(K)	(kcal/mol)				
8.0	332±1	337±1	87±6	140±10	324±1	120±10	-8±2	-13±2		
7.4	334±2	336±1	52±8	110±10	327±1	180±10	-7±2	-10±2		
7.0	337±1	338±1	46±3	110±10	327±1	180±10	-7±2	-11±2		

	hAIFmt <sub>Δ1-77</sub>						CTC (hAIFmt <sub>Δ1-77</sub> :NAD <sup>+</sup> )				T <sub>mCTC</sub> - T <sub>m1</sub>	T <sub>mCTC</sub> - T <sub>m2</sub>
	T <sub>m0</sub>	T <sub>m1</sub>	T <sub>m2</sub>	ΔH <sub>0</sub>	ΔH <sub>1</sub>	ΔH <sub>2</sub>	T <sub>m0CTC</sub>	T <sub>mCTC</sub>	ΔH <sub>0CTC</sub>	ΔH <sub>1CTC</sub>		
	(K)	(K)	(K)	(kcal/mol)	(kcal/mol)	(kcal/mol)	(K)	(K)	(kcal/mol)	(kcal/mol)		
6.2	318±1	328±3	343±4	69±4	41±3	150±20	322±2	329±2	160±20	150±30	1±5	-13±4

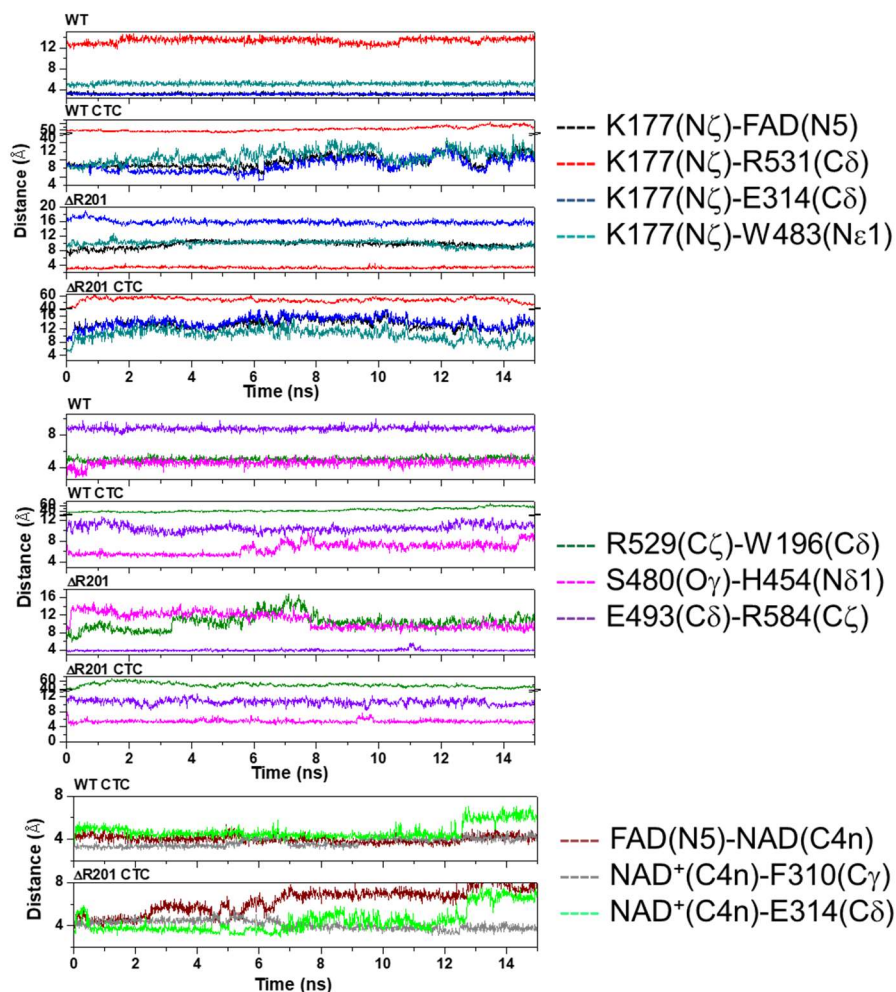


**Figure 4.8: Dynamics of relaxation of models of hAIF $\Delta 1-101$  variants.** Time evolution of selected distances along representative relaxation MD simulations of models for WT hAIF $\Delta 1-101$ , the  $\Delta R201$  variant and their corresponding CTC complexes.

Overlapping of hAIF $\Delta 1-101$  and CTC models along MD relaxation on starting models showed similar RMSD (C $\alpha$ ) values (**Figure 4.7 E**), with the slightly higher CTC value contributed by C-loop disorder and larger flexibility (**Figure 4.7 F**). Evolution of RMSDs for the core protein suggests that, with C-loop exception, both protein forms maintain the fold at 298 K as well as the active site architectures (**Figure 4.8**). The CTC structure shows larger radius of gyration, a decrease in the H-bonds network, and slight increases in molecular and solvent accessible surface areas (**Figures 4.7 G and 4.9**). This agrees with R201- E531 and W196-R529 interactions clapping the C-loop to the 196-201  $\beta$ -hairpin in hAIF $\Delta 1-101$  and contributing to 529-533 residues folding into an  $\alpha$ -helix. Contrarily, in the CTC this region

contributes to the C-loop disorder, making this ensemble less compact than the oxidised form and pointing out to this fact as the main reason for its lower stability.

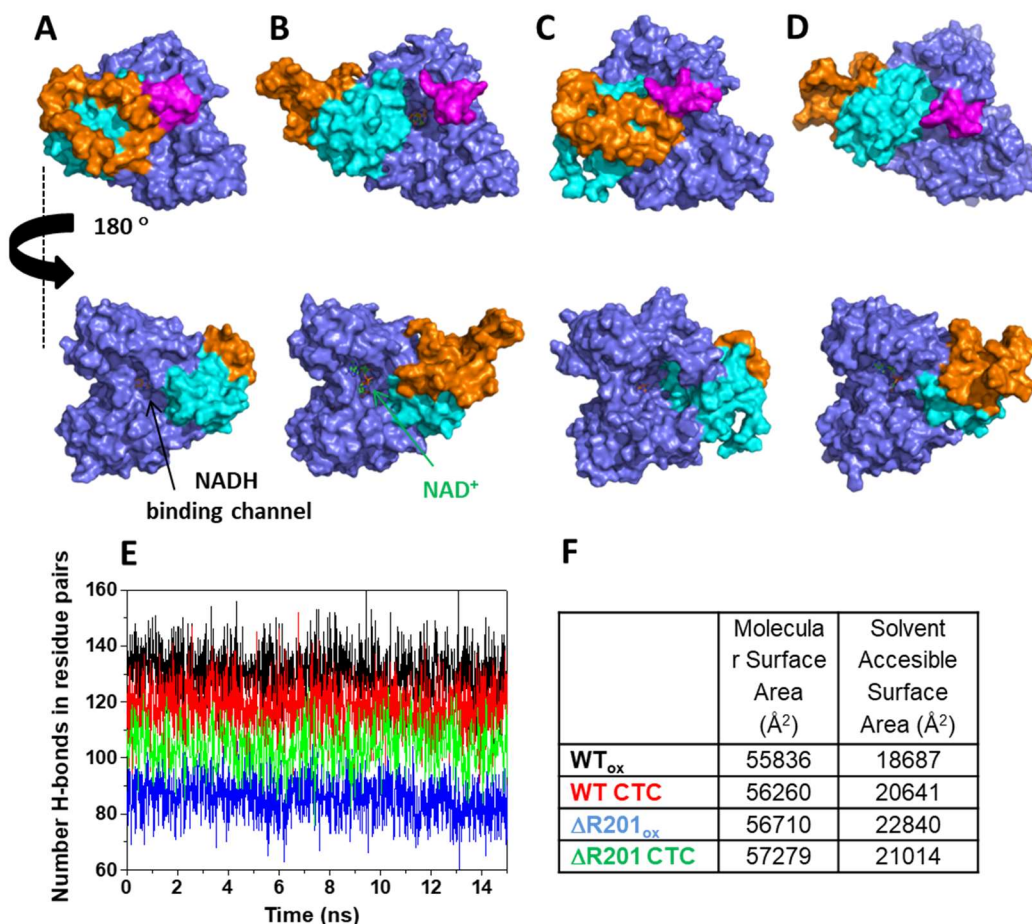


**Figure 4.9: Conformational changes in hAIF $\Delta_{1-101}$  induced by CTC formation and R201 deletion.** Surface representation of the representative model structures of (A) hAIF $\Delta_{1-101}$ , (B) CTC, (C)  $\Delta$ R201 hAIF $\Delta_{1-101}$  and (D)  $\Delta$ R201 CTC after modelling of the missing C-loop residues (546-558), minimization, equilibration at 300 K and short MD relaxation (15 ns) at 300K. The oxidoreductase domain surface is coloured in violet with its  $\beta$ -hairpin in pink, while the apoptotic domain surface is coloured in light blue with the C-loop segment in orange. The FAD and NAD<sup>+</sup> are shown in sticks with carbons in orange and green respectively. (E) Number of H-bonds along the MD simulation production for the different AIF forms. Colour code as in F. (F) Summary of Molecular and Solvent Surface Area at the end of representative MDs relaxations for each hAIF form.

#### 4.5.3 SOME ALLELIC PATHOGENIC MUTATIONS ALTER hAIF $\Delta_{1-101}$ STABILITY

We also evaluated the impact of missense  $\Delta$ R201, G308E, and E493V mutations on protein-FAD interaction integrity and hAIF $\Delta_{1-101}$  stability (Figures 4.7 and 4.10 A-C). G308E and E493V mutations produce modest spectral perturbations (Figures 4.10 and 4.11), as expected from low impact in their crystal structures (Sevrioukova 2016, Rinaldi et al. 2012, Sorrentino et al. 2015, Sorrentino et al. 2017). Nonetheless, small changes in shape and position of 380-400 nm features in their CTC Vis-CD, as well as a slightly lower



quenching of flavin fluorescence in the G308E CTC are noticed (**Figures 4.10 H and 4.11 D**).

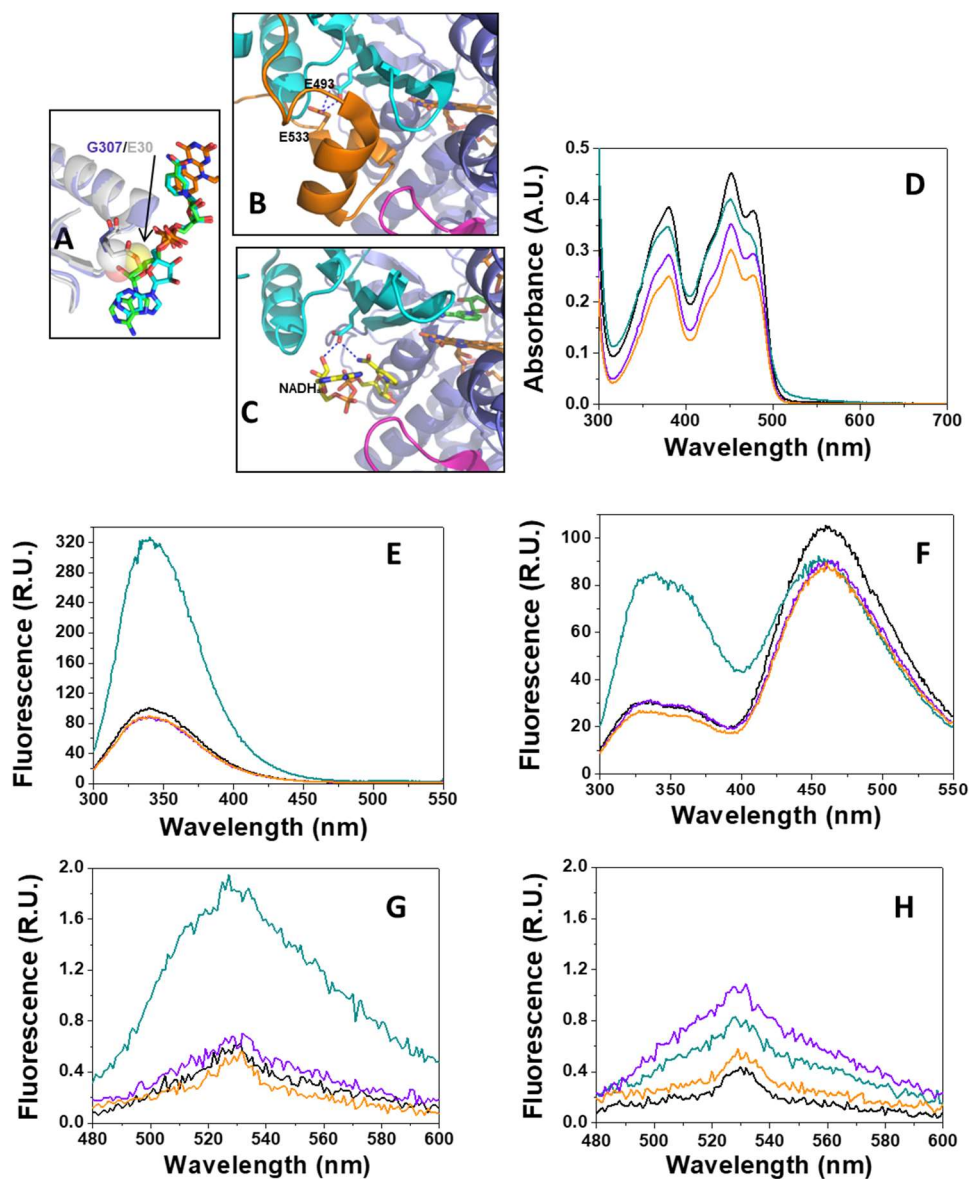


**Figure 4.10: The  $\Delta$ R201, G308E, and E493V hAIF $\Delta$ 1-101 variants.** (A) The G308E substitution alters the NAD<sup>+</sup> ribose conformation in the CTC. The Figure shows the equivalent position environment, G307, in the murine WT CTC structure (PDB 3GD4) in violet with the NAD<sup>+</sup> in green sticks, and in the murine G307E CTC mutant structure in white and with the coenzyme in blue (PDB 5MIV). Spheres show how the introduced Glu side chain uses the place of the coenzyme ribose. (B) E493 in hAIF $\Delta$ 1-101 (PDB 4BV6) H-bonds E533 stabilising the position of the C-loop short helices. (C) In the WT CTC structure (PDB 4BUR), E493 contributes to stabilise the coenzyme molecule that replaces the C-loop short helices. Colour code as in Figure 4.1.7. (D) UV-Visible spectra of WT (33  $\mu$ M),  $\Delta$ R201 (33  $\mu$ M), G308E (26  $\mu$ M) and E493V (22  $\mu$ M) hAIF $\Delta$ 1-101 variants. (E) Fluorescence emission spectra in the aromatic residues region of WT,  $\Delta$ R201, G308E, and E493V hAIF $\Delta$ 1-101 variants (2  $\mu$ M) recorded at 10  $^{\circ}$ C with excitation wavelength of 280 nm. (F) Fluorescence emission spectra in the aromatic residues region of hAIF $\Delta$ 1-101 variants (2  $\mu$ M) in the presence of 200  $\mu$ M NADH recorded at 10  $^{\circ}$ C with excitation wavelength of 280 nm. (G) Fluorescence emission spectra in the flavin region of hAIF $\Delta$ 1-101 variants (2  $\mu$ M) recorded at 10  $^{\circ}$ C with excitation wavelength of 450 nm. (H) Fluorescence emission spectra in the flavin region of hAIF $\Delta$ 1-101 (2  $\mu$ M) in the presence of 200  $\mu$ M NADH recorded at 10  $^{\circ}$ C with excitation wavelength of 450 nm. All measurements were done in 50 mM Kpi, pH 8.0, at a final ionic strength of 150 mM.

In contrast, the R201 deletion clearly alters the protein spectroscopic properties: it modifies the flavin band I (**Figure 4.10 D**), increases the fluorescence quantum yield of at least one tryptophan (**Figure 4.10 E**), attenuates FAD fluorescence quenching (**Figure 4.10 F**), and modifies shape and intensity of the near-UV (300 nm peak) and Vis (450 nm band) CD signals (**Figure 4.10 C**).

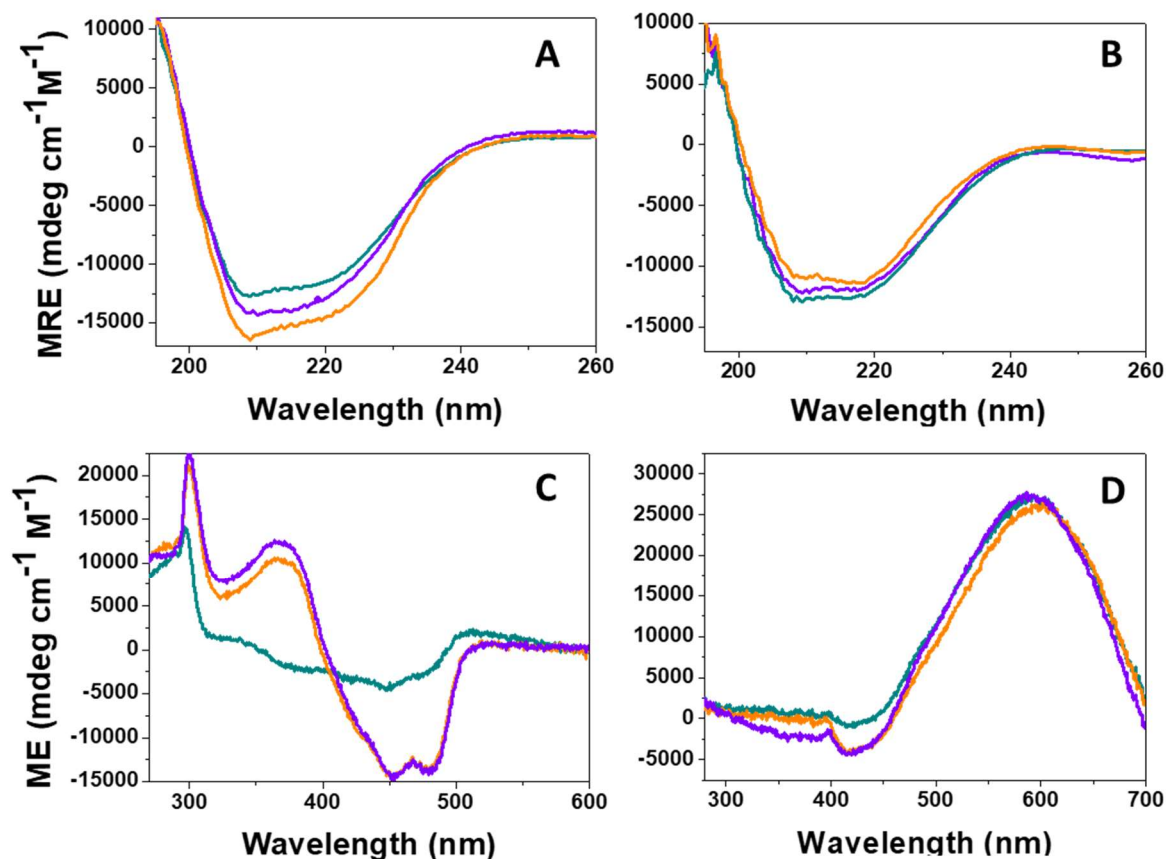


**Figure 4.11: Circular dichroism spectra of  $\Delta$ R201, G308E, and E493V hAIF $_{\Delta 1-101}$  variants.** Far-UV CD spectra of samples containing (A) 1  $\mu$ M hAIF $_{\Delta 1-101}$  and (B) a mixture of 1  $\mu$ M hAIF $_{\Delta 1-101}$  with 100  $\mu$ M NADH for  $\Delta$ R201 (dark cyan line), G308E (violet line), and E493V (orange line) variants. Near-UV-Vis CD spectra of samples containing (C) 20  $\mu$ M hAIF $_{\Delta 1-101}$  and (D) a mixture of 20  $\mu$ M hAIF $_{\Delta 1-101}$  with 2 mM NADH for  $\Delta$ R201 (dark cyan line), G308E (violet line), and E493V (orange line) variants. Spectra were recorded at 25 °C in 50 mM Kpi pH 8.0 at a final ionic strength of 150 mM.

These observations are consistent with the mutation perturbing protein folding and FAD incorporation (Ghezzi et al., 2010, Rinaldi et al., 2012). Noticeably,  $\Delta$ R201 CTC increases FAD fluorescence quenching when compared to  $\Delta$ R201 hAIF $_{\Delta 1-101}$  (**Figure 4.10 H**).

These mutations have a negative impact in thermal stability when compared to WT (**Figures 4.12, 4.13 and Table 4.3**), particularly evident in  $\Delta$ R201 ( $\Delta T_{m1} = -27.7$  °C and  $\Delta T_{m2} = -24.8$  °C). R201 ablation also modifies the unfolding events, so that the FAD cofactor, is released in the first transition (N $\rightarrow$ I) (**Figures 4.12 A and 4.13 A**).



Therefore,  $T_m$  for flavin isoalloxazine release ( $T_{mFAD}$ ) decreases by  $\sim 33^\circ\text{C}$  in  $\Delta R201$  hAIF $_{\Delta 1-101}$  compared to WT, indicating particular destabilisation of the redox active centre. To test the structural impact of this mutation on the multiple protein functional sites, we have produced a  $\Delta R201$  hAIF $_{\Delta 1-101}$  structural homology model.

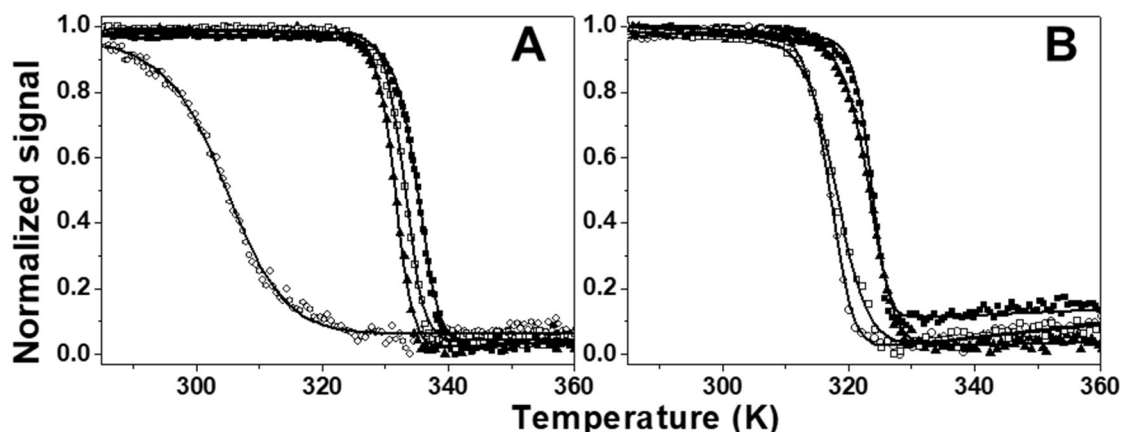


**Figure 4.12: Effect of  $\Delta R201A$ , G308E and E493V hAIF $_{\Delta 1-101}$  pathogenic mutations on the temperature for FAD release.** Curves for FAD thermal release in (A) hAIF $_{\Delta 1-101}$  and (B) its CTC (1:100 hAIF $_{\Delta 1-101}$ :NADH ratio) for WT (black squares),  $\Delta R201$  (open circles), G308E (black triangles), and E493V (open squares), as monitored by flavin fluorescence emission. The curves are shown roughly normalised from 0 to 1, and the fit to a two-state unfolding model is represented by the continuous lines. Data were obtained in 50 mM Kpi, pH 8.0, at a final ionic strength of 150 mM. Protein concentration was  $\sim 2\ \mu\text{M}$ .

Our equilibration routine courses with an overall structure relaxation that was not observed in the WT case, whereas the organization of this structure is maintained in the MD runs to optimise the system (Figures 4.14, 4.8 and 4.9). Thus, this  $\Delta R201$  model predicts important structural and dynamic rearrangements at the oxidoreductase domain, in agreement with R201 defining the  $\beta$ -hairpin length and interactions. These rearrangements alter the network that links the FAD cofactor, the active site residues, the central  $\beta$ -strand, the apoptotic domain, the C-loop, and the  $\beta$ -hairpin itself (Figures 4.8 and 4.9). Increases in radius of gyration, size and number of protein internal cavities, and molecular and solvent accessible surface areas are also predicted (Figures 4.14 and 4.8 F), as well as a considerable reduction in the number of internal H-bonds (Figure 4.14 E). Such facts agree with increased susceptibility to proteolytic cleavage and partial FAD loss (Ghezzi et al., 2010). Therefore, lack of R201 is expected to prevent the b-hairpin-C-loop interaction, to destabilise the 529-533 helix and to release R529 from its stacking to W196. As a consequence, FAD binding debilitates (Figure 4.14 G), and the active site and C-terminal loop of the oxidoreductase domain lose compactness. Such hypothesis agrees with  $\Delta R201$  unfolding data relative to the WT (earlier flavin release, lower conformational

stability and unfolding enthalpies, and less structured active site). The effects of G308E and E493V mutations on denaturation profiles and on  $T_m$  values are milder (3-5 °C decreases) (Table 4.3 and Figure 4.13 B, C).

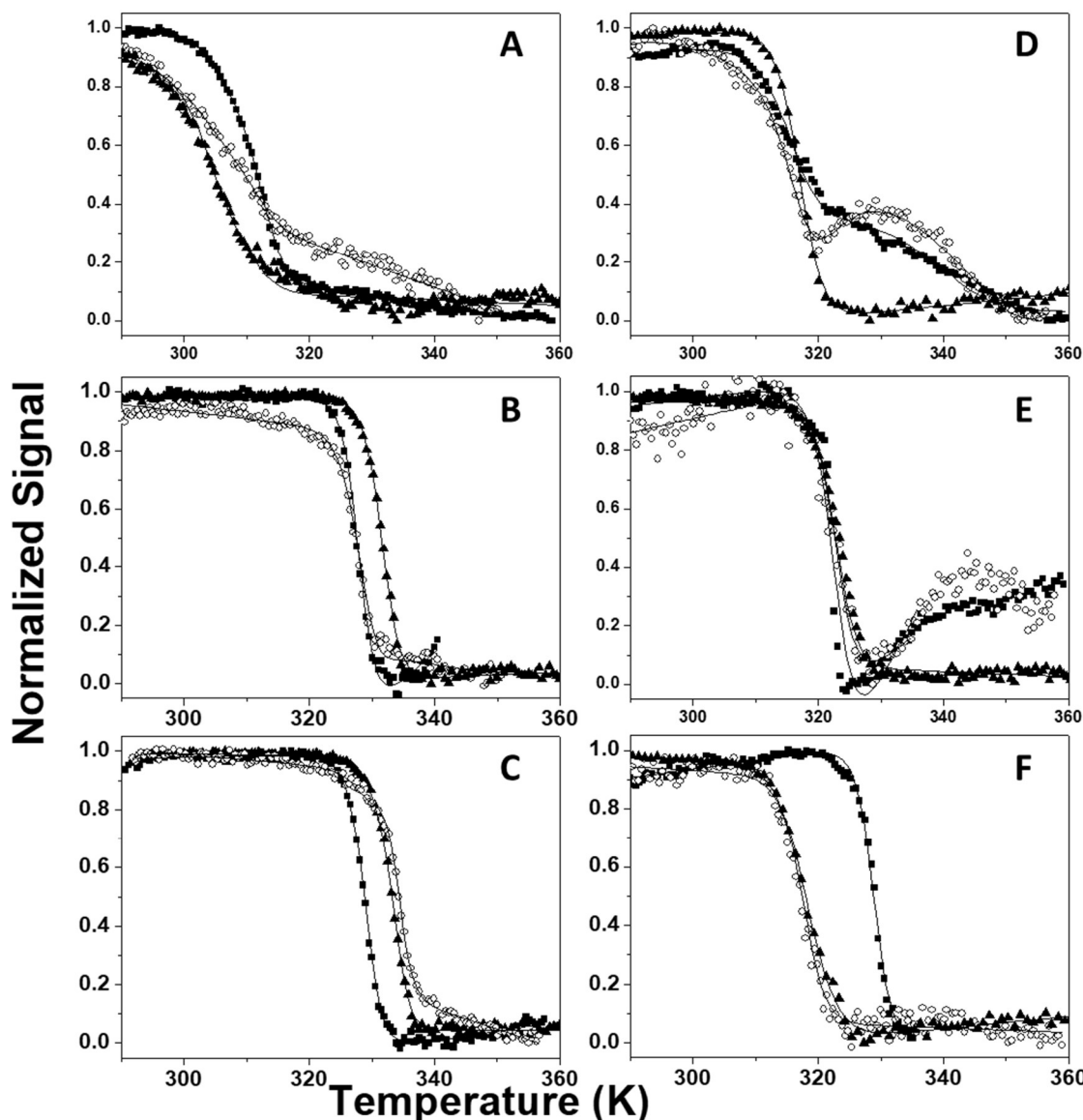


**Figure 4.13:** Unfolding properties of hAIF $_{\Delta 1-101}$  variants. Thermal unfolding curves for (A)  $\Delta R201$ , (B) G308E and (C) E493V hAIF $_{\Delta 1-101ox}$  and for (D, E, F) their corresponding CTC (1:100 hAIF:NADH ratio). Thermal denaturation was monitored by far-UV CD (210 nm, white circles), near-UV CD (300 nm in (A, B, C), black squares) and Vis CD (410 nm in (D, E, F), black squares), and flavin fluorescence emission (black triangles). The curves are shown roughly normalised from 0 to 1, and their global fits to three-state unfolding models are represented by the continuous lines. Curves were recorded in 50 mM Kpi, pH 8.0, at a final ionic strength of 150 mM.

Nevertheless, an increasing contribution of the secondary structure of G308E to the N/I transition suggests that in this variant the isoalloxazine environment might be the region that unfolds the last (Figure 4.13 B).

All, but particularly  $\Delta$ R201 and E493V CTCs, are less stable than the WT CTC (**Table 4.3, Figure 4.13 D-F**). Formation of G308E and E493V CTCs decrease protein stability, and E493V Vis-CD data also suggests aggregation upon thermal denaturation. On the contrary, although the  $\Delta$ R201 CTC is still considerably less stable than the WT CTC, thermal stabilisation is observed when compared to its oxidised state, with some secondary and tertiary structures remaining after flavin release (**Figure 4.13 B**).

Thus, NADH binding and flavin reduction favour the  $\Delta$ R201 folded state. This suggests that the presence of  $\text{NAD}^+$  makes the active site more compact, stabilising the overall structure and, particularly, the FAD site. In agreement, our predicted structural  $\Delta$ R201 CTC model was considerably more compact than that for the oxidised form (**Figures 4.14, 4.8 and 4.9**). Thus, the CTC shifts the  $\Delta$ R201 conformational equilibrium to a more structured ensemble than that of the oxidised state of this allelic variant.

**Table 4.3:** Effect of the  $\Delta R201$ , G308E and E493V hAIF $_{\Delta 1-101}$  mutations on the thermal stability of hAIF $_{\Delta 1-101ox}$  and of its CTC.

	hAIF $_{\Delta 1-101}$				CTC (hAIF $_{\Delta 1-101}$ :NAD <sup>+</sup> )					
	T <sub>m1</sub> (K)	T <sub>m2</sub> (K)	$\Delta H_1$ (kcal/mol)	$\Delta H_2$ (kcal/mol)	T <sub>m1CTC</sub> (K)	T <sub>m2CTC</sub> (K)	$\Delta H_{1CTC}$ (kcal/mol)	$\Delta H_{2CTC}$ (kcal/mol)	T <sub>m1CTC</sub> - T <sub>m1</sub>	T <sub>m1CTC</sub> - T <sub>m2</sub>
<b>WT</b>	332±1	337 ± 1	87 ± 6	140 ± 10	324±1		120±10		-8±2	-13±2
<b><math>\Delta R201</math></b>	304±1 <sup>a</sup>	312 ± 1	64 ± 9 <sup>a</sup>	98 ± 9	316±1	338±1	93±8	37±6	12±2	4±2
<b>G308E</b>	328±1	332±1 <sup>a</sup>	130±10	160±20 <sup>a</sup>	323±1		140±10		-5±2	-9±2
<b>E493V</b>	329±1	334±1	150±10	180±10	318±1 <sup>b</sup>		85±4		-11±2	-16±2

<sup>a</sup>Data revealed by the FAD fluorescence denaturation curve.

<sup>b</sup>Data revealed by the far-UV and FAD fluorescence denaturation curves. Denaturation curve in the Vis at 420 nm shows a T<sub>m</sub> of 329 ± 1 and  $\Delta H$  of 150 ± 10.

Data were obtained by global fitting of the near-CD, far-UV CD and fluorescence thermal denaturation curves to two or three species unfolding mechanisms. Data were obtained in 50 mM Kpi, pH 8.0, at a final ionic strength of 150 mM, from 283.15 to 363.15 K. Protein concentrations were ~1  $\mu$ M, ~2  $\mu$ M, and ~20  $\mu$ M for far-UV CD, fluorescence and near-UV CD respectively

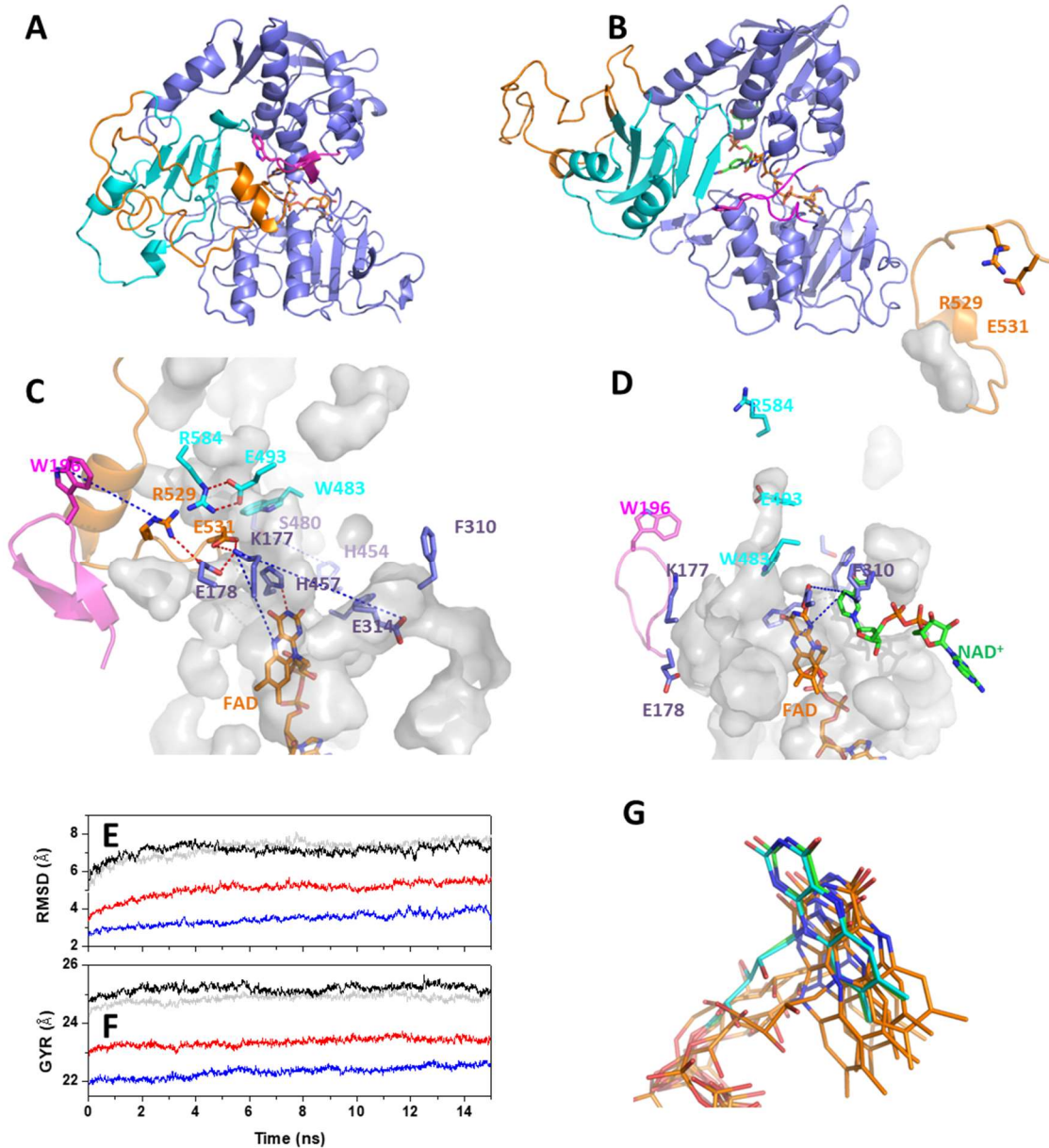


**Figure 4.14: Predicted hAIF $\Delta_{1-101}$  conformational changes by R201 deletion.** Overall representative structural models for (A)  $\Delta$ R201 hAIF $\Delta_{1-101}$  and (B) its CTC after modelling of the missing C-loop residues and deletion of R201, minimization, and 15 ns of MD relaxation at 300 K. Protein chain is represented as cartoon with the oxidoreductase domains in violet and its 191-202  $\beta$ -hairpin in hot pink (R201 and W196 side chains shown in sticks), and the apoptotic domain in light blue with the C-loop (509-560 segment) in orange. FAD is shown in sticks with orange carbons. Active site environment in (C)  $\Delta$ R201 hAIF $\Delta_{1-101}$  and (D) its CTC. Relevant residues are shown in sticks. Blue dashed lines show interactions that were relevant to maintain the active site conformation in WT (Figure 4.7) but that show a considerable increase in the  $\Delta$ R201 model. Red dashed lines show interactions appearing in  $\Delta$ R201 but not in the WT. Grey surfaces show water accessible cavities in the active site environment. (E) RMSD (Ca) of  $\Delta$ R201 hAIF $\Delta_{1-101}$  (grey line) and its CTCs (black line) models along MD when overlapped on their corresponding modelled structures before minimization. Red and blue lines, respectively, represent the RMSD when considering only overlapping of the 128-508 core residues (388 C atoms). (F) Radius of gyration of  $\Delta$ R201 hAIF $\Delta_{1-101}$  and its CTCs along the MD. Colours as in (E). (G) Position of FAD (C in orange) in five replicas after applying the minimization routine to the  $\Delta$ R201 hAIF $\Delta_{1-101}$  homology model, relative to the FAD position in the initial homology modelling (FAD with C in green) and in the template (4BV6, C in blue).

Finally, the  $\Delta R201$  variant also decreases unfolding enthalpy relative to the WT, also consistent with the mutant being less structured. On the contrary, the higher unfolding enthalpies of G308E and E493V hAIF $_{\Delta 1-101}$ , and G308E CTC might relate to them being more prone to aggregate upon unfolding. The decreased E493V CTC enthalpy suggests that this form might be less structured, in agreement with its also modestly lower  $T_{mCTC}$ .

#### 4.5.4 HTS ALLOWED THE IDENTIFICATION OF MOLECULES POTENTIALLY BINDING hAIF $_{\Delta 1-101}$

Since fluorescence changes along thermal denaturation allow evaluating hAIF $_{\Delta 1-101}$  stability, displacements in  $T_{mFAD}$  induced by different molecules appear a feasible approach to identify ligands in HTS plate assays (Cremades et al., 2009). We used NADH (the hAIF coenzyme), the NAD $^+$  product, and ATA (described to interact with hAIF (Chan et al., 2008)) as controls to optimise the method. In agreement with previous sections, incubation of hAIF $_{\Delta 1-101}$  in a well plate with NADH excess diminishes  $T_{mFAD}$  by 14 °C  $\pm$  0.5 °C ( $\Delta T_{mFAD}$ ) (Figure 4.15 A).

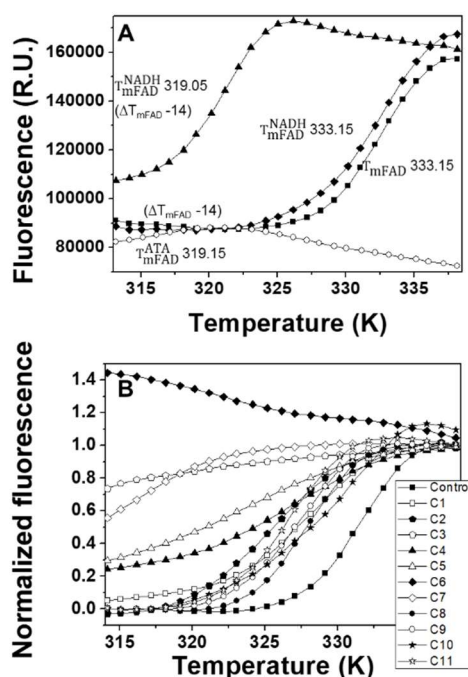


**Figure 4.15: Effect of binders on the thermal stability of hAIF $_{\Delta 1-101}$ .** (A) FAD fluorescence unfolding curves in samples containing hAIF $_{\Delta 1-101OX}$  in the absence of ligands (■), and in the presence of 100  $\mu$ M NADH (▲), 100  $\mu$ M NAD $^+$  (◆), and 500  $\mu$ M ATA (○). (B) FAD fluorescence unfolding curves in samples containing each of the 11 compounds selected by HTS as potential hAIF $_{\Delta 1-101}$  binders. hAIF $_{\Delta 1-101OX}$  samples incubated with 500  $\mu$ M of C1, C2, C3, C4, or C5, or with 100  $\mu$ M of C6, C7, C8, C9, C10, or C11 respectively, showed shifts in  $T_{mFAD}$  of  $-3.0 \pm 0.6$ ,  $-5.0 \pm 0.1$ ,  $-20 \pm 1$ ,  $-3.0 \pm 0.6$ ,  $-5.0 \pm 0.1$ ,  $-23 \pm 3$ ,  $-14 \pm 1$ ,  $-5.0 \pm 0.1$ ,  $-5.0 \pm 0.6$ ,  $-6.0 \pm 0.3$ , and  $-6.0 \pm 0.1$  °C respectively. In all cases, 1  $\mu$ M hAIF $_{\Delta 1-101}$  was placed on each well of 96-well plates together with the ligands, and the changes in fluorescence emission at 530 nm (excitation at 450 nm) were followed during an increasing temperature ramp. Figure shows roughly normalised flavin fluorescence. The experiments were carried out in 50 mM Kpi, pH 8.0.

No dose-dependent response curve is observed, possibly because of formation of (i) the CTC and (ii) the monomer-dimer transition. Incubation with  $\text{NAD}^+$  has no effect on  $T_{\text{mFAD}}$ , consistent with its low affinity for  $\text{hAIF}_{\text{ox}}$  (Ferreira et al., 2014). ATA decreases  $T_{\text{mFAD}}$  similarly to NADH, induces quenching of flavin fluorescence, and produces a dose-response curve (Figure 4.16) that allows estimating a  $K_d^{\text{ATA}}$  of  $10 \pm 4 \mu\text{M}$  (in the range of that reported by isothermal titration calorimetry (ITC),  $19 \pm 5 \mu\text{M}$  (Chan et al., 2008).

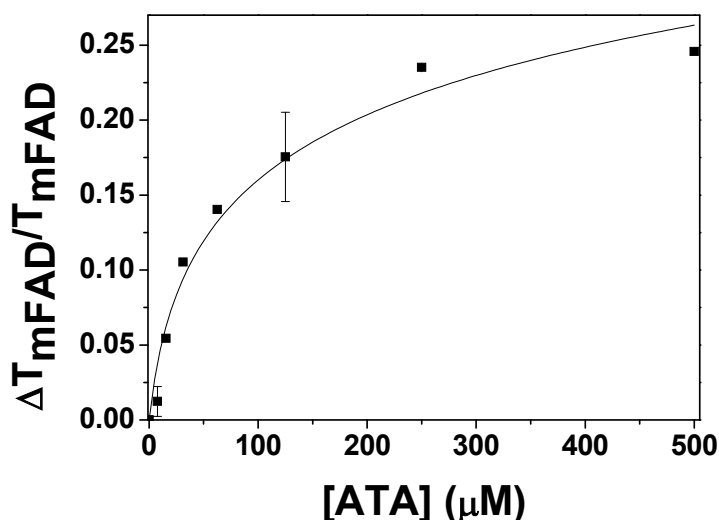


**Figure 4.16: Interaction of  $\text{hAIF}_{\Delta 1-101}$  with ATA.** Dose-response curve for the dependence of the WT  $\text{AIF}_{\Delta 1-101\text{ox}}$   $T_{\text{mFAD}}$  on the ATA concentration.  $1 \mu\text{M}$   $\text{hAIF}_{\Delta 1-101\text{ox}}$  was mixed with increasing concentrations of ATA in 96-well plates. Experiments were done by triplicate. The ATA dissociation constant,  $K_d^{\text{ATA}}$ , was determined by fitting the data to the equation (Cooper and McAuley-Hecht, 1993)  $\frac{\Delta T_{\text{mFAD}}}{T_{\text{mFAD}}} = \frac{nRT_{\text{mFAD}}^0}{\Delta H_0} \ln \left( 1 + \frac{[\text{ATA}]}{K_d^{\text{ATA}}} \right)$  where  $\Delta T_{\text{mFAD}}$  estimates the extent of the ATA-induced protein destabilization ( $\Delta T_{\text{mFAD}} = T_{\text{mFAD}}^0 - T_{\text{mFAD}}$ ); with  $T_{\text{mFAD}}^0$  and  $T_{\text{mFAD}}$  being the midpoint denaturation temperatures in the absence and the presence of ligand, respectively, and  $\Delta H_0$  is the unfolding enthalpy of the protein in the absence of ATA. And  $n$  is the number of ligand molecules bound per  $\text{hAIF}$  molecule.

Therefore, NADH and ATA produce a ligand-induced perturbation consistent with binding and  $\text{hAIF}_{\Delta 1-101}$  destabilisation (Figure 4.15 A). Based on these results, we performed a screening of compounds potentially binding  $\text{hAIF}_{\Delta 1-101}$  using the HitFinder Collection (Maybridge) and the Prestwick Chemical Library (Prestwick Chemical).

Our assessment method identifies as hits those compounds that shift the  $T_{\text{mFAD}}$  more than  $3^\circ\text{C}$  in the same direction by both “midpoint of unfolding” and “inflection point location” methods (Velazquez-Campoy et al., 2016, Cremades et al., 2009). Most of the assayed compounds do not alter  $T_{\text{mFAD}}$ , a few compounds increase it by one evaluation method, and a few more compounds shift it to lower values (Figure 4.17).

We did not find any compound increasing  $T_{mFAD}$  more than 3 °C by both evaluation methods. However, we identified 11 compounds (C1 to C11) shifting  $T_{mFAD}$  between -3 °C and -23 °C by both methods (**Figure 4.15 B and table 4.4**), which might be postulated as hAIF binders. However, other phenomena, such as protein chemical denaturation or aggregation, might be implicated in  $T_{mFAD}$  shifts. Six compounds (C1, C2, C5, C8, C9, and C11) out of the 11 produce a dose-response  $\Delta T_{mFAD}$  indicative of binding, postulating an affinity ranking  $C8 \approx C11 \approx C5 \approx C9 > C1 >>> C2$  ( $K_d$  values in the 3-200  $\mu$ M range).

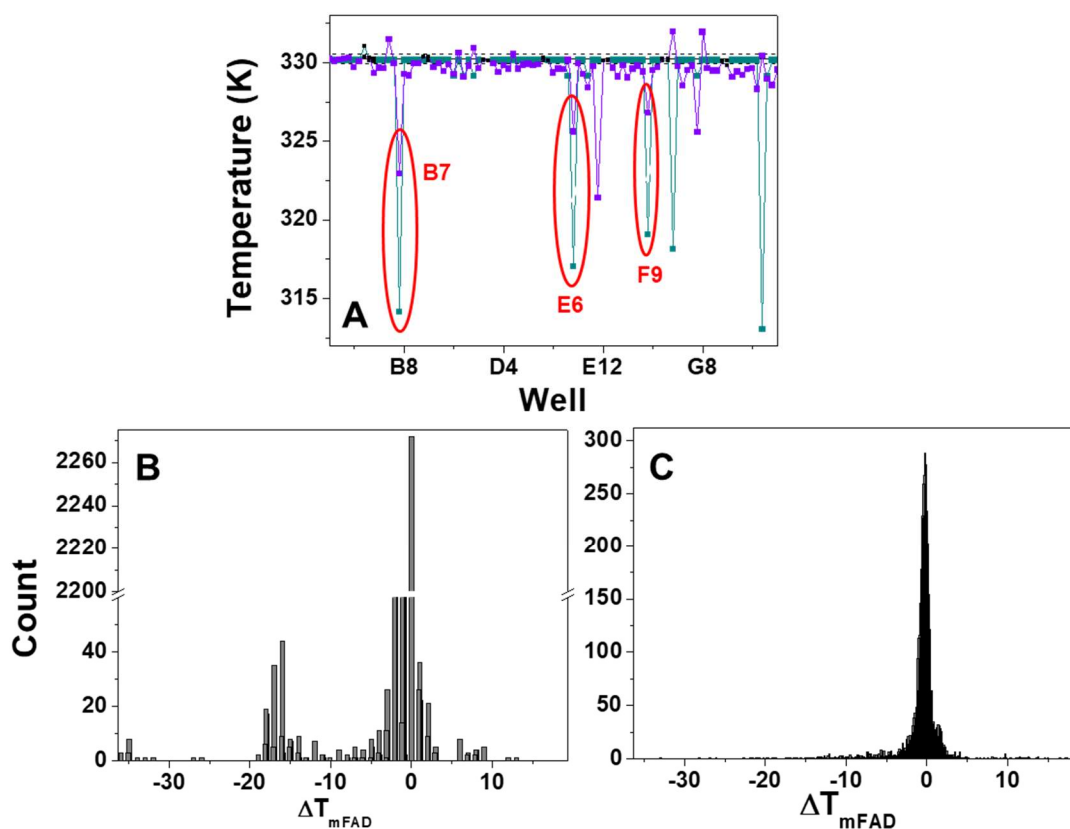


**Figure 4.17: Thermo FAD HTS screening for compounds binding hAIF $_{\Delta 1-101}$ .** (A) Compound-induced decrease in  $T_{mFAD}$  for hAIF $_{\Delta 1-101ox}$  thermal FAD release upon unfolding as detected in a typical assay in a single 96-well plate. Black squares represent  $T_{mFAD}$  values for wells at columns 1 and 12 on each plate, which were used for controls in the absence of compound.  $T_{mFAD}$  values for controls are indicated as a continuous black line, while corresponding SD values are shown as dashed black lines. For samples containing compounds, violet and cyan squares represent  $T_{mFAD}$  values calculated using respectively the midpoint method and the inflection point analysis. Wells identified as containing potential hits by both methods are marked with a red circle. Experiments were performed in 50 mM Kpi, pH 8.0, with 1  $\mu$ M hAIF $_{\Delta 1-101}$ , 100 or 500  $\mu$ M of the compound and 2.5 to 12.5 % DMSO. (B) and (C) show the  $\Delta T_{mFAD}$  histograms of all 11424 compounds calculated using the inflection point analysis method and the midpoint analysis method, respectively.



**Table 4.4:** Properties of hAIF<sub>Δ1-101</sub> HTS hits. ATA and compounds C1 to C5 were purchased from Sigma (Sigma Aldrich), while compounds C6 to C11 were directly obtained from Maybridge (Maybridge Chemical Company).

C	Complete name	MW	Structure	LogP
<b>ATA</b>	5-[(3-carboxy-4-hydroxyphenyl)-(3-carboxy-4-oxocyclohexa-2,5-dien-1-ylidene)methyl]-2-hydroxybenzoic acid (Aurintricarboxylic acid, ATA)	422.34		3.84
<b>C1</b>	(±)-6-Hydroxy-2,5,7,8-tetramethylchromane-2-carboxylic acid (Trolox)	250.29		3.07
<b>C2</b>	2-[(2,6-Dichloro-3-methylphenyl)amino]benzoic acid sodium salt (Meclofenamic acid)	318.13		5.63
<b>C3</b>	2 (3-Chloro-2-methylanilino)benzoic acid, 2-[(3-Chloro-2-methylphenyl)amino]benzoic acid (Tolfenamic acid)	261.70		5.00
<b>C4</b>	3,3',5-triiodothyroacetic acid 4-(4-Hydroxy-3-iodophenoxy)-3,5-diiodophenylacetic acid (Triaticol)	621.93		5.93
<b>C5</b>	3-(3,5-Dibromo-4-hydroxybenzoyl)-2-ethylbenzofuran (Benzbromarone)	424.08		5.70
<b>C6</b>	3-[3-phenoxy-2-thienyl)methylene]-1,3-dihydro-2H-indol-2-one	319.37		3.21
<b>C7</b>	2-[[2-(4-chlorophenyl)-2-oxoethyl]thio]-6-(dimethoxymethyl)nicotinonitrile	362.83		3.28
<b>C8</b>	N-[2-(4-chloro-3,5-dimethylphenoxy)-5-(trifluoromethyl)phenyl]methanesulphonamide	393.80		4.57

<b>C9</b>	5,8-dioxo-5,8-dihydronaphthalen-1-ylbenzoate	278.25	2.45
<b>C10</b>	2-nitro-4-(trifluoromethyl)phenylvinyl sulphone	281.20	2.62
<b>C11</b>	N1-[[4-(2,4-dichlorobenzyl)-1,4-diazepan-1-yl]carbonyl]-4-methylbenzene-1-sulphonamide	456.38	3.92

#### 4.5.5 EFFECT OF HTS HITS ON CELLULAR VIABILITY

Human HeLa cells were exposed to a range of concentrations of these HTS hits. Results show that C1 (up to 1 mM) has no effect on cell viability. For the rest, we observe sigmoidal decreases in cell viability with increasing concentrations, which allow determining the compound concentration for 50 % cell viability (half maximal effective concentration [EC50]) (**Figure 4.18**).

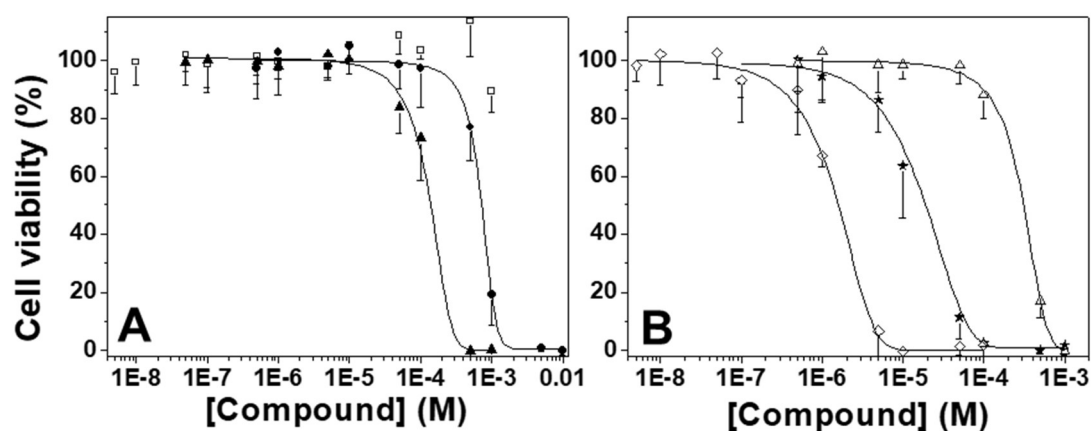


**Figure 4.18: Viability of HeLa cells in the presence of hAIF<sub>Δ1-101</sub> HTS hits.** (A) C1 (□), C2 (●), and C5 (▲). (B) C8 (★), C9 (◇) and C11 (△). HeLa cells were grown for 24 h, then treated with different concentrations of each compound and incubated for another 24 h. Means  $\pm$  SD of at least three independent experiments are shown for each compound at each of the assayed concentrations. Dose-response dependence data were fitted to sigmoidal curves to determine EC50 values.

The toxicity ranges for our HTS hits vary, C9 and C8 being the more toxic (EC50,  $1.3 \pm 0.1$  and  $15 \pm 3$   $\mu$ M respectively), C5 producing an intermediate effect ( $112 \pm 14$   $\mu$ M), and C11 and C2 being the less toxic compounds ( $279 \pm 10$  and  $684 \pm 45$   $\mu$ M, respectively). It is worthy to mention that C9 contains some pan assay interference compound groups and C8 produces

protein precipitation. To evaluate whether binding of HTS hits to hAIF might have a protective effect against AIF-dependent PCD, we also incubated HeLa cells with C1, C2, C5, C8, C9, and C11 for 24 hours, and then added N-methyl-N'-nitrosoguanidine (MNNG), an alkylating agent that provokes AIF-dependent PCD (Capon et al., 2012). Samples containing HTS hits as well as controls without the compounds show 100 % loss of cell viability after 24 hours MNNG treatment. Hence, hits fail to prevent AIF induced PCD.

#### 4.5.6 EFFECTS OF SELECTED HTS HITS ON THE MOLECULAR AND REDOX PROPERTIES OF hAIF<sub>Δ1-101</sub>

Based on the  $\Delta T_{mFAD}$  and cell viability effects, we selected C2 and C11, and included in addition ATA only producing a slight effect on macrophage cell viability after 24 hours (Kuban-Jankowska et al., 2015, Tsi et al., 2002), to comparatively evaluate their influence on the molecular and redox hAIF<sub>Δ1-101</sub> properties. C2 and C11 do not affect the hAIF<sub>Δ1-101ox</sub> visible spectrum, whereas hAIF<sub>Δ1-101</sub> mixing with ATA shows a spectrum combining features of both (**Figure 4.19 A**). hAIF<sub>Δ1-101</sub> far-UV CD spectra suggest no major ATA effects on secondary structure (**Figure 4.19 B**), whereas the spectra with C2 and C11 cannot be recorded due to their low solubility in the absence of dimethyl sulphoxide (DMSO). C2 and particularly ATA induce large changes in the hAIF<sub>Δ1-101</sub> near-UV-vis CD (**Figure 4.19 C**) both preventing detection of the ~300 nm peak (as in the CTC, **Figure 4.3 D**) and ATA also decreasing the flavin signal intensity. ATA also produces noticeable effects on hAIF<sub>Δ1-101ox</sub> fluorescence, dominating the spectrum (broad peak centred at ~440 nm that increases fluorescence yield in the presence of protein) and eliminating tryptophan emission (**Figure 4.19 D**). Such observations indicate quenching of tryptophan fluorescence by energy transfer to ATA. C2 also quenches tryptophan fluorescence, whereas the effect of C11 is milder. Therefore, binding of ATA or C2 affects the environment of one or several tryptophan residues. Finally, ATA slightly increases flavin fluorescence, suggesting an effect on the hAIF<sub>Δ1-101</sub> isoalloxazine environment (**Figure 4.19 E**).

We intended to evaluate affinity of hAIF<sub>Δ1-101</sub> for each of these compounds by ITC and by difference spectroscopy, but the high amounts of ligands required to detect interaction make impossible such determination and indicate low interaction enthalpy. ATA also decreases hAIF<sub>Δ1-101</sub> stability, while C2 and C11 change. In addition, the unfolding mechanism to a two-species mechanism and C2 apparently stabilises some structure after flavin release (**Figure 4.20 A-C and Table 4.5**).

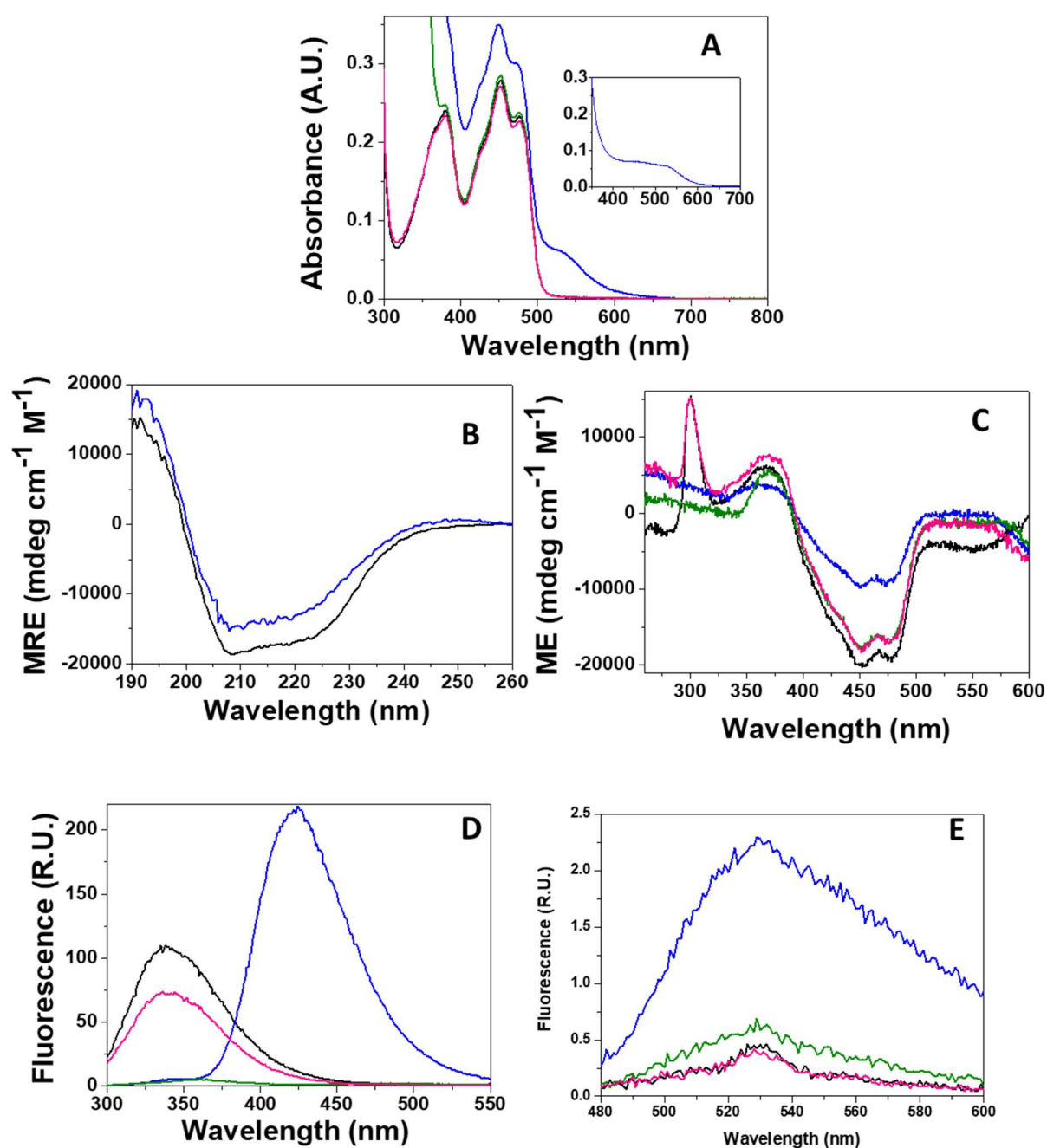


**Figure 4.19: Effect of binders on the spectroscopic properties of hAIF $\Delta$ 1-101.** (A) Visible absorption spectra of hAIF $\Delta$ 1-101 (~20  $\mu$ M) and in mixtures containing ATA (100  $\mu$ M), C2 (500  $\mu$ M), or C11 (100  $\mu$ M). The inset shows the absorbance spectra of ATA (500  $\mu$ M). (B) Far-UV CD spectra of hAIF $\Delta$ 1-101 (1  $\mu$ M) and when containing ATA (500  $\mu$ M). (C) Near-UV CD spectra of hAIF $\Delta$ 1-101 (20  $\mu$ M) and in the presence of ATA, C2, or C11 (all at 500  $\mu$ M). (D) Fluorescence emission spectra in the aromatic residues region of hAIF $\Delta$ 1-101 (2  $\mu$ M) in the presence of ATA, C2, and C11 (all at 500  $\mu$ M). (E) Fluorescence emission spectra in the flavin region of hAIF $\Delta$ 1-101 (2  $\mu$ M) and in the presence of ATA, C2, or C11 (all at 500  $\mu$ M). Spectra were recorded in 50 mM Kpi, pH 8.0, at a final ionic strength of 150 mM. CD spectra were recorded at 25  $^{\circ}$ C. Fluorescence spectra were recorded at 10  $^{\circ}$ C with excitation wavelength at 280 nm for the aromatics region and of 450 nm for the flavin region. Free hAIF $\Delta$ 1-101 is shown as a black line while mixtures with ATA, C2, and C11 are shown as blue, green, and pink lines, respectively.

We also evaluated potential binding modes of these compounds by protein-ligand docking simulations, since attempts to cocrystallise failed. Our highest scoring docking clusters point to our three chemicals preferentially locating at the hAIF<sub>Δ1-101</sub> redox NADH substrate binding channel (**Figure 4.20 D-E**). On the contrary, the NADH allosteric site is the preferred site in the CTC structure when the NAD<sup>+</sup> product occupies the redox binding channel (**Figure 4.20 H, I**). Finally, (**Table 4.6**) summarises the effect of ATA, C2, and C11 on the hAIF<sub>Δ1-101</sub> kinetic parameters. ATA increases by nearly twice the hAIF<sub>Δ1-101</sub> efficiency to oxidise NADH, apparently by favouring its association. C2 and C11 modify enzyme efficiency positively and negatively, respectively, by 25-30 % as a consequence of changes in  $K_m^{NADH}$ . Therefore, C2, C11, and particularly ATA modify the hAIF<sub>Δ1-101</sub> catalytic efficiency by modulating the coenzyme association/dissociation equilibrium.

**Table 4.5:** Effect of ATA, C2 and C11 on the thermal stability of hAIF<sub>Δ1-101ox</sub>. Values in the table were obtained by the global fitting of the near-CD and fluorescence thermal denaturation curves. Data were obtained in 50 mM Kpi, pH 8.0, at a final ionic strength of 150 mM, from 283.15 to 363.15 K. Protein concentrations were ~2 μM and ~20 μM for fluorescence and near-UV CD respectively.

Compound	T <sub>m1</sub> (K)	T <sub>m2</sub> (K)
--	332 ± 1	337 ± 1
ATA	317 ± 1	328 ± 1
C2	329 ± 1	
C11	327 ± 1	

**Table 4.6:** Effect of selected compounds on the steady state kinetic parameters of the hAIF<sub>Δ1-101</sub> DCPIP diaphorase activity. Assays were performed in 50 mM Kpi, pH 8.0, 1 % DMSO.

HIT	[HIT] (μM)	$k_{cat}$ (s <sup>-1</sup> )	$K_m$ (μM)	$k_{cat}/K_m$ (s <sup>-1</sup> mM <sup>-1</sup> )
--		2.4 ± 0.1	430 ± 20	5.6 ± 0.2
ATA	100	1.0 ± 0.1	99 ± 6	10 ± 1
C2	500	2.1 ± 0.1	310 ± 10	6.8 ± 0.2
C11	100	2.1 ± 0.1	600 ± 20	3.5 ± 0.1

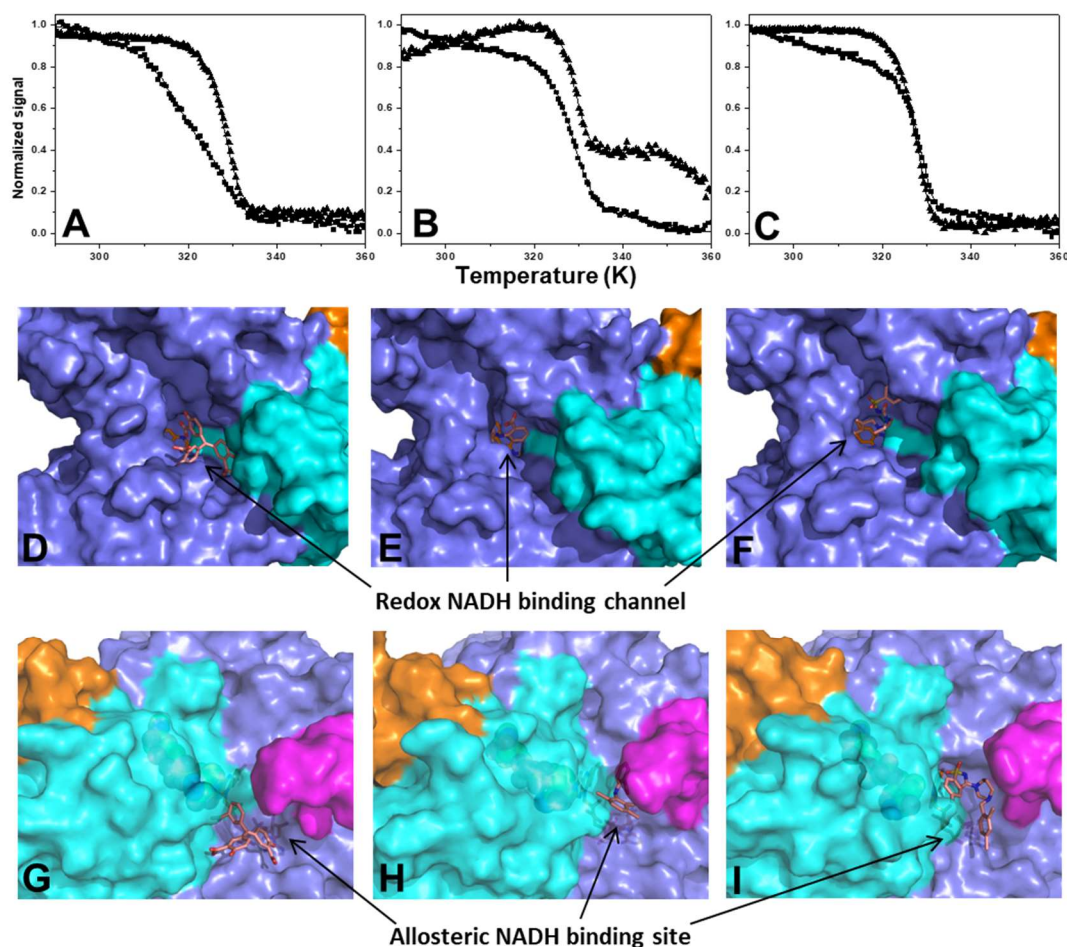


**Figure 4.20: Effect of selected HTS hits on hAIF $\Delta_{1-101}$  thermal unfolding and predicted binding modes.** Thermal denaturation of hAIF $\Delta_{1-101}$  in the presence of (A) ATA, (B) C2, and (C) C11 was monitored by near-UV CD (300 nm, black squares), and flavin fluorescence emission (black triangles). The curves are shown roughly normalised from 0 to 1, and their global fits to a two-transition (ATA) or one-transition (C2, C11) unfolding model are represented by the continuous lines. Curves were recorded in 50 mM Kpi, pH 8.0, at a final ionic strength of 150 mM in the presence of 500  $\mu$ M of each compound. Models for the best docking pose of (D) ATA, (E) C2, and (F) C11 to the hAIF $\Delta_{1-101}$  receptor and of (G) ATA, (H) C2, and (I) C11 to the hAIF $\Delta_{1-101}$ :NADH receptor. Models were optimised by minimization and short MD equilibration routines. ATA, C2, and C11 are shown in pink CPK sticks.

## 4.6 CONCLUSIONS

The data here presented prove that the proteolytic processing of hAIF not only drives to its subcellular localization, but also provides tools for the protein structural adaptation to specific subcellular pH conditions. The apoptotic hAIF $\Delta_{1-101}$  isoform is stable *in vitro*, able to oxidise NADH, and similarly folded at mitochondrial matrix, cytosol, apoptotic cytosol, and nuclei pH, but is an unstable protein at the IMS pH. Nonetheless, the IMS isoform is in fact a longer protein, hAIF $\Delta_{1-54}$ , that is tethered to the IMM when involved in the biogenesis of mitochondrial complexes. Evaluation of the truncated soluble hAIFmt $\Delta_{1-77}$

IMS isoform confirms that the 77-101 traits stabilise the mitochondrial isoform. Although the pH impact on hAIF spectroscopic properties is in general mild, changes in the near-UV CD 300 nm sharp peak are noticeable under different conditions (**Figures 4.3 C and 4.3 D**). In the hAIFmt $_{\Delta 1-77}$  and  $\Delta R201$  forms this peak differs in shape and intensity, while it disappears when the CTC is formed, or when ATA or C2 bind (**Figures 4.3 D, 4.11 C and 4.1.19 C**). Since ATA and C2 are predicted to bind at the WT hAIF $_{\Delta 1-101}$  redox NADH binding site (**Figures 4.20 D, E**), we expect induced redox independent changes in solvent accessibility of at least one tryptophan when ligands block the NADH channel or when the C-loop is released. Regarding the effect of pH on thermal stability it is modest on hAIF $_{\Delta 1-101}$ , although the non-physiological mitochondrial matrix pH slightly shifts  $T_{m1}$  and  $\Delta H_{m1}$  (**Table 4.2**). hAIFmt $_{\Delta 1-77}$  unfolding curves indicate that the 77-101 region stabilises the active site at pH 6.2, but they also point to other protein regions being more dynamic (**Figure 4.6 C-D**). The lower stability and lack of I stabilisation along hAIF $_{\Delta 1-101rd:NAD^+}$  CTC unfolding, compared to hAIF $_{\Delta 1-101}$ , were initially surprising (**Figure 4.5 B**), since protein interaction with small ligands generally increases thermal stability due to the coupling of preferential binding to the N state with unfolding equilibrium (Shrake and Ross, 1992, Brandts and Lin, 1990). Nonetheless, differences between these two structures go beyond the single coenzyme molecule binding. Contrary to hAIF $_{\Delta 1-101}$ , the CTC structure is a dimer with high flexibility in the regulatory C-loop (Ferreira et al., 2014), shows a lack of contacts between apoptotic and FAD-binding domains, and facilitated access to the flavin (**Figure 4.7**). In this context, the ATA, C2 and C11 destabilising effect (**Figure 4.20**) indicates that their binding might also induce C-loop release. This suggests that  $T_m$  reduction induced by these compounds might relate to a preferential binding to partially, or totally, unfolded conformational states that become progressively populated along the thermal unfolding.

Relationships between the effects of mutations on molecular and functional properties of proteins and phenotypes or clinical manifestations are in general complex, but we need to understand them to improve related diseases treatments (Shendure and Akey, 2015). Destabilising mutations may impair intracellular stability, function, regulation, and protein-protein interactions simultaneously and to different extents (Gersting et al., 2008, Medina-Carmona et al., 2017). Considering the hAIF capacity to interact with several partners that modulate its cellular localization and activities, mutations causing biochemical alterations might differently compromise its *in vivo* functions. Structural bases of such intracellular interactions are in most cases hardly known, but those involving hAIF C-loop recognition are expected to be redox controlled.  $\Delta R201$  was the first loss-of-function mutation described in the *aifm1* gene causing progressive mitochondrial encephalomyopathy (Ghezzi et al., 2010). Our unfolding data and structural models indicate very drastic



impacts on hAIF<sub>Δ1-101</sub> stability and conformation (**Figures 4.14 and 4.13**). Break of the R201-E531 salt bridge perturbs various functional sites, confirming the β-hairpin-C-loop connection as a key element to retain a compact active site and the FAD bound (**Figures 4.14 and 4.13**).

The loss of active site compactness affects active site dynamics as well as the AIF allosteric architecture switching (Brosey et al., 2016). This agrees with drastic alterations on the mutant redox properties and, as a consequence, with OXPHOS failure playing a major role in the lethal ΔR201 phenotypes (Ghezzi et al., 2010, Rinaldi et al., 2012). Since the OXPHOS productive AIF-CHCHD4 interaction is conformational, relies on the entire hAIF structure and is favoured in the protein reduced state (Hangen et al., 2015), the conformational stability decreases in the ΔR201 redox active centre would impact CHCHD4 recognition. Interestingly, formation of the CTC stabilises the ΔR201 variant (**Figures 4.12 and 4.14**). Differences in the switch to the CTC between WT and ΔR201 variants will have major effects on hAIF *in vivo* redox conformational dynamics, as well as on the interaction networks with other physiological partners. Our models predict conformational changes in the ΔR201<sub>ox</sub> variant at the region proposed for HSP70 recognition, residues 150-268 (Lui and Kong, 2007, Gurbuxani et al., 2003), which might modulate hAIF retention in the cytoplasm.

Regarding the degradosome: (i) the CypA site in hAIF is mapped as containing the 370-397 3-stranded β-sheet (NADH domain (Farina et al., 2017, Zhu et al., 2007) that apparently is only slightly altered in our ΔR201<sub>ox</sub> model, but not in its CTC model. Since CypA affinity improves in the WT CTC state, a similar effect might be occurring in ΔR201 CTC; (ii) the nuclear H2AX binds to the 544-554 Pro-rich C-loop motif, flexible in WT and ΔR201 isoforms (Baritaud et al., 2010, Wang et al., 2011); (iii) Finally, DNA putatively wraps non-specifically around the FAD and C-terminal domains (Ye et al., 2002), with the ΔR201 mutation apparently increasing its *in vitro* affinity (Ghezzi et al., 2010). Nevertheless, considering that H2AX and DNA binding is contributed by the hAIF intrinsically disordered region, with disorder modulating the binding, the impact of ΔR201 mutation might be low in the *in vivo* overall degradosome assembly, in agreement with PCD being hardly affected by this missense mutation. Noticeably, among the studied AIF variants, ΔR201 is the only one stabilised by coenzyme binding (**Figure 4.12**) and one of the few in which patients supplemented with the FAD riboflavin precursor improved clinical conditions by partially correcting OXPHOS failure (Ghezzi et al., 2010). Thus, the FAD and NADH natural ligands might synergically contribute to *in vivo* overcome the ΔR201



unfolding dynamic negative effect by enhancing protein stability. Such observation has important implications in the search of potential ligands correcting stability and function.

G308E and E493V variants have little effects on hAIF<sub>Δ1-101</sub> thermal stability, in agreement with their less severe phenotypes. The G308E substitution (**Figure 4.10**) slows down CTC formation and abolishes the enzyme ability to discriminate between NADH and NADPH (Sorrentino et al., 2015, Sevrioukova, 2016, Sorrentino et al., 2017). This leads to prenatal OXPHOS-related encephalopathy, muscle atrophy, and early death. G308E oxidised structures (**Figure 4.10**) show that Glu 308 stabilises a different Glu336 conformer that modulates the 334-336, 365-370 and 380-388 interaction networks, which agree with its modest differences in thermal stability (**Table 4.3**) (Sorrentino et al., 2015, Sevrioukova, 2016, Sorrentino et al., 2017). In its CTC form, those structural changes alter the stabilising interaction network of the adenine moiety of the coenzyme and produce its reorientation (Sorrentino et al., 2017).



Envisaging the possibility of distinct CTC conformers, the G308E mutation causes a severe complex (I+IV) deficiency and reduced CHCHD4 binding (Brosey et al., 2016). Altogether, the loss of functionality in this variant appears related to the lower accumulation of its CTCs, rather than to an overall conformational stability lost. The E493V mutation enhances hAIF apoptotic activity in a caspase-independent way, but neither alters the interaction with CHCHD4 nor the respiratory mitochondrial activity (Rinaldi et al., 2012). Mild changes in stability agree with the mutation having no effect on protein folding or cellular expression. Nevertheless, in vitro this variant has increased propensity to NADH oxidation and CTC reoxidation (Rinaldi et al., 2012, Sevrioukova, 2016). In line with its reduced unfolding enthalpy and aggregation propensity (**Table 4.3**).

Thus, the E493V mutation would favour the hAIF monomeric form and its nuclear translocation. E493 is not solvent accessible but assists folding of the regulatory C-loop and contributes to binding of the allosteric NADH. Thus, although the E493V substitution has apparently low impact on the reductase domain, it reduces the CTC dimer stability (Ferreira et al., 2014) and makes it less structured than in the WT. This might also have an impact on the allosteric NADH binding and/or C-loop conformation. Since disordered regions and quaternary organizations are involved in signalling, recognition, regulation, or nuclear translocation (Xie et al., 2007), we can consider that these facts affect the E493V variant interplay with its partners and, in turn, favour its nuclear translocation and DNA degradation. Considering this, the dynamics of the domain-domain and FAD-protein interactions appear to be key elements in hAIF<sub>Δ1-101</sub> stabilisation. hAIF<sub>Δ1-101</sub> and its CTC must be considered very different conformational ensembles from the stability and

structural points of view, with the architecture switch toward the CTC producing a less stable and compact protein that contains an intrinsically disordered region. Such mechanisms are contributors to control hAIF physiological actions by either cellular NADH levels or interaction with other biomolecules (Xie et al., 2007, Brosey et al., 2016).

Altogether, the available information gives a comprehensive picture of stability and local dynamics in aspects of the hAIF function such as the redox-derived allosteric properties and ability to form quaternary assemblies, which will influence the interactions network and the *in vivo* phenotypes consequence of missense mutations. In this context, the flavin redox state and the coenzyme binding are key elements to modulate hAIF dynamics and C-loop ensembles. Some of these hAIF properties might be also modulated by small ligands, setting a molecular framework to discover molecules able to bind hAIF. These molecules might have a rescuing function of pathogenic variants by shielding deleterious effects on protein stability and ligand recognition, but they might also be modulators of the structural protein plasticity. To date, only ATA has been described as able to bind to AIF, but its promiscuity makes of it a bad drug candidate (Kuban-Jankowska et al., 2015, Tsi et al., 2002).

The hits here identified provide a starting point to redesign and open a molecular framework to search for new pharmacological ligands targeting hAIF. Thus, this characterization provides deeper insights into the hAIF conformation as a mechanism to regulate its cellular functions, as well as some of the molecular and cellular pathogenesis associated with its defects.



## *5- W196 AND THE $\beta$ -HAIRPIN MOTIF MODULATE THE CONFORMATIONAL LANDSCAPE AND THE BIOMOLECULAR INTERACTION NETWORK OF THE APOPTOSIS INDUCING FACTOR*

### **PERSONAL CONTRIBUTION**

- Expression and purification of AIF variants, CHCHD4 and CypA
- Spectroscopic characterization of AIF variants
- Kinetic measurements of AIF variants
- Fluorescence and CD assays of AIF variants
- Size exclusion chromatography experiments
- Isothermal titration calorimetry measurements



## 5.1 ABSTRACT

The human Apoptosis Inducing Factor (hAIF) is a moonlight flavoprotein involved in mitochondrial respiratory complex assembly and caspase-independent programmed cell death. These functions might be modulated by its redox-linked structural transition that enables hAIF to act as a NAD(H<sup>+</sup>)-redox sensor. Upon reduction with NADH, hAIF undergoes a conformational reorganization in two specific insertions- the flexible regulatory C-loop and the 190-202  $\beta$ -hairpin promoting protein dimerization and the stabilisation of a long-life charge transfer complex (CTC) that modulates its monomer-dimer equilibrium and its protein interaction network in healthy mitochondria. In this regard, here we investigated the precise function of the  $\beta$ -hairpin in the AIF conformation landscape related to its redox mechanism, by analysing the role played by W196, a key residue in the interaction of this motif with the regulatory C-loop. Mutations at W196 decrease the compactness and stability of the oxidized hAIF, indicating that the  $\beta$ -hairpin and C-loop coupling contributes to protein stability. Kinetic studies complemented with computational simulations reveal that W196 and the  $\beta$ -hairpin conformation modulate the low efficiency of hAIF as NADH oxidoreductase, contributing to configure its active site in a non-competent geometry for hydride transfer, and to stabilise the CTC state by enhancing the affinity for NAD<sup>+</sup>. Finally, the  $\beta$ -hairpin motif contributes to define the conformation of AIF's interaction surfaces with its physiological partners. These findings improve our understanding on the molecular basis of hAIF's cellular activities, a crucial aspect for clarifying its associated pathological mechanisms and developing new molecular therapies.

## 5.2 RESUMEN

El factor de inducción de apoptosis humano (hAIF) es una flavoproteína que participa en el ensamblaje de los complejos respiratorios mitocondriales y en la muerte celular programada independiente de caspasas. Estas funciones podrían ser moduladas por su transición estructural vinculada a su estado redox, que le permite actuar como un sensor redox  $\text{NAD}(\text{H}/^+)$ . Tras la reducción con NADH, hAIF se somete a una reorganización conformacional en dos inserciones específicas. El bucle-C, regulador y flexible, y la  $\beta$ -horquilla 190-202 que promueven la dimerización de la proteína y la estabilización de un complejo de transferencia de carga (CTC) altamente estable, que modula su equilibrio monómero-dímero y su red de interacción con otras proteínas en mitocondrias sanas. En este capítulo, investigamos la función precisa de la horquilla  $\beta$  en el paisaje de conformación del AIF en relación con su mecanismo redox, analizando el papel desempeñado por W196, un residuo clave en la interacción de este motivo con el bucle-C regulador. Las mutaciones en W196 disminuyen la compacidad y la estabilidad del hAIF en el estado oxidado, lo que indica que el  $\beta$ -horquilla y el acoplamiento del bucle C contribuye a la estabilidad de la proteína. Los estudios cinéticos complementados con simulaciones computacionales revelan que W196 y la conformación de la horquilla  $\beta$  modulan la baja eficiencia del hAIF como oxidorreductasa NADH, contribuyendo a configurar su sitio activo en una geometría no competente para la transferencia de hidruro, y a estabilizar el estado CTC aumentando la afinidad por la  $\text{NAD}^+$ . Por último, el motivo de la horquilla  $\beta$  contribuye a definir la conformación de las superficies de interacción de la AIF con sus parejas fisiológicas. Estos hallazgos mejoran nuestra comprensión de la base molecular de las actividades celulares de AIF, un aspecto crucial para aclarar sus mecanismos asociados a situaciones patológicas y desarrollar nuevas terapias moleculares.

### 5.3 INTRODUCTION

The human Apoptosis Inducing Factor (hAIF) was first described as a mitochondrial-released flavoprotein mediating caspase-independent programmed cell death (Susin et al., 1999b). Moreover, this ubiquitously expressed protein across eukaryotes also plays a vital role in cell development and survival (Lorenzo et al., 1999). These survival functions rely on its FAD dependent activities, which contribute to maintain the stability of the mitochondrial electron transfer chain, supercomplex organization and transmembrane potential, as well as to control of mitochondrial reactive oxygen species (ROS) (Delavallée et al., 2020). In healthy mitochondria, the hAIF is processed and the hAIF $_{\Delta 1-53}$  mature protein anchors in the inner membrane (IM) -via its N-terminal segment-, facing the intermembrane space (IMS) and folds in three domains (**Figure 5.1 A**) (Otera et al., 2005, Ye et al., 2002, Maté et al., 2002). More particularly, mammalian AIFs have two specific insertions, a regulatory C-terminal loop (aa 510-560 in hAIF) and a  $\beta$ -hairpin (aa 190-202 in hAIF), that connects the NADH- and FAD-domains to the C-terminal pro-apoptotic domain (**Figure 5.1 A**). AIF conformation is dynamically influenced by the coenzyme substrate binding and by the redox switch of its flavin cofactor, facts believed to modulate its biomolecular interaction network (Villanueva et al., 2019, Churbanova and Sevrioukova, 2008). In oxidized hAIF, the regulatory C-loop is stabilised in the protein core by direct interaction with the  $\beta$ -hairpin, particularly through stacking and H-bonding interactions of W196 and R201 residues with its 517-524 and 529-533 short helices. Binding of one NADH molecule to AIF's active site (NADH<sub>A</sub>) promotes FAD reduction, as well as the stabilisation of a long-lived FADH<sup>-</sup> /NAD<sup>+</sup> charge transfer complex (CTC). This CTC is inefficient in electron transfer, but capable of inducing a redox-linked protein conformational reorganization and its subsequent dimerization. CTC formation displaces the  $\beta$ -hairpin that triggers C-loop remodelling and its release to the solvent. These conformational changes induce i) the allosteric formation of the second non-catalytic NADH binding site (NADH<sub>B</sub>), where stacking interactions with reoriented W196 and F582 side-chains facilitate NADH<sub>B</sub> accommodation, and ii) the dimerization of the protein (**Figure 5.1 C and E**). These facts led to postulate AIF as a redox sensor of NAD(H<sup>+</sup>) cellular levels (Sevrioukova, 2009, Ferreira et al., 2014, Brosey et al., 2016). W196 substitution by alanine disrupts the interaction between the  $\beta$ -hairpin and the C-loop that unwinds the above mentioned 529-533 helix and releases the two specific AIF insertions to the solvent, promoting a permissive mutant dimerization in its oxidized state (W196A hAIF $_{\Delta 1-101}$ , herein W196A) (**Figure 5.1 A and D**) (Brosey et al., 2016). However, the W196A maintains an active-site architecture similar to that of WT hAIF for residues involved in NADH<sub>A</sub> binding with the only exceptions of E453 and H454 (**Figure 5.1 B**).

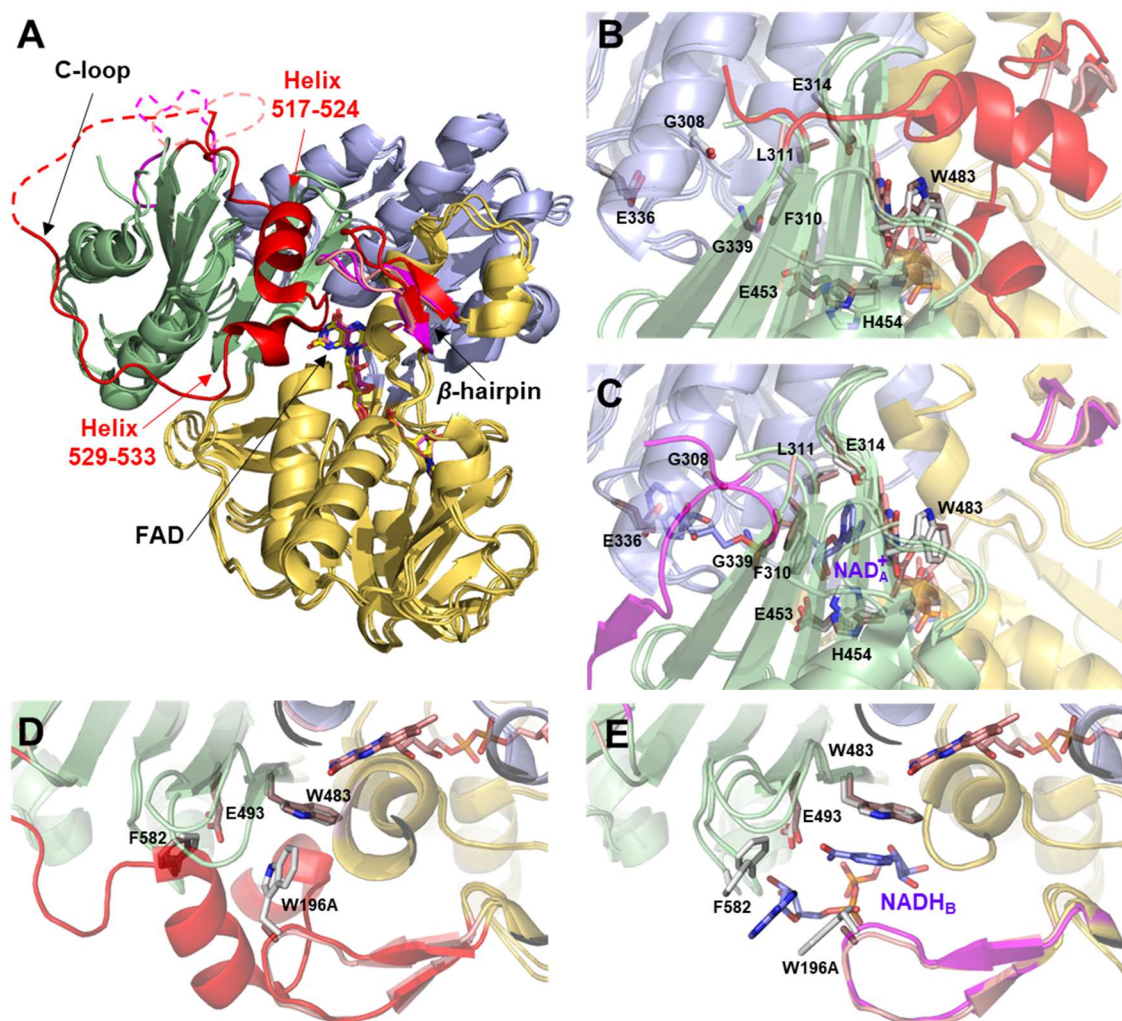


**Figure 5.1: Comparative overview of the crystallographic structures of WT hAIF $\Delta_{1-101}$  (pdb 4BV6), WT CTC hAIF $\Delta_{1-101}$ :2NADH (pdb 4BUR) and W196A<sub>ox</sub> variant (pdb 5KVH). (A)** Cartoon superposition. FAD<sup>-</sup>, NADH<sup>-</sup>, and C-terminal domains coloured in gold, light blue and pale green, respectively. FAD drawn as sticks with C atoms in yellow, salmon and magenta respectively for WT, WT CTC and W196A structures. Visible residues in the  $\beta$ -hairpin and the regulatory 509-560 C loop are shown in red, magenta and salmon respectively for WT, WT CTC and W196A structures. Missing fragments of the C-loop (P545-D559, K518-G557 and A511-D559 in WT<sub>ox</sub> chain A, WT CTC chain C and W196A chain A structures, respectively) are indicated as dashed lines. Detail of the W196A NADH<sub>A</sub> binding site overlaid with (B) WT and (C) WT CTC. Detail of the W196A NAD(H)<sub>B</sub> binding site overlaid with (D) WT and (E) WT CTC. Side-chains for relevant residues are shown as CPK coloured sticks with C atoms in salmon for W196A and in light grey for WT and WT CTC structures. NADH<sub>A</sub> and NADH<sub>B</sub> in the WT CTC structure are shown as CPK coloured sticks with its C atoms in blue.

The  $\beta$ -hairpin release in W196A<sub>ox</sub> also induces the displacement of the central  $\beta$ -strand and the reorientation of E453 and H454 side chains (Figure 5.2 D-E). Thus, H454 disrupts its interaction with S480, producing as a consequence the displacement of the H478 side-chain -sited in the loop connecting the central  $\beta$ -strand and the His-rich helix- towards the C-loop, contributing to its release, and the exposition of the hydrophobic border at the dimerization interfaces in the W196A structure. Such later conformational changes are similar to those reported for the WT CTC structure (Figure 5.2 E-F).



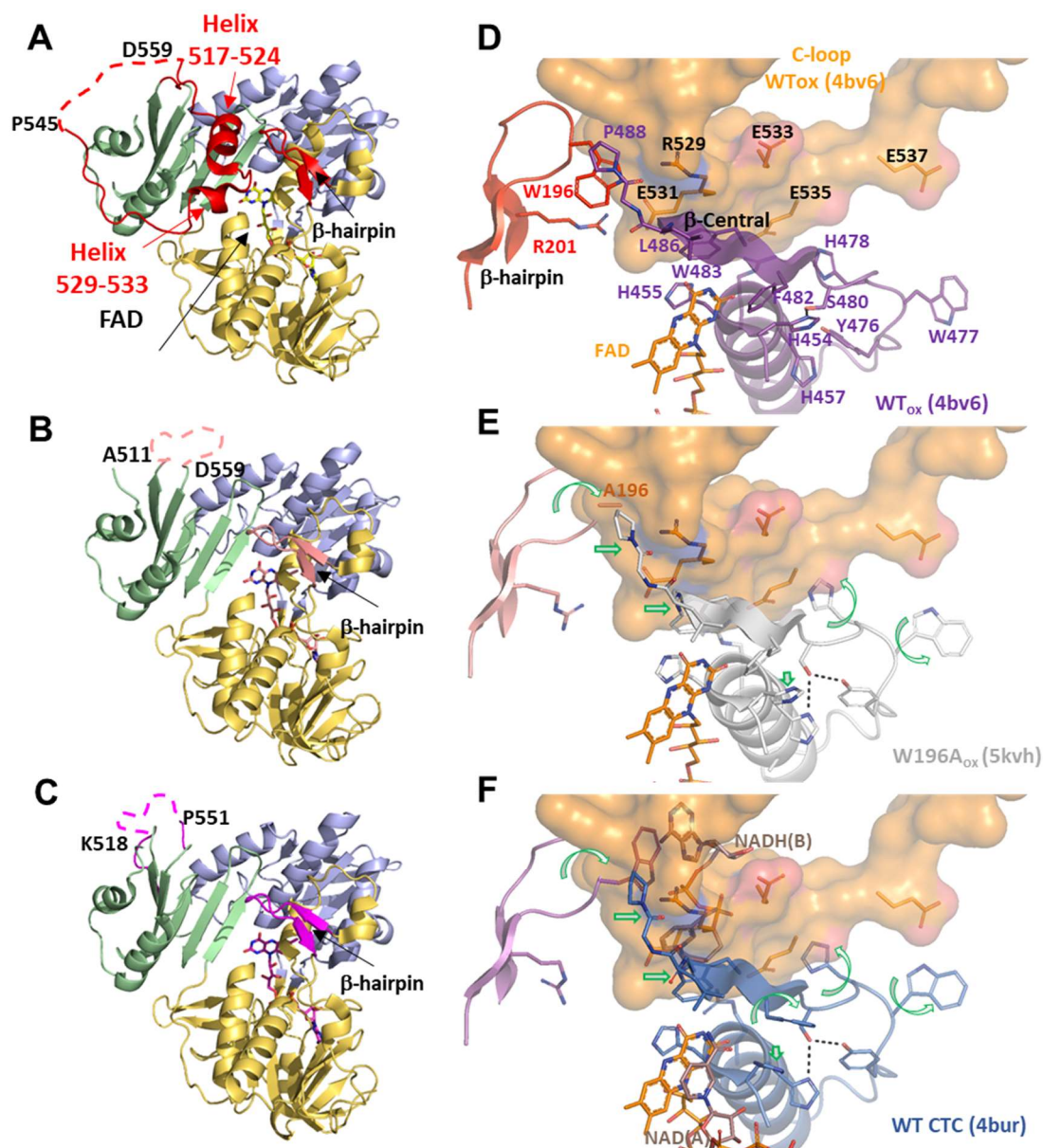


**Figure 5.2: Comparative overview of the crystallographic structures of WT hAIF $_{\Delta 1-101}$  (pdb 4BV6), W196A hAIF $_{\Delta 1-101}$  (pdb 5KVH) and WT hAIF $_{\Delta 1-101}$ :2NADH CTC (pdb 4BUR).** Panels on the left show overall cartoon representations for **(A)** WT<sub>ox</sub> **(B)** W196A, and **(C)** WT CTC. The FAD-, NADH-, and C-terminal domains are respectively coloured in gold, light blue and pale green. FAD is drawn as sticks with C atoms in yellow, salmon and magenta respectively for WT, W196A and WT CTC structures. The  $\beta$ -hairpin as well as visible residues in the regulatory C-loop (residues 509-560) are shown in red, salmon and magenta respectively for WT, W196A and WT CTC structures. Missing fragments of the C-loop (P545-D559, A511-D559 and K518-G557 in WT<sub>ox</sub> chain A, W196A chain A and WT CTC chain C structures, respectively) are drawn as dashed lines. Panels on the right show a detail of the relationship of the  $\beta$ -hairpin with the central  $\beta$ -strand for **(D)** WT, **(E)** W196A, and **(F)** WT CTC. In all cases FAD is drawn as sticks with C atoms in orange. All panels show the regulatory C-loop as seen in the WT structure (this fragment is missing for the other two structures) with an orange transparent surface. Coenzymes in the WT CTC structure are shown as CPK coloured sticks with C atoms in pink. Green arrows indicate relevant displacements of structural elements relative to the crystallographic WT structure.

In healthy cells, hAIF is essential for mitochondrial bioenergetics, being its physical and functional interaction with human CHCHD4 (coiled-coil-helix-coiled-coil-helix domain containing 4) key in the assembly and/or stabilization of multi subunit respiratory transport chain complexes and supercomplexes (Modjtahedi et al., 2015, Hangen et al., 2015, Modjtahedi et al., 2016, Hangen et al., 2010). In IMS, CHCHD4 controls the import and oxidative folding of a set of assembly factors and protein subunits of respiratory complexes, while hAIF would regulate CHCHD4 expression as well as its import and proper IMS localization. Consequently, downregulation or depletion of hAIF give rise to major dysfunctions in oxidative phosphorylation (OXPHOS), secondary to the deficiency of CHCHD4, causing severe neurodegenerative illnesses (Modjtahedi et al., 2015, Modjtahedi et al., 2016, Klein et al., 2002, El Ghouzzi et al., 2007). The hAIF conformation -modulated by its redox NADH-dependent monomer dimer- is suggested to be critical for this interaction (Villanueva et al., 2019, Hangen et al., 2015, Sevrioukova, 2016). Upon lethal cellular stress, hAIF acts as a mediator of necrotic poly(ADPribose)polymerase (PARP)-1-dependent cell death (parthanatos) by its further processing into the soluble pro-apoptotic form (hAIF <sub>$\Delta$ 1-101</sub>) and its release into the cytosol. The regulatory mechanism by which AIF is released is unknown, but could be somehow modulated by its structural reorganization due to depletion of coenzyme levels during PARP-1 hyperactivation (Alano et al., 2010). Once in the cytosol, its interaction with some endonucleases, as cyclophilin A (CypA) favours nuclear co-translocation of the AIF:CypA complex (Susin et al., 1999a, Cande et al., 2004). In this subcellular compartment, the association of this binary complex to the histone H2AX leads to the assembly of the AIF-mediated DNA degradation complex ("degradosome", AIF:CypA:H2AX:DNA), which provokes chromatin condensation and DNA fragmentation (Cande et al., 2004, Artus et al., 2010). Despite the emerging picture of the physiological functions of AIF being modulated by its conformational and redox states, we are only starting to depict the implications of the molecular mechanism regulating its activities. Thus, the molecular basis for the mechanism by which AIF regulates and pivots the redox dependent interaction with CHCHD4, as well as those for the action of the degradosome complex as a death effector remain unknown. Nonetheless, we can envisage that AIF ability to stabilise both stable CTC and dimers -upon interaction with the coenzyme followed by FAD reduction- is surely a key feature to switch among its in vivo roles. In this context, the structural changes induced by CTC formation in native protein, but also shared by W196A<sub>ox</sub>, suggest that W196 and/or the  $\beta$ -hairpin might be relevant for AIF cellular activities. Such hypothesis is further supported by the  $\beta$ -hairpin contributing to binding of the allosteric NADH<sub>B</sub>, as well as by the fact that pathogenic mutations coursing with severe processes of neurodegeneration and early death have been reported at both the NADH<sub>B</sub> binding site and the  $\beta$ -hairpin itself. In the present study,

we particularly investigate the contribution of the  $\beta$ -hairpin to the regulation of hAIF structural stability, coenzyme binding, reductase activity, CTC stability, and interaction with its physiological partners, by generating W196A, W196L and W196Y site-directed mutants. Our results indicate that the W196 side-chain is not only key to establish the  $\beta$ -hairpin and C-loop organization in the oxidized state, but also to regulate the conformational stability and landscape of the protein. Both facts, seem to be relevant to determine AIF efficiency as a cellular redox sensor, as well as to the establishment of specific binary interactions with different partners.

## 5.4 EXPERIMENTAL PROCEDURES

### 5.4.1 EXPRESSION AND PRODUCTION OF PROTEINS

The cDNA encoding for W196Y, W196L and W196A hAIF <sub>$\Delta$ 1-101</sub> variants (UniProtKB O95831) were obtained by site-directed mutagenesis from Mutagenex®, and then subcloned into the pET28a expression vector with a cleavable N-terminal His<sub>6</sub>-tag similarly to that reported for the WT protein (Ferreira et al., 2014). The cDNAs encoding for human CypA (UniProtKB P62937), CHCHD4 (UniProtKB Q8N4Q1), and Histone H2AX (UniProtKB P16104) were synthesized with a cleavable N-terminal His<sub>6</sub>-tag (CACCAT) and codon optimized for *Escherichia coli* expression by GenScript®. The coding sequences were subcloned into the pET28a expression vector between two restriction sites: NdeI-NotI for CypA and CHCHD4; and NcoI-NdeI for H2AX. The resulting constructs were used to transform the *E. coli* C41 (DE3) strain for heterologous protein expression.

For the production of WT hAIF <sub>$\Delta$ 1-101</sub> and its W196Y, W196L and W196A variants, the transformed bacteria were grown in 10 L LB medium containing 30 mg/L kanamycin and supplemented with 0.08 g/L of riboflavin and then incubated at 37°C and 180 r.p.m. At OD<sub>600nm</sub>  $\approx$  0.8, cultures were induced with 1 mM IPTG (BioChemica) and incubated at 25°C and 100 r.p.m for additional 18 h. After that, cells were harvested and proteins were purified by following the procedure already described for the WT (Ferreira et al., 2014). For CypA production, the transformed bacteria were grown in 10 L LB medium containing 30 mg/L kanamycin and incubated at 37°C and 180 r.p.m. At A<sub>600nm</sub>  $\approx$  0.5, protein expression was induced with 0.5 mM IPTG (BioChemica), and bacteria cultures were incubated for 3 additional hours. After that, cells were harvested by centrifugation and subsequently resuspended in 50 mM Tris/HCl, pH 8.0, NaCl 1mM and lysed by sonication on ice. The cell lysate was centrifuged to remove debris, and then was mixed with 5 mL of Ni<sup>2+</sup> IMAC Sepharose 6 Fast Flow gel (GE Healthcare) previously equilibrated in the above buffer containing 4 mM imidazole. The mixture was incubated on a bidirectional orbital

rocker for 1 h at 4 °C, and then loaded into a column. The protein was eluted with a linear imidazole gradient from 40 to 250 mM with 10% glycerol in 50 mM Tris, pH 8.0, 150 mM NaCl. Protein fractions were pooled, concentrated and dialyzed with 50 mM potassium phosphate, pH 7.4. A similar protocol was used for CHCHD4 and H2AX with the differences noted below. For CHCHD4: i) bacteria cultures were induced using 1mM IPTG; ii) the imidazole gradient was from 40 to 1000 mM in 50 mM potassium phosphate pH 7.0, 150 mM NaCl; iii) protein was stored in 50 mM Kpi, pH 7.4, with 10 mM DTT, to maintain the catalytic Cys53-Pro54-Cys55 disulphide motif in reduced state. For H2AX: i) bacteria cultures were induced at  $A_{600nm} \approx 0.6$  with 1mM IPTG; ii) the imidazole gradient was from 40 to 500 mM in 50 mM potassium phosphate pH 7.4, 150 mM NaCl; iii) protein was stored in 50 mM potassium phosphate pH 7.4 at -80 °C.

#### 5.4.2 MOLECULAR WEIGHT DETERMINATION BY SIZE EXCLUSION CHROMATOGRAPHY

The hAIF $_{\Delta 1-101}$  variants, either in the presence or absence of a 10-fold excess of NADH, were loaded onto a HiPrep 26/60 Sephacryl TMS-200 High Resolution (GE Healthcare) column attached to a fast pressure liquid chromatographic system (GE Healthcare). Protein elution was performed in 50 mM phosphate buffer, 150 mM NaCl, pH 7.4, at a flow rate of 0.5 mL/min. The column was previously calibrated with the GE Healthcare LMW calibration kit (6 proteins in the 6400-160000 Da range). The obtained chromatograms were fitted to a set of Gaussian functions.

#### 5.4.3 STABILIZATION OF CROSS-LINKED PROTEIN OLIGOMERS AND ELECTROPHORETIC ANALYSIS

Reaction mixtures containing 4  $\mu$ M of the hAIF $_{\Delta 1-101}$  variants in 10 mM potassium phosphate, pH 7.4, were incubated with a 100-fold excess of the homobifunctional-bis[sulphosuccinimidyl]-suberate (BS<sup>3</sup>) (Pierce) cross-linker at room temperature in the absence or presence of a 10-fold excess of NADH. Reactions were stopped by addition of the denaturing bromophenol blue sample buffer and sample mixtures were then resolved by 12% SDS-PAGE.

#### 5.4.4 SPECTROSCOPIC CHARACTERIZATION

UV-Visible spectra were recorded in a Cary 100 Bio spectrophotometer (Agilent). Protein concentrations were determined using the molar absorbance coefficients of each variant, which were estimated by protein denaturation with 3 M guanidinium chloride in 10 mM phosphate, pH 7.4, followed by quantification of the released FAD. The extinction coefficients for WT, W196A, W196L and W196Y hAIF $_{\Delta 1-101ox}$  were  $\epsilon_{451nm} = 13.7 \text{ M}^{-1}\text{cm}^{-1}$  (Ferreira et al., 2014),  $\epsilon_{451nm} = 13.35 \text{ M}^{-1}\text{cm}^{-1}$ ,  $\epsilon_{451nm} = 13.92 \text{ M}^{-1}\text{cm}^{-1}$ , and  $\epsilon_{452nm} = 14.01 \text{ M}^{-1}\text{cm}^{-1}$ , respectively. Circular dichroism (CD) spectra were recorded in a thermostated Chirascan (Applied Photophysics). Far-UV CD spectra were acquired using 1  $\mu\text{M}$  protein in a 0.1 cm-pathlength cuvette, while near-UV/Vis CD spectra were recorded using 20  $\mu\text{M}$  protein in a 1 cm-pathlength cuvette. Fluorescence spectra were recorded in a thermostated Cary Eclipse. Fluorescence spectrophotometer (Agilent) using 2  $\mu\text{M}$  protein in a 1 cm-pathlength cuvette. Flavin fluorescence emission spectra were acquired in the 480-600 nm range upon excitation at 450 nm. Fluorescence emission spectra of aromatic residues were collected from 300 to 550 nm upon excitation 200 at 280 nm. CD and fluorescence spectra were recorded in the absence and presence of a 100-fold excess of NADH at 10 °C (folded state) and 90 °C (thermally denatured state).

#### 5.4.5 THERMAL DENATURATION ASSAYS

Thermal denaturation curves were followed by changes in the FAD fluorescence emission upon its release from the protein by sample excitation at 450 nm. Curves were monitored from 10 °C to 90 °C with scan rates of 1°C/min, both in the absence and presence of a 100-fold excess of NADH. The curves for each variant were roughly normalized to values between 0 and 1 and globally fitted to a two-step process describing a single transition unfolding equilibrium (native (N)  $\leftrightarrow$  unfolded (U)) by using the following equation (Sancho, 2013):

$$S_{obs} = \frac{S_N + m_N T + (S_U + m_U T) e^{-(\Delta G/RT)}}{1 + e^{-(\Delta G/RT)}} \quad \text{Eq. 5.1}$$

in which  $S_{obs}$  is the measured protein signal at a given temperature (T).  $S_N$ , and  $S_U$  are intercept at 0 K with the y-axis of the linear extrapolation for the native and unfolded pre-

and post-transition regions, respectively, while  $m_N$ , and  $m_U$  are the corresponding slopes. The Stabilisation Gibbs energy depends on the temperature according to

$$\Delta G_i = \Delta H_i \left(1 - \frac{1}{T_{mi}}\right) + \Delta C_{Pi} \left(T - T_{mi} - T \ln \frac{T}{T_{mi}}\right) \quad \text{Eq. 5.2}$$

where  $\Delta H$  is the unfolding enthalpy,  $T_m$  is the mid transition temperature,  $\Delta C_P$  is the unfolding heat capacity change, and  $R$  is the ideal gas constant.

#### 5.4.6 KINETICS MEASUREMENTS

The steady-state diaphorase activity of hAIF $_{\Delta 1-101}$  220 variants were measured in air saturated 50 mM potassium phosphate, pH 8.0, using NADH as the substrate donor and 95  $\mu$ M dichlorophenolindophenol (DCPIP,  $\Delta \epsilon_{620\text{nm}} = 21 \text{ mM}^{-1} \text{ cm}^{-1}$ ) as acceptor (Ferreira et al., 2014). When saturation profiles on the pyridine nucleotide concentration were observed, kinetic constants were estimated by fitting initial reaction rates at different coenzyme concentrations to the Michaelis-Menten equation:

$$\frac{v}{e} = \frac{k_{\text{cat}} [\text{NADH}]}{K_m^{\text{NADH}} + [\text{NADH}]} \quad \text{Eq 5.3}$$

$$\frac{v}{e} = \frac{(k_{\text{cat}}/K_m^{\text{NADH}})[\text{NADH}]}{1 + \frac{(k_{\text{cat}}/K_m^{\text{NADH}})[\text{NADH}]}{k_{\text{cat}}}} \quad \text{Eq 5.4}$$

where  $v$  stands for the initial velocity,  $e$  is the enzyme concentration,  $K_m^{\text{NADH}}$  is the Michaelis constant for the NADH,  $k_{\text{cat}}$  is the turnover number of the enzyme and  $k_{\text{cat}}/K_m^{\text{NADH}}$  the enzyme catalytic efficiency. The reactivity of the CTC towards molecular oxygen was monitored by fully reduction of hAIF $_{\Delta 1-101}$  samples with NADH (1.5-fold the concentration of the protein) in 50 mM phosphate buffer, pH 7.4, and following their reoxidation in a Cary 100 spectrophotometer (Agilent). Absorption spectra were recorded at 25 °C until full oxidation of the flavin cofactor was achieved. For each time the % remaining of CTC versus reoxidation by molecular oxygen was estimated as  $\Delta A_t/\Delta A_{\text{max}}$  where  $\Delta A_{\text{max}}$  is the difference between the minimum and the maximum absorbance at 700 nm, and  $\Delta A_t$  is the difference of each value at 700 nm minus the minimum absorbance at 700 nm. The CTC half-life is the time at which 50 % of CTC still remains. A SX18.MV stopped-flow spectrophotometer (Applied Photophysics), interfaced with the ProData-SX software and a photodiode array detector, was used to investigate the fast kinetics reduction of the hAIF variants by the



NADH coenzyme. Samples of  $\sim 10 \mu\text{M}$   $\text{hAIF}_{\Delta 1-101\text{ox}}$  were mixed with increasing concentrations of NADH (0.03-10 mM) under aerobic conditions in 50 mM potassium phosphate, pH 7.4, at 25 °C. The enzyme and NADH concentrations are the final ones obtained after mixing equal volumes of substrate and enzyme.

Observed rate constants for the Hydride Transfer (HT) event ( $k_{\text{obs}}$ ) were calculated by global analysis and numerical integration methods (simultaneously using all spectral data in the 400-800 nm region along time evolution). A single step model ( $A \rightarrow B$ ) best fitted to describe the overall reaction at all NADH concentrations assayed. Averaged  $k_{\text{obs}}$  values at each NADH concentration were then fitted to the equation that describes the formation of an enzyme:substrate complex prior to the HT event:

$$k_{\text{obs}} = \frac{k_{\text{HT}} \text{NADH}}{K_{\text{d}}^{\text{NADH}} + \text{NADH}} + k_{\text{rev}} \quad \text{Eq 5.4}$$

where  $k_{\text{HT}}$  is the limiting rate constant for HT from the pyridine nucleotide coenzyme to the FAD cofactor of  $\text{hAIF}$ , and  $K_{\text{d}}^{\text{NADH}}$  is the dissociation constant of the transient  $\text{hAIF}_{\Delta 1-101\text{ox}}:\text{NADH}$  complex.

Stopped-flow spectrophotometry was also used to evaluate the rates of CTC formation when mixing photoreduced  $\text{hAIF}_{\Delta 1-101}$  ( $\text{hAIF}_{\Delta 1-101\text{phrd}}$ ) with increasing concentrations of  $\text{NAD}^+$  (0.125-5 mM) under anaerobic conditions.  $\text{hAIF}_{\Delta 1-101\text{phrd}}$  samples were obtained by photoreduction in presence of 5  $\mu\text{M}$  methyl viologen, 3  $\mu\text{M}$  5-deazariboflavin and 20 mM EDTA. The assays were performed at 25 °C in 50 mM potassium phosphate, pH 7.4, under anaerobic conditions (obtained by several cycles of vacuum application and bubbling with  $\text{O}_2$  free argon). Data were global fitted to a single step model ( $A \rightarrow B$ ) and  $k_{\text{obs}}$  were determined at the different  $\text{NAD}^+$  concentrations assayed. These values were then fitted to the equation that describes the formation of a transient  $\text{hAIF}_{\Delta 1-101\text{phrd}}:\text{NAD}^+$  complex prior to the CTC stabilisation:

$$k_{\text{obs}} = \frac{k_{\text{CTC}} [\text{NAD}^+]}{K_{\text{d}}^{\text{NAD}^+} + [\text{NAD}^+]} \quad \text{Eq 5.5}$$

in which  $k_{\text{CTC}}$  is the limiting rate constant for the rearrangement of the encounter complex to form the CTC, and  $K_{\text{d}}^{\text{NAD}^+}$  is the dissociation constant for the mentioned transient encounter complex.

### 5.4.7 ISOTHERMAL TITRATION CALORIMETRY (ITC)

ITC assays were carried out using an Auto-iTC200 (MicroCal, Malvern-Panalytical) thermostated at 25 °C. Typically, 10-20  $\mu$ M protein partner and dsDNA samples-prepared as described below- were used to titrate  $\sim 10$   $\mu$ M hAIF $_{\Delta 1-101}$  variants. All solutions were degassed at 15 °C for 1 min before each assay. A sequence of 2  $\mu$ L injections of titrant solution every 150 s was programmed and the stirring speed was set to 750 rpm. The association constant ( $K_a$ ), the enthalpy of binding ( $\Delta H$ ), and the binding stoichiometry (N) were estimated through non-linear least squares regression of the experimental data employing a single ligand binding site model implemented in Origin 7.0 (OriginLab). The dissociation constant ( $K_d$ ), the free energy change ( $\Delta G$ ), and the entropy change ( $\Delta S$ ) were obtained from basic thermodynamic relationships.

Random 0.5 mM dsDNA samples were prepared from 1 mM solutions of HPLC purified forward and a reverse complementary 15-bp oligonucleotides (5'- GGT 291 TAG TTA TGC GCG -3') synthesized by Integrated DNA Technologies. The pair of oligonucleotides was mixed at an equimolar ratio and annealed by heating 1 min at 99 °C, and performing a 3 h temperature scanning from 95 to 25 °C, decreasing 1 °C each 3 min. 0.5 mM dsDNA stock solutions were obtained.

### 5.4.8 GENERATION OF STRUCTURAL MODELS

Models containing the missing C-loop residues (546-558 and 518-559 respectively for crystal structures of WT hAIF $_{\Delta 1-101}$  and hAIF $_{\Delta 1-101}$ :NADH states), as well as W196A, W196L and W196Y 298 mutations, were built using as templates the coordinates of WT hAIF $_{\Delta 1-101ox}$  (PDB 4BV6) and hAIF $_{\Delta 1-101}$ :NADH (PDB 4BUR) and the Swiss-Model server (Villanueva et al., 2019, Ferreira et al., 2014, Biasini et al., 2014). Routines for minimization and molecular dynamics (MD) simulations followed previous reported protocols (Villanueva et al., 2019) and are summarized in the SI section. Improvements include using a time step of 2 fs and performing five replicas of 10 ns MD production for each model structure.

### 5.4.9 MD SIMULATIONS

Once the protein models were produced, cofactors or coenzymes were reintroduced and 50 ps MD simulations with Generalized-Born -Molecular Volume (GBMV) solvation (Lee



and Salsbury., 2002) and CHARMM c39b1- were carried out to remove potential clashes. Protonation states were assessed using PROPKA 3.0 (Olsson et al., 2011); H131, H457 and H478 were  $\epsilon$ -protonated, while H454 and H455 were  $\delta$ -protonated. MD simulations were performed using CHARMM c39b1 and the charmm36 force field (Brooks et al., 2009). Parameters for FAD, FADH<sup>-</sup>, NADH and NAD<sup>-</sup> were generated using the CgenFF server (Vanommeslaeghe et al., 2010) and density functional theory (DFT). DFT calculations were performed with the Gaussian09 rev.D01 package (Frisch et al., 2016; Grimme, S et al., 2011; Humphrey et al., 1996; Delano, W.L., 2002) at the B3LYP/def2-SVP+GD3BJ level with a water-like polarizable continuum model (Grimme et al., 2011). A Monte-Carlo scheme was used for neutralization, adding ions to 150 mM. A time step of 2 fs, NVT conditions, and a TIP3P water model were used. A standard workflow routine including solvation, neutralization, minimization plus heating and equilibration over 200 ps was performed to the models, followed by a 10 ns MD production run at 298.15 K. Five replicas were performed for each structure. The CHARMM software analysis tools were used to evaluate the resulting conformational ensembles, using a spherical probe with 1.4 Å radius to calculate accessible surfaces. VMD (Humphrey et al., 1996; Delano et al., 2002) were used to analyze and to visualize structural data.

#### 5.4.10 DATA ANALYSIS

Data were fit and shown using SigmaPlot (Systat. Software Inc. Richmond, CA, USA), Origin 7.0 (OriginLab Corporation, Northampton, MA) and Pro-K (Applied Photophysics Ltd. Corporation, Northampton, MA). VMD (Humphrey et al., 1996) and PyMol (Delano, 2002) were used to analyse and visualize structural data, as well as to produce structural figures.

## 5.5 RESULTS AND DISCUSSION

### 5.5.1 MUTATIONS AT W196 RESIDUE HARDLY IMPACT THE OVERALL hAIF $\Delta$ 1-101 CORE CONFORMATIONAL PROPERTIES IN OXIDIZED AND NADH-REDUCED STATES.

The three W196 variants here studied were purified to homogeneity as holoproteins after their expression in *E. coli* as described previously for the WT protein (Ferreira et al., 2014). Their UV-visible absorption spectra showed the characteristic bands I and II of the flavin at 451 and 380 nm, respectively, a shoulder at 476 nm, and  $A_{280}/A_{451}$  ratio  $\approx$  11, indicating that, similarly to the WT protein, the cofactor was in the oxidized state and correctly incorporated to the protein (**Figure 5.3**). Only W196A showed a distorted shape for band-II and lower  $A_{451}/A_{380}$  ratio reflecting some differences in the environment of its flavin ring.

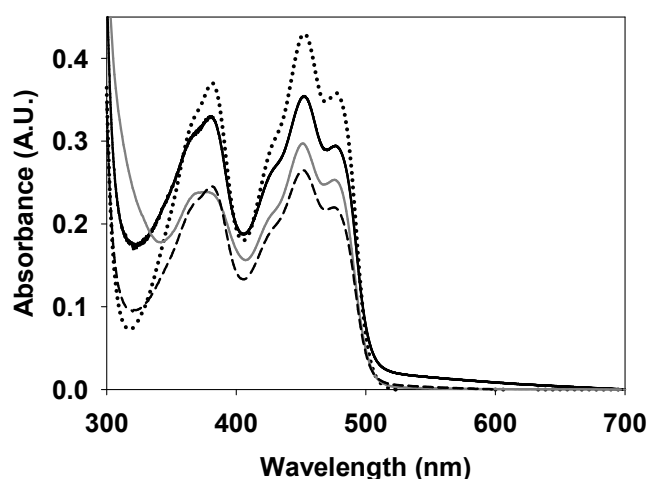


**Figure 5.3: Visible absorption spectra** of WT (16  $\mu$ M), W196Y (39  $\mu$ M), W196L (22  $\mu$ M) and W196A (24  $\mu$ M) hAIF $\Delta$ 1-101 variants. Spectra were recorded in 50 mM potassium phosphate, pH 7.4, at 25  $^{\circ}$ C. Different protein concentrations were used for each variant to clarify the figure.

The W196 variants also had similar far-UV CD spectra to the WT protein, with minima at  $\sim$ 222 and  $\sim$ 208 nm indicative of high  $\alpha$ -helix content (**Figure 5.4 A**). Reduction of the FAD cofactor by NADH produced the decreased in relative intensity of minima at 208 nm for all mutants (**Figure 5.4 B**), as reported for the WT protein. This suggests similar overall conformations in the CTCs (Villanueva et al., 2019). The near-UV/Vis CD spectra of the variants showed the WT characteristic maxima ( $\sim$ 300 nm and  $\sim$ 365 nm) and minima ( $\sim$ 453 and  $\sim$ 477 nm) (**Figure 5.4 C**). Finally, changes observed upon incubation with NADH were also consistent with FAD reduction (lack of near-UV CD signal at 300 nm and in the 350-

500 nm range) and CTC stabilisation (new minima at  $\sim 405$  nm and broad bands at  $\sim 600$  nm) in all variants (**Figure 5.4 D**) (Villanueva et al., 2019).

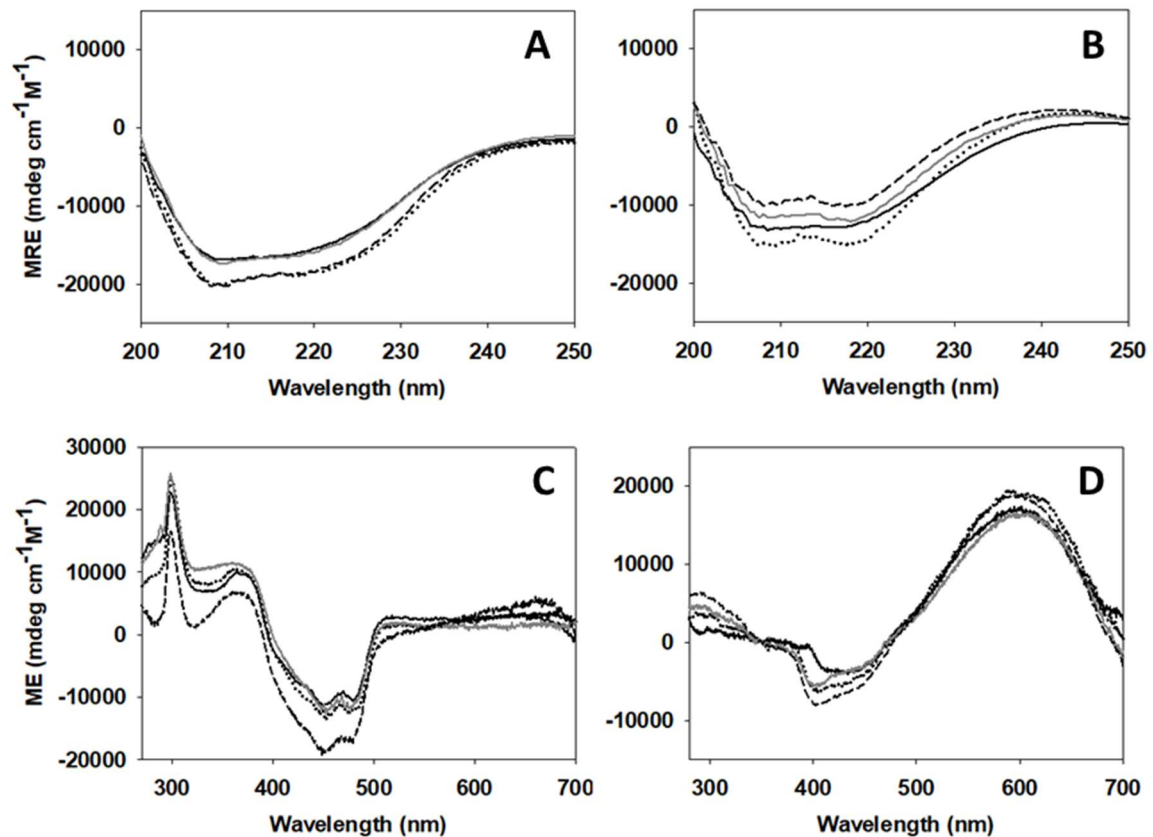


**Figure 5.4: Spectral properties of the W196 hAIF $\Delta 1-101$  variants.** Far-UV CD spectra of (A) the different variants (1  $\mu$ M) and (B) mixtures of each variant (0.5  $\mu$ M) with a 20-fold excess of NADH. Near UV/Vis CD spectra of samples containing (C) the hAIF $\Delta 1-101$  variants (20  $\mu$ M) and (D) mixtures of each variant (20  $\mu$ M) with a 10-fold excess of NADH. CD spectra were recorded at 10  $^{\circ}$ C in 50 mM potassium, pH 7.4, and at final ionic strength of 150 mM. In all panels: WT as solid black line, W196Y as dotted black line, W196L as dashed black line and W196A as grey solid line.

Since the crystal structure is only available for W196A, we built structural models containing the W196 mutations, as well as the missed C-loop residues in the WT X-ray structures, to further evaluate the impact of mutations on the conformation of hAIF $\Delta 1-101$  and its CTC (Villanueva et al., 2019, Ferreira et al., 2014).

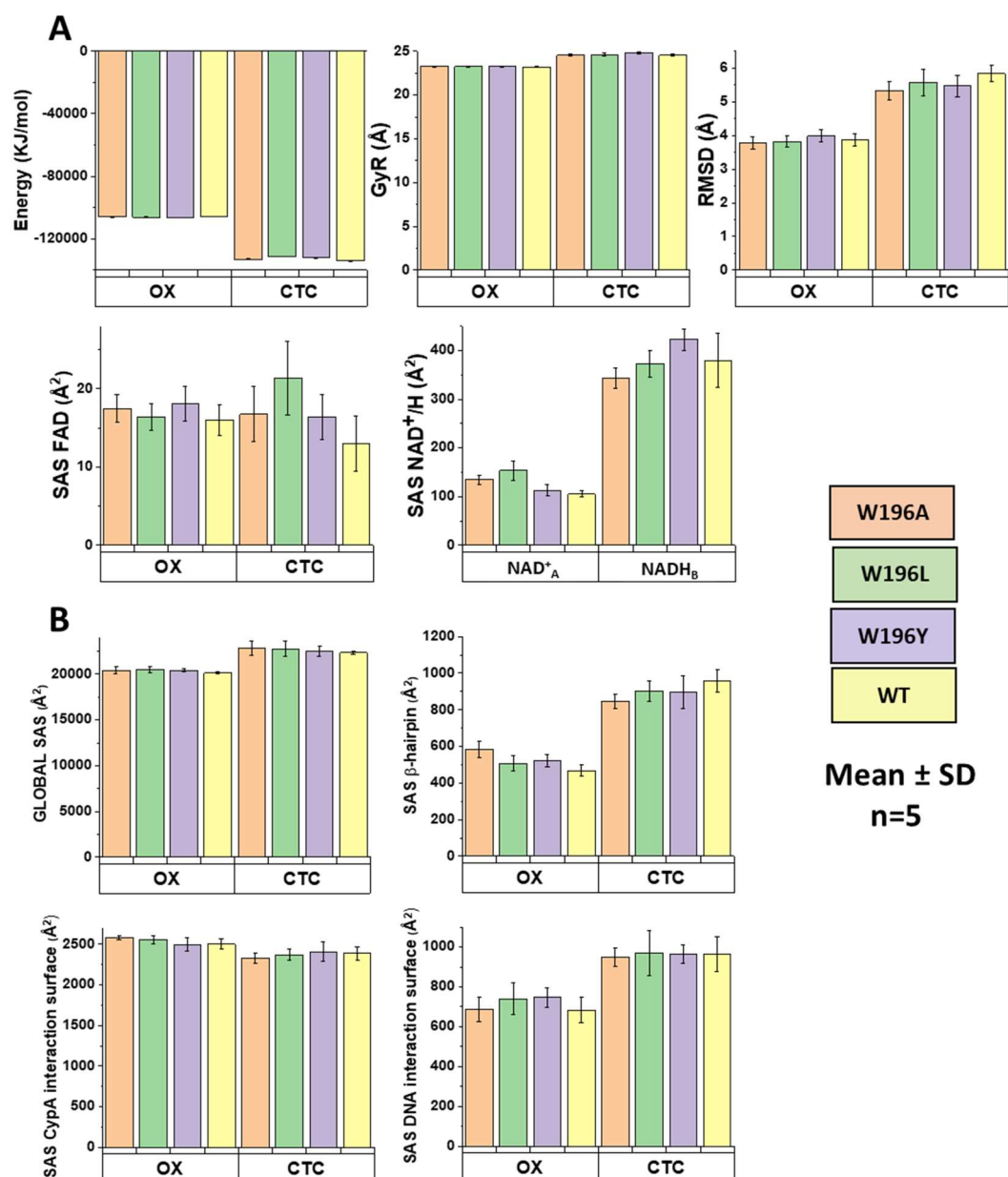


**Figure 5.5:** Dynamics of the models of hAIF $\Delta$ 1-101 variants. **(A)** Averaged values of energy, radius of gyration (RyG), root mean square deviation (RMSD) of backbone, as well as solvent accessible surface (SAS) for the FAD cofactor and the NAD $^{+}$ /H coenzymes. **(B)** Averaged values of SAS for the overall protein, for the  $\beta$ -hairpin, and the predicted interaction surfaces for CypA (residues 345-397), and DNA (residues R265, R446, R449, R450, R451, K510, K518, R584, K590 and K593). All averaged values correspond to the mean of five MD replicates in the 2-10 ns range for each assayed condition. All dynamics equilibrated in the 0-2 ns range.

Models for oxidized variants, including W196A, were built using the WT crystal structure as a template to better evaluate the effect of each mutation on native structures, thus preventing the other variant's models from being "forced" to behave as W196A.

After 10 ns MD relaxation, only small fluctuations within each simulated system were detected for averaged values of energy, radius of gyration, RMSD and solvent accessible surface (SAS) of ligands, as well as for the main interactions coupling the FAD cofactor and NADH coenzyme to the protein (**Figures 5.5 A and 5.6**).

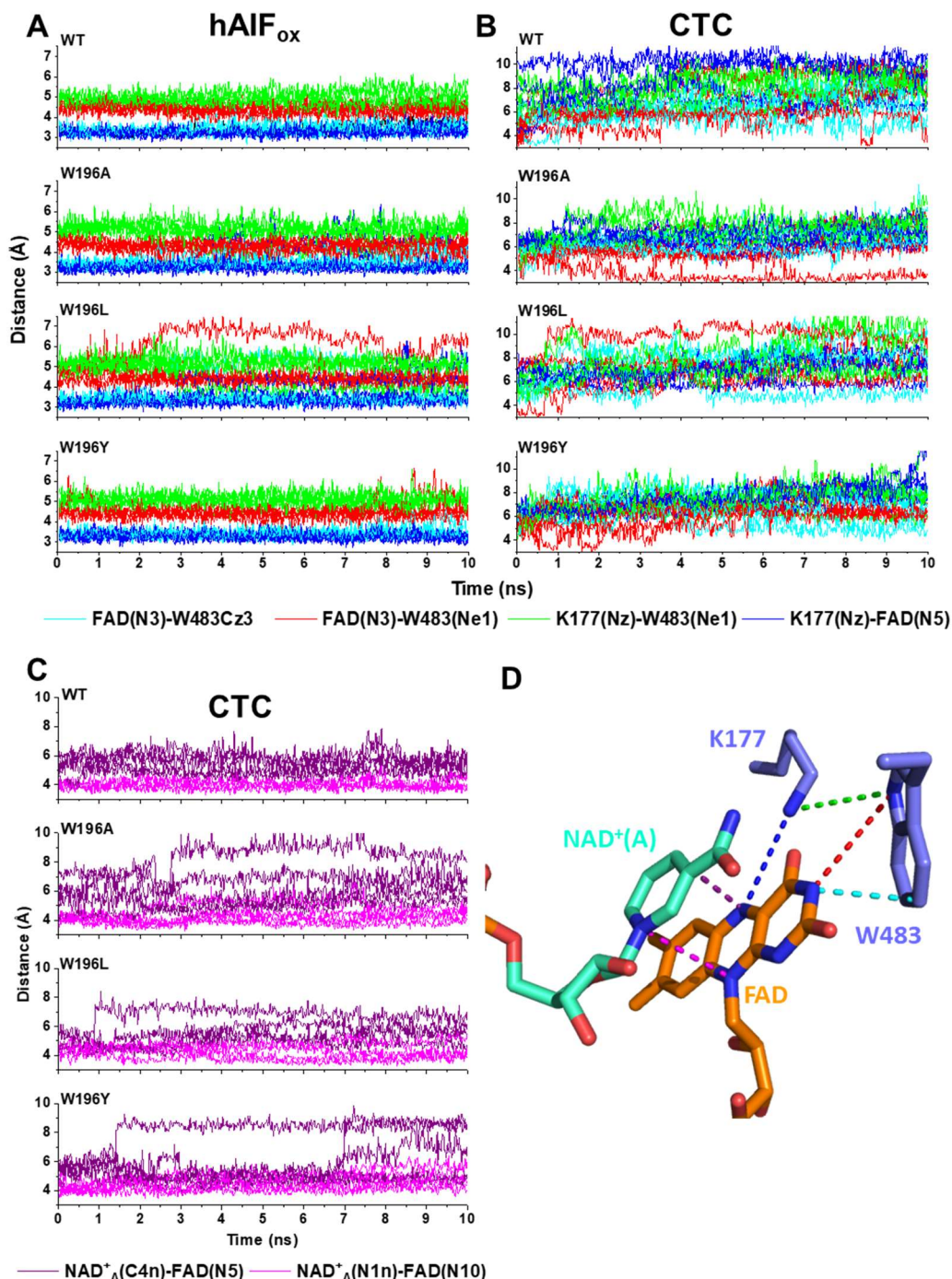


**Figure 5.6: Dynamics of the active site in hAIF<sub>Δ1-101</sub> variants.** Trajectories of selected distances at the active site environment in **(A)** hAIF<sub>Δ1-101</sub> and **(B)** CTC variants, as well as **(C)** between the flavin and nicotinamide reacting rings in CTC models. All panels represent the evolution of distances in five MD replicates run for each model. **(D)** Structural model of the hAIF<sub>Δ1-101</sub> active site with detail of distances represented in the different trajectories.



These observations contrast with those obtained when similarly evaluating the pathogenic deletion of residue R201, situated together with W196 in the  $\beta$ -hairpin and also contributing to C-loop linking (Villanueva et al., 2019). This clinical  $\Delta$ R201 variant rapidly breaks the network linking the FAD cofactor, the  $\beta$ -hairpin itself, the active site residues, the central  $\beta$ -strand, and the C-loop during the MD production (Villanueva et al., 2019). Altogether experimental and modelling evidences indicate that substitutions at W196 retain the WT hAIF $_{\Delta 1-101}$  architecture at the active site and the protein core, in both the oxidized and CTC states. In agreement, W196A<sub>ox</sub> was even able to crystalize (Villanueva et al., 2019).

### 5.5.2 W196 SIDE-CHAIN MODULATES THE MONOMER-DIMER EQUILIBRIUM IN hAIF $_{\Delta 1-101}$ .

Gel filtration chromatography was used to study the impact of mutations on the ability of hAIF $_{\Delta 1-101}$  to undergo NADH-linked dimerization. While, similarly to the WT<sub>ox</sub> protein (**Figure 5.7 A**) (Ferreira et al., 2014), the W196Y mutant eluted as a monomer of apparent molecular weight (MW<sup>app</sup>) ~45-58 kDa (**Figure 5.7 B**), the W196L and W196A variants eluted as considerably broad peaks with lower exclusion volumes.

Peaks deconvolution suggested two populations MW<sup>app</sup> of 63 and 115 kDa for W196L and, 75 and 138 kDa for W196A (**Figure 5.7 C and 5.7 D** respectively), indicating less compact monomeric conformations and/or a quick monomer-dimer exchange. Upon incubation with NADH, the W196Y and W196L variants eluted mainly as a new peak of lower exclusion volume (~145-155 kDa) (**Figure 5.7 B and 5.7 C**) that was previously related to the CTC dimer in the WT protein (**Figure 5.7 A**). Finally, the elution peak for W196A in the presence of NADH, when compared to W196A, also gets narrower and slightly displaced towards the WT CTC dimer elution volume (**Figure 5.7 D**).

Chemical crosslinking with BS<sup>3</sup> -able to covalently conjugate hAIF dimers but not monomers- followed by assessment of species by SDS-PAGE (**Figure 5.7 E**), was then used to evaluate whether the observed chromatographic changes might relate to W196 mutations influencing the compactness of protein conformation and/or the CTC dimer lifetime. Upon incubation with BS<sup>3</sup>, all oxidized mutants exhibited the band of ~55 kDa corresponding to the hAIF $_{\Delta 1-101}$  monomer, although it was in general more diffuse than in the cross-linker absence. When variants were preincubated with both NADH and BS<sup>3</sup>, an additional broad band of ~170 kDa was detected. In WT hAIF $_{\Delta 1-101}$  this band is related to the protein ability to undergo dimerization in the CTC state upon NADH binding and flavin reduction (Ferreira et al., 2014). Noticeably, this band, indicative of dimer stabilisation, was

also observed for W196A (in the absence of the coenzyme), in agreement with the exclusion chromatography data obtained for this variant (**Figure 5.7 D**) and with its reported dimeric crystal structure (Brosey et al., 2016). These data confirm that all W196 variants are able to dimerize upon NADH reduction, but also envisage modulation in the CTC dimer stability upon replacement of W196. They also suggest conformational changes that favour the displacement of the monomer-dimer equilibrium towards the dimer in the oxidized state, particularly in W196A.

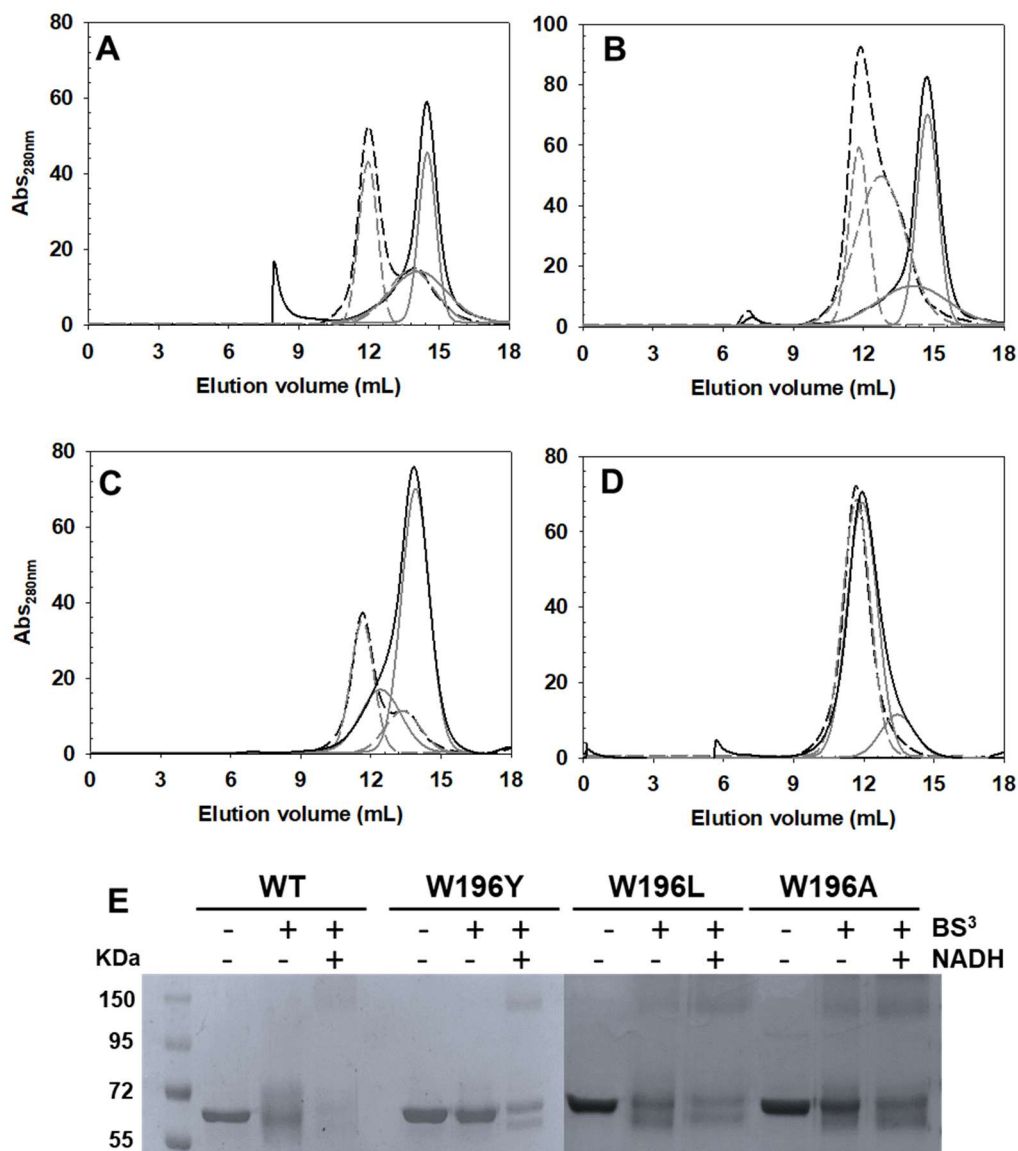


**Figure 5.7: Effect of W196 replacement on the hAIF<sub>Δ1-101</sub> ability to stabilise dimers.** Elution profile of (A) WT, (B) W196Y, (C) W196L, and (D) W196A on a Sephadex S-200 column at 6 °C. The assays were performed in absence and presence of a 10-fold excess of NADH and profiles are respectively shown in black continuous and dashed lines. The respective different populations assigned by Gaussian analysis are depicted in grey lines. (E) Chemical cross-linking of hAIF<sub>Δ1-101</sub> samples (~3 μM proteins) with a 100-fold excess of the BS<sup>3</sup> crosslinker in the absence and presence of NADH (300 μM). After 45 minutes of incubation, the reactions were stopped by the addition of bromophenol sample buffer and resolved by 12% SDS-PAGE.

### 5.5.3 W196 HIGHLY CONTRIBUTES TO MODULATE THE LOW EFFICIENCY OF hAIF $_{\Delta 1-101}$ AS NADH OXIDASE.

Under physiological conditions, hAIF exhibits a NADH oxidase activity that can be in vitro monitored using the steady-state DCPIP dependent diaphorase reaction. When evaluated in this way, all W196 variants showed higher turnover rates than the WT protein (~3-fold increase for W196Y and W196L, and ~5-fold for W196A) (**Table 5.1**).

Regarding  $K_m^{NADH}$ , the W196Y variant value was similar to that for the WT, while the W196L and W196A variants showed a significant decrease (~3-, and 10-fold respectively). Thus, W196Y, W196L and W196A variants were ~3-, ~8 and ~45 more efficient oxidizing NADH than the WT protein. Nonetheless, despite these W196 variants being more efficient as oxidoreductases than WT hAIF $_{\Delta 1-101}$ , they were unable to oxidize NADH when using molecular oxygen as electron acceptor, analogously to the WT protein (Ferreira et al., 2014).

In the light of these results, we studied the impact of the W196 mutations on the HT reaction from NADH to the FAD cofactor of hAIF $_{\Delta 1-101}$  by using stopped-flow transient kinetics. The kinetic traces recorded for all variants at different NADH concentrations indicated an essentially irreversible two-electron reduction of the FAD cofactor with the concomitant formation of a long wavelength broad band related to the formation of the hAIF $_{\Delta 1-101}$ :NADH CTC species (**Figure 5.8 and 5.9**). The intensity of this CTC band (area in the 510–800 nm region minus that of the free protein) for W196A and W196Y variants was in the range of that observed for the WT (Ferreira et al., 2014), indicating similar percentage of CTC stabilisation.



**Table 5.1:** Steady-state and pre-steady state kinetic parameters of WT hAIF $_{\Delta 1-101}$  and its W196 variants.

hAIF	Steady-state			Pre-steady-state					
	$k_{cat}$ (s <sup>-1</sup> )	$K_m^{NADH}$ ( $\mu$ M)	$k_{cat}/K_m^{NADH}$ (s <sup>-1</sup> mM <sup>-1</sup> )	$k_{HT}$ (s <sup>-1</sup> )	$K_d^{NADH}$ ( $\mu$ M)	$k_{HT}/K_d^{NADH}$ (s <sup>-1</sup> mM <sup>-1</sup> )	$k_{CTC}^1$ (s <sup>-1</sup> )	$K_d^{NAD^+}$ ( $\mu$ M)	$k_{CTC}/K_d^{NAD^+}$ (s <sup>-1</sup> mM <sup>-1</sup> )
<b>WT</b>	0.9 $\pm$ 0.1	495 $\pm$ 170	1.9 $\pm$ 0.9	1.5 $\pm$ 0.1	4090 $\pm$ 300	0.4 $\pm$ 0.1	45 $\pm$ 2	2080 $\pm$ 250	22 $\pm$ 3
<b>W196Y</b>	2.7 $\pm$ 0.1	505 $\pm$ 35	5.3 $\pm$ 0.6	12 $\pm$ 1	2870 $\pm$ 320	4.0 $\pm$ 0.8	16 $\pm$ 1	183 $\pm$ 27	87 $\pm$ 14
<b>W196L</b>	2.8 $\pm$ 0.1	187 $\pm$ 18	15 $\pm$ 1.9	36 $\pm$ 1	1725 $\pm$ 210	21 $\pm$ 3	29 $\pm$ 2	433 $\pm$ 11	67 $\pm$ 18
<b>W196A</b>	4.3 $\pm$ 0.2	25 $\pm$ 4	172 $\pm$ 35	126 $\pm$ 1	1070 $\pm$ 40	117 $\pm$ 5.3	30 $\pm$ 1	394 $\pm$ 50	76 $\pm$ 10

Assays were performed at 25 °C in 50 mM potassium phosphate, pH 7.4. (n=3, mean  $\pm$ SD) <sup>1</sup>Kinetic parameters for CTC formations were obtained with hAIF $_{\Delta 1-101phrd}$  variants.

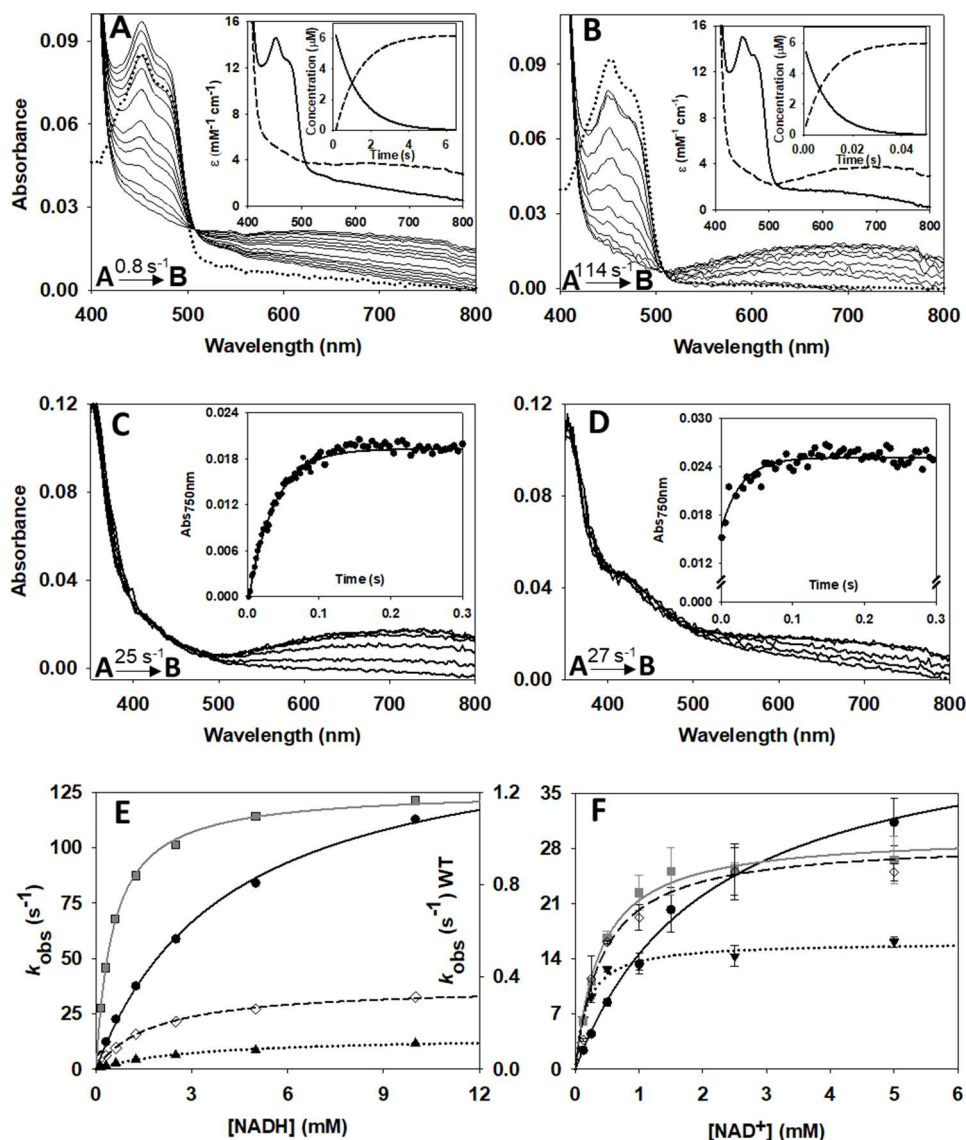
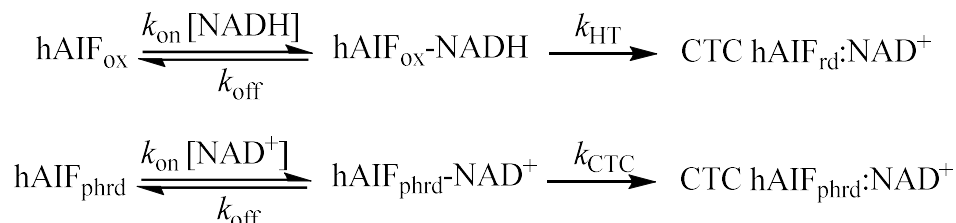


**Figure 5.8: Kinetic characterization of W196 hAIF $\Delta$ 1-101 variants.** Spectral evolution of the reduction of (A) WT ( $\sim 10 \mu\text{M}$ ) and (B) W196A variant ( $\sim 10 \mu\text{M}$ ) when mixed with NADH (2 and 5 mM for WT and W196A respectively). Spectra for the reduction of WT hAIF $\Delta$ 1-101 are shown at 0.15, 1.05, 2.1, 4.2, 6, 10.05, 12.45, 20.1, 30, 40.05, 50.1 s after mixing; and those for W196A at 0.005, 0.05, 0.1, 0.15, 0.2, 0.25, 0.3, 0.45, 0.5, 0.55 s. Dotted lines correspond to the spectra of oxidized enzymes before mixing with the coenzyme. The corresponding insets show the absorbance spectra for the intermediate species obtained by fitting the spectral evolution to a single step model (A $\rightarrow$ B) and the evolution of the concentration of each species. Kinetics of CTC formation upon mixing of the hAIF $\Delta$ 1-101 $_{\text{phrd}}$  forms of (C) WT and (D) its W196A variant with NAD $^{+}$  (5 mM) under anaerobic conditions. Spectral evolution for CTC formation of WT at 0.001, 0.005, 0.01, 0.015, 0.02, 0.07, 0.1, 0.15, 0.2, 0.33, 0.4, 0.5 s after mixing; and those for W196A at 0.001, 0.002, 0.005, 0.006, 0.007, 0.008, 0.009, 0.01, 0.03, 0.05, 0.07, 0.09, 0.1, 0.3 and 0.5 s. The corresponding insets show the absorption evolution at 750 nm (black circle) and the fits (continuous line) at this wavelength after globally fitting evolution at a single step model (A $\rightarrow$ B). (E) Dependence of the observed rate constants for flavin reduction for the WT (black circle), W196Y (black triangle), W196L (black diamond) and W196A (grey square) reactions on the NADH concentration. Lines represent the fits of experimental data to equation 5.3. (F) Dependence of observed rate constants for CTC formation when using WT (black circle), W196Y (black triangle), W196L (black diamond) and W196A (grey square) hAIF $\Delta$ 1-101 $_{\text{phrd}}$  on the NAD $^{+}$  concentration. Lines represent the fit of experimental data to equation 5.4. Assays were performed in a stopped-flow spectrophotometer in 50 mM potassium phosphate, pH 7.4, and at 25  $^{\circ}\text{C}$ . ( $n=3$ , mean  $\pm$  SD).

However, the lower intensity of W196L CTC band  $\sim 76\%$  suggests either different charge distribution between coenzyme and FAD rings in the CTC (suggestive of different CTC geometry) or reduction of the amount of the CTC stabilised. In all cases, global analyses of the spectral range time evolutions best fitted to a one-step model ( $A \rightarrow B$ ).

Thus, the observed processes appeared including the fast formation of the transient  $\text{hAIF}_{\Delta 1-101}:\text{NADH}$  reactive complex followed by the HT reaction and the CTC formation (**Scheme 5.1**).



As consequence, the conformational switches in  $\beta$ -hairpin and C-loop induce protein dimerization in W169 variants, with the potential exception of W196A that presumably is might be mostly a dimer with the C-loop already released in oxidized state (Brosey et al., 2016). The  $k_{\text{obs}}$  values obtained showed hyperbolic dependence on NADH concentration for all variants, allowing  $k_{\text{HT}}$  and  $K_{\text{d}}^{\text{NADH}}$  determination upon fitting to the equation 4 (**Figure 5.8** and **Table 5.1**). All variants showed faster HT rates and higher affinity for the NADH substrate than the WT protein (up to  $\sim 29$ - and  $5$ - fold respectively for W196A). Consequently, W196Y, W196L and W196A were  $\sim 12$ -,  $\sim 24$ -, and up to  $\sim 153$ -fold more efficient than the WT enzyme as hydride acceptors from NADH. Noticeably, and, contrary to that described for WT  $\text{hAIF}_{\Delta 1-101}$ , all these W196 variants showed  $k_{\text{HT}}$  values higher than their turn-over rates, suggesting that HT reaction is not the limiting step during catalysis. Therefore, the W196 side-chain highly contributes to modulate the properties of  $\text{hAIF}_{\Delta 1-101}$  as a non-efficient NADH oxidase.

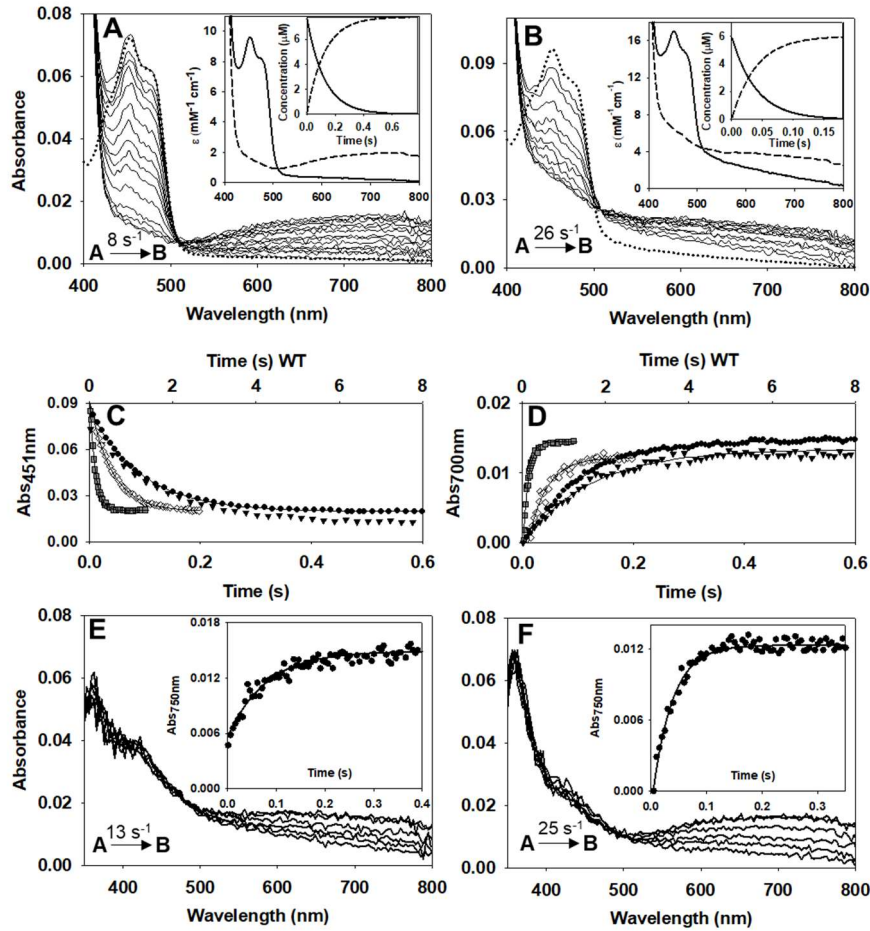


**Figure 5.9: Kinetic characterization of W196 hAIF $\Delta$ 1-101 variants.** Spectral evolution of the reduction of the (A) W196Y ( $\sim 10 \mu\text{M}$ ) and (B) W196L ( $\sim 10 \mu\text{M}$ ) variants when mixed with NADH (5 mM). Spectra for the reduction of W196Y hAIF $\Delta$ 1-101 are shown at 0.001, 0.07, 0.09, 0.477, 0.99, 2, 17, 28, 43, 55 s after mixing and those of W196L at 0.025, 0.05, 0.075, 0.1, 0.15, 0.2, 0.35, 0.55, 0.9 s after mixing. Dotted lines correspond to the spectra of oxidized enzymes before mixing. The insets show the absorbance spectra for the intermediate species obtained by global fitting of the spectral evolution to a single step model (A $\rightarrow$ B) and the evolution of the concentration of each species. Time course of the absorbance changes at (C) the flavin band I (451 nm) and (D) the CTC band (700 nm) reduction by NADH of WT (black), W196Y (dashed line), W196L (dotted line) and W196A (grey) variants. Spectral evolution of CTC formation upon mixing of the hAIF $\Delta$ 1-101<sup>phrd</sup> forms of (E) W196Y ( $\sim 8 \mu\text{M}$ ) and (F) W196L ( $\sim 10 \mu\text{M}$ ) with NAD<sup>+</sup> (5 mM) under anaerobic conditions. Spectra for CTC formation of W196Y are shown at 0.002, 0.004, 0.006, 0.008, 0.01, 0.02, 0.03, 0.05, 0.07, 0.1, 0.2, 0.5, 0.7, 1, 1.5, 2 s after mixing; and those of W196L at 0.001, 0.002, 0.003, 0.006, 0.007, 0.01, 0.02, 0.03, 0.04, 0.05, 0.06, 0.07, 0.08, 0.09, 0.1, 0.2, 0.3, 1 and 2 s after mixing. The insets show the absorbance evolution at 750 nm and the fits at this wavelength when globally fitting evolution at a single step model (A $\rightarrow$ B). Assays were carried out in a stopped-flow spectrophotometer in 50 mM potassium phosphate, pH 7.4, and at 25 °C. All indicated concentrations are final ones.

Structurally, W196 does not form part of the protein redox active site itself. However, its side chain stacks to P488 at the edge of the central  $\beta$ -strand, contributing to situate the  $\beta$ -hairpin and the C-loop so that there is a cavity at the bottom of which sits W483. This residue flanks the pyrimidine ring of FAD stabilising in the NADH binding site (**Figure 5.1 B**). Mutation W196A increases W483 solvent accessibility and C-loop and  $\beta$ -hairpin flexibility, favouring their displacement from their WT positions (**Figure 5.1 C-E and Figure 5.10**).

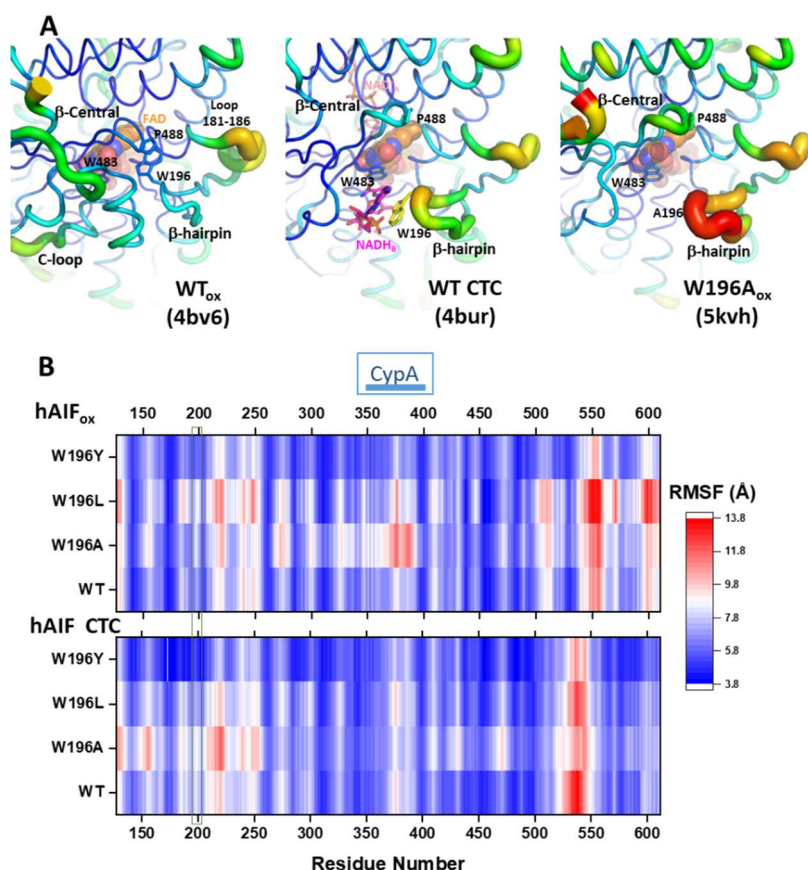


**Figure 5.10: Impact of mutations on hAIF $\Delta_{1-101}$  flexibility.** (A) B-factor putty representation of crystal structures of WT hAIF $\Delta_{1-101}$  (4BV6), WT CTC (4BUR) and W196A hAIF $\Delta_{1-101}$  (5KVH) focusing in the environment of the  $\beta$ -hairpin containing residue 196 and the central  $\beta$ -strand. Orange to red colours and a wider tube indicate regions with higher B-factors, whereas shades of blue and a narrower tube indicate regions with lower B-factors. The FAD cofactor is shown as a stick representation with carbons in orange, while, when present, the NADH<sub>A</sub> and NADH<sub>B</sub> is shown as sphere with carbons in violet. (B) Heat map representation of the average C $\alpha$  root mean square fluctuation (RMSF) of five replicates for 10 ns MD simulations of the different W196 variants in both the hAIF $\Delta_{1-101}$  and CTC states. The region corresponding to the  $\beta$ -hairpin is highlighted with a blue square. Predicted regions for interaction of HSP70, CypA and H2XA are indicated on the top of the panel.

Noticeably, we observed the  $\beta$ -hairpin displacement from P488 as well as the central  $\beta$ -strand retraction from the beginning of our W196A model MD trajectories (starting from WT<sub>ox</sub> structure) (**Figure 5.11 A**). However, the Y196 and L196 side-chains contribute to maintain  $\beta$ -hairpin position in the W196Y and W196L trajectories, and retraction of the central  $\beta$ -strand is hardly guessed for W196L (**Figure 5.11 A**). Trajectories also show a larger increase in the SAS of the  $\beta$ -hairpin of W196A relative to the other two variants and the WT (**Figure 5.5 B**). Thus, MD simulations predict an increase in distances between W483 and atomic positions at the active site of the oxidized variants (**Figure 5.6 A**).

Such changes in W483 solvent accessibility and active site compression must impact substrate affinity and coupling into a competent complex for HT, as well as the FAD midpoint reduction potential and/or electronic distribution as was previously reported for the murine W196A variant (70 mV higher redox potential than those for the WT protein) (Sevrioukova, 2009). In agreement, kinetic parameters show W196A as the variant deviating more from the WT behaviour regarding efficiency for both HT and NADH substrate binding, followed, by far, by W196L and being the aromatic substitution the one producing a milder effect. Dynamics of active site in CTCs show in general higher flexibility regarding oxidized state (**Figure 5.6 A-B**), but WT CTC keeps its characteristic parallel ionic pair through stacking of the NAD<sup>+</sup> nicotinamide and FADH<sup>-</sup> isoalloxazine reacting rings (**Figure 5.6 D**). In such arrangement, the angle formed between the C4n hydride donor, the hydride to be transferred and the N5 acceptor atom (C4n-hydride-N5) appears far from collinearity, involving a large free energy penalty for geometric deformations and partial loss of the  $\pi$  stacking interaction to achieve the transition state (Lans et al., 2010, Lans et al., 2012).

Therefore, despite the C4n-N5 distance being compatible with hydride transfer, the hydride shift can be quite inefficient. This seems to be the situation for HT in WT hAIF, where  $k_{\text{cat}}$  and  $k_{\text{HT}}$  suggest that this protein is a non-efficient NADH oxidase. Noticeably, MD simulations for the W196 CTC variants suggest the distortion of the FADH<sup>-</sup>:NAD<sup>+</sup> and the pulling apart of C4n and N5 reacting atoms (**Figure 5.6 C**).



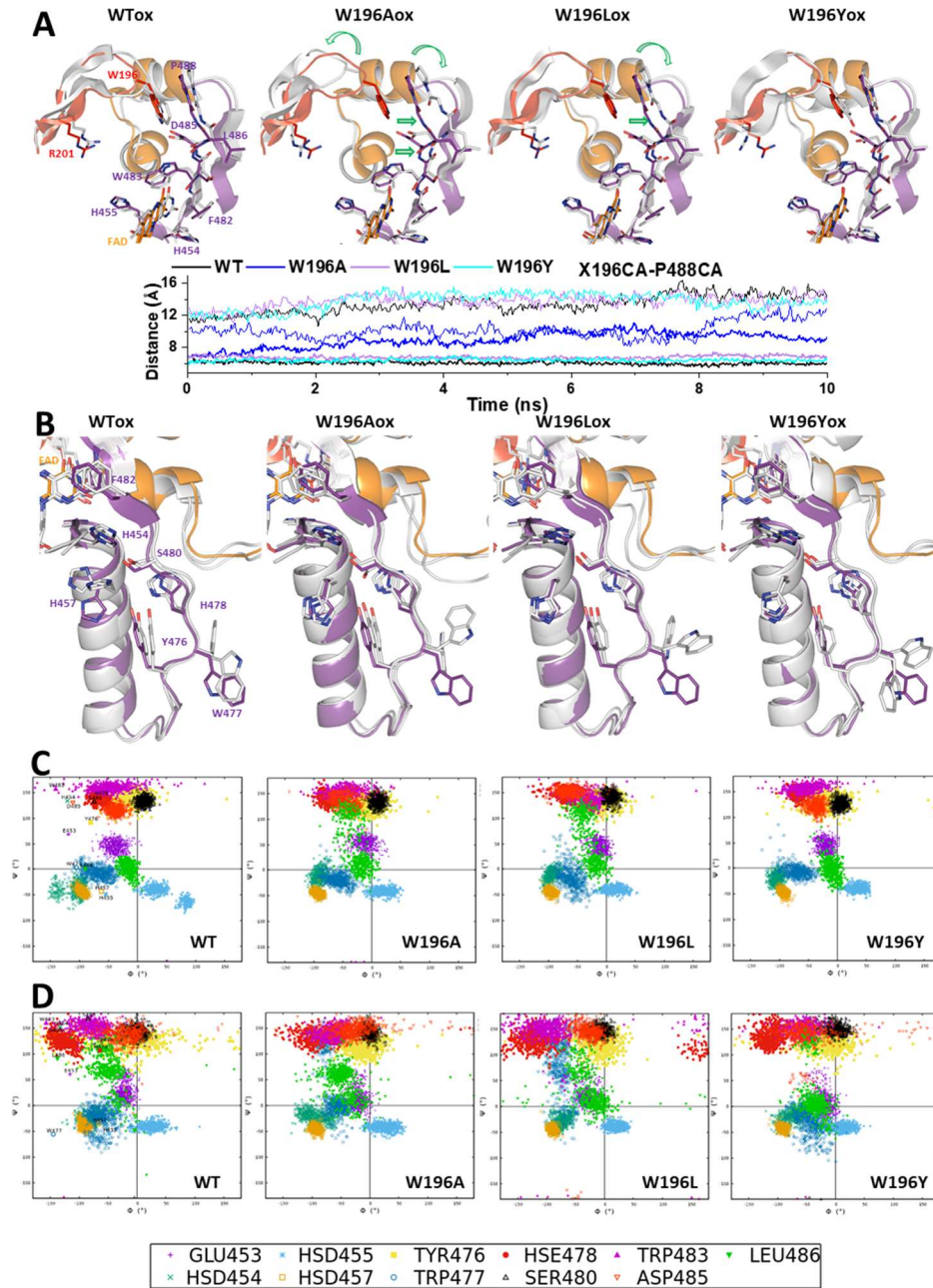


**Figure 5.11: Impact of W196 hAIF $_{\Delta 1-101}$  mutations on the dynamics of the  $\beta$ -hairpin and its environment.** Representative conformations of the **(A)**  $\beta$ -hairpin and the central  $\beta$ -strand and the **(B)** His-rich helix and the loop connecting it to the central  $\beta$ -strand in final MD structures of selected replicates for each W196 variant. MD final replicates are shown in grey in each panel. All panels compare to the crystallographic WT structure (4BV6) that shows the  $\beta$ -hairpin in red, the C-loop in orange and the rest of the protein in purple. Green arrows indicate relevant displacements of structural elements relative to the crystallographic WT structure. The lower panel in **(A)** shows the time evolution of the distances between  $C\alpha$ 's of the residue at position 196 in the  $\beta$ -hairpin and P488 in the  $\beta$ -sheet. For each variant data show averaged values for the 5 MD replicates run for each model in the hAIF $_{\Delta 1-101}$  (bold lines) and CTC (line) states. Ramachandran plots of the distribution of key main chain  $\Phi/\Psi$  conformational along the MD of selected replicates for each **(C)** oxidized and **(D)** reduced W196 variant.

This effect is observed in W196A and W196L CTCs, and to a lower extent in W196Y CTC, in agreement with improvement in their  $k_{HT}$  parameters. Therefore, the size and aromaticity of the side-chain of W196 in hAIF $_{\Delta 1-101}$  is key to fix the  $\beta$ -hairpin position, and both together, despite not forming part of the active site itself, set the active site geometry of this enzyme to make it a non-efficient NADH oxidase.

#### 5.5.4 W196 CONTRIBUTES TO STABILISE THE CTC STATE.

Changes above detected in  $K_m^{NADH}$  and  $K_d^{NADH}$  envisage an important impact of mutations at W196 on the association/dissociation equilibria of NADH and NAD<sup>+</sup> to hAIF $_{\Delta 1-101}$ , we move to evaluate transient rates for CTC formation as well as stability of the CTCs once formed. To determine rates for CTC formation, we mixed hAIF $_{\Delta 1-101phrd}$  samples with different concentrations of NAD<sup>+</sup> in the stopped-flow equipment (**Figure 5.8 C-D, Figure 5.9**).

For all W196 variants, kinetic traces showed CTC formation following an essentially irreversible two species process with  $k_{obs}$  values showing hyperbolic dependence on NAD<sup>+</sup> concentration (**Figure 5.8**). This allows to determine  $K_d^{NAD^+}$  as well as the limiting kinetic constant related to establishment of the nicotinamide:isoalloxazine electronic exchange within the CTC species ( $k_{CTC}$ ) (**Table 5.1, scheme 5.1**). Mutations at W196 produce a strong impact in  $K_d^{NAD^+}$ , whose value decreases by ~5-fold in the Leu and Ala variants, and up to ~11-fold in the Tyr one. This indicates stronger affinity for NAD<sup>+</sup> in the case of the reduced mutants regarding the WT counterpart. On the contrary, the introduced mutations slightly decrease  $k_{CTC}$  values (up to less than 3-fold for W196Y). Therefore, W196 replacement induces stronger affinity of hAIF $_{\Delta 1-101phrd}$  for NAD<sup>+</sup>, but hardly influences the kinetic evolution of the initial transient interacting complex to achieve the final CTC conformation.

These data indicate that replacements at W196 kinetically favour CTC formation by increasing the hAIF $_{\Delta 1-101phrd}$  affinity for NAD<sup>+</sup>. Noticeably, when comparatively evaluating  $K_d^{NADH}$  and  $K_d^{NAD^+}$  values (**Table 5.1**), all W196 variants increase the thermodynamic preference for the binding of NAD<sup>+</sup> over that of NADH regarding the WT.

This agrees with the high impact of mutations on  $k_{HT}$  becoming considerably milder in  $k_{cat}$  values, where release of the NAD<sup>+</sup> product will limit the overall oxidoreductase activity. We then evaluated the mutational effect on the CTC -formed upon NADH oxidation- reactivity towards O<sub>2</sub>. As shown in (**Figure 5.12 A**), the W196A CTC was highly stable versus reoxidation by O<sub>2</sub>, similarly to the WT CTC, (half-lives of 62 and 72 min respectively), while CTC lifetimes were slightly shorter for W196Y and W196L (half-lives of 42 and 32 min



respectively). Therefore, Tyr and Leu replacements favour  $O_2$  access to the FAD cofactor in the CTC. Altogether, these observations point to W196 and the  $\beta$ -hairpin conformation also contributing to the strength of NADH/NAD<sup>+</sup> binding into the hAIF active site.

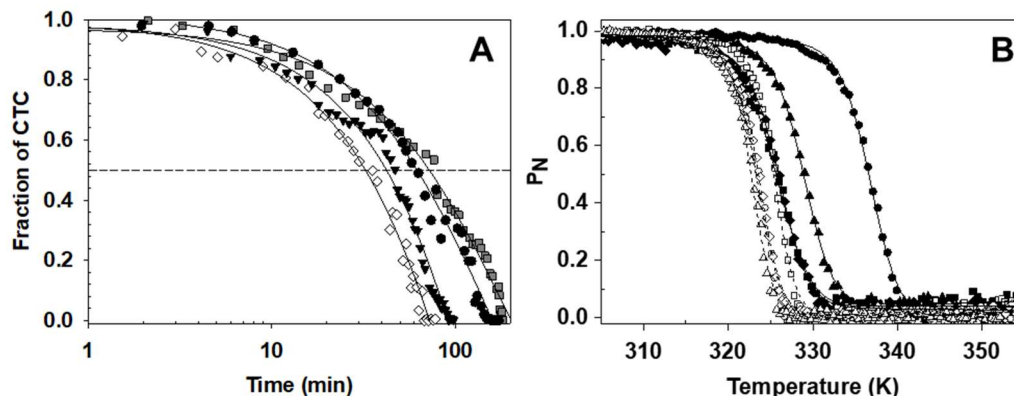


**Figure 5.12: Effect of W196 replacements on the CTC half-life and the thermal stability of hAIF $_{\Delta 1-101}$ .** (A) Reactivity of the CTC towards  $O_2$  in W196 hAIF $_{\Delta 1-101}$  variants. hAIF $_{\Delta 1-101}$ :NADH CTC decay was monitored at 750 nm and 25 °C in air saturated 50 mM potassium phosphate at pH 7.4. CTC hAIF $_{\Delta 1-101}$ :NADH samples were obtained by mixing hAIF $_{\Delta 1-101ox}$  variants with NADH (0.7-fold the enzyme concentration). The traces for WT (black circle), W196Y (black triangle), W196L (black diamond) and W196A (grey square) hAIF $_{\Delta 1-101}$  are shown normalized from 1 to 0 as fraction of CTC remaining along the time. The solid line represents the fit of the traces to a single-exponential decay process to determine CTC half-life. (B) The thermal stability for flavin release ( $T_m^{FAD}$ ) of hAIF $_{\Delta 1-101}$  variants. Curves for FAD thermal release in oxidized variants (closed symbols) and its CTC state (open symbols), as monitored by increase in FAD fluorescence emission upon protein denaturation. The WT, W196A, W196L and W196Y hAIF $_{\Delta 1-101}$  are in black circle, black square, black diamond and black triangle respectively. The curves are roughly normalized to the change in fluorescence signal of the FAD bound fraction ( $P_N$ , from 1 to 0), with their fits to a two-transition unfolding model (continuous and dashed lines for oxidized and reduced states respectively). Decrease in FAD bound fraction was experimentally followed by the increase in its fluorescence upon release from the holoprotein along a 20 to 85 °C temperature ramp. Data were obtained in 50 mM potassium phosphate at pH 7.4 and at a final ionic strength of 150 mM. Protein concentration was  $\sim 2 \mu M$ . The CTC forms were obtained by premixing hAIF $_{\Delta 1-101}$  and NADH at 1:100 ratio.

### 5.5.5 W196 MUTATIONS REDUCE THERMOSTABILITY OF hAIF $_{\Delta 1-101}$ , BUT NOT OF THE CTCs.

Fluorescence emission curves due FAD release upon protein thermal denaturation were then obtained to evaluate the effect of W196 substitution on FAD binding and hAIF $_{\Delta 1-101}$  stability (**Figure 5.12 B**, **Table 5.2**). All W196 variants were less stable than WT, with  $T_m^{FAD}$  dramatically decreasing between  $\sim 8$  and  $\sim 11$  °C. Formation of the WT CTC upon NADH mixing has an even more negative impact in WT hAIF $_{\Delta 1-101}$  stability, decreasing  $T_m^{FAD}$  for the CTC ( $T_{m\ CTC}^{FAD}$ ) by  $\sim 13$  °C relative to  $T_m^{FAD}$  (Villanueva et al., 2019). This destabilising effect was related to release of the regulatory C-loop in the hAIF $_{\Delta 1-101}$  apoptotic domain promoting looser tertiary structure contacts at the active site fostering cofactor dissociation (Villanueva et al., 2019). Interestingly, all reduced CTC variants showed similar  $T_{m\ CTC}^{FAD}$  to the WT CTC. This reflects that CTC formation induces a considerably lower destabilising effect in W196L and W196Y relative to the oxidized state than in WT case ( $T_{m\ CTC}^{FAD} \sim 2$  and  $\sim 6$  °C lower than their  $T_m^{FAD}$  respectively), while no destabilisation is produced at all for W196A. These data suggest that the decrease in compactness of the hAIF $_{\Delta 1-101}$  active site depends on W196 mutation. In agreement, structural predictions indicate that W196A has a larger propensity for  $\beta$ -hairpin release, increasing of  $\beta$ -hairpin SAS as well as conformational rearrangement of the central  $\beta$ -strand and the loop connecting it to the His-rich helix (**Figure 5.11** and **Figure 5.5 B**). Thus, W196A backbone dynamics at these regions envisages a behaviour more similar to the CTC than to WT, while an intermediate situation appears for W196L and W196Y (**Figure 5.11 C** and **5.11 D**). On its side, the very low impact of mutations on  $T_{m\ CTC}^{FAD}$  agrees with conformational rearrangements already produced upon CTC formation, having the W196 side chain less relevance in contributing to the active site compactness (**Figure 5.11 C** and **5.11 D**). Finally, since, according to the WT CTC crystal structure, the W196 side chain contributes to stack the adenine moiety of NADH<sub>B</sub> (**Figure 5.1 E**), such lack of effect is suggestive of NADH<sub>B</sub> binding being considerably weaker than that of NADH<sub>A</sub>. This is clearly supported by the larger SAS for NADH<sub>B</sub> over NADH<sub>A</sub> in the MD simulations, which is in addition variant independent (**Figure 5.5 A**).

**Table 5.2:** Thermal stability for flavin release of WT and W196 hAIF $_{\Delta 1-101}$  variants in oxidized and CTC states.

hAIF	hAIF $_{\Delta 1-101}$			CTC hAIF $_{\Delta 1-101}$ :NADH			
	$T_m^{FAD}$ (K)	$\Delta H$ (kcal/mol)	$\Delta T_m^{FAD}$ (K)	$T_m^{FAD_{CTC}}$ (K)	$\Delta H$ (kcal/mol)	$\Delta T_m^{FAD_{CTC}}$ (K)	$T_m^{FAD_{CTC}} - T_m^{FAD}$ (K)
<b>WT</b>	337 $\pm$ 1	128 $\pm$ 3	--	324 $\pm$ 1	150 $\pm$ 4	--	-13 $\pm$ 2
<b>W196Y</b>	329 $\pm$ 1	123 $\pm$ 3	-8 $\pm$ 2	323 $\pm$ 1	167 $\pm$ 4	-1 $\pm$ 2	-6 $\pm$ 2
<b>W196L</b>	326 $\pm$ 1	118 $\pm$ 3	-11 $\pm$ 2	324 $\pm$ 1	159 $\pm$ 4	0	-2 $\pm$ 2
<b>W196A</b>	326 $\pm$ 1	103 $\pm$ 3	-11 $\pm$ 2	326 $\pm$ 1	170 $\pm$ 4	2 $\pm$ 2	0

Values obtained by fitting fluorescence thermal denaturation curves to a two-state unfolding model. Data obtained in 50 mM potassium phosphate, pH 7.4, at a final ionic strength of 150 mM, from 283.15 to 363.15 K. Protein concentrations was  $\sim$ 2  $\mu$ M and NADH concentration was in 100-fold excess. (n=3, mean  $\pm$  SD).

Therefore, these thermal stability analyses suggest that mutations at W196 decrease the compactness of hAIF $_{\Delta 1-101}$ . Noticeably, some of the pathogenic mutations located at  $\beta$ -hairpin,  $\Delta$ A201, or involved in interaction between the  $\beta$ -hairpin and the regulatory C-loop, F210S/L, are reported to also loss compactness and/or stability (Villanueva et al., 2019, Sancho et al., 2017, Hu et al., 2017).

### 5.5.6 W196 HAS A KEY IMPACT IN THE CONFORMATION OF THE INTERACTION SURFACES OF hAIF $_{\Delta 1-101}$ WITH ITS PHYSIOLOGICAL PARTNERS.

AIF plays a key role in cell death and life through its interaction with nucleotides, but also with DNA and a broad number of proteins. We selected some representative ligands to evaluate the mutational effect of W196 on the hAIF interaction network: CHCHD4 as mitochondrial partner key in OXPHOS and energy homeostasis, and the nuclease CypA and DNA as nuclear partners for chromatinolysis and PCD. We determined the binding parameters that describe the formation of binary complexes using ITC (**Table 5.3, Figure 5.13, 5.14 and 5.15**).

Due the observed W196L tendency to denaturalize during ITC assays, these studies were restricted to WT, W196A and W196Y variants. For all ligands, the binding isotherms adequately fit to a model of a single binding site with  $K_d$  in the micromolecular range.

A bunch of evidences place CHCHD4 in the pathway linking AIF to the biogenesis of mitochondrial complexes by facilitating the mitochondrial import of CHCHD4 and its proper

localization in IMS (Modjtahedi et al., 2015). Nonetheless, heat exchange was not observed when titrating WT<sub>ox</sub> and W196Y with CHCHD4, resulting in binding thermograms characteristic of non-interacting systems (not shown). In contrast, the titration of W196A with CHCHD4 revealed a strong binding of CHCHD4 to W196A ( $K_d \sim 0.4 \mu\text{M}$ ). Binding was entropically driven with the enthalpic contribution opposing (**Figure 5.13 C and 5.15 A**), suggesting that non-specific forces contribute to this interaction. When we analysed the interaction of all CTC variants –obtained by preincubation with NADH- with CHCHD4 (**Figure 5.13 and 5.15 A**), binding was detected, in agreement with previous studies that described such interaction as NADH-dependent (Hangen et al., 2015). The WT CTC:CHCHD4 interaction was driven by a large favourable enthalpic contribution indicative of specific binding, while the entropic contribution being unfavourable. This suggests a complex structurally more organized than its separated protein components. W196Y CTC and W196A CTC kept a similar thermodynamic profile to WT CTC, but the mutations decreased the magnitude of the favourable enthalpic contribution to the binding while made the entropic term considerably less and slightly more unfavourable respectively.

Regarding CHCHD4 affinity, no significant effect was produced by the alanine substitution in both redox states relative to WT CTC, but the W196Y CTC significantly decreased it ( $K_d \sim 10$ -fold higher). Structurally, W196A in solution appears to be mainly as a dimer with a disordered C-loop (Brosey et al., 2016), sharing these features with WT CTC.

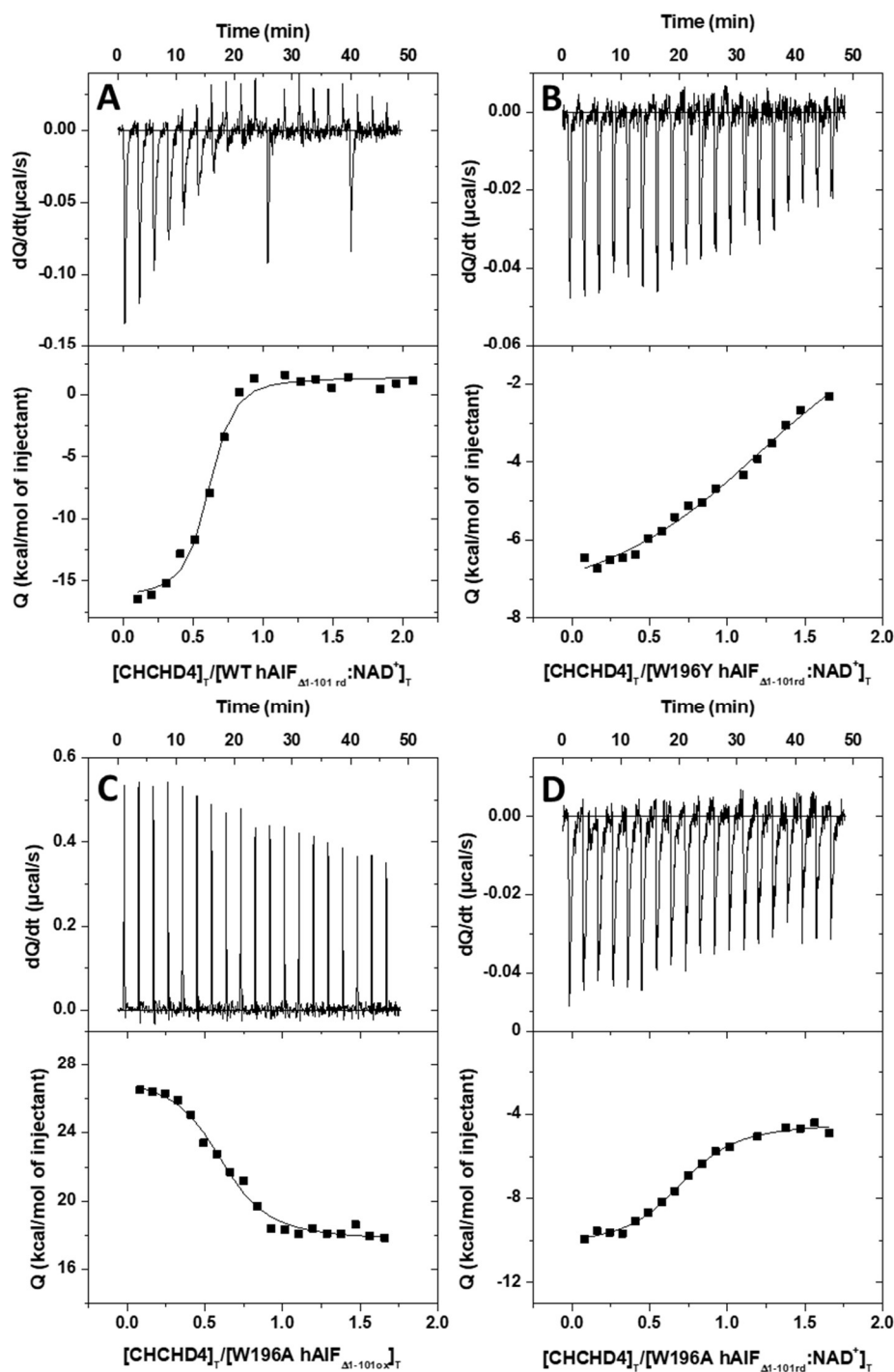


**Figure 5.13:** Effect of the W196 replacement in the binding of CHCHD4 to hAIF $_{\Delta 1-101}$ . Calorimetric titrations of (A) WT CTC, (B) W196Y CTC, (C) W196A (D) W196A CTC with CHCHD4. The upper plots show the thermograms (thermal power as a function of time), whereas the lower plots show the binding isotherm (normalized heats as a function of the CHCHD4/hAIF molar ratio). Measurements were carried out in 50 mM potassium phosphate, pH 7.4 at 25 °C. The CTC forms were obtained by premixing hAIF $_{\Delta 1-101}$  and NADH at 1:100 ratio.

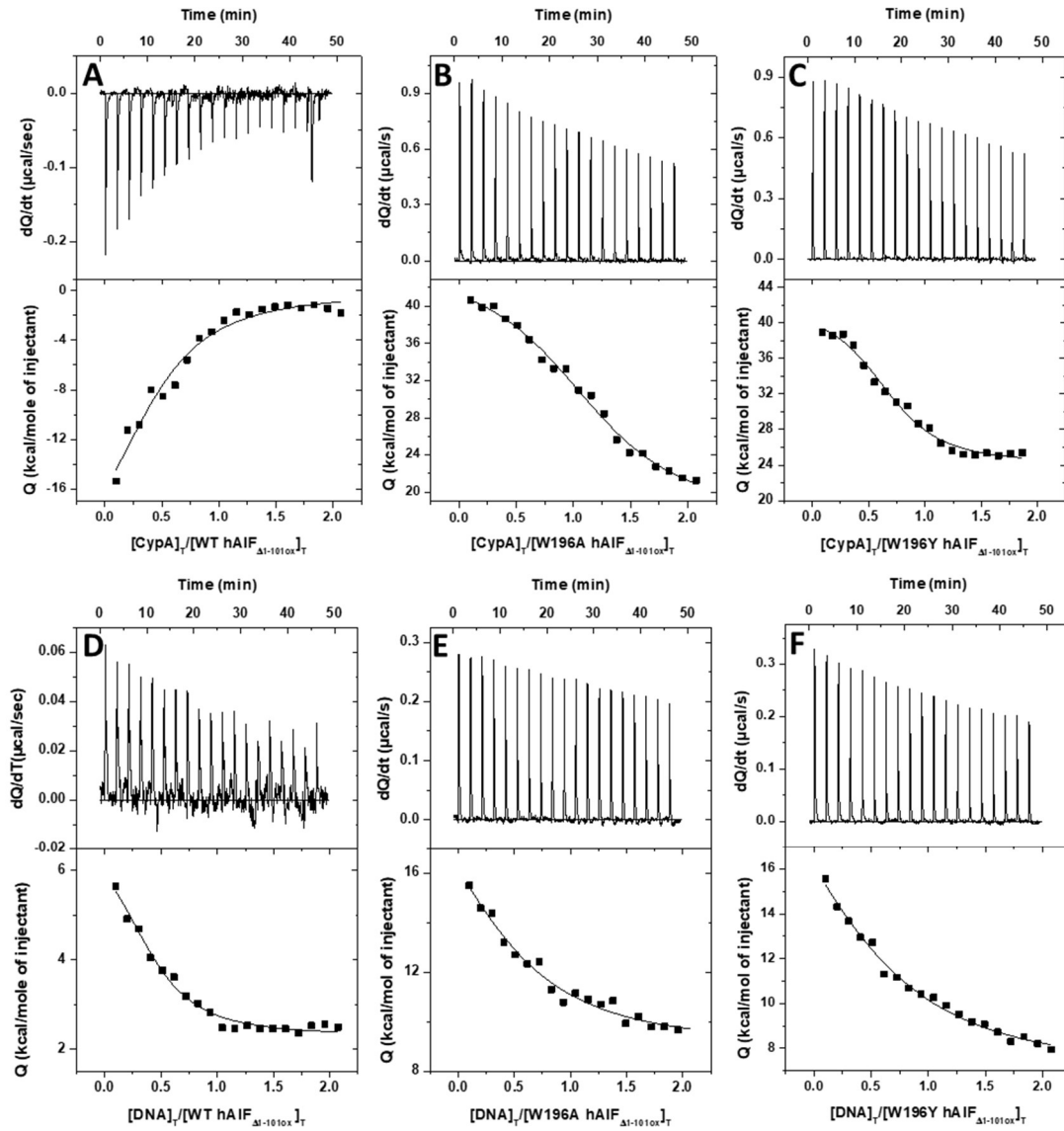


**Figure 5.14: Effect of W196 mutations on the binding to CypA and dsDNA to hAIF $\Delta$ 1-101.** Thermograms (upper panels) and binding isotherms with integrated heat (lower panels) for the calorimetric titration of (A) WT, (B) W196Y, and (C) W196A hAIF $\Delta$ 1-101 with CypA and of (B) WT, (C) W196Y, and (D) W196A hAIF $\Delta$ 1-101 with dsDNA. Titrations were carried out in 50 mM potassium phosphate, pH 7.4, at 25 °C.

Thus, our data might support an essential role of the arrangement of either the dimer conformation, or the site-exposed by C-loop displacement, or even the C-loop itself in the interaction with CHCHD4. Such observations agree with deletion mutants and pathogenic point-mutations at the NADH-domain of hAIF that compromise NADH oxidase activity and CTC structural rearrangements, as a consequence affecting CHCHD4 binding and producing mitochondriopathy phenotypes (Hangen et al., 2015, Berger et al., 2011). However, the W196A enthalpic/entropic thermodynamic binding profile for CHCHD4 is indicate of non-specific interactions, while those for CTCs suggest specific organized interactions (Figure 8, Table 5.3).

A defined interacting region for CHCHD4 has not been identified yet in hAIF, suggesting a relevant role for its entire ternary organization. On the contrary, CHCHD4 binds through a short N-terminal 27-amino-acid-long fragment, while its redox state appears irrelevant for the interaction. This N-terminus is unstructured when CHCHD4 is free (Banci et al., 2009), but appears to get a defined and organized structure when interacting with the CTC (Hangen et al., 2015). This agrees with our data that clearly indicates a specific CHCHD4 binding to WT CTC. On the contrary, the thermodynamic parameters here reported for CHCHD4 binding to W196A, suggest that, despite the conformational changes produced by the mutation allow CHCHD4 recognition, the formed complex will be far from the specific interaction presumably produced with WT CTC. Therefore, structural NADH-dependent changes in AIF, must play a key role in binding of the CHCHD4. This is further supported by the Tyr and Leu replacements for W196 also having a strong impact in the specificity and organization of this interaction. Altogether, these observations suggest that: i) the competent interaction of hAIF with CHCHD4 relies on the adequate CTC architecture to favour the assembly of potentially disorder regions from both proteins to achieve a specific conformation, and ii) W196 contributes to provide such CTC architecture, potentially by regulating the proper  $\beta$ -hairpin configuration that is key for the structural transition of AIF and its role in mitochondrial homeostasis. In agreement, a non-productive interaction between hIAF-CHCHD4 has been suggested for the clinical mutation F210L that results in abnormal assembly of mitochondrial complex I and III (Hu et al., 2017). Parameters for the titration of WT<sub>ox</sub> with CypA indicated the enthalpically driven formation of a binary complex with unfavourable entropic binding contribution (**Table 5.3, Figures 5.14 A and 5.15 B**). This agrees with the large number of electrostatic contacts reported for the CypA interaction with the AIF synthetic peptide (370-394) (Farina et al., 2017, Farina et al., 2018, Monti et al., 2020), as well as with conformational selection and the complex adopting a large complementarity of the two protein.

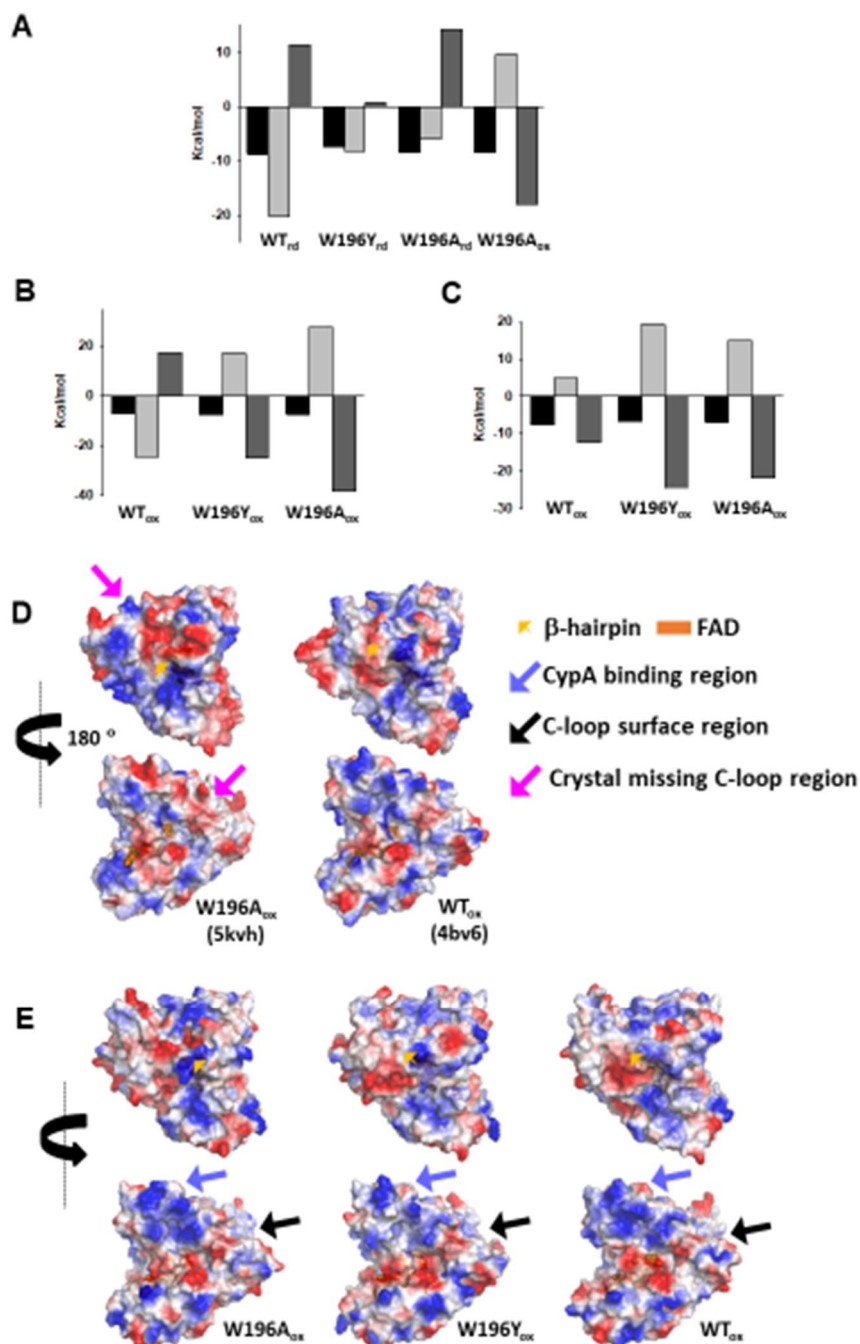


**Figure 5.15: Thermodynamic dissection of the interaction of the different hAIF $\Delta$ 1-101 variants with interacting partners.** (A) CHCHD4, (B) CypA and (C) DNA. Measurements were carried out in 50 mM potassium phosphate, pH 7.4, at 15 °C for DNA and 25 °C for protein partners. The Gibbs energy ( $\Delta G$ ), enthalpy ( $\Delta H$ ), and entropy ( $-\Delta S$ ) contributions to the binding are indicated in black, light grey and dark grey bars, respectively. (D) Comparison of the overall electrostatic potential surfaces of the 3D crystallographic structures of W196A and WT. Positions where the C-loop is missing are particularly highlighted by a pink arrow. (E) Comparison of the overall electrostatic potential surfaces of final structures for representative replicates of the MD simulations for the modelled structures of W196A, W196Y and WT. The interaction region predicted for CypA binding are particularly highlighted by a violet arrow.



Noticeably, the enthalpic contribution to the CypA binding turned into unfavourable for W196Y and W196A (Table 5.3, Figures 5.14 B-C and 5.15 B).

**Table 5.3:** Thermodynamic parameters for the binary interaction of hAIF $_{\Delta 1-101}$  variants with CHCHD4, CypA and DNA.

hAIF form	Titration ligand	$K_d$ ( $\mu$ M)	$\Delta H$ (kcal/mol)	$\Delta G$ (kcal/mol)	$-T\Delta S$ (kcal/mol)
<b>WT and W196Y</b>	CHCHD4				
<b>W196A</b>	CHCHD4	0.4	9.6	-8.4	-18.0
<b>WT CTC</b>	CHCHD4	0.2	-20.1	-8.7	11.4
<b>W196Y CTC</b>	CHCHD4	2.1	-8.2	-7.5	0.7
<b>W196A CTC</b>	CHCHD4	0.5	-5.9	-8.3	14.2
<b>WT</b>	CypA	2.7	-24.5	-7.3	17.2
<b>W196Y</b>	CypA	1.0	17.0	-7.9	-24.9
<b>W196A</b>	CypA	1.8	27.3	-7.6	-34.9
<b>WT</b>	dsDNA	1.6	4.8	-7.6	-12.4
<b>W196Y</b>	dsDNA	6.9	19.2	-6.8	-26.0
<b>W196A</b>	dsDNA	5.8	15.0	-6.9	-22.0

Values obtained from ITC assays at 25°C in 50 mM potassium phosphate, pH 7.4. N is the calculated binding stoichiometry. The thermodynamic parameters were calculated by  $K_d = (K_a)^{-1}$ ,  $\Delta G = RT \ln K_d$  and  $-T\Delta S = \Delta G - \Delta H$ . Errors considered in the measured parameters ( $\pm 20\%$  in  $K_d$  and  $\pm 0.3$  kcal/mol in  $\Delta H$  and  $-T\Delta S$ ) were taken larger than the standard deviation between replicates and the numerical error after the fitting analysis.

This is however compensated by change in the sign of the binding entropic contribution that became highly favourable and made the mutational effect being insignificant regarding overall affinity. However, the mutational switch in thermodynamic contributions to the AIF:CypA binding suggests specificity decrease and production of non-native-like conformations. This is interesting, because W196 and the  $\beta$ -hairpin do not share the protein surface with the AIF NADH-domain where the 370-394  $\beta$ -sheet is situated (Figure 5.16). Nonetheless, replacements at W196 have important effects in hAIF $_{\Delta 1-101}$  stability (Table 5.2), as well as in the conformation of the C-loop, the central  $\beta$ -strand and the dimerization interface sited far away from W196. Therefore, conformational changes occurring in the  $\beta$ -hairpin might be also transmitted to the CypA binding site identified in hAIF. These conformational changes on one site might hinder charge contacts of the 370-394  $\beta$ -sheet to CypA, while on the other they might favour CypA binding to hAIF by C-loop

structural transition towards a more organized and favourable conformation as indicated by the entropy becoming favourable. In agreement, reduction of the flexibility of a stapled peptide analogue of AIF(370-394) to stabilise its  $\beta$ -strand organization in AIF considerably improved its affinity for CypA (Monti et al., 2020). Therefore, the improved specificity for CypA in WT versus the W196 variants might derive from its increased conformational rigidity favouring an induced-fit mechanism of recognition, while increasing protein flexibility turns into an un-specific interaction.

Finally, positive charges clustered along the AIF surface are suggested to contribute to DNA binding, but a clear sequence specificity is not expected since AIF recognizes DNA, RNA as well as a large panel of ribonucleoproteins (Vahsen et al., 2006). Our thermograms for WT titration with dsDNA further confirm such lack of specificity, since they show an entropically driven binding with an unfavourable enthalpy contributing to the interaction (**Figures 5.14 D and 5.15 C, Table 5.3**). W196A and W196Y mutation hardly impair the hAIF $_{\Delta 1-101}$  affinity for DNA in binary complexes ( $K_d$  values  $\sim 4$ -fold higher than WT). However, although thermodynamic patterns resembled the WT ones, entropic and enthalpic binding contributions were respectively more favourable and less unfavourable (**Figures 5.14 E-F and 5.15 C, Table 5.3**). Structurally, binding of DNA to hAIF $_{ox}$  is proposed through the nucleotide strand wrapping around a protein positive charge crown. This crown appears considerably modulated in shape as well as accessibility when comparing crystallographic WT to W196A structure as well as in MD models for all variants (**Figure 5.16**), in agreement with the modulation observed in experimental binding parameters.

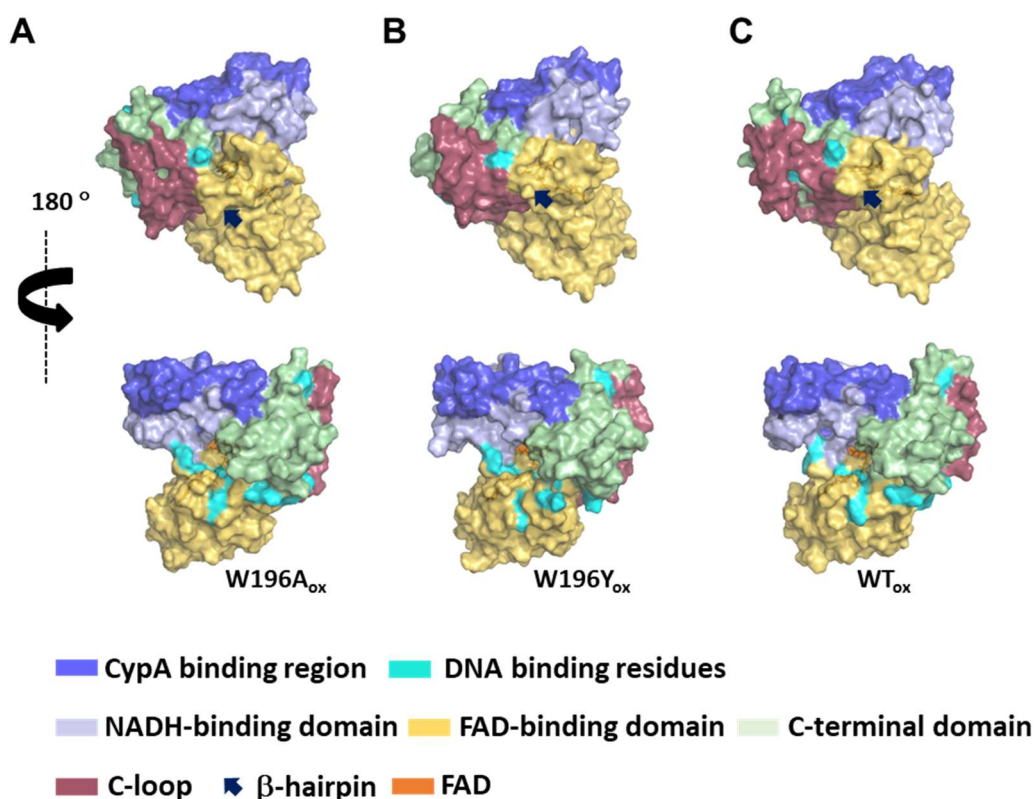


**Figure 5.16: Dynamics of the interaction surfaces for partners in hAIF<sub>Δ1-101</sub> variants.** Comparative overview of surfaces for equilibrated structures for **(A)** W196A, **(B)** W196Y, **(C)** WT. Colour codes of surfaces of interaction and of ligands are as indicated below the figure. Ligands are also shown as sticks within the surfaces. Each figure shows the final structure of one representative replicate of the MD production.

Altogether, these results show that the W196 side-chain influences the enthalpic and entropic contributions to the free energy of binding in binary complexes with CHCHD4, CypA and DNA. Moreover, its replacement has in general a negative impact on the enthalpic binding contribution, while improves the entropic contribution (with the only exception of W196A CTC:CHCHD4 complex). Therefore, W196 contributes to stabilise the conformation of the interaction surfaces of hAIF with CHCHD4, CypA and DNA.

### 5.5.7 W196 CONTRIBUTES TO CONTROL THE hAIF CONFORMATIONAL LANDSCAPE TO ADAPT TO ITS PHYSIOLOGICAL ROLES

AIF is a mitochondrial protein with moonlighting functions in the mitochondria, cytosol and nuclei, where it appears to behave as a redox sensor of NAD<sup>+</sup>/NADH cellular levels (Sevrioukova, 2009, Ferreira et al., 2014, Brosey et al., 2016). The cellular redox state may modulate the AIF conformational landscape regarding both overall protein

conformation and quaternary organization, which in turn appear critical to establish its biomolecular interaction network in a cellular context. The C-loop in AIF is a predicted internally disordered region that tends to adopt an organized conformation in the protein oxidized state (**Figure 5.1, 5.15 and 5.16**), but that is released upon NADH-dependent protein reduction, CTC formation and protein dimerization. The structural properties of W196A suggested that the W196 side-chain and the  $\beta$ -hairpin coupling to the C-loop are key to modulate the structural transition of hAIF in a cellular context.

In healthy mitochondria, hAIF is present in a monomer-dimer equilibrium -regulated by the cytoplasmic NADH pools- that modulates its participation in respiratory complex assembly by physical interactions with CHCHD4 (Ferreira et al., 2014, Modjtahedi et al., 2015, Hangen et al., 2015, Modjtahedi et al., 2016). This AIF switching may be critical for maintaining mitochondrial homeostasis along changes in NAD<sup>+</sup>/NADH ratios in response to diet, diseases such as neurodegenerative disorders, and other processes associated to NAD-consuming enzymes -particularly PARP-1 whose activity is increased during aging due to DNA damage accumulation- (Verdin, 2015, Lautrup et al., 2019). In response to NAD<sup>+</sup> depletion by hyperstimulation of PARP-1, hAIF is released from the mitochondria to the cytosol, allowing its translocation to the nucleus and promoting parthanatos cell death. PARP-1 binding to hAIF has been proved to mediate AIF release from IM by likely inducing conformational changes in hAIF (Wang et al., 2011). Curiously, the expression levels of AIF were found to be gradually decreased during development and growth in spiral ganglion neurons involved in auditory neuropathy spectrum disorder, a disease caused by point mutations in hAIF, while increased in the aging-related cell dysfunctions where AIF role as apoptosis inducer might be more important (Zong et al., 2020). To investigate the different potential roles of hAIF during development and aging and their regulatory mechanisms, future studies will be required. In the last years, a significant number of rare mitochondrial diseases caused by more than 20-point mutations in the AIFM1 gene have been identified. Some mutations in the cell death domain give rise to phenotypes with progressive disorders from childhood, as the Cowchock syndrome. On their side, mutations affecting the hAIF reductase properties decrease the content of respiratory complexes and produce cell respiration deficiencies, while some of them prevent in addition the correct folding of the protein by decreasing its conformational stability. In this later case, the search of molecular chaperones represents an alternative therapeutic strategy yet poorly explored (Villanueva et al., 2019, Berger et al., 2011, Diodato et al., 2016, Ardisson et al., 2015, Sorrentino et al., 2017, Heimer et al., 2018). These mutations produce serious mitochondrial encephalopathies, in many cases with severe processes of neurodegeneration and early death. Noticeably, all characterized pathogenic hAIF

mutants show a substantially decrease in CTC lifetime, suggesting that its stability is crucial for mitochondrial homeostasis and human health (Sevrioukova, 2016, Rinaldi et al., 2012). Further molecular and cellular studies will be required to determine the impact of these pathogenic mutations on the hAIF intracellular processing and interaction with its physiological partners, as well as their link to their multiple clinical neurodegenerative phenotypes.

## 5.6 CONCLUSIONS

This report provides insights into the role in hAIF of W196 and  $\beta$ -hairpin motif in the molecular basis of its cellular activities. Our mutational study shows that, contrary to the pathogenic  $\Delta$ R201 mutation -another residue located in the  $\beta$ -hairpin and involved in the interaction with the regulatory C-loop, changes at W196 residue hardly impacts the overall conformation of hAIF in oxidized and NADH-reduced states. Nonetheless, W196 is key to stabilise  $\beta$ -hairpin motif conformation by ternary contacts and interactions that are substantially diminished and impaired in all characterized W196 variants. Moreover, the W196 and the  $\beta$ -hairpin motif conformation strongly modulate the redox-linked monomer-dimer structural transition in hAIF.

The size and aromaticity of the side chain of W196 is key to:

- i) Maintain the proper  $\beta$ -hairpin position that stabilises and retains the regulatory C-loop in the protein core of oxidized hAIF, favouring protein compactness and stability;
- ii) Configure the NADH active site making hAIF inefficient for NADH oxidation and trigger the C-loop release to the solvent in the reduced state; critical factors for CTC stability and mitochondrial homeostasis;
- iii) Define the interaction surfaces with CHCHD4, CypA and DNA, by modulating the enthalpic and entropic contributions to the free energy of binding. These features contribute to modulate hAIF monomer-dimer equilibrium in a cellular context, which might be relevant for its proper function as a redox sensor of NAD(H<sup>+</sup>) levels and for its interaction network.





## ***6- ANALYSIS OF MITOCHONDRIAL VARIANTS IN THE REDOX FUNCTION OF HUMAN APOPTOSIS INDUCING FACTOR***

### **PERSONAL CONTRIBUTION**

- Expression and purification of AIF and CHCHD4.
- Spectroscopic characterization of AIF variants
- Isothermal titration calorimetry measurements
- Size exclusion chromatography experiments
- Kinetics measurements





## 6.1 ABSTRACT

The human Apoptosis inducing factor (hAIF) is a multifunction protein that participates in the life-death decision of cells. Under physiological conditions in mitochondria, hAIF exhibits its pro-life functions in a monomer-dimer equilibrium that moves towards the dimer due to NADH binding and reduction of its FAD cofactor. Oxidation of NADH by hAIF, produces a highly oxygen-stable FADH:NAD<sup>+</sup> charge transfer complex (CTC) along with the equilibrium shift towards the dimeric form of the protein. Recently, the role of hAIF has been accepted as a regulator agent involved in the mitochondrial intermembrane space (IMS) import machinery and in the assembly of respiratory complexes by assisting the chaperone CHCHD4. Thus, the hAIF-CHCHD4 interaction represents a crucial finding in understanding the vital role of hAIF in the mitochondrial life cycle. Therefore, further studies are needed to better understand the regulation of this interaction at the molecular level.

Most of the available information on the hAIF-CHCHD4 interaction has been reported using the apoptotic form of hAIF, hAIF<sub>Δ1-101</sub>, which is not found in the IMS. To gain insights into the molecular basis of the hAIF-CHCHD4 interaction and its contribution to the NADH oxidase activity of hAIF in mitochondria, here, we used a construct of a mitochondrial soluble variant of hAIF, hAIFmt<sub>Δ1-77</sub>, as well as of its corresponding triple mutant (hAIF E413A/R422A/R430A) unable to dimerize. Our data demonstrate that, contrary to what was found with hAIF<sub>Δ1-101</sub>, mitochondrial variants are able to bind CHCHD4 when oxidized. Furthermore, they show that the presence of CHCHD4 favours the activity of hAIFmt<sub>Δ1-77</sub> as a NADH oxidase by particularly increasing the affinity of the protein for the coenzyme. These observations contribute to our better understanding at the molecular level of the effects of the hAIF-CHCHD4 interaction on the NADH-dependent redox activity of this flavoenzyme.

## 6.2·RESUMEN

El factor de inducción de apoptosis humano (hAIF) es una proteína multifuncional que participa en la decisión de vida-muerte de las células. En condiciones fisiológicas, en las mitocondrias, hAIF exhibe sus funciones pro-vida en un equilibrio monómero-dímero que se desplaza hacia el dímero debido a la unión del NADH y la reducción de su cofactor FAD. La oxidación del NADH por la hAIF, produce un complejo de transferencia de carga (CTC) FADH:NAD<sup>+</sup> altamente estable frente a la reoxidación por oxígeno, junto con el desplazamiento de equilibrio hacia la forma dimérica. Recientemente, se ha aceptado el papel de hAIF como agente regulador del mecanismo de importación de proteínas en el espacio intermembrana mitocondrial (IMS) y del ensamblaje de los complejos respiratorios, a través de su cooperación con la chaperona CHCHD4. Así, la interacción hAIF-CHCHD4 representa un hallazgo crucial para entender el papel de hAIF en el ciclo vital mitocondrial. Por lo tanto, se necesitan más estudios para entender la regulación de esta interacción y su impacto a nivel molecular.

La mayor parte de la información disponible sobre la interacción hAIF-CHCHD4 se ha descrito utilizando la forma apoptótica de hAIF, hAIF<sub>Δ1-101</sub>, que no se encuentra en el IMS. Para conocer mejor la interacción hAIF-CHCHD4 y su contribución a la actividad NADH oxidasa de hAIF en las mitocondrias, hemos usado una construcción de una variante soluble mitocondrial de hAIF, hAIFmt<sub>Δ1-77</sub>, así como su correspondiente triple mutante (hAIF E413A/R422A/R430A) incapaz de dimerizar. Nuestros datos demuestran que, al contrario que hAIF<sub>Δ1-101</sub>, las variantes mitocondriales en su estado oxidado son capaces de unirse a CHCHD4. Además, los datos presentados aquí muestran que la presencia de CHCHD4 favorece la actividad de hAIFmt<sub>Δ1-77</sub> como NADH oxidasa al aumentar, especialmente, la afinidad de la proteína por la coenzima. Estas observaciones contribuyen a una mejor comprensión a nivel molecular de los efectos de la interacción hAIF-CHCHD4 sobre la actividad redox dependiente de NADH de esta flavoenzima.

## 6.3 INTRODUCTION

The protein apoptosis-inducing factor (hAIF) was first described as a mitochondrial flavoprotein involved in caspase-independent programmed cell death (PCD) (Susin et al., 1999b). However, a key role of this protein in the integrity and/or biogenesis of respiratory complexes became apparent shortly thereafter (Vahsen et al., 2004). Thus, hAIF is a pluripolar protein involved in the "decision" between cell life and cell death (Jeffery, 2014). The precursor of functional forms of hAIF is synthesized in the cytosol, and after its importation into the intermembrane mitochondrial space (IMS) is enzymatically removed its N-terminal region producing the mature mitochondrial form (hAIF<sub>Δ1-54</sub> in *Homo sapiens*). The N-terminus of this mitochondrial form is anchored to the inner mitochondrial membrane (IMM), whereas its soluble region folds into the IMS and incorporates the FAD cofactor (Otera et al., 2005). It is proposed that this mitochondrial form plays a role in the biogenesis of respiratory chain complexes through its attachment to the coiled-helix domain-containing protein-4 (CHCHD4), without requiring additional partners.

CHCHD4 is a chaperone that promotes the import of selected proteins into the IMS, including within its primary targets several disulphide bond-containing subunits of the respiratory chain complexes. The cysteine-proline-cysteine (CPC) motif of CHCHD4 promotes the oxidative folding of the imported proteins by oxidizing their cysteine groups to disulphide bonds, resulting in the reduced state of CHCHD4 (Murschall et al., 2020; Hangen et al., 2015). Consequently, CHCHD4 depletion has been shown to decrease the expression levels of several respiratory chain subunits, resulting in functional defects in complexes I and IV (Otera et al., 2005). It is then proposed that the CPC motif of CHCHD4 is reoxidised by transferring the acquired electrons to the FAD cofactor of the hepatic regulated reductase (ALR, Erv1-linked sulfhydryl oxidase in *S. cerevisiae*), regenerating CHCHD4 to initiate a new cycle (Chatzi et al., 2016). However, translation-dependent import events at the IMS of CHCHD4 have been shown to require hAIF, making this downstream protein an essential factor in biogenesis, maintenance of respiratory complexes, mitochondrial integrity, as well as cell survival and proliferation (Murschall et al., 2020).

The mechanism by which the interaction of hAIF with CHCHD4 contributes to the assembly of respiratory complexes is not yet well understood, but it is known to occur through the NADH-oxidase activity of hAIF and is favoured when the enzyme is reduced (Modjtahedi et al., 2015). In the IMS, hAIF<sub>Δ1-54</sub> is present in a monomer-dimer equilibrium that shifts towards dimer due to NADH binding and reduction of its cofactor FAD (Ferreira et al., 2014). *In vitro* studies have shown that NADH oxidation by the apoptotic form of

AIF<sub>Δ1-101</sub> (the one that translocates to the cytosol under conditions of apoptotic insult) is a relatively inefficient redox process that produces a highly oxygen-stable FADH:NAD<sup>+</sup> charge transfer complex (CTC) coupled to protein dimerization. The 3D crystallographic structure of the hAIF CTC shows that NADH coenzyme accommodation and FAD reduction induce the restructuring of a 50-residue region at the C-terminus (C-loop 509-560) that becomes disordered and gives way to the creation of a second non-catalytic NADH-binding site (Ferreira et al., 2014). Furthermore, CTC stabilisation induces hAIF dimerization through the establishment of salt bridges between the two protomers. Their binding is stabilised through a network of H-bonds involving several residues (G308, F310, L311, E314, E336, G399, E453, H454 and W483). In addition, the non-dimerizable hAIF<sub>Δ1-101</sub> E413A/R422A/R430A variant exhibits reduced CTC stabilization due to disruption of the interaction at the dimerization surface. Thus, the global conformation of hAIF is regulated by binding to NADH and by the redox state of its FAD cofactor. This indicates that redox sensing of the cell's NADH/NAD<sup>+</sup> levels by hAIF will impact the interaction with its protein partners in the different cellular compartments in which it is found throughout the cell life cycle (Villanueva et al., 2019, Churbanova and Sevrioukova, 2008, Brosey et al., 2016, Sevrioukova, 2009).

In this context, NADH-dependent structural changes associated with hAIF reduction are essential for its specific binding to CHCHD4, suggesting that the interaction site in hAIF might be conformational, although for CHCHD4 the first 27 N-terminal residues have been reported to be sufficient (Romero-Tamayo et al., 2021; Hangen et al., 2015). The hAIF-CHCHD4 interaction represents a crucial finding, but, so far, most *in vitro* studies characterizing it have been reported using the apoptotic form, hAIF<sub>Δ1-101</sub>, which is not found in the IMS. To better understand the impact of the hAIF-CHCHD4 interaction and its contribution to the NADH oxidase activity of hAIF, here we used a mitochondrial soluble variant of AIF from *Homo sapiens*, hAIFmt<sub>Δ1-77</sub>. hAIFmt<sub>Δ1-77</sub> lacks the anchoring helix of the IMM but contains the entire soluble portion of the protein. In addition, we used the mitochondrial form of the non-dimerizable E413A/R422A/R430A mutant of hAIFmt<sub>Δ1-77</sub> (Ferreira et al., 2014), hereafter hAIF3Mmt<sub>Δ1-77</sub>, to assess the relevance of the mitochondrial protein dimer in the interaction with CHCHD4. Our results indicate that, unlike the apoptotic form, hAIFmt<sub>Δ1-77</sub> is able to bind CHCHD4 in its oxidized state. However, hAIFmt<sub>Δ1-77</sub> reduction by NADH, despite increasing the affinity of the interaction with the chaperone, forms a weaker complex than that observed for the NADH reduced apoptotic form. These results will contribute to the better understanding of the relevance of hAIF FAD redox activity in mitochondrial bioenergetic metabolism as part of its pro-life functions.

## 6.4 MATERIAL AND METHODS

### 6.4.1 OVEREXPRESSION AND PURIFICATION OF hAIF AND CHCHD4 VARIANTS

The apoptotic form of *Homo sapiens* AIF, hAIF<sub>Δ1-101</sub>, and its triple mutant, hAIF3M<sub>Δ1-101</sub>, were produced as previously described (Ferreira *et al.*, 2014). To produce the corresponding soluble mitochondrial hAIFmt<sub>Δ1-77</sub> and hAIF3Mmt<sub>Δ1-77</sub> variants, GenScript synthesized the cDNA constructs encoding them (optimized codon for expression in *Escherichia coli* C41 (DE3)) with a C-terminal His<sub>6</sub>-tag and, subcloned them into the expression vector pET28a (pET28-hAIFmt<sub>Δ1-77</sub> and pET28-hAIF3Mmt<sub>Δ1-77</sub>). Further information can be found at the materials and methods chapter of this thesis. *E. coli* cells transformed with the hAIF<sub>Δ1-101</sub>, hAIFmt<sub>Δ1-77</sub> plasmids and their corresponding triple mutants were grown in 10 L LB medium containing 30 mg/L kanamycin and supplemented with 0.08 g/L riboflavin. Cell cultures were incubated at 37 °C and 180 r.p.m. At an OD<sub>600nm</sub> ≈ 0.8, cultures were induced with 1 mM IPTG (BioChemica) and incubated for an additional 18-24 h. Cells were then harvested and proteins were purified following the procedure already described for hAIF<sub>Δ1-101</sub> (Ferreira *et al.*, 2014). Briefly, the pellet was resuspended in 50 mM Tris/HCl, pH 8.0 and lysed by sonication on ice. The cell lysate was centrifuged to remove debris, and then mixed with 2.5 mL of Ni<sup>2+</sup> IMAC Sepharose 6 Fast Flow gel (GE Healthcare) previously equilibrated in the afore mentioned buffer. The mixture was incubated in a bidirectional rocker for 1 h at 4 °C with 0.4 M KCl and 4 mM imidazole, and then loaded onto a column. Protein samples were eluted with a linear gradient of 40-500 mM imidazole in 50 mM Kpi, pH 7.4.

A similar protocol was used for CHCHD4 production with some differences: i) cultures were induced at OD<sub>600nm</sub> ≈ 0.5, then incubated for additional 3 h; ii) the imidazole gradient was 40 to 1000 mM in 50 mM Kpi, pH 7.0, 150 mM NaCl; iii) the protein was stored in 50 mM Kpi, pH 7.4, for use within a few days, while for longer storage time it was supplemented with 10 mM DTT to maintain the catalytic disulphide motif Cys53-Pro54-Cys55 in reduced state.

## 6.4.2 SPECTROSCOPIC CHARACTERIZATION

UV-Visible spectra were recorded at 25 °C in a Cary 100 Bio spectrophotometer (Agilent technologies) using 1 cm cuvettes. Protein concentrations were determined using the molar absorbance extinction coefficient determined for each protein ( $\epsilon_{451\text{nm}}$  of 13.6 and 13.4  $\text{mM}^{-1}\cdot\text{cm}^{-1}$  for hAIF $_{\Delta 1-77}$  and hAIF3M $_{\Delta 1-77}$  respectively, and  $\epsilon_{280\text{nm}}$  of 13.3  $\text{mM}^{-1}\cdot\text{cm}^{-1}$  for CHCHD4). Coefficients for hAIF variants were calculated by spectroscopic methods following previously described protocols (Ferreira *et al.*, 2014), and the one for CHCHD4 is the theoretical one obtained using the ProtParam tool. All values are shown in **Table 3.9**.

## 6.4.3 EVALUATION OF MONOMER-DIMER STATES BY SIZE-EXCLUSION CHROMATOGRAPHY

The dimerization capacity of the apoptotic and mitochondrial forms of hAIF was assessed by molecular exclusion chromatography. Protein samples, both in the absence and presence of a 10-fold excess of NADH, were loaded onto a HiPrep 26/60 Sephacryl TMS-200 High Resolution column (GE Healthcare) coupled to a fast pressure liquid chromatography system (GE Healthcare). Protein elution was performed in 50 mM Kpi buffer, 150 mM NaCl, pH 7.4, or 6.2 for the hAIF $_{\Delta 1-77}$  form, and at a flow rate of 0.5 mL/min and 6 °C. The column was previously calibrated with the GE Healthcare LMW calibration kit (6 proteins in the range 6400-160000 Da). The chromatograms obtained were fitted to a set of Gaussian functions.

The ability of hAIF and CHCHD4 to interact was also assessed by molecular exclusion chromatography. Reduced hAIF was incubated with a 10-fold excess of NADH in the presence or absence of CHCHD4 in a 1:3 ratio for 15 min at room temperature in 50 mM Kpi, pH 7.4. The samples were then loaded onto a Sephadex S-200 column. Chromatography was carried out using the above buffer supplemented with 10 mM NaCl.

## 6.4.4 ISOTHERMAL TITRATION CALORIMETRY (ITC)

Since the AIF-CHCHD4 interaction is crucial for understanding the vital role of hAIF in mitochondria, the thermodynamic parameters for the interaction of different hAIF forms with CHCHD4 was assessed by isothermal titration calorimetry (ITC) using an Auto-iTC200 MicroCal microcalorimeter (Malvern Instruments). Typically, 10  $\mu\text{M}$  of hAIF proteins were titrated with 100  $\mu\text{M}$  solutions of CHCHD4. Prior to each assay, solutions were degassed at 15 °C for at least 2 min. A sequence of injections of 2  $\mu\text{L}$  of titrating solution was programmed

every 150 s and the stirring speed was set at 750 r.p.m Titration assays with CHCHD4 were performed at 25 °C. The association constant ( $K_a$ ), enthalpy change ( $\Delta H$ ) and binding stoichiometry ( $n$ ) were estimated by nonlinear regression of the experimental data employing a single ligand binding site model (1:1 protein:ligand stoichiometry) implemented in Origin 7.0 (Velázquez-Campoy et al., 2006; Wiseman et al., 1989). The errors in the measured parameters were  $\pm 0.3$  kcal/mol for the thermodynamic parameters ( $\Delta H$ ,  $\Delta G$  and  $T\Delta S$ ) and  $\pm 20\%$  for the binding constants ( $K_a$  and  $K_d$ ).

#### 6.4.5 KINETIC MEASUREMENTS

Steady-state kinetic analyses were performed to determine the influence of CHCHD4 on the NADH oxidase activity of hAIF. Measurements were performed in a Cary 100 Bio spectrophotometer (Varian) in 50 mM air-saturated Kpi, pH 7.4, at 25 °C. Different pH values were used to resemble physiological conditions: pH 6.2 resembling IMS, pH 7.4 in the cytosolic/nuclear environments. NADH (Sigma Aldrich) was used as substrate donor and 95  $\mu$ M dichlorophenolindophenol (DCPIP) (Sigma Aldrich) as acceptor (Ferreira et al., 2014). The reactions were followed by the reduction of DCPIP at 620 nm ( $\epsilon_{\Delta 620\text{nm}} = 21 \text{ mM}^{-1}\cdot\text{cm}^{-1}$ ). The reaction was initiated when NADH was added to mixtures containing premixed samples of the reagents to give a final concentration of 75 nM hAIF and 0.2  $\mu$ M CHCHD4. The kinetic parameters were determined by fitting the data to the Michaelis-Menten equation.

Stopped-flow measurements to assess the rates of hydride transfer (HT) processes from NADH to hAIF were carried out under aerobic conditions on an SX18.MV (Applied Photophysics) instrument using a photodiode array detector and ProData-XS software, as reported previously (Ferreira et al., 2014). Measurements were performed using 15  $\mu$ M hAIF and 40  $\mu$ M CHCHD4, while the final NADH concentrations in the mixing chamber were 0.15, 0.3, 0.6, 1.25, 2.5, 5 and 10  $\mu$ M. The observed rates ( $k_{\text{obs}}$ ) for the HT event were calculated by global analysis and numerical integration methods fitting a one-step model ( $A \rightarrow B$ ) (using simultaneously all spectral data in the 400-800 nm region along the time evolution). When a saturation profile in pyridine nucleotide concentration was observed, the values of  $k_{\text{obs}}$  were fitted to equation 3.18

$$k_{\text{obs}} = \frac{k_{\text{HT}}\text{NADH}}{K_d^{\text{NADH}} + \text{NADH}} + k_{\text{rev}}$$

describing the formation of a protein:substrate complex prior to the HT process, where  $k_{\text{HT}}$  is the rate-limiting rate constant for HT from NADH to the FAD cofactor of hAIF, and  $K_d$  is the hAIF:coenzyme dissociation constant.

Steady-state measurements to assess the reaction time of CTC reoxidation by molecular oxygen were also performed. CTC samples were prepared by mixing hAIFmt $\Delta_{1-77}$  variants with NADH in a 1:1.5 ratio in 50 mM Kpi, pH 6.2, at 25 °C. After exposure of CTC samples to molecular oxygen, CTC decay was monitored at 750 nm. The samples were kept under stirring during the whole process and absorption spectra were recorded at 25 °C until complete reoxidation of the flavin cofactor was achieved. For each time the remaining % CTC is calculated according to equation 3.9. Once the % CTC for each time is known, the CTC half-life is the time in which 50 % CTC is still in solution.

## 6.4.6 DATA ANALYSIS AND STATISTICS

Data were analysed and plotted using Pro-K (Applied Photophysics), Sigma plot (11.0) and Origin (OriginLab). Results are expressed as the mean  $\pm$  standard deviation (SD) or as the mean  $\pm$  standard error (SE) of the regression analysis.

## 6.5 RESULTS AND DISCUSSION

### 6.5.1 QUATERNARY ORGANIZATION OF MITOCHONDRIAL VARIANTS AND THE INFLUENCE OF CHCHD4 ON THEIR STABILITY

Gel filtration chromatography was used to corroborate the ability of hAIFmt $\Delta_{1-77}$  to NADH-linked dimerization (**Figure 6.1**). Chromatographic profiles of hAIFmt $\Delta_{1-77ox}$  indicated that the protein behaves primarily as a monomer with a MW<sup>app</sup> of nearly 50 kDa (peak 2) at both pH 6.2 and pH 7.4, with a smaller proportion of the species previously identified as the dimer (Ferreira et al., 2014).. Treatment of hAIFmt $\Delta_{1-77}$  with NADH produced different effects on the chromatographic profile of the protein as a function of pH. A shift of the main protein population towards higher MW<sup>app</sup> (peak 1) was observed at pH 7.4, in agreement with the dimerization of the protein (**Figure 6.1 B**). However, at pH 6.2 only a small shift of the main protein peak towards slightly lower elution volumes was observed, whereas the peak corresponding to the protein dimer is considerably reduced regarding pH 7.4 (**Figure 6.1 A**). This suggests that at pH 6.2 the monomeric conformations are less compact and/or there is rapid monomer-dimer exchange despite the presence of NADH (peak 1). Finally, the profiles of hAIF3Mmt $\Delta_{1-77}$  in the absence and presence of NADH were quite similar (**Figure 6.1 C**), and indicated that this variant is inviable for dimerization, in agreement with what that reported for the corresponding apoptotic mutant (Ferreira et al., 2014). All these data are summarized in **Table 6.1**.



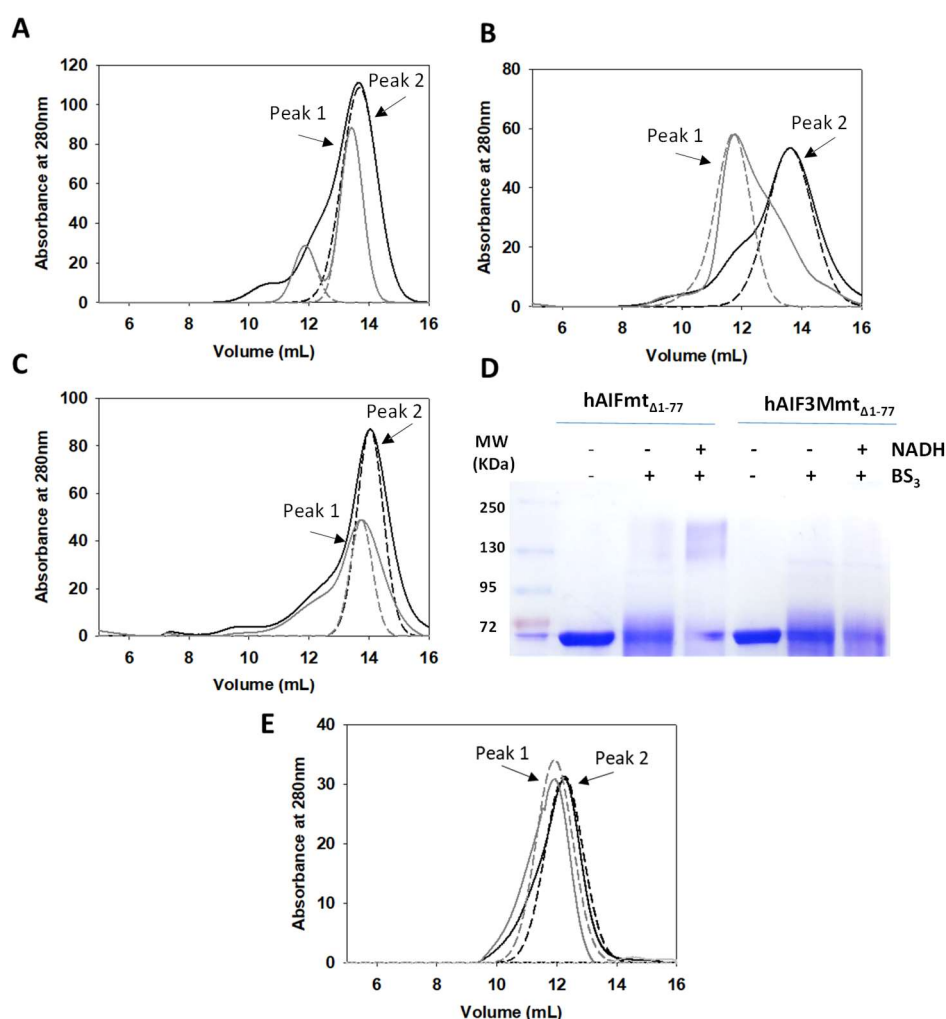


**Figure 6.1: NADH-induced dimerization of hAIF variants.** Elution profiles on a Sephadex S-200 column for **(A)** hAIFmt $\Delta$ 1-77 at pH 6.2, **(B)** hAIFmt $\Delta$ 1-77 at pH 7.4, and **(C)** hAIF3Mmt $\Delta$ 1-77 at pH 7.4. Assays were performed at 6 °C in the absence and presence of a 10-fold excess of NADH. Profiles are shown in black and grey respectively in the absence and presence of NADH. Gaussian deconvolutions are represented in dashed line. **(D) Cross-linking analysis of NADH-dependent dimerization.** ~3  $\mu$ M proteins were incubated with a 100-fold excess of BS<sup>3</sup> in the absence or presence of 300  $\mu$ M NADH for 1 h at room temperature, and then resolved by 15% SDS-PAGE. Lanes 1-3 hAIFmt $\Delta$ 1-77 and 4-6 hAIF3Mmt $\Delta$ 1-77. **(E) Elution profile of hAIF $\Delta$ 1-101 interaction assays with CHCHD4.** The hAIF $\Delta$ 1-101 was incubated with NADH (in 10-fold excess) in the presence or absence of CHCHD4 (1:3 ratio) for 15 min at room temperature in 50 mM Kpi, pH 7.4 and then resolved on a Sephadex S-200 column. Chromatography was performed in the same buffer supplemented with 10 mM NaCl. The elution profiles obtained for the mixture are shown in grey, and the corresponding control profiles for free hAIF $\Delta$ 1-101:NADH and CHCHD4 are in black (Not shown), while the Gaussian deconvolutions are in dashed lines.

Chemical cross-linking with BS<sup>3</sup> -capable of covalently conjugating hAIF dimers but not monomers (Ferreira et al., 2014)- followed by evaluation of the species by SDS-PAGE was also used to assess the ability of the different variants to stabilise dimers (**Figure 6.1 D**). After incubation with BS<sup>3</sup>, hAIFmt $\Delta$ 1-77ox and hAIF3Mmt $\Delta$ 1-77 variants showed a single electrophoretic band of ~50 kDa. This band corresponded to the monomer and was generally more diffuse than in the absence of the crosslinker. When the variants were preincubated with NADH and BS<sup>3</sup>, an additional broad band of ~120 kDa appeared for

hAIFmt $\Delta$ 1-77, at the expense of the monomeric form, showing the ability of the mitochondrial protein to undergo dimerization after binding to NADH and flavin reduction. This band was not observed in hAIF3Mmt $\Delta$ 1-77 when treated similarly (**Figure 6.1 D**), also in agreement with the exclusion chromatography data for this variant (**Figure 6.1 C**). These data confirm that while the native mitochondrial variant dimerizes, the E413A/R422A/R430A triple mutation prevents its dimerization. Therefore, both mitochondrial forms behave similarly to their corresponding apoptotic forms in terms of NADH-induced dimerization (Ferreira et al., 2014).

Molecular exclusion chromatography was also used to test whether this methodology allows us to assess the binding of CHCHD4 to the mitochondrial variant (**Figure 6.1.E and Table 6.1**). For this purpose, the apoptotic reduced variant hAIF $\Delta$ 1-101 was used since this form only interacts with CHCHD4 in the presence of NADH. The data in the presence of CHCHD4 indicate a shift of the hAIF peaks to a slightly lower elution volume, i.e. the mixtures have a slightly higher MW<sup>app</sup> than free hAIF, which binds the sum of both proteins. Variation in elution volume and ability to calculate the MW<sup>app</sup> justified that the binding has a stoichiometry of 1:1.

**Table 6.1:** Apparent molecular weights of major hAIF eluting peaks detected by molecular exclusion chromatographic profiling in the absence and presence of NADH and when incubated with CHCHD4, as depicted.

Sample	NADH absence	NADH presence	
	Peak 2	Peak 1 (kDa)	Peak 2 (kDa)
hAIFmt $\Delta$ 1-77 <sup>a</sup>	47	85	49
hAIFmt $\Delta$ 1-77 <sup>b</sup>	47	83	47
hAIF3Mmt $\Delta$ 1-77 <sup>a</sup>	42	54	42
hAIF $\Delta$ 1-101:CHCHD4 <sup>c</sup>	ND	85	75

The MW<sup>app</sup> of the elution peaks were obtained by Gaussian deconvolution of the gel filtration elution profiles.

<sup>a</sup>Tests carried out in Kpi 50 mM, pH 7.4.

<sup>b</sup>Tests carried out in 50 mM Kpi, pH 6.2.

<sup>c</sup>Assays performed in 50 mM Kpi, pH 7.4, 10 mM NaCl.

### 6.5.2 hAIF MITOCHONDRIAL VARIANT AFFINITY FOR CHCHD4

Since hAIF:CHCHD4 in mitochondria plays a key role in OXPHOS and energy homeostasis, we also used ITC to determine the binding parameters describing the interaction, as well as its modulation by the presence of NADH (Table 6.2, Figure 6.2).

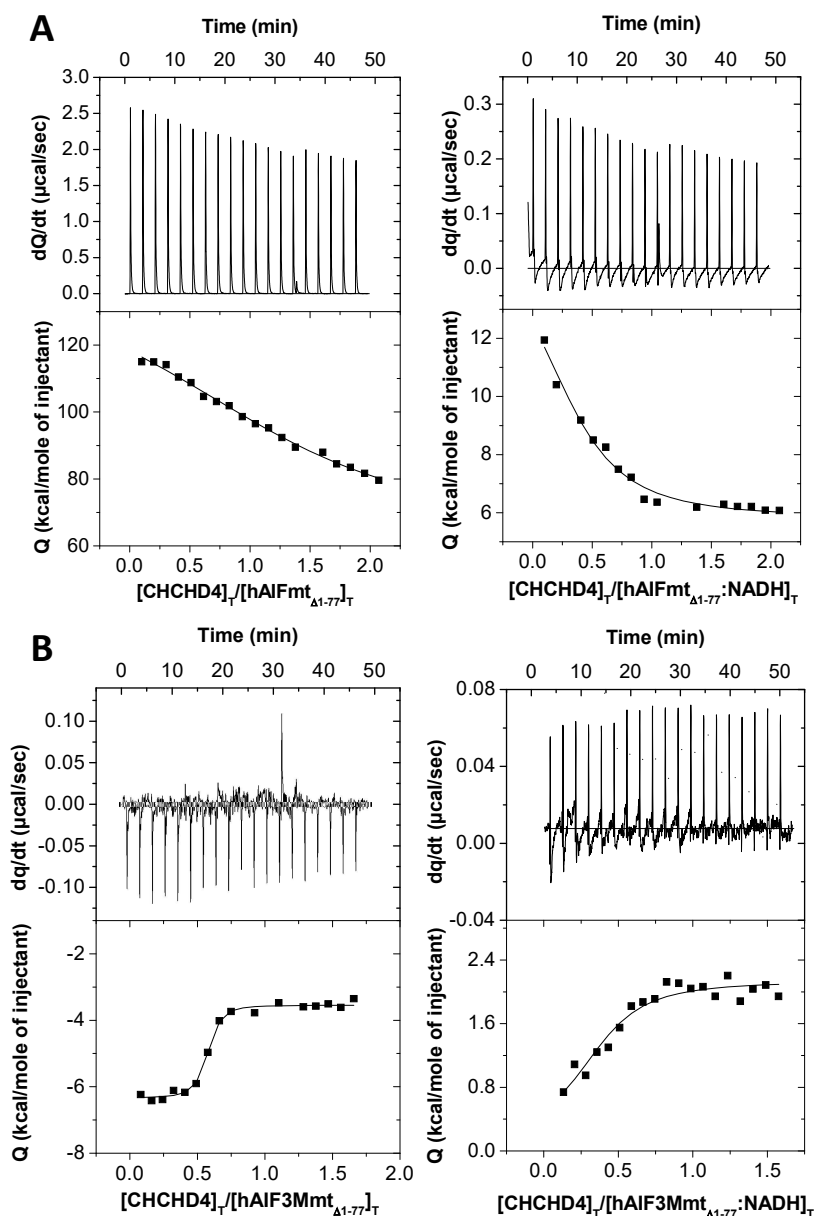


**Figure 6.2: Interaction of the mitochondrial forms of hAIF with CHCHD4.** ITC titration of (A) hAIFmt $\Delta_{1-77}$  and (B) hAIF3Mmt $\Delta_{1-77}$  (10  $\mu$ M in the calorimetric cell) with CHCHD4 (100  $\mu$ M CHCHD4 in the syringe) in the absence (left panels) and presence (right panels) of NADH (10  $\mu$ M in the calorimetric cell). Experiments performed at 25  $^{\circ}$ C in 50 mM Kpi, pH 6.2 for hAIFmt $\Delta_{1-77}$  and pH 7.4 for hAIF3Mmt $\Delta_{1-77}$ . In each panel, the upper graph shows the interaction thermogram (heat power as a function of time), while the lower graph shows the binding isotherm with integrated heats as a function of ligand/protein molar ratio. The data were fitted to a house-derived model for a single binding site.

**Table 6.2:** Thermodynamic parameters for the interaction of hAIF<sub>Δ1-101</sub> and hAIFmt<sub>Δ1-77</sub> with CHCHD4.

Sample	$K_d$ ( $\mu$ M)	n	$\Delta H$ (Kcal/mol)	$\Delta G$ (Kcal/mol)	$-T\Delta S$ (Kcal/mol)
hAIF <sub>Δ1-101</sub>	ND				
hAIF3M <sub>Δ1-101</sub>	ND				
hAIFmt <sub>Δ1-77</sub>	6.2	0.3	-6.9	-6.9	0.1
hAIF3Mmt <sub>Δ1-77</sub>	2.7	0.4	-9.4	-7.3	2.1
<b>NADH</b>					
hAIF <sub>Δ1-101</sub>	0.2	0.6	-20.0	-8.7	11.4
hAIF3M <sub>Δ1-101</sub>	ND				
hAIFmt <sub>Δ1-77</sub>	2.3	0.4	10	-7.4	-17.5
hAIF3Mmt <sub>Δ1-77</sub>	1.2	0.4	-1.9	-7.8	-5.9

Values were obtained from ITC. Assays were performed at 25 °C in 50 mM Kpi, pH 7.4, except for hAIFmt<sub>Δ1-77</sub> which was performed at pH 6.2. Thermodynamic parameters were calculated by  $K_d = (K_a)^{-1}$ ,  $\Delta G = RT \ln K_d$  and  $-T\Delta S = \Delta G - \Delta H$ . The absolute errors are:  $\pm 0.1$  kcal/mol in  $\Delta G$  and  $\pm 0.3$  kcal/mol in  $\Delta H$  and  $-T\Delta S$ , and  $\pm 20$  % in  $K_d$ .

Thermograms of the protein titrations with CHCHD4 (**Figure 6.2, Table 6.2**) indicated that there are substantial differences in the interaction with CHCHD4 between oxidized and reduced, and mitochondrial or apoptotic forms.

Thus, only the mitochondrial forms in their oxidized form are able to interact with the CHCHD4 protein, as opposed to the apoptotic forms which are not able to interact with the CHCHD4 protein. Furthermore, the binding isotherms fit well to a single binding site model and allow the interaction parameters to be determined. The  $K_d$  values calculated for interactions of CHCHD4 with both oxidized mitochondrial forms are in the micromolar range.

When interactions with the NADH-reduced forms are observed, only the triple, non-dimerizable apoptotic mutant is unable to bind CHCHD4. The native apoptotic hAIF<sub>Δ1-101</sub>:NADH variant binds to CHCHD4 with a  $K_d$  in the submicromolar range, suggesting specific binding in a structurally organized complex. The two NADH-reduced mitochondrial variants bind CHCHD4 with a slightly higher affinity than their oxidized forms. However, the corresponding  $K_d$  remains in the micromolar range. Therefore, under conditions mimicking IMS (pH and mitochondrial form of hAIF), the effect of NADH reduction and hAIF dimerization on CHCHD4 binding affinity are milder than expected when assessing the apoptotic form.

However, the enthalpic and entropic contributions to CHCHD4 binding to hAIFmt $_{\Delta 1-77}$  variants (**Figure 6.3**) are highly influenced by the NADH-induced redox state. CHCHD4 binding to hAIFmt $_{\Delta 1-77}$  and hAIF3Mmt $_{\Delta 1-77}$  is enthalpically guided with a small opposing entropic contribution. However, the binding of CHCHD4 to the corresponding reduced forms, hAIFmt $_{\Delta 1-77}$ :NADH and hAIF3Mmt $_{\Delta 1-77}$ :NADH, is entropically guided. Particularly notable is the strong opposing enthalpic contribution to binding in the case of the hAIFmt $_{\Delta 1-77}$ :NADH form which is offset by an even greater favourable entropic contribution. It is also interesting to note that this effect is considerably reduced in the case of the non-dimerizable mitochondrial variant, where enthalpic contributions also moderately favour binding. Furthermore, we should note that the binding profiles of CHCHD4 to the mitochondrial NADH variants differ considerably from those of binding to the native apoptotic variant, where a very strong enthalpic contribution to binding, with an also relatively strong entropic contribution against, lead the interaction.

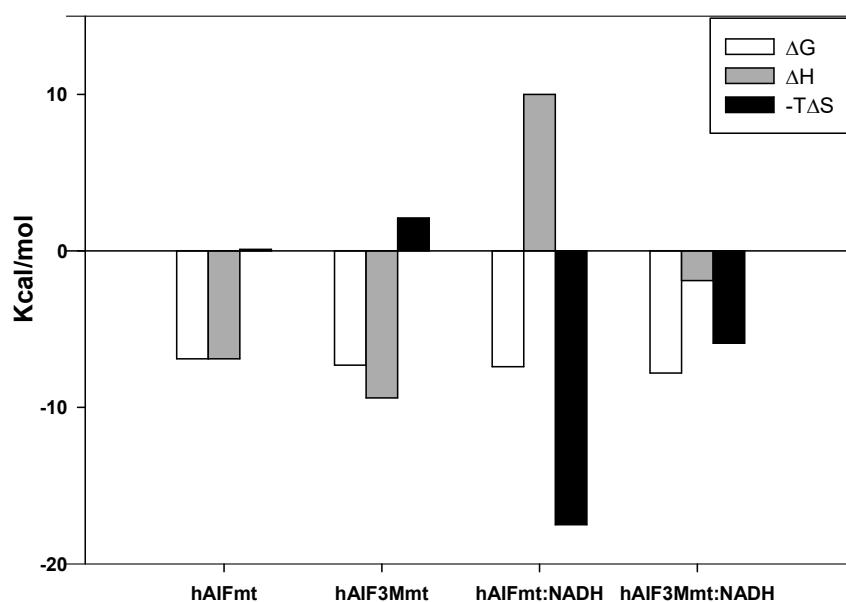


**Figure 6.3: Thermodynamic contributions to the binding of CHCHD4 to the hAIFmt variants in the absence or presence of NADH (1:100 in cell).**

In conclusion, these data show that the 77-101 segment of hAIF modulates its interaction with CHCHD4. Thus, its presence allows the recognition of CHCHD4 independently of the redox state of hAIFmt $_{\Delta 1-77}$  with similar overall affinity. Furthermore, our data also show that the thermodynamic profile contributing to the binding of CHCHD4 to hAIFmt $_{\Delta 1-77}$  is highly influenced by the redox state and quaternary organization of hAIFmt $_{\Delta 1-77}$ . Taken together, these observations suggest that the interaction of both proteins in the IMS has an important conformational component that will depend on whether hAIFmt $_{\Delta 1-77}$  is a monomer or a

dimer, as well as whether it has a folded (in the oxidized state) or released (in the CTC state) C-loop. According to the data presented here, all these forms of hAIFmt<sub>Δ1-77</sub> will be able to bind to CHCHD4, but through different binding modes.

### 6.5.3 IMPACT OF CHCHD4 ON THE STEADY STATE KINETIC PARAMETERS OF MITOCHONDRIAL hAIF.

Under physiological conditions, hAIF exhibits NADH oxidase activity that can be monitored *in vitro* by the steady-state DCPIP-dependent diaphorase reaction. Here, we have used this assay to emulate hAIFmt<sub>Δ1-77</sub> activity in the IMS in the presence of CHCHD4 (**Table 6.3**). Our data show that the turnover for catalysis ( $k_{cat}$ ) for hAIFmt<sub>Δ1-77</sub> and hAIF3Mmt<sub>Δ1-77</sub> are similar to those for the corresponding apoptotic forms. In turn, the  $K_m^{NADH}$  values of the hAIF<sub>Δ1-101</sub> apoptotic form are almost two fold those of the mitochondrial one, making hAIFmt<sub>Δ1-77</sub> twice as efficient as its apoptotic counterpart.

**Table 6.3:** Kinetic parameters of hAIF variants in steady state and pre-steady state

hAIF	Steady state			Pre-steady state		
	$k_{cat}$ (s <sup>-1</sup> )	$K_m^{NADH}$ (μM)	$k_{cat}/K_m^{NADH}$ (s <sup>-1</sup> mM <sup>-1</sup> )	$k_{HT}$ (s <sup>-1</sup> )	$K_d^{NADH}$ (μM)	$k_{HT}/K_d^{NADH}$ (s <sup>-1</sup> mM <sup>-1</sup> )
hAIFmt <sub>Δ1-77</sub>	1.7 ± 0.1	207 ± 44	8.3 ± 2.1	4.0 ± 0.1	1795 ± 130	2.2 ± 0.1
hAIF3Mmt <sub>Δ1-77</sub>	1.1 ± 0.1	401 ± 69	2.9 ± 0.4	2.7 ± 0.1	2088 ± 96	1.3 ± 0.1
hAIFmt <sub>Δ1-77</sub> :CHCHD4	1.1 ± 0.1	15 ± 3	73 ± 15	1.7 ± 0.1	152 ± 35	11 ± 1.6
hAIF3Mmt <sub>Δ1-77</sub> :CHCHD4	1.6 ± 0.1	19 ± 6	85 ± 23	3.2 ± 0.1	2705 ± 74	1.2 ± 0.1
hAIF <sub>Δ1-101</sub>	0.9 ± 0.1	494 ± 99	2.1 ± 0.4	1.9 ± 0.1	3911 ± 264	0.5 ± 0.1
hAIF3M <sub>Δ1-101</sub>	0.4 ± 0.1	264 ± 37	1.5 ± 0.2	1.1 ± 0.1	4012 ± 140	0.3 ± 0.1
hAIF <sub>Δ1-101</sub> :CHCHD4	1.9 ± 0.1	244 ± 36	7.7 ± 1.0	1.5 ± 0.2	2605 ± 765	0.6 ± 0.1

Tests carried out at 25°C in 50 mM Kpi, pH 7.4.  
(n=3, mean ±SD)

No affinity-enhancing effect was observed in the presence of CHCHD4 for the apoptotic forms, probably due to their inability to interact under physiological conditions. However, CHCHD4 produced notable effects on the NADH oxidase activity of the mitochondrial variants. Thus, the presence of CHCHD4 reduced the  $K_m^{NADH}$  of hAIFmt<sub>Δ1-77</sub> by a factor of 50, making it 7-fold more efficient. For the triple mitochondrial variant hAIF3Mmt<sub>Δ1-77</sub> the efficiency is similar, but its affinity for NADH is slightly improved in the presence of CHCHD4.

Taken together, these data indicate that CHCHD4 favours the NADH oxidase activity of hAIF by decreasing  $K_m^{NADH}$ , an observation that may be related to either a decreased affinity for

the  $\text{NAD}^+$  product, favouring its release from the CTC, or to an increased affinity for the NADH substrate.

#### 6.5.4 PRE-STEADY-STATE PARAMETERS FOR THE CTC FORMATION

Attending to the steady-state results and to further determine whether there are main effects on  $K_d$  for NADH binding or  $\text{NAD}^+$  dissociation, we used transient stopped-flow kinetics to assess the impact of CHCHD4 on the HT reaction from NADH to the FAD cofactor of hAIFmt $_{\Delta 1-77}$  and its triple mutant.

The kinetic traces recorded for all variants evaluated at different NADH concentrations indicated an essentially irreversible two-electron reduction of the FAD cofactor with concomitant formation of a broad wavelength band related to the formation of the hAIFmt $_{\Delta 1-77}$ : $\text{NAD}^+$  CTC (**Figure 6.4 A-D**). However, the presence of CHCHD4 resulted in a considerable decrease in the overall magnitude of the maximum CTC band observed during the process as well as at the end (**Figure 6.4 A-E**).

The spectral evolution was best fitted to a two-step process in all cases, allowing the determination of the corresponding  $k_{\text{obs}}$  values for the HT steps at different NADH concentrations. Furthermore,  $k_{\text{obs}}$  showed in all cases a saturation profile on the coenzyme concentration that allowed estimation of the corresponding limiting  $K_d^{\text{NADH}}$  and  $k_{\text{HT}}$  parameters (**Table 6.3**).

Overall, the parameters for the reduction of hAIFmt $_{\Delta 1-77}$  and hAIF3Mmt $_{\Delta 1-77}$  by NADH are in the range of those reported for the corresponding apoptotic forms, with only slight increases in  $k_{\text{HT}}$  values and decreases in  $K_d^{\text{NADH}}$ . Thus, the mitochondrial variants are only slightly more efficient than their apoptotic counterparts.

Moreover, the presence of CHCHD4 in the reaction mixture was found to barely modulate the efficiency of the native apoptotic form. In contrast, CHCHD4 has a clear impact on the HT of NADH to hAIFmt $_{\Delta 1-77}$ , particularly by decreasing  $K_d^{\text{NADH}}$ . Notably, when assessing the HT from NADH to hAIF3Mmt $_{\Delta 1-77}$ , CHCHD4 only produces a very marginal effect on the determined parameters, even though it also reduced the maximal amount of stabilised CTC.

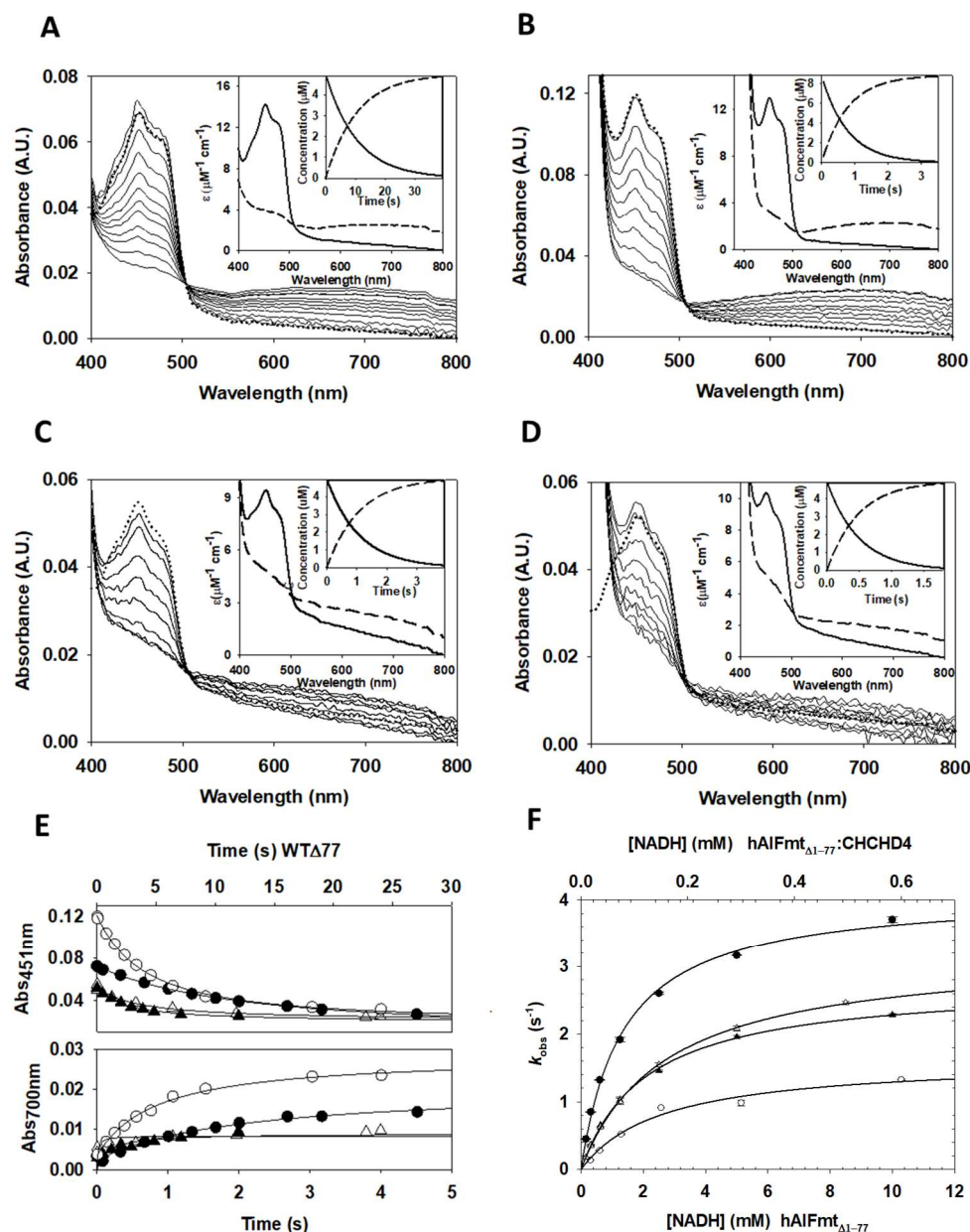


**Figure 6.4: Effect of CHCHD4 on the pre-steady-state kinetics for the reduction of hAIFmt $_{\Delta 1-77}$  and its triple variant by NADH.** Spectral evolution for the reduction of (A) hAIFmt $_{\Delta 1-77}$  at 0.005, 0.5, 2, 4, 6, 8, 8, 10, 12, 16, 18, 27, 60 s after mixing. (B) hAIF3Mmt $_{\Delta 1-77}$  at 0.006, 0.01, 0.13, 0.25, 0.4, 0.5, 0.7, 1, 1.5, 3, 4 s after mixing. (C) hAIFmt $_{\Delta 1-77}$ :CHCHD4 at 0.002, 0.006, 0.212, 0.548, 1.064, 1.964, 3.788, 3.992 s after mixing. (D) hAIF3Mmt $_{\Delta 1-77}$ :CHCHD4 at 0.002, 0.0018, 0.0081, 0.201, 0.337, 0.483, 0.645, 0.803, 1.18, 1.99 s after mixing. Dotted lines show spectra of oxidized enzymes ( $\sim 7 \mu\text{M}$ ) before mixing with 5 mM NADH. Insets show the spectroscopic properties of the species produced during the HT reactions by fitting a one-step model (A $\rightarrow$ B) and the evolution of these species over time. (E) Evolution of the kinetic traces at 451 and 700 nm respectively related to FAD reduction (upper panel) and CTC formation (lower panel) for hAIFmt $_{\Delta 1-77}$  (black circles), hAIFmt $_{\Delta 1-77}$ :CHCHD4 (white triangles), hAIF3Mmt $_{\Delta 1-77}$  (white circles) and hAIF3Mmt $_{\Delta 1-77}$ :CHCHD4 (black triangles). (F) Dependence of the observed rate constants for HT on NADH concentration for hAIFmt $_{\Delta 1-77}$  (black circles), hAIFmt $_{\Delta 1-77}$ :CHCHD4 (white triangles), hAIF3Mmt $_{\Delta 1-77}$  (white circles) and hAIF3Mmt $_{\Delta 1-77}$ :CHCHD4 (black triangles) versus coenzyme concentration. The lines represent fits of the experimental data to a hyperbola. All experiments were carried out at pH 7.4.



Therefore, the CHCHD4 protein modulates the NADH oxidase activity of the native mitochondrial variant and makes it more efficient by particularly favouring NADH binding to hAIFmt $_{\Delta 1-77}$  when this protein is able to stabilise dimers. As for the apoptotic native form, it is noteworthy that CHCHD4 also produces a similar, albeit moderate effect on NADH oxidase activity.

### 6.5.5 STABILITY OF CHARGE TRANSFER COMPLEXES

The stability of the CTCs was tested by measuring the time it takes for the complex to reoxidise.

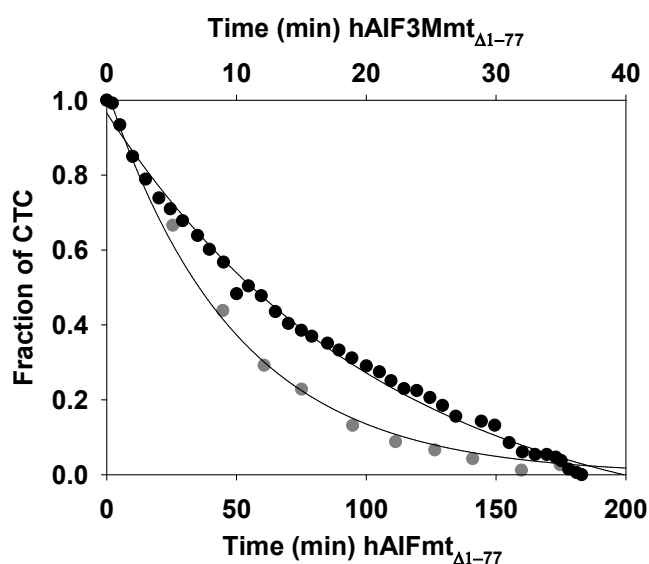


**Figure 6.5: Lifetime for hAIFmt $_{\Delta 1-77}$  and hAIF3Mmt $_{\Delta 1-77}$  CTCs versus molecular oxygen reoxidation.** The decay of CTC was monitored at 750 nm and 25 °C in 50 mM Kpi saturated air, pH 6.2 for the hAIFmt $_{\Delta 1-77}$  form and pH 7.4 for the hAIF3Mmt $_{\Delta 1-77}$  form. CTC samples were obtained by mixing the hAIFmt $_{\Delta 1-77}$  variants with NADH (0.7-fold enzyme concentration) and then exposed to air. Traces for hAIFmt $_{\Delta 1-77}$  (black circles) and hAIF3Mmt $_{\Delta 1-77}$  (grey circles) are shown normalized from 1 to 0 as fraction of CTC remaining over time.

For this, the reactivity of hAIFmt $_{\Delta 1-77}$  and hAIF3Mmt $_{\Delta 1-77}$  CTCs (formed after the oxidation of NADH) towards O<sub>2</sub> was tested as shown in **Figure 6.5**.

Similar to the hAIF $_{\Delta 1-101}$  CTC (not shown, **Figure 5.2**), hAIFmt $_{\Delta 1-77}$  CTC is highly stable against molecular oxygen reoxidation: half-lives of 51 and 62 min respectively. However, removal of the dimerizing ability of the mitochondrial variant in the triple mutant considerably

reduces the CTC lifetime: half-life of approximately 12 min. Therefore, the mitochondrial form is stable against O<sub>2</sub> reoxidation similarly to the apoptotic form.

## 6.6 CONCLUSIONS

In recent years, it has been accepted that hAIF participates in cell survival by assisting CHCHD4 in the biogenesis and maintenance of respiratory complexes (Kroemer and Reed., 2000). Therefore, the discovery and characterization at the molecular level of the AIF-CHCHD4 interaction represents a crucial finding in the deeper understanding of the vital role of hAIF.

However, no major studies on the effect of CHCHD4 on the redox capacities of hAIF have been reported so far. Moreover, studies on this interaction have been carried out using only the apoptotic isoform of AIF, which *in vivo* is not found in the IMS, and, therefore, does not participate in the supportive functions of CHCHD4. To better understand at the molecular level the regulation of the assembly of this protein, we further studied this interaction and the redox consequences on hAIF by using an isoform that will better resemble its *in vivo* behaviour in the IMS. For this purpose, a mitochondrial soluble variant, hAIFmt $\Delta$ 1-77, was used in this study, as well as its triple mutant.

The dimerization ability of NADH-bound hAIFmt $\Delta$ 1-77 revealed that the mitochondrial form, except for its triple variant, was able to dimerize and maintain a stable conformation. Molecular exclusion chromatography also showed that CHCHD4 effectively binds to the reduced form of the apoptotic variant. The mitochondrial forms (WT and its triple mutant) were shown to kinetically favour CTC formation by increasing the affinity of hAIFmt $\Delta$ 1-77 for NADH. All mitochondrial forms increase the thermodynamic preference for NADH binding relative to apoptotic.

The effect of CHCHD4 binding on mitochondrial hAIFs is of utmost relevance. For all variants, the reduction with NADH increases affinity for CHCHD4. Therefore, NADH-dependent structural changes in hAIF must play a key role in CHCHD4 binding. In addition, the CTC of the mitochondrial variant is stable against O<sub>2</sub> reoxidation, and NADH/NAD<sup>+</sup> binding in the active site is stronger than in the apoptotic form. This would justify that the mitochondrial variant is stable to participate in mitochondrial bioenergetic processes. Compared with the apoptotic constructs, the mitochondrial variants are catalytically more efficient in NADH oxidation. Taken together, these data indicate that CHCHD4 favours the NADH oxidase activity of hAIF by decreasing  $K_m^{\text{NADH}}$ . Therefore, the CHCHD4 protein modulates the NADH oxidase activity of the native mitochondrial variant. This was expected, since it is in the mitochondria where the oxidoreductase activity of hAIF is carried out. The

physiological and more favourable binding of the mitochondrial variant to CHCHD4 and the hAIF role as a redox sensor, may explain the mitochondrial form having higher catalytic efficiency. The results obtained in this work contribute thus to better understand the redox role of hAIF and its redox dependent interplay with CHCHD4.





## ***7- INSIGHTS INTO THE DEGRADOSOME FORMATION: HUMAN APOPTOSIS INDUCING FACTOR INTERACTION WITH PRO-APOPTOTIC PARTNERS***

### **PERSONAL CONTRIBUTION**

- Expression and purification of hAIF and protein partners.
- Isothermal titration calorimetry measurements
- Size exclusion chromatography experiments
- Electrophoretic gel and Western blot assays



## 7.1 ABSTRACT

The human apoptosis-inducing factor (hAIF) is a mitochondrial flavoprotein that contributes to cell life and cell death cycles. hAIF maintains mitochondrial structure and plays an essential role in oxidative phosphorylation under physiological conditions. In contrast, when mitochondria receive an apoptotic stimulus, hAIF becomes a key mediator of cell death independent of caspases. The molecular basis of the pro-death mechanism of hAIF has not yet been fully described in detail, but it is essential that hAIF translocates from mitochondria to the nucleus. Once in the nucleus, the ternary complex of hAIF-CypA-H2AX, known as the "degradosome", is proposed to play a key role in hAIF-mediated chromatin condensation and DNA degradation through the formation of the DNA-degradosome complex, key in the caspase-independent necroptosis function of hAIF.

In the present work we have studied the interactions among all the proteins involved in the formation of the degradosome, as well as with DNA. The binding cooperativity due to the presence of CypA or H2AX in the affinity for DNA has also been evaluated. Our data demonstrate the *in vitro* formation of the ternary degradosome complex, as well as its interaction with dsDNA. Furthermore, we provide thermodynamic parameters for all binary, ternary and quaternary interactions occurring in the DNA-degradosome complex and establish a potential hypothesis for the mechanism of their association process.

## 7.2 RESUMEN

El factor de inducción de apoptosis humano (hAIF) es una flavoproteína mitocondrial que contribuye tanto a la vida como a la muerte celular. hAIF mantiene la estructura mitocondrial y desempeña un papel esencial en la fosforilación oxidativa en condiciones fisiológicas. En cambio, cuando las mitocondrias reciben un estímulo apoptótico, hAIF se convierte en un mediador clave de la muerte celular independiente de caspasas. El mecanismo de muerte celular mediado por hAIF aún no se ha descrito completamente en detalle, pero es esencial que hAIF se transloque de las mitocondrias al núcleo. Una vez en el núcleo, el complejo ternario de hAIF-CypA-H2AX, conocido como "degradosoma", desempeña un papel clave en la condensación de la cromatina mediada por hAIF y en la degradación del ADN mediante la formación del complejo ADN-degradosoma, clave en la función necroptótica independiente de caspasas de hAIF.

En el presente trabajo se han estudiado las interacciones entre todas las proteínas implicadas en la formación del degradosoma, así como con el ADN. Además, se ha evaluado la cooperatividad debida a la presencia CypA y a la H2AX en la unión del ADN. Nuestros datos demuestran la formación *in vitro* del degradosoma, así como su interacción con el dsADN. Además, proporcionamos los parámetros termodinámicos para todas las interacciones binarias, ternarias y cuaternarias que ocurren en el complejo ADN-degradosoma y establecemos una hipótesis potencial para el mecanismo de su proceso de asociación



### 7.3 INTRODUCTION

The human apoptosis-inducing factor (hAIF) is a mitochondrial flavoprotein that contributes to both cell life and death (Susin *et al.*, 1999). Under physiological conditions, hAIF is attached to the mitochondrial inner membrane, facing the intermembrane space where it interacts with CHCHD4 (coiled-coil-helix-coiled-coil-helix domain containing 4) -a key assembly factor for multisubunit respiratory electron transport chain complexes- and plays an essential role in the maintenance of mitochondrial structure and oxidative phosphorylation (Delavallée *et al.*, 2020, Hangen *et al.*, 2015). Conversely, under pathological conditions, hAIF is one of the main effectors of caspase-independent necroptosis. This mode of programmed cell death (PCD) involves the redistribution of hAIF to the nuclear compartment where it induces chromatin condensation, large-scale DNA fragmentation ( $\approx 50$  kb) and DNA loss (Artus *et al.*, 2010, Cabon *et al.*, 2012).

In response to a variety of cytotoxic stimuli, oxidative stress or alkylating DNA damage agents, the hyperactivation of the nuclear polymerase-1-dependent cell death (PARP-1) initiates a signalling cascade that provokes mitochondrial damage. This results in the release of the soluble pro-apoptotic hAIF -truncated form, hAIF $_{\Delta 1-101}$  in humans, cleaved by activated calpains proteases- from the mitochondria to the cytosol. Interestingly, the translocation of hAIF to the nucleus is hindered or activated through its physical interaction with either the heat shock protein-70 (HSP70) or cyclophilin A (CypA) respectively, by a mechanism still not completely understood (Gurbuxani *et al.*, 2003, Zhu *et al.*, 2007). Once in the nucleus, the lethal activity of hAIF depends on its ability to associate or activate nucleases, since it is expected to lack endonuclease activity by itself despite being able to bind chromatin (Susin *et al.*, 1999, Vahsen *et al.*, 2006, Joza *et al.*, 2009, Ye *et al.*, 2002). In support of this, the synchronized action of hAIF, phosphorylated histone H2AX and nuclease CypA is required to provoke chromatin remodelling and DNA loss in alkylating DNA damage upon methylnitronitrosoguanidine (MNNG)-mediated necroptosis (Artus *et al.*, 2010). Indeed, there is strong evidence of nuclear hAIF/H2AX interplay (Artus *et al.*, 2010). This might in some way promote the activation of the latent nuclease activity of CypA, as well as to support the association of hAIF, H2AX and CypA in a multi-protein complex commonly referred to as the DNA degradosome (Artus *et al.*, 2010). Of note, H2AX participates in DNA damage repair in response to DNA double-strand breaks, but also has a key role in PCD, likely inducing DNA restructuring to improve accessibility to endonucleases (Baritaud *et al.*, 2012, Fernandez-Capetillo *et al.*, 2003). Furthermore, hAIF might cooperate directly with CypA to promote neuronal death in response to different cellular stress conditions (Cande *et al.*, 2004, Zhu *et al.*, 2007). In particular, upon cerebral

hypoxia-ischemia, the cytosolic hAIF/CypA interaction has been also proposed to favour the nuclear co-translocation of both proteins (Zhu *et al.*, 2007). In this context, further studies are needed to clarify the molecular mechanisms through which these DNA-degrading complexes execute their lethal action as a function of particular apoptotic stimuli and even cell type or tissue.

In this scenario, hAIF is proposed as a platform for the assembly of an active DNA-degrading complex during PCD (Baritaud *et al.*, 2010). This is supported by the fact that hAIF may concurrently interact with the rest of the degradosome's components through different interaction regions. hAIF would interact with H2AX through a proline-rich motif (aa 544-554 of hAIF at the flexible regulatory C-loop) in its apoptotic C-terminal domain that results essential for its apoptogenic capacity (Artus *et al.*, 2010). On its side, CypA would specifically associate with the hAIF 370-394 amino acid region that forms part of the NAD-binding domain (Farina *et al.*, 2018). Finally, hAIF interacts with DNA in a sequence-independent manner based on electrostatic interactions around a positively charged protein crown (Ye *et al.*, 2002). Considering these facts, a plausible molecular model for this nuclear chromatinolytic complex was proposed (Baritaud *et al.*, 2010). Furthermore, little is known about the physiological relevance of the mutual interactions among these proteins, their cooperativity or how they operate to promote chromatinolysis.

## 7.4 EXPERIMENTAL PROCEDURES

### 7.4.1 OVEREXPRESSION AND PURIFICATION OF PROTEINS

hAIF<sub>Δ1-101</sub> (Apoptosis inducing factor in its apoptotic form, UniProtKB O95831), CypA (PPIA peptidyl prolyl isomerase A, UniProtKB P62937) and histone H2AX (h2afx H2A histone family member X, UniProtKB P16104) from *Homo sapiens* were heterologously expressed in *Escherichia coli* C41 (DE3) as recombinant proteins with an N-terminus His<sub>6</sub>-tag using the pET-28a(+) vector. Constructs used to overexpress hAIF<sub>Δ1-101</sub> and CypA were previously reported in chapter material and methods (Romero-Tamayo *et al.*, 2021). Similarly, the cDNA encoding for H2AX was codon optimised for *E. coli* expression and synthesized with a cleavable N-terminal His<sub>6</sub>-tag (CATCATCATCATCATCAT) followed by a cleavable recognition site for PreScission Plus protease by GenScript®. The encoding sequence was subcloned between NcoI and NdeI sites of plasmid pET-28a(+).

hAIF<sub>Δ1-101</sub> and CypA were produced and purified using Ni<sup>2+</sup> affinity chromatography as described previously in chapter material and methods (Romero-Tamayo *et al.*, 2021). For H2AX overexpression, *E. coli* cultures were grown at 37 °C and 180 r.p.m in LB

supplemented with 30 mg/L of Kanamycin (Sigma-Aldrich). When cultures reached  $OD_{600nm} \sim 0.6$ , 1 mM IPTG was added to induce protein expression, and then incubated for 3 additional h. Cells were then harvested, resuspended in 100 mL of Tris-HCl 50 mM pH 8.0, and lysed by sonication on ice. The cell lysate was centrifuged to remove debris, and then mixed with  $Ni^{2+}$ -IMAC Sepharose 6 Fast Flow gel (GE Healthcare) equilibrated in the aforementioned buffer supplemented with 0.4 M KCl and 4 mM of imidazole. This mixture was incubated on a bidirectional rocker for 1 h at 4 °C, and then loaded into a column. H2AX was eluted with a linear 40-500 mM imidazole gradient in 50 mM Kpi, 150 mM NaCl, pH 7.4. H2AX fractions were pooled, concentrated and dialysed in 50 mM potassium phosphate, pH 7.4. In all cases, protein purity was assessed by SDS-PAGE and molecular exclusion chromatography.

The hAIF $_{\Delta 1-101}$  concentration was determined using the  $\epsilon_{451nm}$  of  $13.77 \text{ mM}^{-1} \cdot \text{cm}^{-1}$  previously reported (Ferreira *et al.*, 2014). To determine CypA and H2AX concentrations theoretical  $\epsilon_{280nm}$  values obtained from the ProtParam tool (ExPASy) were used ( $8.73 \text{ mM}^{-1} \cdot \text{cm}^{-1}$  and  $5.96 \text{ mM}^{-1} \cdot \text{cm}^{-1}$ , respectively). All proteins were stored in 50 mM Kpi, pH 7.4 at -80 °C.

## 7.4.2 CLEAR NATIVE AND 2D DENATURING ELECTROPHORESIS

Mixtures of hAIF $_{\Delta 1-101}$  with its different nuclear partners were incubated for 15 min in 50 mM Kpi, pH 7.4, at 25 °C. Samples were then separated by Clear Native-PAGE (CN-PAGE) gradient electrophoresis (polyacrylamide concentration gradient 4 to 20%). For that, the electrophoresis was first run at 80 V and 4 °C for 25-30 min, and then the amperage was set at 12 mA/gel and the voltage limited to 300 V until the sample front reached the bottom of the gel (~120 min in total). Afterwards, gels were processed for Western blotting (WB) and two-dimensional (2D) SDS-PAGE. For 2D analysis, the first-dimension lane was cut out from the gel, incubated 1 h at 25 °C in 1% SDS and 1%  $\beta$ -mercaptoethanol, and run in a 15% second-dimension denaturing gel. The 2D SDS-PAGE was run at 4 °C and 30 V for 25-30 min, and then the voltage was set in the 80-120 V range until the dye reached the bottom of the gel. After electrophoresis, the gels were electroblotted onto Hybond-P PVDF membranes (Amersham) and then sequentially probed with specific antibodies against hAIF, CypA and H2AX (**Table 3.8**). Detection of immunoreactive proteins was performed using HRP-conjugated secondary antibodies (Thermo Fisher Scientific). Signals were detected using the EZ-ECL Chemiluminescence Detection kit from HRP (Pierce™), and immunoblot images were obtained in an automated WB processor Amersham™ Imager 600 (GE Healthcare).

### 7.4.3 SIZE EXCLUSION CHROMATOGRAPHY

hAIF<sub>Δ1-101</sub> was incubated with its different nuclear protein partners (1:3 proportion) for 15 min at 25 °C in 50 mM Kpi, pH 7.4. Samples were then loaded into a HiPrep 26/60 Sephacryl TMS-200 High Resolution (GE Healthcare) column connected to an Äkta Purifier HPLC system (GE Healthcare). Protein elution was performed in 50 mM Kpi, 10 mM NaCl, pH 7.4, at a flow rate of 0.4 mL/min. The column was previously calibrated with the GE Healthcare low molecular weight (MW) calibration kit (6 proteins in the 6400-160000 Da range). The obtained chromatograms were fitted to a set of Gaussian functions.

### 7.4.4 ATOMIC FORCE MICROSCOPY

Atomic Force Microscopy (AFM) measurements were carried out with a Cervantes FullMode Scanning Probe Microscope (Nanotec Electrónica S.L) at room conditions. Mixtures of proteins forming the degradosome were prepared by mixing hAIF<sub>Δ1-101</sub> (0.5 μM) with 1:1 molar ratio of CypA or/and H2AX for 10 min at 4°C under mild stirring. These mixtures, as well as free proteins, were also mixed with 0.05 ng/μL pET-28a plasmid - linearized with EcoR1- to visualize protein binding to dsDNA. Final concentrations were chosen to ensure the observation of individual features and thus, to facilitate complex identification and further analysis. All samples were prepared in PBS pH 7.0 (Thermo Scientific). For DNA degradation assays, mixtures were prepared in the presence of 5 mM CaCl<sub>2</sub> and 5 mM MgCl<sub>2</sub> to stimulate CypA nucleolytic activity. Samples were incubated on fresh cleaved mica pieces (Electron Microscopy Sciences) for 10 min at room temperature to achieve molecular immobilization. In the case of samples involving dsDNA, a pre-treatment with 200 mM MgCl<sub>2</sub> was applied for 2 min to favour attachment of its strands to the negative hydroxyl groups at the mica surface (Pallarés *et al.*, 2014). Then, the mica pieces were washed three times with the same buffer to prevent non-desirable interactions among free biomolecules and the AFM tip that might disturb image acquisition. AFM images were acquired using the intermittent force Jumping Mode (Sotres *et al.*, 2007) at low applied forces to minimise lateral forces and dragging effects (Sotres *et al.*, 2008). Ultrasharp silicon nitride soft microlevers exhibiting 0.01-0.03 N/m calibrated spring constants were used (MSNL; Bruker Probes). At least 10 representative images from 10 different areas of 200 x 200 nm and 400 x 400 nm were analysed for protein and protein-DNA samples, respectively. The resolution of all AFM images was at least of 512 x 512 pixels and the acquisition rate was defined at 0.5 Hz. Estimation of percentages and their associated error was calculated as previously described for the different association states

(Lostao *et al.*, 2010 ). Raw AFM images were analysed using the WSxM free software (Horcas *et al.*, 2007).

#### 7.4.5 ISOTHERMAL TITRATION CALORIMETRY

Isothermal titration calorimetry (ITC) measurements were carried out using an Auto-iTC200 microcalorimeter MicroCal (Malvern Instruments). Typically, a 10  $\mu$ M sample of the desired protein in the calorimetric cell was titrated with 100  $\mu$ M of either dsDNA or its protein partner. Before each assay, solutions were degassed at 15  $^{\circ}$ C for at least 2 min. A sequence of 2  $\mu$ L-injections of titrant solution every 150 s was programmed and the stirring speed was set to 750 r.p.m. Titration assays with dsDNA were performed at 15  $^{\circ}$ C and 25  $^{\circ}$ C, while those with proteins were carried out at 25  $^{\circ}$ C. The association constant ( $K_a$ ), the enthalpy change ( $\Delta H$ ), and the binding stoichiometry ( $n$ ) were estimated through non-linear regression of the experimental data employing a single ligand binding site model (1:1 protein:ligand stoichiometry) implemented in Origin 7.0 (Velazquez-Campoy *et al.*, 2006, Wiseman *et al.*, 1989). Random dsDNA samples (0.5 mM) for ITC titrations were prepared by annealing 1 mM solutions of the forward and reverse ssDNA 15-bp oligonucleotides (5'- GGT TAG TTA TGC GCG -3' and 5'- CGC GCA TAA CTA ACC -3'; synthesized by Integrated DNA Technologies) upon incubation at 99  $^{\circ}$ C for 1 min, followed by a 3-h temperature gradient from 95 to 25 $^{\circ}$ C (decreasing 1  $^{\circ}$ C each 3 min).

To evaluate the buffer independent binding enthalpy ( $\Delta H^{\circ}$ ), titrations were carried out using a set of buffers with different ionisation enthalpies (**Table 7.1**).

Fitting of the dependence of the observed binding enthalpy ( $\Delta H$ ) of the buffer ionisation enthalpy ( $\Delta H_{ion}$ ) to the equation:

$$\Delta H = \Delta H^{\circ} + n_{H^{+}} \cdot \Delta H_{ion} \text{ (Eq. 1).}$$

allowed determination of  $\Delta H^{\circ}$  and the number of protons exchanged between the complex components and the bulk solution ( $n_{H^{+}}$ ). If  $n_{H^{+}}$  is positive, the complex formation occurs with capture of protons from the solvent, while a negative value indicates releasing protons to the solvent (Martinez-Julvez *et al.*, 2012).

In general, errors in the determined parameters were  $\pm 0.3 \text{ kcal.mol}^{-1}$  for thermodynamic parameters ( $\Delta H$ ,  $\Delta G$ , and  $T\Delta S$ ) and  $\pm 25\%$  for binding constants,  $K_a$  and  $K_d$ .

To determine the binding cooperativity of ligands to hAIF, sets of experiments were performed by locating on the calorimetric sample cell mixtures containing 10  $\mu$ M hAIF $_{\Delta 1-}$ .

101 and 10, 20, 40 or 80  $\mu\text{M}$  dsDNA. They were then titrated with either CypA or H2AX (100  $\mu\text{M}$  in the syringe) and analysed as binary titrations. For ternary mixtures, sample cells containing 10  $\mu\text{M}$  hAIF $_{\Delta 1-101}$ :CypA complex (1:1) and 10, 20, 40 or 80  $\mu\text{M}$  H2AX were titrated with dsDNA (100  $\mu\text{M}$  in the syringe). These experiments allowed to determine the association constant for the titrating-ligand to either hAIF $_{\Delta 1-101}$  or the hAIF $_{\Delta 1-101}$ :CypA complex ( $K_{a, \text{app, titrating-ligand}}$ ) at different concentrations of the cell-ligand. These values were fit to equation 2, which describes the dependency of  $K_{a, \text{app, titrating-ligand}}$  as a function of the concentration of the cell-ligand bound to hAIF or hAIF:CypA complex and of the cooperation constant ( $\alpha$ ) (Velazquez-Campoy et al., 2006):

$$K_{a, \text{app, titrating-li}} = K_a^{\text{titrating-}} \cdot \frac{1 + \alpha K_a^{\text{cell-ligan}} \cdot [\text{cell-ligand}]}{1 + K_a^{\text{cell-ligand}} \cdot [\text{cell-ligand}]} \text{ (Eq. 2).}$$

where  $K_{a, \text{app, titrating-ligand}}$  is the association constant for the ligand (partner) in the syringe at each concentration of the in cell-ligand,  $K_a^{\text{cell-ligand}}$  is the association constant for the ligand in the cell in binary complex with hAIF or in ternary complex with hAIF:CypA, and [cell-ligand] is the concentration of cell-ligand in the calorimetric cell.

**Table 7.1:** Enthalpies of ionisation of different buffers used

Buffer	Reaction	pK <sub>a</sub>	$\Delta H^\circ$ (kcal/mol)
Phosphate	$\text{H}_2\text{PO}_4^- = \text{H}^+ + \text{HPO}_4^{2-}$	7.19	0.86
HEPES	$\text{HL}^\pm = \text{H}^+ + \text{L}^-$ (HL = C <sub>8</sub> H <sub>18</sub> N <sub>2</sub> O <sub>4</sub> S)	7.56	4.80
MOPS	$\text{HL}^\pm = \text{H}^+ + \text{L}^-$ (HL = C <sub>7</sub> H <sub>15</sub> NO <sub>4</sub> S)	7.18	5.04
TES	$\text{HL}^\pm = \text{H}^+ + \text{L}^-$ (HL = C <sub>6</sub> H <sub>15</sub> NO <sub>6</sub> S)	7.76	7.80
TRIS/HCl	$\text{HL}^+ = \text{H}^+ + \text{L}$ (HL = C <sub>4</sub> H <sub>11</sub> NO <sub>3</sub> )	8.07	11.51
Values measured at 298.15 K and 0.1 MPa. Data from (Goldberg, Kishore & Lennen., 2002)			

## 7.5 RESULTS AND DISCUSION

### 7.5.1 VISUALISING THE DEGRADOSOME ASSEMBLY AT MOLECULAR LEVEL.

Evidence accumulated during the last years suggests that hAIF associates in a multi-complex structure called degradosome to enlarge efficiency on DNA chromatinolysis (Baritaud et al., 2010). In view of this, we first proved the ability of hAIF to *in vitro* assemble the degradosome upon interplay with CypA and H2AX. For that, hAIF $_{\Delta 1-101}$  (67 kDa) was incubated with 3-fold excess of either H2AX or CypA (16 and 18 kDa respectively), or with both proteins simultaneously. The resulting mixtures were then separated by high-



resolution CN-PAGE for the specific detection of hAIF. As shown in the immunoblot analysis (**Figure 7.1 A**), hAIF $_{\Delta 1-101}$  migrates as a unique band that shifts its position towards higher MW in the presence of CypA and H2AX.

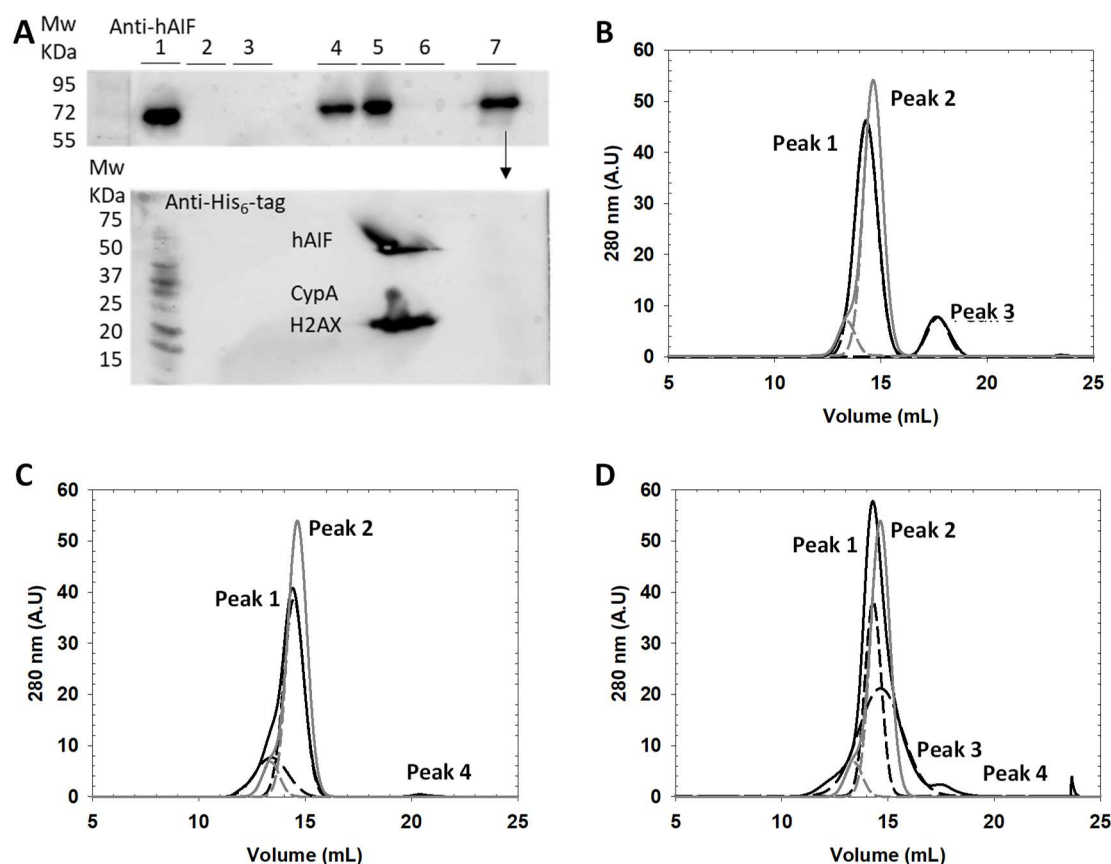


**Figure 7.1: Quaternary composition of the degradosome. (A)** Western blot analysis of the degradosome components after separation of proteins by high-resolution CN-PAGE. Lane 1, hAIF $_{\Delta 1-101}$ ; lane 2, CypA; lane 3, H2AX; lane 4, hAIF $_{\Delta 1-101}$ :CypA (1:3 ratio); lane 5, hAIF $_{\Delta 1-101}$ :H2AX; lane 6, CypA:H2AX (1:3 ratio); lane 7, hAIF $_{\Delta 1-101}$ :CypA:H2AX (1:3:3 ratio, degradosome). Mixtures were incubated for 15 min at 25 °C in 50 mM Kpi, pH 7.4, prior to gel electrophoresis loading. After separation, the blot was probed with hAIF $_{\Delta 1-101}$  specific antibodies. Subsequently, the lane corresponding to a duplicate of the degradosome sample (hAIF $_{\Delta 1-101}$ :CypA:H2AX His-tagged in all components) in the CN-PAGE was excised and loaded in a second SDS-PAGE dimension to separate proteins by MW. Protein spots were then Western-analysed using anti-His-tag. **Chromatographic deconvolution profiles of mixtures of AIF $_{\Delta 1-101}$  with (B) CypA, (C) H2AX, and (D) both nuclear proteins.** hAIF $_{\Delta 1-101}$  was incubated with its nuclear partners (1:3 proportion) for 15 min at 25 °C in Kpi 50 mM, pH 7.4, before passing through a Sephadex S-200 column using the same buffer supplemented with 10 mM NaCl. The elution profiles obtained for each mixture are shown in black lines, while control profiles for hAIF $_{\Delta 1-101}$  and CypA are in grey. The respective different populations assigned by Gaussian analysis are depicted in dashed lines.

The progressive reduction of electrophoretic mobility observed, hAIF $_{\Delta 1-101}$  > hAIF $_{\Delta 1-101}$ :H2AX > hAIF $_{\Delta 1-101}$ :CypA > hAIF $_{\Delta 1-101}$ :H2AX:CypA, correlates well with the expected MW of the corresponding binary and ternary complexes (83, 85 and 101 kDa respectively). In

order to verify co-migration of proteins, a duplicated lane containing the degradosome mixture was excised from the gel and analysed by a two-dimensional SDS-PAGE.

A total of three protein spots were detected with MWs that corresponded to those for hAIF $_{\Delta 1-101}$ , HA2X and CypA. This evidences for the first time the simultaneous interplay of hAIF with these two nuclear proteins to assemble the degradosome.

In the light of these results, we also studied the stability and stoichiometry of the degradosome complex by using gel filtration chromatography (**Figure 7.1 B-D**). For that, we used freshly purified fractions of hAIF $_{\Delta 1-101}$ , CypA and H2AX that eluted as monomeric proteins with apparent MW ( $MW^{app}$ ) of 47, 13 and 5 kDa respectively.

For all mixtures assayed, the observed behaviour is consistent with the formation of stable complexes (**Table 7.2**). Binary mixtures of hAIF $_{\Delta 1-101}$  with CypA and H2AX eluted mainly as new broad peaks of lower exclusion volume than that of free hAIF $_{\Delta 1-101}$ , corresponding to  $MW^{app}$  of ~53 for hAIF $_{\Delta 1-101}$ :CypA mixtures and ~50 kDa for hAIF $_{\Delta 1-101}$ :H2AX mixtures. The  $MW^{app}$  s of these new species agree with a hetero-dimer stoichiometry of one protomer of hAIF per protomer of CyA/H2AX. In the case of ternary mixtures, the deconvolution of the principal eluted peak suggests two populations with  $MW^{app}$  of ~57 and ~47 kDa in similar proportions. They would correspond to the degradosome assembly and the monomeric hAIF respectively.

**Table 7.2:** Quaternary assemblies of hAIF $_{\Delta 1-101}$  with its apoptotic partners.

Sample	Apparent molecular weight (kDa)				Complex assembly (stoichiometry)
	Peak 1	Peak 2	Peak 3	Peak 4	
<b>hAIF<math>_{\Delta 1-101}</math></b>		47			Monomer
<b>CypA</b>			13		Monomer
<b>H2AX</b>				5	Monomer
<b>hAIF<math>_{\Delta 1-101}</math>:CypA</b>	53		13		Hetero-Dimer (1:1)
<b>hAIF<math>_{\Delta 1-101}</math>:H2AX</b>	50			5	Hetero-Dimer (1:1)
<b>hAIF<math>_{\Delta 1-101}</math>:CypA:H2AX</b>	57	47	14	nd	Hetero-Trimer (1:1:1)

Free proteins and pre-formed mixtures of hAIF $_{\Delta 1-101}$  with the different partners (1:3 ratio) in 50 mM Kpi, pH 7.4, were passed through a Sephadex S-200 column in the same buffer supplemented with 10 mM NaCl.  $^{app}MW$ s of the elution peaks were obtained by peak identification upon Gaussian deconvolution of the elution profiles. Table shows the calculated MWs for the principal components of every population. nd: no detected.

The multimeric state of single, binary and ternary mixtures of the three proteins involved in the formation of the degradosome was also analysed at the single molecule level by



using AFM. As observed in **Figure 7.2**, under the assayed conditions, the populations of hAIF<sub>Δ1-101</sub>, CypA and H2AX were monomeric (95-98%) (**Figure 7.2 A, B, C**, respectively), and no features bigger than occasional homo-dimers were observed (**Table 7.3**). Thus, average heights of  $6.3 \pm 0.9$  nm,  $3.9 \pm 0.6$  nm and  $4.6 \pm 0.7$  nm for hAIF<sub>Δ1-101</sub>, CypA and H2AX, respectively, agree with data of the corresponding PDB structures (PDB codes: 4BV6 and 2CPL for hAIF<sub>Δ1-101</sub> and CypA, respectively; 6K1K for H2AX from nucleosome core particle). When similarly evaluating mixtures containing hAIF<sub>Δ1-101</sub> and either CypA or H2AX (**Figure 7.2 D E**), monomers corresponding well to the dimensions of isolated proteins were identified, but new imaging features were also observed. Differences of these new features regarding to monomeric and homo-dimeric features of isolated proteins (**Figure 7.2 A-C**) indicates that they are compatible with formation of stable hetero-dimeric complexes with similar angles among the two protein components for both complexes ( $\sim 135^\circ$ ) (**Figure 7.2 D and E**). The hetero-dimers population appears higher for CypA (**Figure 7.2 D**) than for H2AX (**Figure 7.2 E**) (53 % vs 30 % (**Table 7.3**), respectively). This might indicate a more stable complex for hAIF<sub>Δ1-101</sub>:CypA, which might support this interaction forming first. hAIF<sub>Δ1-101</sub>:H2AX and hAIF<sub>Δ1-101</sub>:CypA hetero-dimers display analogous angles among the two component molecules in the complexes ( $\sim 135^\circ$ ) (**Figure 7.8 D and E** respectively). Finally, simultaneous incubation of the three degradosome components produces 25 % of monomers, 43 % of hetero-dimers and 32 % of hetero-trimers (**Table 7.3**). Heights of the quaternary features remained similar than those of monomers previously indicated. This suggests that protein association takes place at the same mica plane.

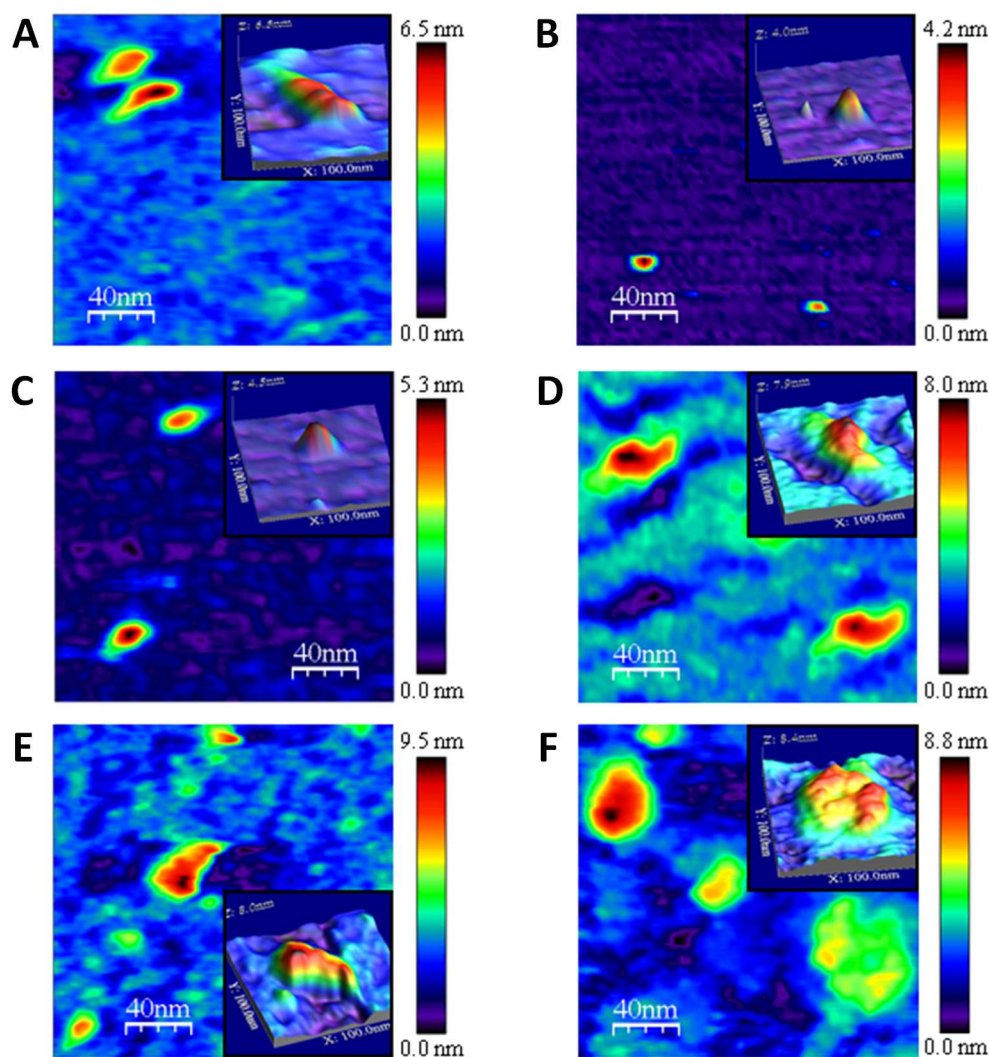


**Figure 7.2: AFM imaging of proteins involved in the degradosome formation and of their binary and ternary associations.** (A) hAIF $\Delta_{1-101}$ . (B) CypA. (C) H2AX. (D) hAIF $\Delta_{1-101}$ :CypA. (E) hAIF $\Delta_{1-101}$ :H2AX. (F) hAIF $\Delta_{1-101}$ :CypA:H2AX. hAIF $\Delta_{1-101}$  (0.5  $\mu$ M) was incubated with its nuclear partners (1:1 ratio) for 10 min at 4  $^{\circ}$ C in PBS, pH 7.0. Scan size 200 nm x 200 nm. The inset panels depict zooms of representative 3-D AFM images of the studied protein or protein complexes. Scan size 100 nm x 100 nm for all inset images.

**Table 7.3:** Distribution of quaternary species identified by AFM imaging for free AIF $_{\Delta 1-101}$ , CypA, H2AX, as well as for their binary and ternary complexes.

Sample mixtures	Monomers (%)	Hetero-Dimers (%)	Hetero-Trimers (%)
hAIF $_{\Delta 1-101}$	98	2*	-
CypA	95	5*	-
H2AX	95	5*	-
hAIF $_{\Delta 1-101}$ + CypA	45	53	2
hAIF $_{\Delta 1-101}$ + H2AX	70	30	-
hAIF $_{\Delta 1-101}$ + CypA + H2AX	25	43	32

Protein samples in PBS, pH 7.0. Protein mixtures containing 0.5  $\mu$ M of each protein were pre-incubated before the AFM analysis. Percentages are referred to the total number of protein molecules analysed. Percentage error is within 5-10 %.

\*In these cases correspond to homo-dimers.

This degradosome assembly would promote larger interaction areas with the DNA strands (**Figure 7.2 F**). This agrees with docking simulation studies that demonstrated the flexibility of the hAIF $_{\Delta 1-101}$ :CypA:H2AX complex (Baritaud et al., 2010).

## 7.5.2 BINARY INTERACTIONS BETWEEN DEGRADOSOME COMPONENTS.

ITC was used to determine the affinity and thermodynamic parameters of binary interactions among the components of the DNA-degradosome active complex, namely hAIF $_{\Delta 1-101}$ , CypA, H2AX and dsDNA. **Figures 7.3** and **7.4** summarise the interaction profiles and thermodynamic parameters derived for such binary interactions, which further confirm that in all cases 1:1 complex were produced.

Thermograms for the titration of hAIF $_{\Delta 1-101}$  with its protein partners, CypA and H2AX, (**Figure 7.3 A-B**) indicated binding with moderate affinities in both cases, with  $K_d$  values in the low micromolar range. However, when depicting the thermodynamic contributions to the binding, it is observed that the interaction of hAIF $_{\Delta 1-101}$  with H2AX was entropically guided, whereas binding of CypA to hAIF $_{\Delta 1-101}$  was driven by a strong enthalpic contribution with an important opposing entropic contribution to the binding. The corresponding numerical data are shown in **Table 7.4**.

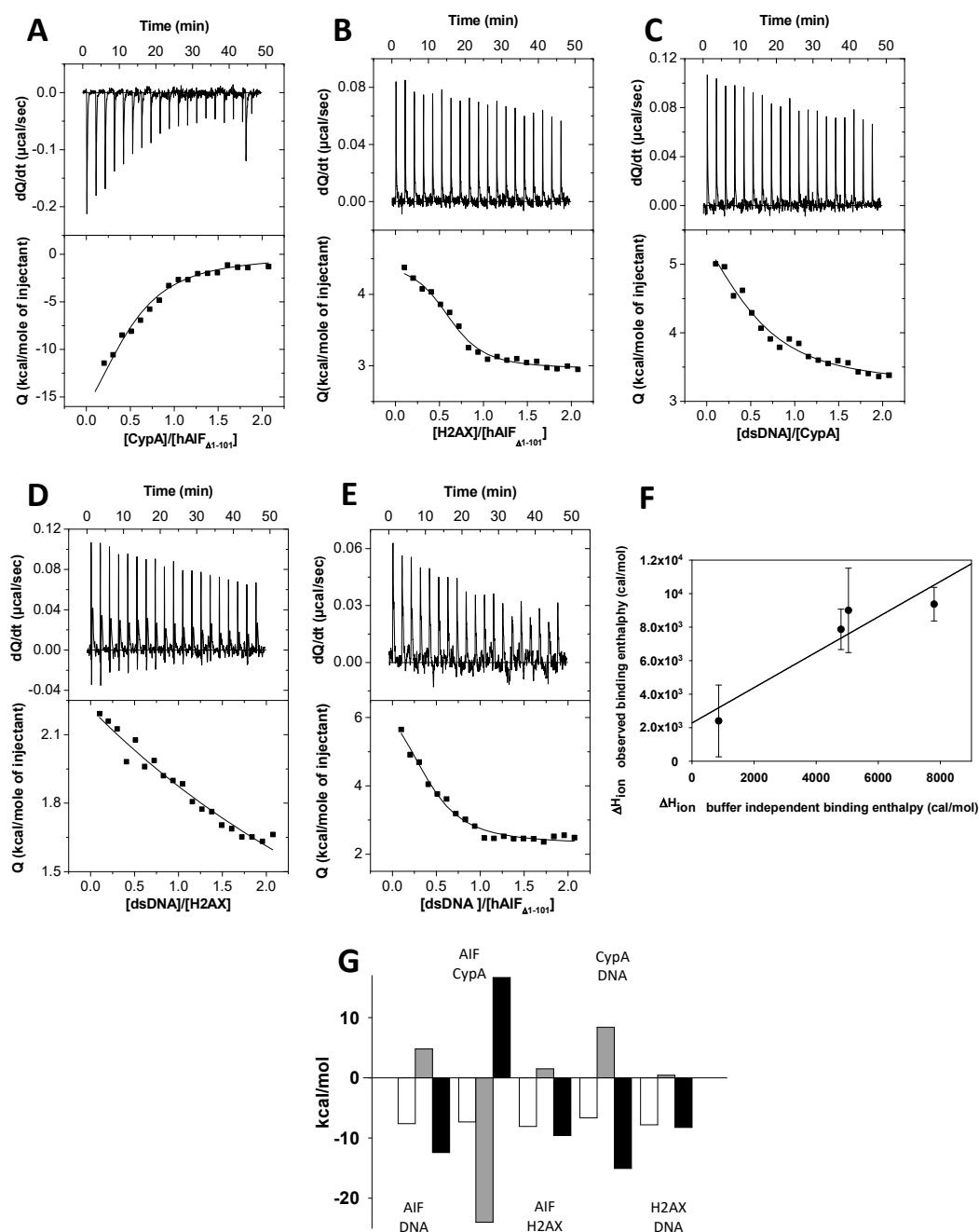


**Figure 7.3: Calorimetric titrations and thermodynamic parameters for binary interactions among the DNA-degradosome components. (A)** hAIF $\Delta_{1-101}$ :CypA. **(B)** hAIF $\Delta_{1-101}$ :H2AX. **(C)** CypA:dsDNA. **(D)** H2AX:dsDNA. **(E)** H2AX:dsDNA. ITC measurements were performed in 50 mM Kpi, pH 7.4, at 25 °C or at 15 °C when evaluating interactions involving DNA or H2AX. The upper panels show the thermograms for the interactions, whereas the lower panels show the corresponding binding isotherms with integrated heats. Data were fitted to a home-derived model for a single binding site (continuous lines in binding isotherms). **(F)** Dependence of the observed binding enthalpy ( $\Delta H$ ) for the hAIF $\Delta_{1-101}$ :dsDNA complex formation on the buffer ionisation enthalpy ( $\Delta H_{\text{ion}}$ ) at 15 °C (mean  $\pm$  SD,  $n=3$ ). Used buffers were Kpi, TES, MOPS and HEPES at 150 mM ionic strength. The pH was 7.4 and 7.5 respectively in Kpi and TES buffers, and 8.0 for HEPES and MOPS. The solid line represents the linear regression fit to equation 1. It provides estimation of the buffer independent enthalpy ( $\Delta H^\circ$ ) and of the net number of exchanged protons ( $n_{\text{H}^+}$ ) upon complex formation. **(G) Thermodynamic dissection of the interactions.** Gibbs energy ( $\Delta G$ ), enthalpic ( $\Delta H$ ), and entropic ( $-\Delta S$ ) contributions to the binding are represented in white, grey and black bars, respectively.

Binding of dsDNA to each of the three single proteins was also evaluated (**Figures 7.3 E-G**). In all cases, dsDNA binding was characterised by moderate affinity ( $K_d$  also in the low micromolar range), being in all cases the binding entropically driven and the enthalpic contribution to the binding unfavourable. These data are consistent with the interaction of hAIF $_{\Delta 1-101}$  and dsDNA being described as a surface-charge interaction where surface desolvation is needed for the interaction to occur.

**Table 7.4:** Thermodynamic parameters for the interaction of hAIF $_{\Delta 1-101}$  with CypA, H2AX and dsDNA

Sample mixture in calorimetric cells	Titration ligand	$K_d$ ( $\mu$ M)	N	$\Delta H$ (kcal/mol)	$\Delta G$ (kcal/mol)	$-T\Delta S$ (kcal/mol)
Binary complexes						
hAIF $_{\Delta 1-101}$	CypA	0.8	0.6	-13.2	-8.3	4.9
hAIF $_{\Delta 1-101}$	H2AX	0.7	0.6	1.5	-8.1	-9.6
hAIF $_{\Delta 1-101}$	dsDNA	1.6	0.4	4.9	-7.6	-12.4
CypA	dsDNA	8.9	0.6	8.4	-6.7	-15.1
H2AX	dsDNA	1.2	0.8	0.4	-7.8	-8.2

Values obtained from ITC assays at 25 °C or at 15 °C, when evaluating interactions in presence of DNA or H2AX respectively in 50 mM Kpi, pH 7.4. N is the calculated binding stoichiometry. The thermodynamic parameters were calculated by  $K_d = (K_a)^{-1}$ ,  $\Delta G = RT \ln K_d$  and  $-T\Delta S = \Delta G - \Delta H$ . Errors considered in the measured parameters ( $\pm 20\%$  in  $K_a$  and  $\pm 0.3$  kcal/mol in  $\Delta H$  and  $-T\Delta S$ ).

Therefore, we also estimated the buffer-independent binding enthalpy for the hAIF $_{\Delta 1-101}$ :dsDNA interaction and the net number of protons exchanged upon complex formation. For this purpose, experiments were performed using buffers with different  $\Delta H_{ion}$  (**Figure 7.3 F, Table 7.5**). These experiments determined a buffer-independent ionisation free enthalpy of 2.2 Kcal/mol, and indicated that upon association of dsDNA to hAIF $_{\Delta 1-101}$  about 1 proton is released into the bulk solution (i.e. at least one ionisable group is involved in this proton exchange process). Therefore, the affinity of the hAIF $_{\Delta 1-101}$ :dsDNA association will be pH-dependent.

Moreover, under the assayed conditions, the interactions of hAIF $_{\Delta 1-101}$  and H2AX with dsDNA were stronger regarding the CypA:dsDNA one. In the case of H2AX this is particularly due to a considerably less unfavourable enthalpic contribution to the binding, despite a milder favourable entropic contribution.

**Table 7.5:** Thermodynamic parameters for the interaction of AIF $\Delta$ 1-101 with dsDNA in different buffers.

Buffer	$K_d$ ( $\mu$ M)	N	$\Delta H$ (kcal/mol)	$\Delta G$ (kcal/mol)	$-T\Delta S$ (kcal/mol)
Kpi pH 7.4	1.6	0.4	4.9	-7.6	-12.4
HEPES pH 8.0	1.1	0.4	8.5	-7.8	-16.3
MOPS pH 8.0	1.0	1.1	8.8	-7.9	-16.7
TES pH 7.6	0.1	0.7	9.3	-9.1	-18.4

Values obtained from ITC assays at 15 °C and at 150 mM ionic strength. Data calculated as in Table 7.4.

Altogether these data indicate that the binary interactions of hAIF $\Delta$ 1-101 with its nuclear partners, CypA and H2AX, are slightly stronger than with dsDNA, and show CypA as the degradosome component with less affinity for dsDNA under the assayed conditions.

### 7.5.3 DNA-DEGRADOSOME ASSEMBLY AND COOPERATIVE EFFECTS

We then proceeded to study the binding contributions for the formation of the ternary complexes among the DNA-degradosome complex components (**Figure 7.4**). Formation of different ternary complexes, including the degradosome, was studied by titrating mixtures containing either two proteins or one protein and DNA, with any of the remaining proteins or with dsDNA. Finally, assays to study the DNA-degradosome complex formation were performed using mixtures containing equimolecular amounts of hAIF $\Delta$ 1-101 and CypA and different concentrations of H2AX, which were then titrated with dsDNA.

Binding and thermodynamic parameters obtained from these assays are summarised in **Table 7.6**. In general, these interactions are entropically guided, with opposing enthalpic contributions to the binding. It is worth to note the particularly favourable entropic contribution leading binding, and the strong opposing enthalpic one, for dsDNA binding to the preformed hAIF $\Delta$ 1-101:H2AX complex. Comparison of these data with those for the formation of the hAIF $\Delta$ 1-101:dsDNA binary complex (**Table 7.4**) indicates that H2AX modulates the interaction mode of hAIF $\Delta$ 1-101 with the dsDNA, despite having minor influence in the strength of the binding. The only exception to this behaviour is found for the binding of CypA to the preformed hAIF $\Delta$ 1-101:dsDNA complex that is enthalpically guided, similarly to that observed for the formation of the hAIF $\Delta$ 1-101:CypA binary complex (**Table 7.4**). Nonetheless, it is worth to mention that the presence of dsDNA reduces the

favourable enthalpic contribution to the CypA binding to hAIF<sub>Δ1-101</sub> and turns the entropic contribution also into favourable. Thus, among the studied ternary interactions the most favourable ones were those for the binding of H2AX to the preformed hAIF<sub>Δ1-101</sub>:dsDNA complex, and that for the formation of the degradosome upon binding of H2AX to hAIF<sub>Δ1-101</sub>:CypA. Both of these interactions were driven by strong entropic binding contributions.

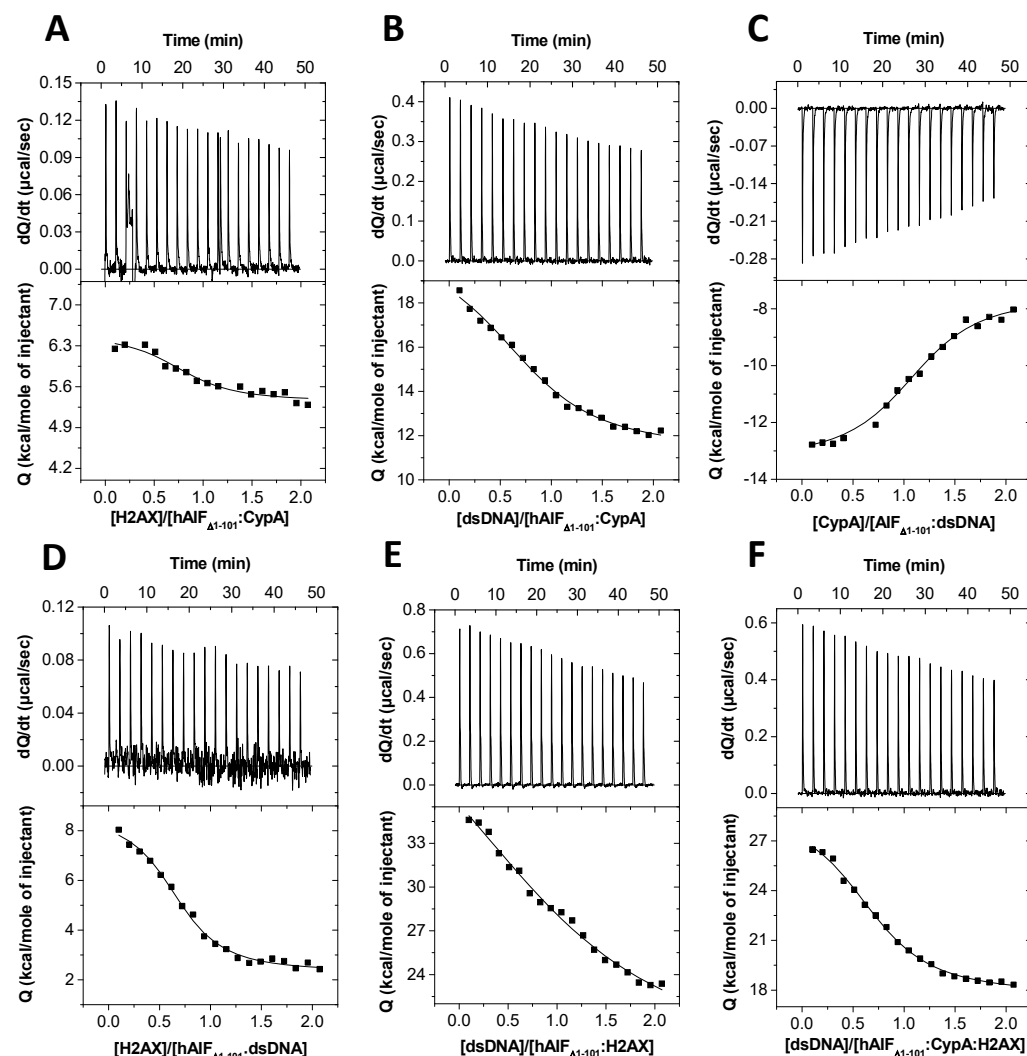


**Figure 7.4: Calorimetric titrations for ternary and quaternary interactions among the different DNA-degradosome complex components.** Titrations of hAIF<sub>Δ1-101</sub>:CypA mixtures with (A) H2AX and (B) DNA. Titrations of hAIF<sub>Δ1-101</sub>:dsDNA mixtures with (C) CypA and (D) H2AX. (E) Titration of hAIF<sub>Δ1-101</sub>:H2AX mixtures and of the (F) degradosome with dsDNA. The upper panels show the thermograms for the interactions and the lower panels show the corresponding binding isotherms with integrated heats. Data were obtained by fitting ITC thermograms to a home-derived model for a single binding site (continuous lines in binding isotherms). The pre-formed mixtures (1:1: ratio) were incubated 15 min in 50 mM Kpi, pH 7.4, at 25 °C. ITC measurements were performed in the same buffer at 25°C or at 15 °C when evaluating interactions involving H2AX or DNA.

Finally, binding of dsDNA to the hetero-trimer degradosome complex was also entropically-driven, with the simultaneous presence of H2AX and CypA modulating

enthalpic and entropic contributions to the binding to intermediate values of those reported for dsDNA binding to hAIF<sub>Δ1-101</sub> and to its protein-binary preformed complexes.

**Table 7.6:** Influence of the association order of components of the DNA-degradosome on the binding thermodynamic parameters.

Initial mixtures	Titration ligand	$K_d$ ( $\mu$ M)	N	$\Delta H$ (kcal/mol)	$\Delta G$ (kcal/mol)	$-T\Delta S$ (kcal/mol)
<b>Ternary complex</b>						
<b>hAIF<sub>Δ1-101</sub>:dsDNA (1:1)</b>	CypA	1.2	0.8	-5.5	-8.1	-2.6
<b>hAIF<sub>Δ1-101</sub>:dsDNA (1:2)</b>	CypA	1.9	0.7	-4.8	-7.6	-2.7
<b>hAIF<sub>Δ1-101</sub>:dsDNA (1:4)</b>	CypA	2.2	0.5	-3.3	-7.5	-4.2
<b>hAIF<sub>Δ1-101</sub>:dsDNA (1:8)</b>	CypA	2.6	0.7	-2.0	-7.4	-5.3
<b>hAIF<sub>Δ1-101</sub>:dsDNA (1:1)</b>	H2AX	0.53	0.7	6.3	-8.3	-14.6
<b>hAIF<sub>Δ1-101</sub>:dsDNA (1:2)</b>	H2AX	0.36	0.7	1.5	-8.5	-10.0
<b>hAIF<sub>Δ1-101</sub>:dsDNA (1:4)</b>	H2AX	0.30	0.7	1.2	-8.6	-10.0
<b>hAIF<sub>Δ1-101</sub>:dsDNA (1:8)</b>	H2AX	0.26	0.7	1.0	-8.7	-9.6
<b>hAIF<sub>Δ1-101</sub>:CypA (1:1)</b>	dsDNA	2.4	0.8	9.1	-7.7	-16.8
<b>hAIF<sub>Δ1-101</sub>:CypA (1:8)</b>	dsDNA	4.1	0.8	14.2	-7.3	-21.5
<b>hAIF<sub>Δ1-101</sub>:H2AX (1:1)</b>	dsDNA	3.2	1.1	18.2	-7.5	-25.7
<b>hAIF<sub>Δ1-101</sub>:H2AX (1:8)</b>	dsDNA	1.5	0.5	6.4	-7.9	-14.3
<b>Degradosome</b>						
<b>hAIF<sub>Δ1-101</sub>:CypA (1:1)</b>	H2AX	0.8	0.7	1.1	-8.3	-9.4
<b>DNA-Degradosome</b>						
<b>hAIF<sub>Δ1-101</sub>:CypA:H2AX (1:1:1)</b>	dsDNA	1.6	0.7	11.4	-7.9	-19.3
<b>hAIF<sub>Δ1-101</sub>:CypA:H2AX (1:1:2)</b>	dsDNA	1.5	1.5	11.5	-7.9	-19.4
<b>hAIF<sub>Δ1-101</sub>:CypA:H2AX (1:1:4)</b>	dsDNA	0.9	0.9	10.8	-8.2	-19.0
<b>hAIF<sub>Δ1-101</sub>:CypA:H2AX (1:1:8)</b>	dsDNA	0.7	1.1	16.7	-8.4	-25.1

Values obtained from ITC assays at 15 °C in 50 mM Kpi, pH 7.4. N is the calculated binding stoichiometry.



The thermodynamic values of the ternary and quaternary complexes, tested at 1:1 ratio, are given in **Figure 7.5**, indicating that all are energetically favourable. With the only exception for the interaction of hAIF $_{\Delta 1-101}$ :DNA with CypA, which is enthalpy-driven, the rest of the assays are dominated by the entropic contribution, indicative of important contributions of conformational effects to the binding.

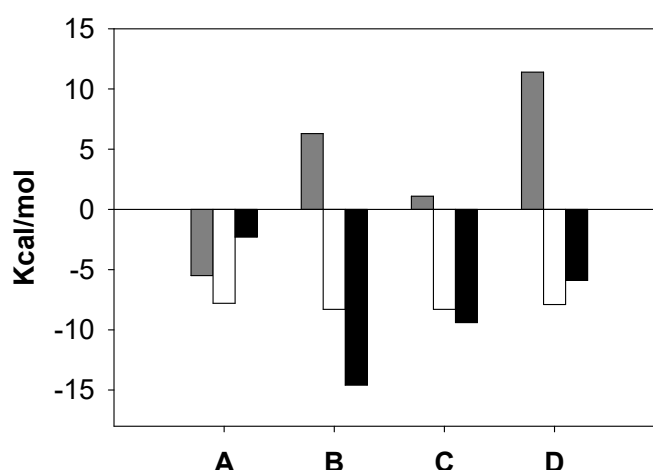


**Figure 7.5: Thermodynamic dissection of the interactions in ternary and quaternary organizations.** (A), hAIF $_{\Delta 1-101}$ :DNA-CypA; (B), hAIF $_{\Delta 1-101}$ :DNA-H2AX; (C), Degradosome; and (D), DNA-Degradosome. Gibbs energy ( $\Delta G$ ), enthalpy ( $\Delta H$ ), and entropy ( $-T\Delta S$ ) contributions to the binding are represented in white, grey and black bars, respectively.

**Table 7.7:** Cooperativity coefficients ( $\alpha$ ) for the binding to hAIF $_{\Delta 1-101}$  of the different components of the DNA-degradosome complex.

Binary mixture in calorimetric cell	Titration Ligand	$\alpha$	$K_a^{\text{titrating-ligand}}$ ( $\mu\text{M}^{-1}$ )	$K_a^{\text{cell-ligand}}$ ( $\mu\text{M}^{-1}$ )
hAIF $_{\Delta 1-101}$ :dsDNA	CypA	$0.30 \pm 0.02$	$1.2 \pm 0.1$	$0.75 \pm 0.02$
hAIF $_{\Delta 1-101}$ :dsDNA	H2AX	$2.7 \pm 0.2$	$1.5 \pm 0.1$	$0.10 \pm 0.04$

ITC assays were performed at 15 °C in 50 mM Kpi, pH 7.4.  $\alpha$  represents the cooperativity coefficient of the ligand binding,  $K_a$  ligand represents the association constant for the titrating ligand binding to the free hAIF $_{\Delta 1-101}$  or to the hAIF $_{\Delta 1-101}$ :CypA complex.  $\alpha$  and  $K_a$  values estimated from the fit to equation 2.

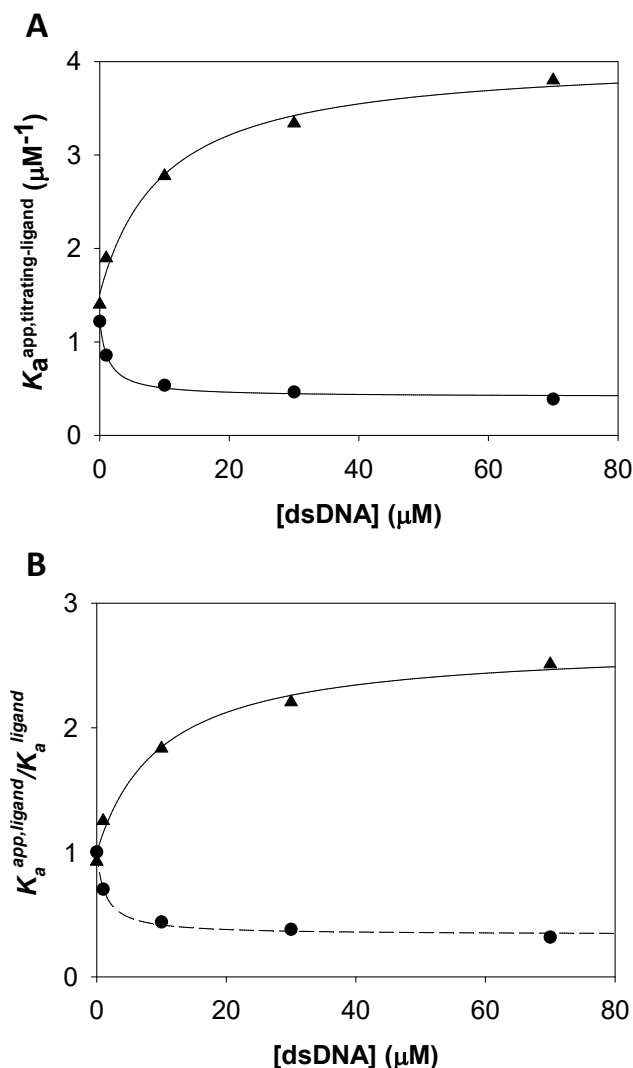


**Figure 7.6:** Binding cooperativity of the DNA-degradosome components to hAIF $_{\Delta 1-101}$ . **(A)** Dependence on the sample concentration of dsDNA for the apparent association constants of CypA ( $K_a^{app, CypA}$ , closed circles) and H2AX ( $K_a^{app, H2AX}$ , closed triangles) to hAIF $_{\Delta 1-101}$ :dsDNA mixtures. Data were fitted to eq. 2 and the fits are represented by lines. Evolution of **(B)**  $K_a^{app, ligand} / K_a^{ligand}$  ratios as a function of the dsDNA concentration. Lines are included only as visual cues for the data evolution. All experiments were performed in 50 mM Kpi, pH 7.4, at 15 °C.

Once the binding parameters were obtained for all possible combinations of hAIF $_{\Delta 1-101}$  with its nuclear partners, the binding cooperativity between them was assessed. For this purpose,  $K_a^{app, titrating-ligand}$  values for the formation of ternary complexes were determined by titrating with each of the different partners, ligands CypA, H2AX and dsDNA, in-cell preformed mixtures of hAIF $_{\Delta 1-101}$  with different concentrations of one of the other partners (combinations shown in **Table 6**). Evolution of  $K_a^{app}$  values envisage negative and positive cooperativity, respectively, for the binding of CypA-dsDNA and of H2AX-dsDNA to hAIF $_{\Delta 1-101}$ .

#### 7.5.4 FREE GIBBS ENERGY FLOW IN THE DEGRADOSOME ASSEMBLY

The free energy values ( $\Delta G$ ) and the relative fraction of the protein (N, binding stoichiometry) involved in the interaction for all sequential combinations of hAIF $_{\Delta 1-101}$  with its protein partners and dsDNA, were used to evaluate the energy of the interaction network to form the DNA-degradosome. This network is summarised in the diagram shown in **Figure 7.7**. The diagram suggests that from the thermodynamic point of view hAIF $_{\Delta 1-101}$  binds slightly stronger CypA than H2AX, and that binding of any of them is favoured over that of dsDNA. In addition, the subsequent pathways leading to the transformation of binary complexes into ternary complexes show the degradosome complex as lower in energy as compared with ternary complexes lacking either CypA or H2AX but including dsDNA. Moreover, the pathway initiated by CypA binding is the one showing binding stoichiometries closer to 1. Therefore, these data envisage hAIF $_{\Delta 1-101}$ :CypA as the most likely initial interaction in the degradosome formation, and indicate that H2AX might be incorporated subsequently to finally bind the dsDNA. This fits with the fact that the hAIF $_{\Delta 1-101}$ :CypA complex may already combine with the cytosol to favour its entrance into the nucleus, so it is normal that this is the first interaction that occurs. Nonetheless, further studies for the titration of hAIF $_{\Delta 1-101}$ :H2AX with CypA are required to unambiguously prove such path.

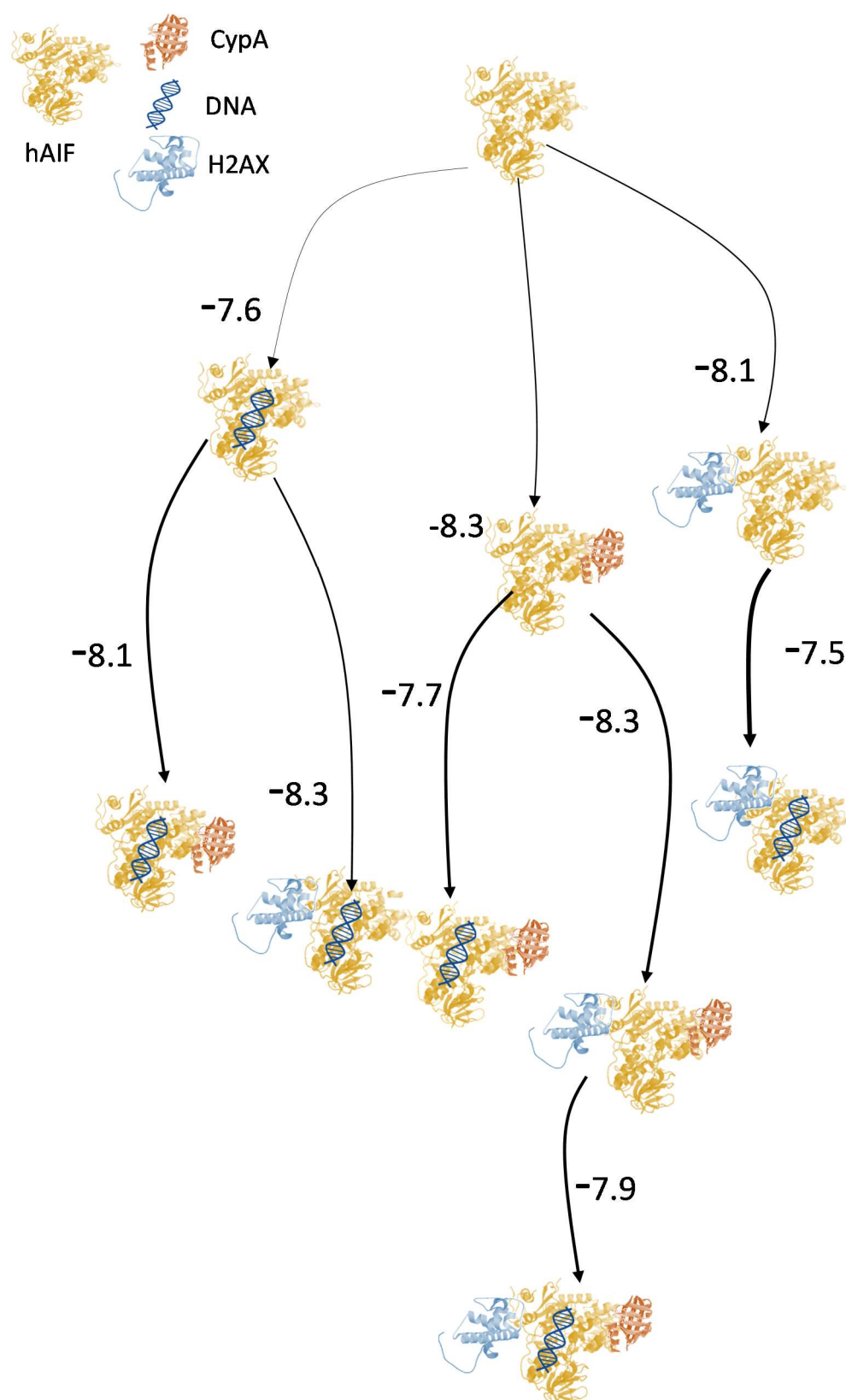


**Figure 7.7: Free Gibbs energy flow in the DNA-degradosome assembly.** The diagram summarises the thermodynamics of the interactions of hAIF<sub>Δ1-101</sub> with its different ligands. The length of the arrows is proportional to the ΔG for the interaction (values in kcal/mol are indicated in numbers), and its thickness is representative of the fraction of hAIF<sub>Δ1-101</sub> binding the titrating ligand (N).

### 7.5.5 PROTEIN-DNA VISUALIZATION BY AFM IMAGING

The effect of dsDNA on the topological organisation of the single, binary and ternary hetero-protein systems involved in formation of the degradosome was also analysed at the single molecule level using AFM.

Experiments in presence of dsDNA do not show significant changes in protein association percentages (**Table 7.8**). hAIF $_{\Delta 1-101}$  binds as monomer to dsDNA strands (**Figure 7.8 A**). The size observed for hAIF $_{\Delta 1-101}$  bound to dsDNA,  $\sim 9$  nm, agrees with the measurements obtained for the free protein ( $6.3 \pm 0.9$  nm) bound to free DNA ( $1.5 \pm 0.5$  nm) on cleaved mica (not shown). Noticeably, hAIF $_{\Delta 1-101}$  induces the stretching and opening of dsDNA (**Figure 7.8 A**).

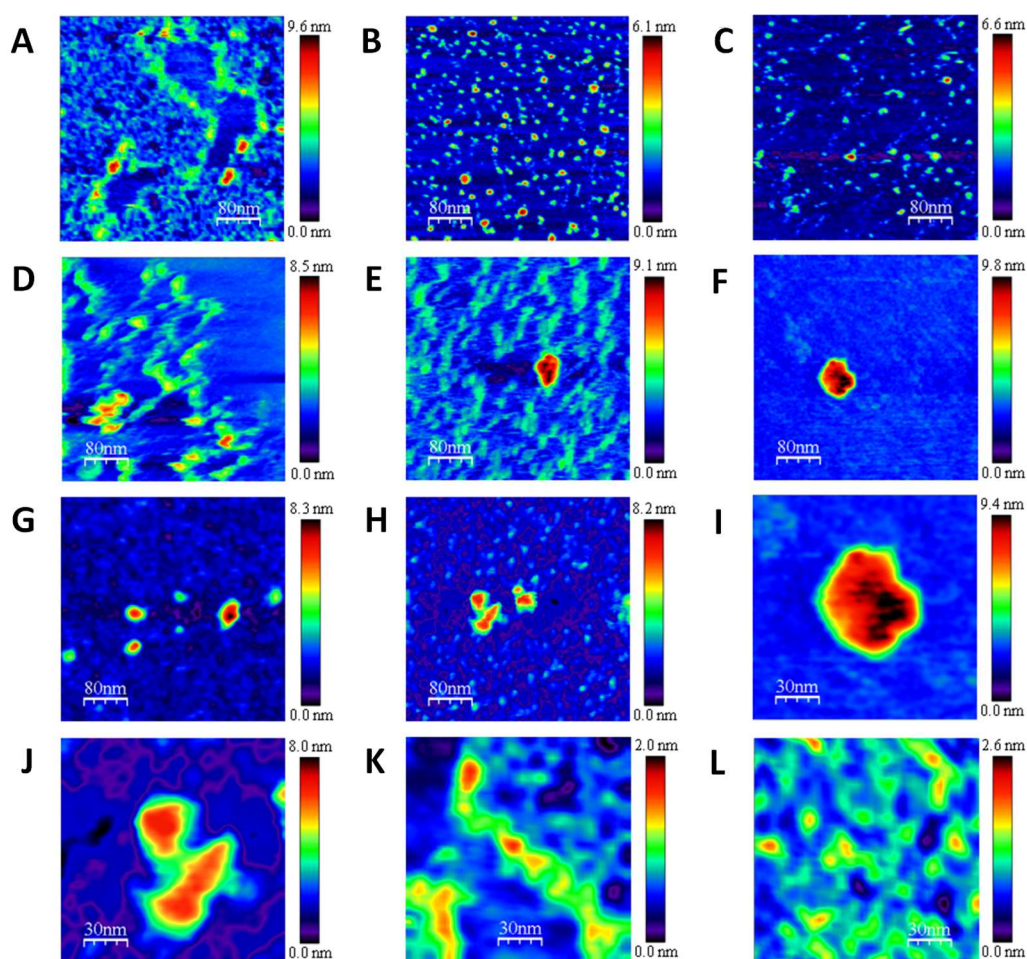


**Figure 7.8: AFM imaging study of the binding of dsDNA to the degradosome components.** (A) hAIF $_{\Delta 1-101}$ :dsDNA. (B) CypA:dsDNA. (C) H2AX:dsDNA. (D) hAIF $_{\Delta 1-101}$ :CypA:dsDNA. (E) hAIF $_{\Delta 1-101}$ :H2AX:dsDNA. (F) hAIF $_{\Delta 1-101}$ :CypA:H2AX:dsDNA. (G) Impact of  $\text{Ca}^{2+}$  and  $\text{Mg}^{2+}$  ions on dsDNA degradation by hAIF $_{\Delta 1-101}$ :CypA:dsDNA. (H) Impact of  $\text{Ca}^{2+}$  and  $\text{Mg}^{2+}$  ions on hAIF $_{\Delta 1-101}$ :CypA:H2AX:dsDNA topology. (I) and (J) are zoom images of (F) and (H), respectively, to better observe the integrity of the trimers. (K) pET-28a(+) DNA plasmid free. (L) DNA fragmented by the CypA endonuclease activity in presence of  $\text{Ca}^{2+}$  and  $\text{Mg}^{2+}$  ions. Scan size 400 nm x 400 nm (A-H) and 150 x 150 nm (I-L).

Distinct sequences along the strands of dsDNA bind hAIF<sub>Δ1-101</sub> with similar efficacy, indicating that the binding is not sequence-specific. Moreover, many flavoenzyme molecules are attached to few dsDNA strands in a clustered fashion, like “beads on a necklace”, indicating that the hAIF<sub>Δ1-101</sub>:dsDNA interaction displays cooperativity. A wide range of different mechanisms is used by the DNA to specifically bind proteins. Basically, the main readout strategies are based on the chemical recognition of DNA bases and on identification of the DNA contour (Rosh et al., 2010). In this second scenario, it has been shown that β-sheet helix arrangement deviations induce the DNA binding specificity changing the number of non-polar interactions or hydrogen bonds between the protein-DNA complex (Hegde et al., 1992).

Further research at nanoscale level must be devoted to better understand how the proteins are interacting on the binding sites of the dsDNA. Thus, it has been demonstrated that elongated strands allow the specific binding with other biomolecules enabling their proper recognition of defined sites (Pallarés et al., 2014). This behaviour could be based on the synergic effect of proteins which are involved in the degradosome formation to their dsDNA recognition and further binding (Sevrioukova, 2010). No condensation of DNA strands is observed in these redox conditions. According to the height profiles perpendicular to dsDNA molecules, CypA and H2AX also bind to DNA as monomers (**Table 7.8, Figure 7.8 B and C**, respectively).

Binary protein systems hAIF<sub>Δ1-101</sub>:CypA and hAIF<sub>Δ1-101</sub>:H2AX were also assayed in the presence of dsDNA. Percentages of protein association remained in the same range for both complexes when bound to dsDNA (**Tables 7.3 and 7.8**). In the case of hAIF<sub>Δ1-101</sub>:H2AX, a certain increase of multimeric species is found upon association with dsDNA (38-2 % of dimer-trimer vs 30 % dimers, respectively; **Table 7.8**). This might be attributed to unspecific electrostatic interactions between the negative charges of phosphate groups at the dsDNA helix and the positive H2AX surface (isoelectric point of 10.7) at the working pH. Dimers of hAIF<sub>Δ1-101</sub>:CypA and hAIF<sub>Δ1-101</sub>:H2AX bind tightly dsDNA (**Figure 7.8 D and E** respectively). hAIF<sub>Δ1-101</sub>:CypA produces a stretching effect on the strands that is not clearly observed when hAIF<sub>Δ1-101</sub>:H2AX binds dsDNA. The morphology and angle of the dimers are maintained when they are interacting with the dsDNA. Only a certain ratio presents a smaller angle that could be based on the flexible nature of the complexes formed between AIF<sub>Δ1-101</sub>:CypA and AIF<sub>Δ1-101</sub>:H2AX, especially in presence of dsDNA (Farina et al., 2017). This agrees with H2AX showing flexible domains such as the C-terminus that binds to the dsDNA helix or the L1 region that allows the interaction with other histones (Bonich and Hake, 2012).

**Table 7.8:** Effect of dsDNA binding on the quaternary organisation distribution of the degradosome components, when free or in binary and ternary complexes, as visualised by AFM imaging.

Sample mixtures	Monomers (%)	Hetero-Dimers (%)	Hetero-Trimers (%)	dsDNA effect
<b>hAIF<sub>Δ1-101</sub>:dsDNA</b>	98	2	-	Monomer binding Stretching and opening
<b>CypA:dsDNA</b>	95	5	-	Monomer binding
<b>CypA:DNA:Ca<sup>2+</sup>/Mg<sup>2+</sup></b>	95	5	-	Monomer binding Fragmentation
<b>H2AX:DNA</b>	97	3	-	Monomer binding
<b>hAIF<sub>Δ1-101</sub>:CypA:DNA</b>	45	55	-	Dimer binding Stretching
<b>hAIF<sub>Δ1-101</sub>:CypA:DNA:Ca<sup>2+</sup>/Mg<sup>2+</sup></b>	53	47	-	Binding and Fragmentation
<b>hAIF<sub>Δ1-101</sub>:H2AX:DNA</b>	60	38	2	Dimer binding Stretching
<b>hAIF<sub>Δ1-101</sub>:CypA:H2AX:DNA</b>	16	32	52	Protein complexes binding
<b>hAIF<sub>Δ1-101</sub>:CypA:H2AX:DNA:Ca<sup>2+</sup>/Mg<sup>2+</sup></b>	28	35	37	Binding and Fragmentation

Assays in PBS, pH 7.0. Percentages are referred to the total number of protein molecules. The incubation concentrations were 0.5 μM, 5 mM and 0.05 ng/μL for proteins, divalent cations and dsDNA, respectively. Percentage error is within 5-10 %.

The last condition studied with dsDNA was in presence of all the proteins involved in the degradosome formation (**Figures 7.8 F and 7.8 I**). The percentage of trimers bound to dsDNA increases almost two-fold times (from 32 up to 52 %), with a modest decrease of dimers and monomers (32 % and 16 %, respectively; **Table 7.8**). Hardly any trimer was found attached to mica instead of dsDNA, as observed by general colour scales and verified by height profiles. This observation could be explained by the net charge exhibited by the proteins which form the degradosome due to the differences observed in terms of their isoelectric points. At working pH, hAIF does not present electrical charge since their isoelectric point is neutral (Caned et al., 2002). CypA is slightly negatively charged with pI of 6.4-6.5 and as above described, H2AX is positively charged with pI of 10.7. These

differences of charge will induce protein recognition and specific orientation to enable the degradosome formation.

$\text{Ca}^{2+}$  and  $\text{Mg}^{2+}$  ions were added to analyse the effect of the CypA endonuclease activity on dsDNA. **Figure 7.8 G** and **7.8 H** show representative images for  $\text{hAIF}_{\Delta 1-101}:\text{CypA}:\text{dsDNA}$  and  $\text{hAIF}_{\Delta 1-101}:\text{CypA}:\text{H2AX}:\text{dsDNA}$  in the presence of both cations, respectively. The evaluated concentrations of ions seem to overcome the threshold needed by these complexes to degrade dsDNA strands into very small fragments, since fragmentation appears clear in different parts of the samples. Finally, zoom images of the dsDNA strands are shown to better visualise the CypA endonuclease activity in presence of  $\text{Ca}^{2+}$  and  $\text{Mg}^{2+}$  ions. Interestingly, the degradosome complex presents an equilibrium among open and compact morphology states. In absence of dsDNA the majority of molecules adopt close forms (**Figure 7.8 F**) that compact more when bound to dsDNA (**Figure 7.8 I**), and open after fragmentation has been produced (**Figure 7.8 J**). Thus, dsDNA strands preserve their integrity when the CypA endonuclease activity does not take place (**Figure 7.8 K**), but their fragmentation occurs when the CypA endonuclease activity carries out its function (**Figure 7.8 I**).

## 7.6 CONCLUSIONS

As it is known that DNA damage-mediated PCD requires nuclear interaction of  $\text{hAIF}_{\Delta 1-101}$ , H2AX and CypA, the existence of an hAIF dependent degradosome complex was previously predicted (Baritaud et al., 2010). In this study we have proven its *in vitro* formation. We also hypothesise a possible mechanism for its association.

Our results indicate that  $\text{hAIF}_{\Delta 1-101}$  can interact with all the components of the DNA-degradosome complex separately, and that all these intermediate complexes can interact with dsDNA. This finding is at odds with previous results (Baritaud et al., 2010) that stated no interaction between  $\text{hAIF}_{\Delta 1-101}$  and CypA in the absence of H2AX. Here, we have verified by CN-PAGE, molecular exclusion chromatography and AFM that all these binary and ternary interactions occur, and making use of ITC we have been able to obtain their thermodynamic binding parameters. Considering these data, we can hypothesise that the first occurring interaction might be the  $\text{hAIF}_{\Delta 1-101}:\text{CypA}$ , being this observation in agreement with this being the hetero-dimer more populated in AFM images and the one previously described in the literature (Cande et al., 2004). Consequently, considering free energy values for the evaluated interaction processes, it is feasible to expect subsequent binding of H2AX to the  $\text{hAIF}_{\Delta 1-101}:\text{CypA}$  complex to form the degradosome, which finally binds to the dsDNA. In addition, ITC data also show that the presence of dsDNA decreases



the affinity of CypA for hAIF<sub>Δ1-101</sub>. This might indicate a partial sweep of CypA from the degradosome by dsDNA, which might favour its nuclease action in the presence of Mg<sup>2+</sup> (as revealed by AFM data). In this sense, our results proof the formation of the degradosome and pave the way for a better understanding of its formation and of the pro-apoptotic function of hAIF<sub>Δ1-101</sub> at the molecular level.





## ***8-DISCUSSION***



The importance of hAIF in human health is becoming increasingly relevant. The aim of this thesis was to better understand at the molecular and conformational levels the factors that determine the interaction of hAIF with different biomolecules, including the coenzyme NADH, its different protein partners (H2AX, CypA, CHCHD4) and dsDNA, and, as a consequence, how they modulate its mitochondrial and nuclear functions. This required, as a first aim, the recombinant overproduction and purification of hAIF $_{\Delta 1-77}$  and hAIF $_{\Delta 1-101}$  isoforms, as well as of CHCHD4, CypA and H2AX. In addition, several hAIF $_{\Delta 1-101}$  and hAIF $_{\Delta 1-77}$  mutants, some of them related to diseases and other at key structural positions, were prepared for this study.

## 8.1 MULTIPLE FACTORS DETERMINE CONFORMATION AND STABILITY OF hAIF

To better understand the factors that can modulate the plasticity of hAIF in a cellular context, we have here evaluated the effect of subcellular pH values, CTC formation and pathogenic mutations on its stability. Since hAIF undergoes proteolytic processing from translation to incorporation and maturation in the mitochondrion, as well as upon mitochondrial apoptotic stimulation for its participation in parthanatos, this processing must contribute to the hAIF functions in its different cellular localisations. Therefore, we have also considered its different functional transcripts depending on the subcellular location. Thus, we have addressed the effect of NADH-dimerization, pH-dependent as well as protein length on the conformation of the hAIF to learn about the structural adaptation of the protein to specific subcellular conditions.

We first evaluated the stability of hAIF under different redox conditions. Our data indicate that in hAIF $_{\Delta 1-101ox}$  the R201-E531 and W196-R529 interactions contribute to residues 529-533 at the C-loop folding into an  $\alpha$ -helix. In contrast, in CTC this region contributes to the disorder of the C-loop, making this assembly less compact than the oxidised form and pointing to this fact as the main reason for its lower stability. The data also indicate that the redox-dependent conformational changes associated with the interaction of hAIF with NADH result in strong binding of the coenzyme in the NAD<sup>+</sup> form and in the dimerization of the protein, but have a negative impact on the overall stability of hAIF.

Upon analysing the stability of different hAIF constructs, hAIF $_{\Delta 1-77}$  and hAIF $_{\Delta 1-101}$ , at different pH values and different redox states, we also found that residues 77-101 were critical in the stability of mitochondrial hAIF. Moreover, they also favour the hAIF interaction

with CHCHD4, in agreement with this interaction occurring physiologically in the IMS (Hangen et al., 2015).

Once the influence of length and pH was assessed, the influence of pathogenic mutations, as well as key structural residues for interaction with their associated proteins or DNA, was considered. Thus, pathogenic variants of hAIF G308E, E493V and  $\Delta$ R201 were studied to assess how they may alter the stability and, consequently, their cellular activities, regulation and protein-protein interactions. Since hAIF interacts with several partners that can modulate its localisation and cellular activities, mutations causing biochemical alterations may compromise its *in vivo* functions. For the G308E and E493V mutations, our data indicate that the mutations have little effect on the thermal stability of hAIF $_{\Delta 1-101}$ , indicating that the effects observed for these pathogenic mutations *in vivo* do not appear related to a reduction in protein stability.

Therefore, these mutations would rather produce other effects on its *in vivo* activity. For example, the E493V mutation has been shown to increase the apoptotic activity of hAIF in a caspase-independent manner (Hangen et al., 2015), without altering the interaction with CHCHD4 or mitochondrial respiratory activity (Hangen et al., 2015). In contrast, the G308E mutation causes severe deficiency of the (I+IV) complex and decreases CHCHD4 binding (Hangen et al., 2015). However, these effects must rather be produced by altering the position of the adenylate moiety of NAD<sup>+</sup>, which has been shown to slow CTC formation and decrease the ability of the enzyme to discriminate between NADH and NADPH (Sorrentino et al., 2017).

The data we obtained for the  $\Delta$ R201 mutation indicate very drastic impacts on the stability and conformation of hAIF $_{\Delta 1-101}$ . As first, this deletion results in the disruption of the R201-E531 salt bridge, perturbing several functional sites and confirming that the  $\beta$ -hairpin-C-loop connection is a key in maintaining a compact active site and bound FAD. This correlates with loss of active site compactness, particularly affecting active site dynamics as well as changing the allosteric architecture of hAIF (Brosey et al., 2016). R201 was the first loss-of-function mutation described in the *aifm1* gene that causes progressive mitochondrial encephalopathy (Ghezzi et al., 2010). This is consistent with the drastic alterations in the redox properties of the mutant and, as a consequence, with the failure of OXPHOS playing an important role in the lethal phenotypes of R201 (Ghezzi et al., 2010, Rinaldi et al., 2012).

Beyond pathogenic mutations, we also studied the relevance of W196, also at the  $\beta$ -hairpin, in protein stability, working with three mutations, W196A, W196Y and W196L. Kinetic studies complemented with computational simulations reveal that W196 and the

conformation of the  $\beta$ -hairpin modulate the low efficiency of hAIF as a NADH oxidoreductase, contributing to configure its active site in a geometry not competent for turnover, so it particularly stabilises the CTC state by increasing the affinity for the NAD<sup>+</sup> product. These findings are consistent with other studies that envisaged the relevance of this residue (Brosey et al., 2016; Ferreira et al., 2014).

To understand the importance of W196 in hAIF conformation and of the  $\beta$ -hairpin motif in defining the conformation of hAIF interaction surfaces with their physiological partners we studied the interaction of the native and mutant proteins with CypA and DNA.

The interaction of native hAIF with CypA indicated binding with favourable enthalpy and unfavourable entropy. This agrees with the large number of electrostatic contacts reported for the interaction of CypA with the 370-394 synthetic peptide of AIF (Farina et al., 2017, Farina et al., 2018, Monti et al., 2020), as well as with the conformational selection and complex adopting high complementarity of the two proteins. It is notable that the enthalpic contribution to CypA binding became unfavourable for W196Y and W196A. However, this is compensated by the change in the sign of the entropic contribution to binding, which became highly favourable and made the mutational effect negligible with respect to the overall affinity. However, the W196 mutational modulation of the thermodynamic contributions to hAIF:CypA binding suggests a decrease in specificity and the production of non-native conformations. This is interesting because W196 and the  $\beta$ -hairpin do not share the protein surface with the NADH domain of AIF where the 370-394  $\beta$ -sheet is located. However, substitutions in W196 have important effects on the stability of hAIF $_{\Delta 1-101}$ , as well as on the conformation of the C-loop, the central strand and the dimerization interface located away from W196. Therefore, conformational changes occurring at the  $\beta$ -hairpin could also be transmitted to the CypA binding site. Therefore, the enhanced specificity for CypA in WT versus W196 variants could derive from its increased conformational rigidity that favours an induced recognition mechanism, while the increased flexibility of the protein becomes a non-specific interaction. This is consistent with what was described using a stapled peptide analogue of hAIF (370-394) to stabilise its C-loop organisation, which had less flexibility but considerably improved its affinity for CypA (Monti et al., 2020).

Regarding the interaction with DNA, it is suggested that positive charges clustered along the surface of AIF contribute to DNA binding, but no clear sequence specificity is expected as AIF recognises DNA, RNA as well as a large panel of ribonucleoproteins (Vahsen et al., 2006). Our thermograms for WT titration with dsDNA further confirm this lack of specificity as they show an entropically driven binding with an unfavourable enthalpy

contributing to the interaction. The W196A and W196Y mutations hardly alter the affinity of hAIF<sub>Δ1-101</sub> for DNA. However, although the thermodynamic patterns resembled those of WT, the entropic and enthalpic contributions to binding were respectively more favourable and less unfavourable. Structurally, DNA binding to hAIF is proposed via the nucleotide strand that envelops a positive shift crown of the protein. This crown appears considerably modulated in both shape and accessibility when comparing the WT crystallographic structure with W196A, as well as in structural models for all variants.

Taken together, these results show that the W196 side chain influences the enthalpic and entropic contributions to the binding free energy in binary complexes. Moreover, its substitution generally has a negative impact on the enthalpic contribution to the binding, whereas it enhances the entropic contribution. Therefore, W196 contributes to stabilise the conformation of the hAIF interaction surfaces with its partners.

We have also searched for new molecules that modulate the association/dissociation equilibrium of NADH/NAD<sup>+</sup> to hAIF and that can regulate its catalytic efficiency. We have used fluorescence changes that upon thermal denaturation allow us to assess the stability of hAIF<sub>Δ1-101</sub>. Shifts in  $T_{mFAD}$  induced by different molecules seem a feasible approach to identify ligands in HTS plate assays (Cremades et al., 2009).

Only one small molecule, aurintricarboxylic acid (ATA), have been before identified to bind hAIF by screening photonic crystal biosensors (Chan et al., 2008). In this study, we have identified some molecules that can serve as a starting point in the development of bioactive hAIF compounds with low cellular toxicity. ATA decreases  $T_{mFAD}$  similarly to NADH, induces quenching of flavin fluorescence and produces a dose-response curve, which allows estimation of a  $K_d^{ATA}$ .

Thus, NADH and ATA produce a ligand-induced perturbation consistent with binding and destabilisation of hAIF<sub>Δ1-101</sub>. Based on these results, we screened for compounds potentially binding hAIF<sub>Δ1-101</sub> using the HitFinder collection (Maybridge) and the Prestwick chemical library (Prestwick Chemical). We identified 11 compounds (C1 to C11) that shift  $T_{mFAD}$  between -3 °C and -23 °C, which could be postulated as hAIF binders. However, other phenomena, such as chemical denaturation of the protein or aggregation, could be involved in  $T_{mFAD}$  displacements. Six compounds (C1, C2, C5, C8, C9 and C11) out of 11 produce a dose-response  $\Delta T_{mFAD}$  indicative of binding. Only ATA, C2 and C11 have a destabilising effect on hAIF thermal conformation. Their binding may induce C-loop release, as occurs upon NADH binding and flavin reduction. Therefore, we have identified new molecules that modulate the association/dissociation equilibrium of NADH/NAD<sup>+</sup> to hAIF and regulate its catalytic efficiency



## 8.2 THE REDOX MITOCHONDRIAL ROLE OF hAIF

Upon reduction by NADH, hAIF undergoes dimerization and forms highly stable CTCs. Upon reduction, two NADH molecules are bound per protomer: NADH<sub>A</sub> and NADH<sub>B</sub> (**Figure 1.6**). In addition, hAIF undergoes conformational reorganisation into two specific insertions - the flexible regulatory C-loop and the  $\beta$ -hairpin 190-202 - that promote protein dimerization and stabilisation of a long-lasting CTC that modulates a monomer-dimer equilibrium and the protein interaction network in healthy mitochondria (Mate et al. 2002; Ferreira et al. 2014). Thus, hAIF is proposed to act as a sensor molecule of the mitochondrial redox state (Churbanova and Sevrioukova 2008; Ferreira et al. 2014).

In the present work we have shown that the W196 residue and the  $\beta$ -hairpin conformation contribute to configuring the NADH active site by rendering hAIF inefficient for NADH oxidation, as well as triggering the release of the C-loop in the reduced state. Furthermore, we have determined that both W196 and  $\beta$ -hairpin contribute to stabilise the CTC state of hAIF by increasing the affinity for NAD<sup>+</sup>. This agrees with the proposed role of W196 as a critical residue for CTC stability, mitochondrial homeostasis, as well as maintenance of the active site conformation and interaction surfaces with its partners (Brosey et al., 2016).

Just as we studied the interaction with CypA and DNA, we studied their interaction with CHCHD4, using ITC analysis of their interactions. The calorimetry results of the W196 mutants and the native protein in their interaction with CHCHD4 support an essential role of the conformational arrangement of the dimer, or of the site exposed by the C-loop displacement, or even of the C-loop itself in the interaction with CHCHD4. However, the entropic thermodynamic binding profile of oxidised W196A to CHCHD4 is indicative of non-specific interactions, whereas the data from the reduced forms suggest organised specific interactions. This agrees with specific binding of CHCHD4 to the native reduced protein. In contrast, the thermodynamic parameters reported here for CHCHD4 binding to W196A suggest that, although the conformational changes produced by the mutation allow CHCHD4 recognition, the complex formed will be far from the specific interaction presumably produced with the native reduced protein.

Therefore, NADH-dependent structural changes in AIF must play a key role in CHCHD4 binding. This is supported by Tyr and Leu replacements in W196 that also have a strong impact on the specificity and organisation of this interaction. Thus, the competent interaction of hAIF with CHCHD4 depends on the appropriate reduced protein architecture to favour the assembly of potentially disordered regions of both proteins to achieve a specific conformation. Moreover, the W196 residue contributes to providing such a CTC

architecture, potentially regulating the appropriate  $\beta$ -hairpin configuration that is key to the structural transition of AIF and its role in mitochondrial homeostasis.

Consistent with what is described in the literature, the N-terminus (key to the interaction), is unstructured when CHCHD4 is free (Banci et al., 2009), but appears to obtain a defined and organised structure when interacting in the reduced form (Hangen et al., 2015). This might be related with the fact that a non-productive hAIF-CHCHD4 interaction was suggested for the clinical F210L mutation resulting in abnormal assembly of mitochondrial complex I and III (Hu et al., 2017).

Studies on the effect of this chaperone on the redox capacities of hAIF have so far been scarcely reported. Moreover, when performed, they used the apoptotic isoform, which *in vivo* is not found in the IMS and thus does not participate in the supportive functions of CHCHD4. Therefore, we have here used a mitochondrial soluble variant.

In the present study, we have seen that hAIFmt $\Delta$ 1-77 is able to dimerise after reduction by NADH, forming a stable dimer. Moreover, this isoform favours the formation of the CTC by increasing the affinity for NADH. To further evaluate the hAIF-CHCHD4 molecular interaction, we have used both the apoptotic and mitochondrial forms of hAIF and its corresponding non-dimerizable forms (hAIF E413A/R422A/R430A), both in the oxidised and NADH-reduced states. We observed that the mitochondrial isoform was able to dimerise and maintain a dimeric stable conformation, while its triple mutant was not. In addition, for all constructs NADH reduction increases affinity for CHCHD4, indicating that NADH-dependent structural changes in hAIF modulate CHCHD4 binding. Therefore, NADH-dependent structural changes in hAIF must play a key role in CHCHD4 binding. In agreement, previously reported data indicated a lower expression of some respiratory complexes in cells unable to stabilise hAIF (Hangen et al. 2015).

We also studied the involvement of CHCHD4 in the oxidoreductase activity of mitochondrial hAIF. Compared to the apoptotic constructs, the mitochondrial variants were catalytically more efficient because they kinetically favour CTC formation by increasing the affinity of hAIF $\Delta$ 1-77 for the coenzyme in both redox states. Moreover, all mitochondrial forms increase the thermodynamic preference for NADH binding relative to the apoptotic form.

These observations agree with the fact that it is in the mitochondria where the hAIF oxidoreductase activity is carried out. The data obtained with the native mitochondrial variant indicate that the presence of CHCHD4 makes it catalytically more active, what might justify the importance of CHCHD4 in mitochondrial bioenergetics. This is related to the fact that residues 77-101 are critical in the stability of the mitochondrial hAIF (Romero-

Tamayo et al., 2021). In agreement, this region has been identified at the cellular level as key for the interaction with the chaperone (Hangen et al., 2015), interaction that was also shown to be key for the correct assembly and maintenance of the ETC (**Figure 1.15**) (Meyer et al. 2015; Modjtahedi et al., 2015).

### 8.3 hAIF ON THE PROGRAMMED CELL DEATH: MOLECULAR ASPECTS IN THE FORMATION OF THE DEGRADOSOME

This PhD thesis also aimed to *in vitro* characterise the molecular interactions of hAIF with DNA, CypA and H2AX to shed light on the degradosome formation mechanism.

After proteolytic processing and translocation of hAIF to the cytosol, it is proposed that it may bind to Hsp70, restricting its nuclear translocation, or to CypA, which could contribute to its nuclear translocation (Gurbuxani et al. 2003; Lui and Kong 2007; Matsumori et al. 2005; Ravagnan et al. 2001). hAIF lacks nuclease activity (Susin et al. 1999b), so to carry out its proposed role in PCD, it needs to form a DNA degradation complex with nucleases (Artus et al. 2010; Baritaud et al. 2012).

In addition, once in the nucleus hAIF has been shown to form a complex with phosphorylated H2AX, which also lacks DNAase activity. Thus, it is proposed that the hAIF/H2AX interaction promotes PCD by generating an active DNA degradation complex involving the nuclease CypA (Artus et al. 2010; Cande et al. 2004). Nonetheless, there is some controversy about the order of interaction of these proteins, as some studies suggest that the hAIF/CypA complex forms in the cytosol, before entering the nucleus (Cande et al. 2004).

In this work, as described in chapter 7, we have contributed to the description of the degradosome formation. Using 2D electrophoresis, size exclusion chromatography, AFM and ITC, we have thermodynamically described the interaction between all these biomolecules and established a possible sequence for the molecular events required for degradosome assembly during caspase-independent programmed necrosis (**Figure 8.1**).

To propose the mechanism, we first studied binary interactions including apoptotic hAIF, CypA, H2AX and dsDNA. Once thermodynamics of these interactions were known, they provided us with relevant information about the binary interaction mechanisms. Subsequently, we studied the interactions within tertiary complexes.

We probed that hAIF can interact with all its partners separately and that these complexes can interact with DNA. This finding contradicts previous results, which stated that there

was no interaction between hAIF and CypA in the absence of histone H2AX (Baritaud et al., 2010). Moreover, this allowed us to verify cooperativity in the binding of some of the components of the degradosome to hAIF $_{\Delta 1-101}$ .

Our AFM data also show that hAIF $_{\Delta 1-101}$  can induce dsDNA stretching by itself, and that this might favour its association with CypA and H2AX to form the degradosome. The degradosome might bind to the dsDNA in a closed conformation, and in the presence of a threshold concentration of  $\text{Ca}^{2+}$  and  $\text{Mg}^{2+}$  ions it would execute dsDNA degradation. The complex would then open, freeing itself from the strands.

Although further studies are necessary, the data presented here may lead to hypothesise a possible mechanism of the degradosome formation and of its binding to dsDNA (**Figure 8.1**). In this sequential mechanism, hAIF (yellow) binds to CypA (orange) in the cytosol, promoting its nuclear translocation. Once in the nucleus, the hAIF $_{\Delta 1-101}$ :CypA complex recruits H2AX and forms the degradosome. This is consistent with what is theorised in the literature. As hAIF moves from the mitochondria to the cytoplasm in its apoptotic form it interacts with CypA, which could facilitate its transport to the nucleus (Farina et al., 2017, Zhu et al., 2007, Cande et al., 2004, Doti 2014). There, this complex interacts with H2AX to promote chromatolysis. Once the three proteins hAIF, H2AX and CypA bind, DNA degradation proceeds through the degradosome structure and the nuclease activity of CypA.

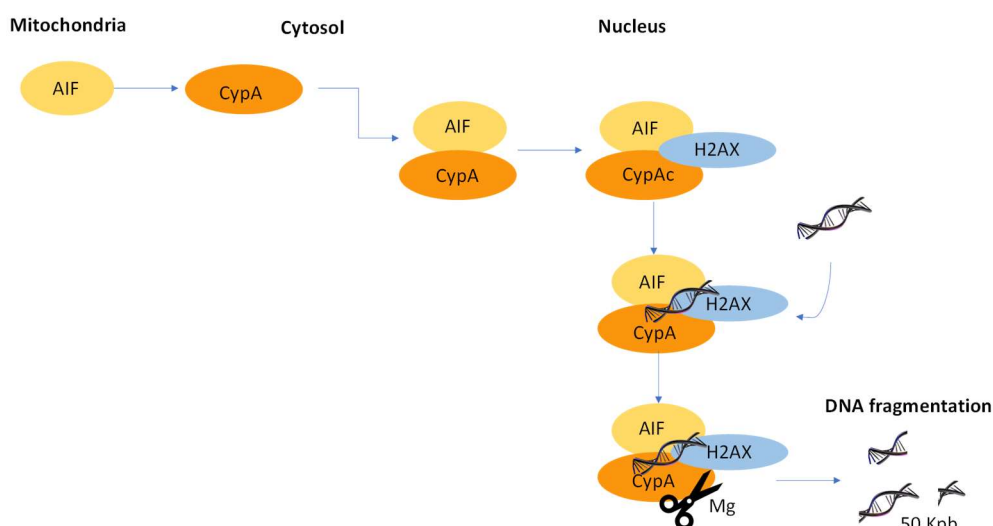


**Figure 8.1:** Proposed Model for the degradosome formation. and DNA fragmentation in PCD. hAIF $_{\Delta 1-101}$  (yellow) would bind to CypA (orange) in the cytosol, promoting its nuclear translocation. Once in the nucleus, the hAIF $_{\Delta 1-101}$ :CypA complex recruits H2AX and forms the degradosome that binds to the dsDNA and causes its fragmentation.



## ***9-CONCLUSIONS***



## 9.1- MULTIPLE FACTORS DETERMINE CONFORMATION AND STABILITY OF hAIF

9.1.1 NADH–redox-linked conformation changes in hAIF course with strong NAD<sup>+</sup> binding and protein dimerization, but they produce a negative impact in overall hAIF stability.

9.1.2 Residues 77-101 of hAIF stabilise its mitochondrial isoform at the IMS pH, confirming that proteolytic processing of hAIF contributes to its conformational adaptation to specific subcellular pH environments.

9.1.3 Mutations at W196 decrease the compactness and stability of hAIF, indicating that the  $\beta$ -hairpin and C-loop coupling contribute to protein stability.

9.1.4 W196 is key to maintaining the proper position of the  $\beta$ -hairpin that stabilises and retains the C-loop in hAIF, promoting protein compactness and stability.

9.1.5 W196 and the conformation of the  $\beta$ -hairpin motif strongly modulate the redox-linked monomer-dimer structural transition in hAIF.

9.1.6 Loss of functionality in the pathogenic R201 deletion mutant of hAIF is due to distortion of its active site architecture.

9.1.7 The pathogenic G308E and E493V hAIF variants have little effect on the thermal stability of hAIF <sub>$\Delta$ 1-101</sub>.

9.1.8 The loss of functionality in G308E hAIF appears related to the lower accumulation of its CTCs, rather than to an overall conformational stability lost.

9.1.9 The E493V substitution makes its CTC dimer less structured than the WT CTC, this fact can affect the E493V variant interplay with partners.

9.1.10 Some molecules that may serve as leads in the development of hAIF bioactive compounds have been identified.

9.1.11 ATA, C2 and C11 have a de-stabilising effect on hAIF thermal conformation. Their binding may induce C-loop release, as occurs upon NADH binding and flavin reduction.

## 9.2- THE REDOX MITOCHONDRIAL ROLE OF hAIF

9.2.1 W196 and the  $\beta$ -hairpin conformation contribute to configure the NADH active site, making hAIF inefficient for NADH oxidation as well as to trigger the release of the C-loop in the reduced state.

9.2.2 W196 and the  $\beta$ -hairpin contribute to stabilise the hAIF CTC state by enhancing the affinity for NAD<sup>+</sup>. W196 is therefore critical for CTC stability and mitochondrial homeostasis.

9.2.3 W196 and the  $\beta$ -hairpin motif contribute to define the interaction surfaces of hAIF with its physiological partners CHCHD4, CypA and DNA by modulating the enthalpic and entropic contributions to their binding.

9.2.4 hAIFmt <sub>$\Delta$ 1-77</sub> is able to dimerise upon reduction by NADH, forming a stable dimer.

9.2.5 hAIFmt <sub>$\Delta$ 1-77</sub> favours CTC formation over hAIF <sub>$\Delta$ 1-101</sub> by increasing the enzyme affinity for NADH.

9.2.6 Mitochondrial isoform and its triple mutant are more efficient oxidising NADH than the corresponding apoptotic ones.

9.2.7 Binding of CHCHD4 to hAIFmt <sub>$\Delta$ 1-77</sub> promotes its efficiency as NADH oxidase by increasing the affinity for the NADH substrate.

9.2.8 The NADH dependent reduction of hAIF increases its affinity for CHCHD4, indicating that NADH dependent structural changes in hAIF modulate CHCHD4 binding.

### **9.3- hAIF ON THE PROGRAMMED CELL DEATH: MOLECULAR ASPECTS IN THE ASSEMBLY OF THE DEGRADOSOME**

9.3.1 hAIF <sub>$\Delta$ 1-101</sub> can interact with all components of the DNA-degradosome complex separately, and all protein-hAIF <sub>$\Delta$ 1-101</sub> binary complexes are able to interact with dsDNA.

9.3.2 hAIF <sub>$\Delta$ 1-101</sub> is able to simultaneously interact with CypA, H2AX and dsDNA. Therefore, it has been proven the *in vitro* formation of the hAIF <sub>$\Delta$ 1-101</sub> based degradosome and its interaction with dsDNA.

9.3.3 H2AX and dsDNA show positive cooperativity for binding to hAIF <sub>$\Delta$ 1-101</sub>, while CypA and dsDNA show negative cooperativity for binding to hAIF <sub>$\Delta$ 1-101</sub>.

9.3.4 A hypothesis for the possible sequence of molecular events in the degradosome formation is presented. hAIF first can interact with CypA, which might facilitate its transport to the nucleus. There, this complex recruits H2AX. Once the degradosome is formed, it binds DNA and its degradation proceeds due to the nuclease activity of CypA within the DNA-degradosome complex.



## CONCLUSIONS

Altogether, the findings here reported improve our understanding on the molecular basis of hAIF's cellular activities, a crucial aspect for clarifying its associated pathological mechanisms and developing new molecular therapies.





## *10-BIBLIOGRAPHY*



- Abeliovich, H. 2005. An empirical extremum principle for the hill coefficient in ligand-protein interactions showing negative cooperativity. *Biophys J*, 89, 76-9.
- Alano, C. C., Garnier, P., Ying, W., Higashi, Y., Kauppinen, T. M. & Swanson, R. A. 2010. NAD<sup>+</sup> depletion is necessary and sufficient for poly(ADP-ribose) polymerase-1-mediated neuronal death. *J Neurosci*, 30, 2967-78.
- Aramaki, H., Kabata, H., Takeda, S., Itou, H., Nakayama, H. & Shimamoto, N. 2011. Formation of repressor-inducer-operator ternary complex: negative cooperativity of d-camphor binding to CamR. *Genes Cells*, 16, 1200-7.
- Ardissone, A., Piscosquito, G., Legati, A., Langella, T., Lamantea, E., Garavaglia, B., Salsano, E., Farina, L., Moroni, I., Pareyson, D. & Ghezzi, D. 2015. A slowly progressive mitochondrial encephalomyopathy widens the spectrum of AIFM1 disorders. *Neurology*, 84, 2193-5.
- Artus, C., Boujrad, H., Bouharrou, A., Brunelle, M. N., Hoos, S., Yuste, V. J., Lenormand, P., Rousselle, J. C., Namane, A., England, P., Lorenzo, H. K. & Susin, S. A. 2010. AIF promotes chromatinolysis and caspase-independent programmed necrosis by interacting with histone H2AX. *EMBO J*, 29, 1585-99.
- Avron, M. & Jagendorf, A. T. 1956. A TPNH diaphorase from chloroplasts. *Arch Biochem Biophys*, 65, 475-90.
- Banci, L., Bertini, I., Cefaro, C., Ciofi-Baffoni, S., Gallo, A., Martinelli, M., Sideris, D. P., Katrakili, N. & Tokatlidis, K. 2009. MIA40 is an oxidoreductase that catalyzes oxidative protein folding in mitochondria. *Nat Struct Mol Biol*, 16, 198-206.
- Bano, D., Dinsdale, D., Cabrera-Socorro, A., Maida, S., Lambacher, N., McColl, B., Ferrando-May, E., Hengartner, M. O. & Nicotera, P. 2010. Alteration of the nuclear pore complex in Ca(2+)-mediated cell death. *Cell Death Differ*, 17, 119-33.
- Bano, D. & Prehn, J. H. M. 2018. Apoptosis-Inducing Factor (AIF) in Physiology and Disease: The Tale of a Repented Natural Born Killer. *EBioMedicine*, 30, 29-37.
- Barile, M., Giancaspero, T. A., Brizio, C., Panebianco, C., Indiveri, C., Galluccio, M., Vergani, L., Eberini, I. & Gianazza, E. 2013. Biosynthesis of flavin cofactors in man: implications in health and disease. *Curr Pharm Des*, 19, 2649-75.
- Baritaud, M., Boujrad, H., Lorenzo, H. K., Krantic, S. & Susin, S. A. 2010. Histone H2AX: The missing link in AIF-mediated caspase-independent programmed necrosis. *Cell Cycle*, 9, 3166-73.
- Bénit, P., Goncalves, S., Dassa, E. P., Brière, J. J. & Rustin, P. 2008. The variability of the harlequin mouse phenotype resembles that of human mitochondrial-complex I-deficiency syndromes. *PLoS One*, 3, e3208.
- Berger, I., Ben-Neriah, Z., Dor-Wolman, T., Shaag, A., Saada, A., Zenvirt, S., Raas-Rothschild, A., Nadjari, M., Kaestner, K. H. & Elpeleg, O. 2011. Early prenatal ventriculomegaly due to an AIFM1 mutation identified by linkage analysis and whole exome sequencing. *Mol Genet Metab*, 104, 517-20.
- Berger, J. R. 2011. Infectious myelopathies. *Continuum (Minneapolis)*, 17, 761-75.
- Biasini, M., Bienert, S., Waterhouse, A., Arnold, K., Studer, G., Schmidt, T., Kiefer, F., Gallo Cassarino, T., Bertoni, M., Bordoli, L. & Schwede, T. 2014. SWISS-MODEL: modelling protein tertiary and quaternary structure using evolutionary information. *Nucleic Acids Res*, 42, W252-8.
- Bich, L., Pradeu, T. & Moreau, J. F. 2019. Understanding Multicellularity: The Functional Organization of the Intercellular Space. *Front Physiol*, 10, 1170.
- Bradshaw, J. M. & Waksman, G. 1998. Calorimetric investigation of proton linkage by monitoring both the enthalpy and association constant of binding: application to the interaction of the Src SH2 domain with a high-affinity tyrosyl phosphopeptide. *Biochemistry*, 37, 15400-7.

- Brandts, J. F. & Lin, L. N. 1990. Study of strong to ultratight protein interactions using differential scanning calorimetry. *Biochemistry*, 29, 6927-40.
- Breuer, M. E., Koopman, W. J., Koene, S., Nooteboom, M., Rodenburg, R. J., Willems, P. H. & Smeitink, J. A. 2013. The role of mitochondrial OXPHOS dysfunction in the development of neurologic diseases. *Neurobiol Dis*, 51, 27-34.
- Brooks, B. R., Brooks, C. L., Mackerell, A. D., Nilsson, L., Petrella, R. J., Roux, B., Won, Y., Archontis, G., Bartels, C., Boresch, S., Caflisch, A., Caves, L., Cui, Q., Dinner, A. R., Feig, M., Fischer, S., Gao, J., Hodoscek, M., Im, W., Kuczera, K., Lazaridis, T., Ma, J., Ovchinnikov, V., Paci, E., Pastor, R. W., Post, C. B., Pu, J. Z., Schaefer, M., Tidor, B., Venable, R. M., Woodcock, H. L., Wu, X., Yang, W., York, D. M. & Karplus, M. 2009. CHARMM: the biomolecular simulation program. *J Comput Chem*, 30, 1545-614.
- Brose, C. A., Ho, C., Long, W. Z., Singh, S., Burnett, K., Hura, G. L., Nix, J. C., Bowman, G. R., Ellenberger, T. & Tainer, J. A. 2016. Defining NADH-Driven Allostery Regulating Apoptosis-Inducing Factor. *Structure*.
- Brown, D., Yu, B. D., Joza, N., Bénit, P., Meneses, J., Firpo, M., Rustin, P., Penninger, J. M. & Martin, G. R. 2006. Loss of Aif function causes cell death in the mouse embryo, but the temporal progression of patterning is normal. *Proc Natl Acad Sci USA*, 103, 9918-23.
- Cabon, L., Galán-Malo, P., Bouharrou, A., Delavallée, L., Brunelle-Navas, M. N., Lorenzo, H. K., Gross, A. & Susin, S. A. 2012. BID regulates AIF-mediated caspase-independent necroptosis by promoting BAX activation. *Cell Death Differ*, 19, 245-56.
- Cande, C., Vahsen, N., Kouranti, I., Schmitt, E., Daugas, E., Spahr, C., Luban, J., Kroemer, R. T., Giordanetto, F., Garrido, C., Penninger, J. M. & Kroemer, G. 2004. AIF and cyclophilin A cooperate in apoptosis-associated chromatinolysis. *Oncogene*, 23, 1514-21.
- Chan, L. L., Pineda, M., Heeres, J. T., Hergenrother, P. J. & Cunningham, B. T. 2008. A general method for discovering inhibitors of protein-DNA interactions using photonic crystal biosensors. *ACS Chem Biol*, 3, 437-48.
- Chatzi, A., Manganas, P. & Tokatlidis, K. 2016. Oxidative folding in the mitochondrial intermembrane space: A regulated process important for cell physiology and disease. *Biochim Biophys Acta*, 1863, 1298-306.
- Chinta, S. J., Rane, A., Yadava, N., Andersen, J. K., Nicholls, D. G. & Polster, B. M. 2009. Reactive oxygen species regulation by AIF- and complex I-depleted brain mitochondria. *Free Radic Biol Med*, 46, 939-47.
- Churbanova, I. Y. & Sevrioukova, I. F. 2008. Redox-dependent changes in molecular properties of mitochondrial apoptosis-inducing factor. *J Biol Chem*, 283, 5622-31.
- Cooper, A. & McAuley-Hecht, K. E. 1993. Microcalorimetry and the Molecular Recognition of Peptides and Proteins.
- Cortese, J. D., Voglino, A. L. & Hackenbrock, C. R. 1991. Ionic strength of the intermembrane space of intact mitochondria as estimated with fluorescein-BSA delivered by low pH fusion. *J Cell Biol*, 113, 1331-40.
- Cremades, N., Velázquez-Campoy, A., Martínez-Júlvez, M., Neira, J. L., Pérez-Dorado, I., Hermoso, J., Jimenez, P., Lanás, A., Hoffman, P. S. & Sancho, J. 2009. Discovery of specific flavodoxin inhibitors as potential therapeutic agents against *Helicobacter pylori* infection. *ACS Chem Biol*, 4, 928-38.
- Daugas, E., Nochy, D., Ravagnan, L., Loeffler, M., Susin, S. A., Zamzami, N. & Kroemer, G. 2000. Apoptosis-inducing factor (AIF): a ubiquitous mitochondrial oxidoreductase involved in apoptosis. *FEBS Lett*, 476, 118-23.

- Delano, W. L. 2002. The PyMOL molecular graphics system. *DeLano Scientific, San Carlos, CA, USA*, <http://www.pymol.org>.
- Delavallée, L., Mathiah, N., Cabon, L., Mazeraud, A., Brunelle-Navas, M. N., Lerner, L. K., Tannoury, M., Prola, A., Moreno-Loshuertos, R., Baritaud, M., Vela, L., Garbin, K., Garnier, D., Lemaire, C., Langa-Vives, F., Cohen-Salmon, M., Fernández-Silva, P., Chrétien, F., Migeotte, I. & Susin, S. A. 2020. Mitochondrial AIF loss causes metabolic reprogramming, caspase-independent cell death blockade, embryonic lethality, and perinatal hydrocephalus. *Mol Metab*, 101027.
- Delettre, C., Yuste, V. J., Moubarak, R. S., Bras, M., Lesbordes-Brion, J. C., Petres, S., Bellalou, J. & Susin, S. A. 2006a. AIFsh, a novel apoptosis-inducing factor (AIF) pro-apoptotic isoform with potential pathological relevance in human cancer. *J Biol Chem*, 281, 6413-27.
- Delettre, C., Yuste, V. J., Moubarak, R. S., Bras, M., Robert, N. & Susin, S. A. 2006b. Identification and characterization of AIFsh2, a mitochondrial apoptosis-inducing factor (AIF) isoform with NADH oxidase activity. *J Biol Chem*, 281, 18507-18.
- DeSa, R. J. & Gibson, Q. H. 1969. A practical automatic data acquisition system for stopped-flow spectrophotometry. *Comput Biomed Res*, 2, 494-505.
- Diodato, D., Tasca, G., Verrigni, D., D'Amico, A., Rizza, T., Tozzi, G., Martinelli, D., Verardo, M., Invernizzi, F., Nasca, A., Bellacchio, E., Ghezzi, D., Piemonte, F., Dionisi-Vici, C., Carrozzo, R. & Bertini, E. 2016. A novel AIFM1 mutation expands the phenotype to an infantile motor neuron disease. *Eur J Hum Genet*, 24, 463-6.
- Eccleston, J. F., Hutchinson, J. P. & White, H. D. 2001. Stopped-flow techniques. In: HARDING, S. E. & CHOWDHRY, B. Z. (eds.) *Protein-ligand interactions. Structure and Spectroscopy: A Practical Approach*. Oxford/New York: Oxford University Press.
- El Ghouzzi, V., Csaba, Z., Olivier, P., Lelouvier, B., Schwendimann, L., Dournaud, P., Verney, C., Rustin, P. & Gressens, P. 2007. Apoptosis-inducing factor deficiency induces early mitochondrial degeneration in brain followed by progressive multifocal neuropathology. *J Neuropathol Exp Neurol*, 66, 838-47.
- Farina, B., Di Sorbo, G., Chambery, A., Caporale, A., Leoni, G., Russo, R., Mascanzoni, F., Raimondo, D., Fattorusso, R., Ruvo, M. & Doti, N. 2017. Structural and biochemical insights of CypA and AIF interaction. *Sci Rep*, 7, 1138.
- Farina, B., Sturlese, M., Mascanzoni, F., Caporale, A., Monti, A., Di Sorbo, G., Fattorusso, R., Ruvo, M. & Doti, N. 2018. Binding mode of AIF(370-394) peptide to CypA: insights from NMR, label-free and molecular docking studies. *Biochem J*, 475, 2377-2393.
- Ferreira, P., Villanueva, R., Martínez-Júlvez, M., Herguedas, B., Marcuello, C., Fernandez-Silva, P., Cabon, L., Hermoso, J. A., Lostao, A., Susin, S. A. & Medina, M. 2014. Structural insights into the coenzyme mediated monomer-dimer transition of the pro-apoptotic apoptosis inducing factor. *Biochemistry*, 53, 4204-15.
- Ferreira, P., Villanueva, R., Martínez-Julvez, M. & Medina, M. 2018. Apoptosis-Inducing Factor 1, Mitochondrion-associated, 1. In: CHOI, S. (ed.) *Encyclopedia of Signaling Molecules*. 2nd Edition ed.
- Ferreira, P., Medina, M. 2021. Anaerobic Stopped-Flow Spectrophotometry with Photodiode Array Detection in the Presteady State: An Application to Elucidate Oxidoreduction Mechanisms in Flavoproteins. In Barile M. (eds) *Flavins and Flavoproteins. Methods in Molecular Biology*, vol 2280. Springer.

- Forneris, F., Orru, R., Bonivento, D., Chiarelli, L. R. & Mattevi, A. 2009. ThermoFAD, a ThermoFluor-adapted flavin ad hoc detection system for protein folding and ligand binding. *FEBS J*, 276, 2833-40.
- Frisch, M. J., Trucks, G. W., H., Schlegel, B., G. E. Scuseria, M. A. Robb, J. R. Cheeseman, G. Scalmani, V., Barone, G. A. Petersson, H. Nakatsuji, X. Li, M. C., A. Marenich, J., Bloino, B. G. Janesko, R. Gomperts, B. Mennucci, H. P. Hratchian, J. V. Ortiz, A. F. Izmaylov, J. L. Sonnenberg, D. Williams-Young, F. Ding, F. Lipparini, F., Egidi, J. Goings, B. Peng, A. Petrone, T. Henderson, D. Ranasinghe, G., V., Zakrzewski, J. Gao, N. Rega, G. Zheng, W. Liang, M. Hada, M. Ehara, K. Toyota, R. Fukuda, J. Hasegawa, M. Ishida, T. Nakajima, Y. Honda, O. Kitao, H. Nakai, T. Vreven, K. Throssell, J. A. Montgomery, J., J. E. Peralta, F. Ogliaro, M., Bearpark, J. J. Heyd, E. Brothers, Kudin, K. N., V. N. Staroverov, T. Keith, R., Kobayashi, J. Normand, K. Raghavachari, A. Rendell, J. C. Burant, S., S., Iyengar, J. Tomasi, M. Cossi, J. M. Millam, M. Klene, C. Adamo, R. Cammi, W., J., Ochterski, Martin, R. L., Morokuma, K., Farkas, O., Foresman, J. B. & Fox, D. J. 2016. Gaussian 09, Revision D.01. Wallingford CT: Gaussian, Inc.
- Galluzzi, L., Vitale, I., Aaronson, S. A., Abrams, J. M., Adam, D., Agostinis, P., Alnemri, E. S., Altucci, L., Amelio, I., Andrews, D. W., Annicchiarico-Petruzzelli, M., Antonov, A. V., Arama, E., Baehrecke, E. H., Barlev, N. A., Bazan, N. G., Bernassola, F., Bertrand, M. J. M., Bianchi, K., Blagosklonny, M. V., Blomgren, K., Borner, C., Boya, P., Brenner, C., Campanella, M., Candi, E., Carmona-Gutierrez, D., Cecconi, F., Chan, F. K., Chandel, N. S., Cheng, E. H., Chipuk, J. E., Cidlowski, J. A., Ciechanover, A., Cohen, G. M., Conrad, M., Cubillos-Ruiz, J. R., Czabotar, P. E., D'Angiolella, V., Dawson, T. M., Dawson, V. L., De Laurenzi, V., De Maria, R., Debatin, K. M., DeBerardinis, R. J., Deshmukh, M., Di Daniele, N., Di Virgilio, F., Dixit, V. M., Dixon, S. J., Duckett, C. S., Dynlacht, B. D., El-Deiry, W. S., Elrod, J. W., Fimia, G. M., Fulda, S., García-Sáez, A. J., Garg, A. D., Garrido, C., Gavathiotis, E., Golstein, P., Gottlieb, E., Green, D. R., Greene, L. A., Gronemeyer, H., Gross, A., Hajnoczky, G., Hardwick, J. M., Harris, I. S., Hengartner, M. O., Hetz, C., Ichijo, H., Jäättelä, M., Joseph, B., Jost, P. J., Juin, P. P., Kaiser, W. J., Karin, M., Kaufmann, T., Kepp, O., Kimchi, A., Kitsis, R. N., Klionsky, D. J., Knight, R. A., Kumar, S., Lee, S. W., Lemasters, J. J., Levine, B., Linkermann, A., Lipton, S. A., Lockshin, R. A., López-Otín, C., Lowe, S. W., Luedde, T., Lugli, E., MacFarlane, M., Madeo, F., Malewicz, M., Malorni, W., Manic, G., et al. 2018. Molecular mechanisms of cell death: recommendations of the Nomenclature Committee on Cell Death 2018. *Cell Death Differ*, 25, 486-541.
- Galluzzi, L., Vitale, I., Abrams, J. M., Alnemri, E. S., Baehrecke, E. H., Blagosklonny, M. V., Dawson, T. M., Dawson, V. L., El-Deiry, W. S., Fulda, S., Gottlieb, E., Green, D. R., Hengartner, M. O., Kepp, O., Knight, R. A., Kumar, S., Lipton, S. A., Lu, X., Madeo, F., Malorni, W., Mehlen, P., Nuñez, G., Peter, M. E., Piacentini, M., Rubinsztein, D. C., Shi, Y., Simon, H. U., Vandenabeele, P., White, E., Yuan, J., Zhivotovsky, B., Melino, G. & Kroemer, G. 2012. Molecular definitions of cell death subroutines: recommendations of the Nomenclature Committee on Cell Death 2012. *Cell Death Differ*, 19, 107-20.
- Gersting, S. W., Kemter, K. F., Staudigl, M., Messing, D. D., Danecka, M. K., Lagler, F. B., Sommerhoff, C. P., Roscher, A. A. & Muntau, A. C. 2008. Loss of function in phenylketonuria is caused by impaired molecular motions and conformational instability. *Am J Hum Genet*, 83, 5-17.
- Ghezzi, A. 2010. Therapeutic strategies in childhood multiple sclerosis. *Ther Adv Neurol Disord*, 3, 217-28.



- Ghezzi, D., Sevrioukova, I., Invernizzi, F., Lamperti, C., Mora, M., D'Adamo, P., Novara, F., Zuffardi, O., Uziel, G. & Zeviani, M. 2010. Severe X-linked mitochondrial encephalomyopathy associated with a mutation in apoptosis-inducing factor. *Am J Hum Genet*, 86, 639-49.
- Gibson, Q. H. & Milnes, L. 1964. Apparatus for rapid and sensitive spectrophotometry. *Biochem J*, 91, 161-71.
- Goldberg, R. N., Kishore, N. & Lennen, R. M. 2002. Thermodynamic quantities for the ionization reactions of buffers. *J. Phys. Chem. Ref. Data*, 31, 231-370.
- Gorman, C. M., Ray, N. J. & Burke, F. M. 2016. The effect of endodontic access on all-ceramic crowns: A systematic review of in vitro studies. *J Dent*, 53, 22-9.
- Grimme, S., Ehrlich, S. & Goerigk, L. 2011. Effect of the damping function in dispersion corrected density functional theory. *J Comput Chem*, 32, 1456-65.
- Gurbuxani, S., Schmitt, E., Cande, C., Parcellier, A., Hammann, A., Daugas, E., Kouranti, I., Spahr, C., Pance, A., Kroemer, G. & Garrido, C. 2003. Heat shock protein 70 binding inhibits the nuclear import of apoptosis-inducing factor. *Oncogene*, 22, 6669-78.
- Hangen, E., Blomgren, K., Bénit, P., Kroemer, G. & Modjtahedi, N. 2010. Life with or without AIF. *Trends Biochem Sci*, 35, 278-87.
- Hangen, E., Féraud, O., Lachkar, S., Mou, H., Doti, N., Fimia, G. M., Lam, N. V., Zhu, C., Godin, I., Muller, K., Chatzi, A., Nuebel, E., Ciccocanti, F., Flamant, S., Bénit, P., Perfettini, J. L., Sauvat, A., Bennaceur-Griscelli, A., Ser-Le Roux, K., Gonin, P., Tokatlidis, K., Rustin, P., Piacentini, M., Ruvo, M., Blomgren, K., Kroemer, G. & Modjtahedi, N. 2015. Interaction between AIF and CHCHD4 Regulates Respiratory Chain Biogenesis. *Mol Cell*, 58, 1001-14.
- Heimer, G., Eyal, E., Zhu, X., Ruzzo, E. K., Marek-Yagel, D., Sagiv, D., Anikster, Y., Reznik-Wolf, H., Pras, E., Oz Levi, D., Lancet, D., Ben-Zeev, B. & Nissenkorn, A. 2018. Mutations in AIFM1 cause an X-linked childhood cerebellar ataxia partially responsive to riboflavin. *Eur J Paediatr Neurol*, 22, 93-101.
- Hengen, P. 1995. Purification of His-Tag fusion proteins from Escherichia coli. *Trends Biochem Sci*, 20, 285-6.
- Hu, B., Wang, M., Castoro, R., Simmons, M., Dortch, R., Yawn, R. & Li, J. 2017. A novel missense mutation in AIFM1 results in axonal polyneuropathy and misassembly of OXPHOS complexes. *Eur J Neurol*, 24, 1499-1506.
- Humphrey, W., Dalke, A. & Schulten, K. 1996. VMD: visual molecular dynamics. *J Mol Graph*, 14, 33-8, 27-8.
- Hurst, S., Hoek, J. & Sheu, S. S. 2017. Mitochondrial Ca. *J Bioenerg Biomembr*, 49, 27-47.
- Ignéy, F. H. & Krammer, P. H. 2002. Death and anti-death: tumour resistance to apoptosis. *Nat Rev Cancer*, 2, 277-88.
- Jacobson, M. D. 1997. Programmed cell death: a missing link is found. *Trends Cell Biol*, 7, 467-9.
- Jeffery, C. J. 2014. An introduction to protein moonlighting. *Biochem Soc Trans*, 42, 1679-83.
- Jonckheere, A. I., Smeitink, J. A. & Rodenburg, R. J. 2012. Mitochondrial ATP synthase: architecture, function and pathology. *J Inherit Metab Dis*, 35, 211-25.
- Jones, G., Willett, P., Glen, R. C., Leach, A. R. & Taylor, R. 1997. Development and validation of a genetic algorithm for flexible docking. *J Mol Biol*, 267, 727-48.
- Jorns, M. S., Baldwin, E. T., Sancar, G. B. & Sancar, A. 1987. Action mechanism of Escherichia coli DNA photolyase. II. Role of the chromophores in catalysis. *J Biol Chem*, 262, 486-91.

- Joza, N., Pospisilik, J. A., Hangen, E., Hanada, T., Modjtahedi, N., Penninger, J. M. & Kroemer, G. 2009. AIF: not just an apoptosis-inducing factor. *Ann N Y Acad Sci*, 1171, 2-11.
- Kadam, A. A., Jubin, T., Mir, H. A. & Begum, R. 2016. Potential role of Apoptosis Inducing Factor in evolutionarily significant eukaryote, *Dictyostelium discoideum* survival. *Biochim Biophys Acta*, 1861, 2942-2955.
- Kettwig, M., Schubach, M., Zimmermann, F. A., Klinge, L., Mayr, J. A., Biskup, S., Sperl, W., Gärtner, J. & Huppke, P. 2015. From ventriculomegaly to severe muscular atrophy: Expansion of the clinical spectrum related to mutations in AIFM1. *Mitochondrion*, 21C, 12-18.
- Klein, J. A., Longo-Guess, C. M., Rossmann, M. P., Seburn, K. L., Hurd, R. E., Frankel, W. N., Bronson, R. T. & Ackerman, S. L. 2002. The harlequin mouse mutation downregulates apoptosis-inducing factor. *Nature*, 419, 367-74.
- Koopman, W. J., Beyrath, J., Fung, C. W., Koene, S., Rodenburg, R. J., Willems, P. H. & Smeitink, J. A. 2016. Mitochondrial disorders in children: toward development of small-molecule treatment strategies. *EMBO Mol Med*, 8, 311-27.
- Kroemer, G. & Reed, J. C. 2000. Mitochondrial control of cell death. *Nat Med*, 6, 513-9.
- Kuban-Jankowska, A., Sahu, K. K., Niedzialkowski, P., Gorska, M., Tuszyński, J. A., Ossowski, T. & Wozniak, M. 2015. Redox process is crucial for inhibitory properties of aurintricarboxylic acid against activity of YopH: virulence factor of *Yersinia pestis*. *Oncotarget*, 6, 18364-73.
- Kütt, A., Leito, I., Kaljurand, I., Sooväli, L., Vlasov, V. M., Yagupolskii, L. M. & Koppel, I. A. 2006. A comprehensive self-consistent spectrophotometric acidity scale of neutral Brønsted acids in acetonitrile. *J Org Chem*, 71, 2829-38.
- Ladbury, J. E. & Chowdhry, B. Z. 1996. Sensing the heat: the application of isothermal titration calorimetry to thermodynamic studies of biomolecular interactions. *Chem Biol*, 3, 791-801.
- Laemmli, U. K. 1970. Cleavage of structural proteins during the assembly of the head of bacteriophage T4. *Nature*, 227, 680-5.
- Lagorce, D., Sperandio, O., Baell, J. B., Miteva, M. A. & Villoutreix, B. O. 2015. FAF-Drugs3: a web server for compound property calculation and chemical library design. *Nucleic Acids Res*, 43, W200-7.
- Lans, I., Medina, M., Rosta, E., Hummer, G., Garcia-Viloca, M., Lluch, J. M. & González-Lafont, A. 2012. Theoretical study of the mechanism of the hydride transfer between ferredoxin-NADP<sup>+</sup> reductase and NADP<sup>+</sup>: the role of Tyr303. *J Am Chem Soc*, 134, 20544-53.
- Lans, I., Peregrina, J. R., Medina, M., Garcia-Viloca, M., González-Lafont, A. & Lluch, J. M. 2010. Mechanism of the hydride transfer between Anabaena Tyr303Ser FNR(rd)/FNR(ox) and NADP<sup>+</sup>/H. A combined pre-steady-state kinetic/ensemble-averaged transition-state theory with multidimensional tunneling study. *J Phys Chem B*, 114, 3368-79.
- Lautrup, S., Sinclair, D. A., Mattson, M. P. & Fang, E. F. 2019. NAD<sup>+</sup> in Brain Aging and Neurodegenerative Disorders. *Cell Metabolism*, 30, 630-655.
- Le Guilloux, V., Schmidtke, P. & Tuffery, P. 2009. Fpocket: an open source platform for ligand pocket detection. *BMC Bioinformatics*, 10, 168.
- Lee, M., R. Salsbury, F. & Brooks, C. 2002. *Novel generalized Born Methods*.
- Lipinski, C. A., Lombardo, F., Dominy, B. W. & Feeney, P. J. 2001. Experimental and computational approaches to estimate solubility and permeability in drug discovery and development settings. *Adv Drug Deliv Rev*, 46, 3-26.

- Lipton, S. A. & Bossy-Wetzel, E. 2002. Dueling activities of AIF in cell death versus survival: DNA binding and redox activity. *Cell*, 111, 147-50.
- Llopis, J., McCaffery, J. M., Miyawaki, A., Farquhar, M. G. & Tsien, R. Y. 1998. Measurement of cytosolic, mitochondrial, and Golgi pH in single living cells with green fluorescent proteins. *Proc Natl Acad Sci U S A*, 95, 6803-8.
- Loeffler, M., Daugas, E., Susin, S. A., Zamzami, N., Metivier, D., Nieminen, A. L., Brothers, G., Penninger, J. M. & Kroemer, G. 2001. Dominant cell death induction by extramitochondrially targeted apoptosis-inducing factor. *Faseb J*, 15, 758-67.
- Łopatniuk, P. & Witkowski, J. M. 2011. Conventional calpains and programmed cell death. *Acta Biochim Pol*, 58, 287-96.
- López, L. C., Dos-Reis, S., Espargaró, A., Carrodegua, J. A., Maddelein, M. L., Ventura, S. & Sancho, J. 2012. Discovery of novel inhibitors of amyloid  $\beta$ -peptide 1-42 aggregation. *J Med Chem*, 55, 9521-30.
- Lorenzo, H. K. & Susin, S. A. 2007. Therapeutic potential of AIF-mediated caspase-independent programmed cell death. *Drug Resist Updat*, 10, 235-55.
- Lorenzo, H. K., Susin, S. A., Penninger, J. & Kroemer, G. 1999. Apoptosis inducing factor (AIF): a phylogenetically old, caspase-independent effector of cell death. *Cell Death Differ*, 6, 516-24.
- Lui, J. C. & Kong, S. K. 2007. Heat shock protein 70 inhibits the nuclear import of apoptosis-inducing factor to avoid DNA fragmentation in TF-1 cells during erythropoiesis. *FEBS Lett*, 581, 109-17.
- Macheroux, P. 1999. UV-visible spectroscopy as a tool to study flavoproteins. *Methods Mol Biol*, 131, 1-7.
- Mahmood, T. & Yang, P. C. 2012. Western blot: technique, theory, and trouble shooting. *N Am J Med Sci*, 4, 429-34.
- Martínez-Júlvez, M., Medina, M. & Velázquez-Campoy, A. 2009. Binding thermodynamics of ferredoxin:NADP<sup>+</sup> reductase: two different protein substrates and one energetics. *Biophys J*, 96, 4966-75.
- Massey, V., Stankovich, M. & Hemmerich, P. 1978. Light-mediated reduction of flavoproteins with flavins as catalysts. *Biochemistry*, 17, 1-8.
- Maté, M. J., Ortiz-Lombardía, M., Boitel, B., Haouz, A., Tello, D., Susin, S. A., Penninger, J., Kroemer, G. & Alzari, P. M. 2002. The crystal structure of the mouse apoptosis-inducing factor AIF. *Nat Struct Biol*, 9, 442-6.
- Matsuyama, S., Llopis, J., Deveraux, Q. L., Tsien, R. Y. & Reed, J. C. 2000. Changes in intramitochondrial and cytosolic pH: early events that modulate caspase activation during apoptosis. *Nat Cell Biol*, 2, 318-25.
- Medina-Carmona, E., Neira, J. L., Salido, E., Fuchs, J. E., Palomino-Morales, R., Timson, D. J. & Pey, A. L. 2017. Site-to-site interdomain communication may mediate different loss-of-function mechanisms in a cancer-associated NQO1 polymorphism. *Sci Rep*, 7, 44532.
- Metha, D., Gulati, A., Basappa, N. & Raju, O. S. 2012. Esthetic rehabilitation of severely decayed primary incisors using glass fiber reinforced composite: a case report. *J Dent Child (Chic)*, 79, 22-5.
- Meyer, K., Buettner, S., Ghezzi, D., Zeviani, M., Bano, D. & Nicotera, P. 2015. Loss of apoptosis-inducing factor critically affects MIA40 function. *Cell Death Dis*, 6, e1814.
- Michaelis, L. & Menten, M. 1913. Die Kinetik der Intertinwirkung. *Biochem Z*, 49, 333-369.
- Mierzevska, H., Rydzanicz, M., Biegański, T., Kosinska, J., Mierzevska-Schmidt, M., Ługowska, A., Pollak, A., Stawiński, P., Walczak, A., Kędra, A., Obersztyn, E.,

- Szczepanik, E. & Płoski, R. 2017. Spondyloepimetaphyseal dysplasia with neurodegeneration associated with AIFM1 mutation - a novel phenotype of the mitochondrial disease. *Clin Genet*, 91, 30-37.
- Miramar, M. D. 2008. *Caracterización redox de Apoptosis Inducing Factor y estudio de los mecanismos moleculares implicados en su transferencia electrónica*. PhD, University of Zaragoza.
- Miramar, M. D., Costantini, P., Ravagnan, L., Saraiva, L. M., Haouzi, D., Brothers, G., Penninger, J. M., Peleato, M. L., Kroemer, G. & Susin, S. A. 2001. NADH oxidase activity of mitochondrial apoptosis-inducing factor. *J Biol Chem*, 276, 16391-8.
- Modjtahedi, N., Giordanetto, F., Madeo, F. & Kroemer, G. 2006. Apoptosis-inducing factor: vital and lethal. *Trends Cell Biol*, 16, 264-72.
- Modjtahedi, N., Hangen, E., Gonin, P. & Kroemer, G. 2015. Metabolic epistasis among apoptosis-inducing factor and the mitochondrial import factor CHCHD4. *Cell Cycle*, 14, 2743-7.
- Modjtahedi, N., Tokatlidis, K., Dessen, P. & Kroemer, G. 2016. Mitochondrial Proteins Containing Coiled-Coil-Helix-Coiled-Coil-Helix (CHCH) Domains in Health and Disease. *Trends Biochem Sci*, 41, 245-260.
- Monti, A., Sturlese, M., Caporale, A., Roger, J. A., Mascanzoni, F., Ruvo, M. & Doti, N. 2020. Design, synthesis, structural analysis and biochemical studies of stapled AIF(370-394) analogues as ligand of CypA. *Biochim Biophys Acta Gen Subj*, 1864, 129717.
- Morton, S. U., Prabhu, S. P., Lidov, H. G., Shi, J., Anselm, I., Brownstein, C. A., Bainbridge, M. N., Beggs, A. H., Vargas, S. O. & Agrawal, P. B. 2017a. AIFM1 mutation presenting with fatal encephalomyopathy and mitochondrial disease in an infant. *Cold Spring Harb Mol Case Stud*, 3, a001560.
- Morton, S. U., Prabhu, S. P., Lidov, H. G. W., Shi, J., Anselm, I., Brownstein, C. A., Bainbridge, M. N., Beggs, A. H., Vargas, S. O. & Agrawal, P. B. 2017b. mutation presenting with fatal encephalomyopathy and mitochondrial disease in an infant. *Cold Spring Harb Mol Case Stud*, 3, a001560.
- Natarajan, S. K. & Becker, D. F. 2012. Role of apoptosis-inducing factor, proline dehydrogenase, and NADPH oxidase in apoptosis and oxidative stress. *Cell Health Cytoskeleton*, 2012, 11-27.
- Norberg, E., Orrenius, S. & Zhivotovsky, B. 2010. Mitochondrial regulation of cell death: processing of apoptosis-inducing factor (AIF). *Biochem Biophys Res Commun*, 396, 95-100.
- Olsson, M. H. M., Søndergaard, C. R., Rostkowski, M. & Jensen, J. H. 2011. PROPKA3: Consistent Treatment of Internal and Surface Residues in Empirical pKa Predictions. *Journal of Chemical Theory and Computation*, 7, 525-537.
- Orij, R., Postmus, J., Ter Beek, A., Brul, S. & Smits, G. J. 2009. In vivo measurement of cytosolic and mitochondrial pH using a pH-sensitive GFP derivative in *Saccharomyces cerevisiae* reveals a relation between intracellular pH and growth. *Microbiology*, 155, 268-78.
- Otera, H., Ohsakaya, S., Nagaura, Z., Ishihara, N. & Mihara, K. 2005. Export of mitochondrial AIF in response to proapoptotic stimuli depends on processing at the intermembrane space. *EMBO J*, 24, 1375-86.
- Polster, B. M., Basañez, G., Etxebarria, A., Hardwick, J. M. & Nicholls, D. G. 2005. Calpain I induces cleavage and release of apoptosis-inducing factor from isolated mitochondria. *J Biol Chem*, 280, 6447-54.

- Porcelli, A. M., Ghelli, A., Zanna, C., Pinton, P., Rizzuto, R. & Rugolo, M. 2005. pH difference across the outer mitochondrial membrane measured with a green fluorescent protein mutant. *Biochem Biophys Res Commun*, 326, 799-804.
- Pospisilik, J. A., Knauf, C., Joza, N., Benit, P., Orthofer, M., Cani, P. D., Ebersberger, I., Nakashima, T., Sarao, R., Neely, G., Esterbauer, H., Kozlov, A., Kahn, C. R., Kroemer, G., Rustin, P., Burcelin, R. & Penninger, J. M. 2007. Targeted deletion of AIF decreases mitochondrial oxidative phosphorylation and protects from obesity and diabetes. *Cell*, 131, 476-91.
- Ravagnan, L., Gurbuxani, S., Susin, S. A., Maise, C., Daugas, E., Zamzami, N., Mak, T., Jäättelä, M., Penninger, J. M., Garrido, C. & Kroemer, G. 2001. Heat-shock protein 70 antagonizes apoptosis-inducing factor. *Nat Cell Biol*, 3, 839-43.
- Rinaldi, C., Grunseich, C., Sevrioukova, I. F., Schindler, A., Horkayne-Szakaly, I., Lamperti, C., Landourey, G., Kennerson, M. L., Burnett, B. G., Bonnemant, C., Biesecker, L. G., Ghezzi, D., Zeviani, M. & Fischbeck, K. H. 2012. Cowchock syndrome is associated with a mutation in apoptosis-inducing factor. *Am J Hum Genet*, 91, 1095-102.
- Robinson, K. M. & Lemire, B. D. 1996. A requirement for matrix processing peptidase but not for mitochondrial chaperonin in the covalent attachment of FAD to the yeast succinate dehydrogenase flavoprotein. *J Biol Chem*, 271, 4061-7.
- Romero-Tamayo S., Laplaza R, Velazquez-Campoy A., Villanueva R., Medina M & Ferreira P. 2021. W196 and the  $\beta$ -Hairpin Motif Modulate the Redox Switch of Conformation and the Biomolecular Interaction Network of the Apoptosis-Inducing Factor. *Oxid Med Cell Longev*, v.2021; 2021.
- Rosenberg, A. H., Lade, B. N., Chui, D. S., Lin, S. W., Dunn, J. J. & Studier, F. W. 1987. Vectors for selective expression of cloned DNAs by T7 RNA polymerase. *Gene*, 56, 125-35.
- Sambrook, J. & Gething, M. J. 1989. Protein structure. Chaperones, paperones. *Nature*, 342, 224-5.
- Sambrook, J. & Russell, D. W. 2001. *Molecular cloning : a laboratory manual*, Cold Spring Harbor, N.Y., Cold Spring Harbor Laboratory Press.
- Sancho, J. 2013. The stability of 2-state, 3-state and more-state proteins from simple spectroscopic techniques... plus the structure of the equilibrium intermediates at the same time. *Arch Biochem Biophys*, 531, 4-13.
- Sancho, P., Sánchez-Monteagudo, A., Collado, A., Marco-Marín, C., Domínguez-González, C., Camacho, A., Knecht, E., Espinós, C. & Lupo, V. 2017. A newly distal hereditary motor neuropathy caused by a rare AIFM1 mutation. *Neurogenetics*, 18, 245-250.
- Schägger, H. & von Jagow, G. 1991. Blue native electrophoresis for isolation of membrane protein complexes in enzymatically active form. *Anal Biochem*, 199, 223-31.
- Schmitt, E., Parcellier, A., Gurbuxani, S., Cande, C., Hammann, A., Morales, M. C., Hunt, C. R., Dix, D. J., Kroemer, R. T., Giordanetto, F., Jaattela, M., Penninger, J. M., Pance, A., Kroemer, G. & Garrido, C. 2003. Chemosensitization by a non-apoptogenic heat shock protein 70-binding apoptosis-inducing factor mutant. *Cancer Res*, 63, 8233-40.
- Schreiber, C., Müller, H., Birrenbach, O., Klein, M., Heerd, D., Weidner, T., Salzig, D. & Czermak, P. 2017. A high-throughput expression screening platform to optimize the production of antimicrobial peptides. *Microb Cell Fact*, 16, 29.
- Seksek, O. & Bolard, J. 1996. Nuclear pH gradient in mammalian cells revealed by laser microspectrofluorimetry. *J Cell Sci*, 109 ( Pt 1), 257-62.

- Senda, T., Yamada, T., Sakurai, N., Kubota, M., Nishizaki, T., Masai, E., Fukuda, M. & Mitsuidagger, Y. 2000. Crystal structure of NADH-dependent ferredoxin reductase component in biphenyl dioxygenase. *J Mol Biol*, 304, 397-410.
- Sevrioukova, I. F. 2009. Redox-linked conformational dynamics in apoptosis-inducing factor. *J Mol Biol*, 390, 924-38.
- Sevrioukova, I. F. 2011. Apoptosis-inducing factor: structure, function, and redox regulation. *Antioxid Redox Signal*, 14, 2545-79.
- Sevrioukova, I. F. 2016. Structure/Function Relations in AIFM1 Variants Associated with Neurodegenerative Disorders. *J Mol Biol*, 428, 3650-65.
- Shelar, S. B., Kaminska, K. K., Reddy, S. A., Kumar, D., Tan, C. T., Yu, V. C., Lu, J., Holmgren, A., Hagen, T. & Chew, E. H. 2015. Thioredoxin-dependent regulation of AIF-mediated DNA damage. *Free Radic Biol Med*, 87, 125-36.
- Shendure, J. & Akey, J. M. 2015. The origins, determinants, and consequences of human mutations. *Science*, 349, 1478-83.
- Shrake, A. & Ross, P. D. 1992. Origins and consequences of ligand-induced multiphasic thermal protein denaturation. *Biopolymers*, 32, 925-40.
- Sorrentino, L., Calogero, A. M., Pandini, V., Vanoni, M. A., Sevrioukova, I. F. & Aliverti, A. 2015. Key Role of the Adenylate Moiety and Integrity of the Adenylate-Binding Site for the NAD(+)/H Binding to Mitochondrial Apoptosis-Inducing Factor. *Biochemistry*, 54, 6996-7009.
- Sorrentino, L., Cossu, F., Milani, M., Aliverti, A. & Mastrangelo, E. 2017. Structural bases of the altered catalytic properties of a pathogenic variant of apoptosis inducing factor. *Biochem Biophys Res Commun*, 490, 1011-1017.
- Stein, A., Whitlock, J. P. & Bina, M. 1979. Acidic polypeptides can assemble both histones and chromatin in vitro at physiological ionic strength. *Proc Natl Acad Sci U S A*, 76, 5000-4.
- Studier, F. W. & Moffatt, B. A. 1986. Use of bacteriophage T7 RNA polymerase to direct selective high-level expression of cloned genes. *J Mol Biol*, 189, 113-30.
- Studier, F. W., Rosenberg, A. H., Dunn, J. J. & Dubendorff, J. W. 1990. Use of T7 RNA polymerase to direct expression of cloned genes. *Methods Enzymol*, 185, 60-89.
- Susin, S. A., Daugas, E., Ravagnan, L., Samejima, K., Zamzami, N., Loeffler, M., Costantini, P., Ferri, K. F., Irinopoulou, T., Prévost, M. C., Brothers, G., Mak, T. W., Penninger, J., Earnshaw, W. C. & Kroemer, G. 2000. Two distinct pathways leading to nuclear apoptosis. *J Exp Med*, 192, 571-80.
- Susin, S. A., Lorenzo, H. K., Zamzami, N., Marzo, I., Brenner, C., Larochette, N., Prevost, M. C., Alzari, P. M. & Kroemer, G. 1999a. Mitochondrial release of caspase-2 and -9 during the apoptotic process. *J Exp Med*, 189, 381-94.
- Susin, S. A., Lorenzo, H. K., Zamzami, N., Marzo, I., Snow, B. E., Brothers, G. M., Mangion, J., Jacotot, E., Costantini, P., Loeffler, M., Larochette, N., Goodlett, D. R., Aebersold, R., Siderovski, D. P., Penninger, J. M. & Kroemer, G. 1999b. Molecular characterization of mitochondrial apoptosis-inducing factor. *Nature*, 397, 441-6.
- Susin, S. A., Zamzami, N., Castedo, M., Hirsch, T., Marchetti, P., Macho, A., Daugas, E., Geuskens, M. & Kroemer, G. 1996. Bcl-2 inhibits the mitochondrial release of an apoptogenic protease. *J Exp Med*, 184, 1331-41.
- Taylor, R. G., Walker, D. C. & McInnes, R. R. 1993. E. coli host strains significantly affect the quality of small scale plasmid DNA preparations used for sequencing. *Nucleic Acids Res*, 21, 1677-8.
- Thériault, S., Don-Wauchope, A., Chong, M., Lali, R., Morrison, K. M. & Paré, G. 2016. Frameshift mutation in the APOA5 gene causing hypertriglyceridemia in a

- Pakistani family: Management and considerations for cardiovascular risk. *J Clin Lipidol*, 10, 1272-7.
- Tollin, G., Hurley, J. K., Hazzard, J. T. & Meyer, T. E. 1993. Use of laser flash photolysis time-resolved spectrophotometry to investigate interprotein and intraprotein electron transfer mechanisms. *Biophys Chem*, 48, 259-79.
- Tsi, C. J., Chao, Y., Chen, C. W. & Lin, W. W. 2002. Aurintricarboxylic acid protects against cell death caused by lipopolysaccharide in macrophages by decreasing inducible nitric-oxide synthase induction via IkappaB kinase, extracellular signal-regulated kinase, and p38 mitogen-activated protein kinase inhibition. *Mol Pharmacol*, 62, 90-101.
- Turnbull, D. M. & Rustin, P. 2016. Genetic and biochemical intricacy shapes mitochondrial cytopathies. *Neurobiol Dis*, 92, 55-63.
- Urbano, A., Lakshmanan, U., Choo, P. H., Kwan, J. C., Ng, P. Y., Guo, K., Dhakshinamoorthy, S. & Porter, A. 2005. AIF suppresses chemical stress-induced apoptosis and maintains the transformed state of tumor cells. *Embo J*, 24, 2815-26.
- Vahsen, N., Cande, C., Briere, J. J., Benit, P., Joza, N., Larochette, N., Mastroberardino, P. G., Pequignot, M. O., Casares, N., Lazar, V., Feraud, O., Debili, N., Wissing, S., Engelhardt, S., Madeo, F., Piacentini, M., Penninger, J. M., Schagger, H., Rustin, P. & Kroemer, G. 2004. AIF deficiency compromises oxidative phosphorylation. *Embo J*, 23, 4679-89.
- Vahsen, N., Cande, C., Dupaigne, P., Giordanetto, F., Kroemer, R. T., Herker, E., Scholz, S., Modjtahedi, N., Madeo, F., Le Cam, E. & Kroemer, G. 2006. Physical interaction of apoptosis-inducing factor with DNA and RNA. *Oncogene*, 25, 1763-74.
- van den Berg, P. A., van Hoek, A., Walentas, C. D., Perham, R. N. & Visser, A. J. 1998. Flavin fluorescence dynamics and photoinduced electron transfer in Escherichia coli glutathione reductase. *Biophys J*, 74, 2046-58.
- Vanommeslaeghe, K., Hatcher, E., Acharya, C., Kundu, S., Zhong, S., Shim, J., Darian, E., Guvench, O., Lopes, P., Vorobyov, I. & Mackerell, A. D. 2010. CHARMM general force field: A force field for drug-like molecules compatible with the CHARMM all-atom additive biological force fields. *J Comput Chem*, 31, 671-90.
- Velázquez-Campoy, A., Goñi, G., Peregrina, J. R. & Medina, M. 2006. Exact analysis of heterotropic interactions in proteins: Characterization of cooperative ligand binding by isothermal titration calorimetry. *Biophys J*, 91, 1887-904.
- Velazquez-Campoy, A., Sancho, J., Abian, O. & Vega, S. 2016. Biophysical Screening for Identifying Pharmacological Chaperones and Inhibitors Against Conformational and Infectious Diseases. *Curr Drug Targets*, 17, 1492-505.
- Verdin, E. 2015. NAD<sup>+</sup> in aging, metabolism, and neurodegeneration. *Science*, 350, 1208.
- Villanueva, R., Ferreira, P., Marcuello, C., Usón, A., Miramar, M. D., Peleato, M. L., Lostao, A., Susin, S. A. & Medina, M. 2015. Key Residues Regulating the Reductase Activity of the Human Mitochondrial Apoptosis Inducing Factor. *Biochemistry*, 54, 5175-84.
- Villanueva, R., Romero-Tamayo, S., Laplaza, R., Martínez-Olivan, J., Velázquez-Campoy, A., Sancho, J., Ferreira, P. & Medina, M. 2019. Redox- and Ligand Binding-Dependent Conformational Ensembles in the Human Apoptosis-Inducing Factor Regulate Its Pro-Life and Cell Death Functions. *Antioxid Redox Signal*, 30, 2013-2029.
- Vivian, J. T. & Callis, P. R. 2001. Mechanisms of tryptophan fluorescence shifts in proteins. *Biophys J*, 80, 2093-109.

- Vosler, P. S., Sun, D., Wang, S., Gao, Y., Kintner, D. B., Signore, A. P., Cao, G. & Chen, J. 2009. Calcium dysregulation induces apoptosis-inducing factor release: cross-talk between PARP-1- and calpain-signaling pathways. *Exp Neurol*, 218, 213-20.
- Wang, C. & Youle, R. J. 2009. The role of mitochondria in apoptosis\*. *Annu Rev Genet*, 43, 95-118.
- Wang, Y., Kim, N. S., Haince, J. F., Kang, H. C., David, K. K., Andrabi, S. A., Poirier, G. G., Dawson, V. L. & Dawson, T. M. 2011. Poly(ADP-ribose) (PAR) binding to apoptosis-inducing factor is critical for PAR polymerase-1-dependent cell death (parthanatos). *Sci Signal*, 4, ra20.
- Wang, Y., Kim, N. S., Li, X., Greer, P. A., Koehler, R. C., Dawson, V. L. & Dawson, T. M. 2009. Calpain activation is not required for AIF translocation in PARP-1-dependent cell death (parthanatos). *J Neurochem*, 110, 687-96.
- Whitmore, L. & Wallace, B. A. 2008. Protein secondary structure analyses from circular dichroism spectroscopy: methods and reference databases. *Biopolymers*, 89, 392-400.
- Wiseman, T., Williston, S., Brandts, J. F. & Lin, L. N. 1989. Rapid measurement of binding constants and heats of binding using a new titration calorimeter. *Anal Biochem*, 179, 131-7.
- Xie, H., Vucetic, S., Iakoucheva, L. M., Oldfield, C. J., Dunker, A. K., Uversky, V. N. & Obradovic, Z. 2007. Functional anthology of intrinsic disorder. 1. Biological processes and functions of proteins with long disordered regions. *J Proteome Res*, 6, 1882-98.
- Ye, H., Cande, C., Stephanou, N. C., Jiang, S., Gurbuxani, S., Larochette, N., Daugas, E., Garrido, C., Kroemer, G. & Wu, H. 2002. DNA binding is required for the apoptogenic action of apoptosis inducing factor. *Nat Struct Biol*, 9, 680-4.
- Zamzami, N., Marchetti, P., Castedo, M., Hirsch, T., Susin, S. A., Masse, B. & Kroemer, G. 1996. Inhibitors of permeability transition interfere with the disruption of the mitochondrial transmembrane potential during apoptosis. *FEBS Lett*, 384, 53-7.
- Zanetti, G. & Curti, B. 1980. Ferredoxin-NADP<sup>+</sup> oxidoreductase. In: SAN PIETRO, A. (ed.) *Part C: Photosynthesis and Nitrogen Fixation*. Academic Press.
- Zhang, Y., Han, T., Zhu, Q., Zhang, W., Bao, W., Fu, H. J., Yang, J., Huang, X. J., Wei, J. X., Meng, Y. L., Zhao, J., Cao, Y. X., Jia, L. T. & Yangi, A. G. 2009. The proapoptotic activity of C-terminal domain of apoptosis-inducing factor (AIF) is separated from its N-terminal. *Biol Res*, 42, 249-60.
- Zhu, C., Wang, X., Deinum, J., Huang, Z., Gao, J., Modjtahedi, N., Neagu, M. R., Nilsson, M., Eriksson, P. S., Hagberg, H., Luban, J., Kroemer, G. & Blomgren, K. 2007. Cyclophilin A participates in the nuclear translocation of apoptosis-inducing factor in neurons after cerebral hypoxia-ischemia. *J Exp Med*, 204, 1741-8.
- Zong, L., Guan, J., Ealy, M., Zhang, Q., Wang, D., Wang, H., Zhao, Y., Shen, Z., Campbell, C. A., Wang, F., Yang, J., Sun, W., Lan, L., Ding, D., Xie, L., Qi, Y., Lou, X., Huang, X., Shi, Q., Chang, S., Xiong, W., Yin, Z., Yu, N., Zhao, H., Wang, J., Salvi, R. J., Petit, C., Smith, R. J. & Wang, Q. 2015. Mutations in apoptosis-inducing factor cause X-linked recessive auditory neuropathy spectrum disorder. *J Med Genet*, 52, 523-31.
- Zong, L., Zhao, J., Wu, W., Wang, J., Huang, D. & Liu, M. 2020. AIF knockdown induce apoptosis and mitochondrial dysfunction in cochlear spiral ganglion neurons in vitro. *Mol Med Rep*, 21, 1910-1920.







**Universidad**  
Zaragoza



Instituto Universitario de Investigación  
**Biocomputación y Física**  
**de Sistemas Complejos**  
**Universidad Zaragoza**

